Observational and theoretical study of the point sources of very high energy γ-ray emission

by

M.Sc. Iurii Babyk

A thesis is submitted to Dublin City University

for the degree of Doctor of Philosophy

in the School of Physical Sciences

Supervisors: Dr. M. Chernyakova, Prof. G. Hughes

January 2017

Declaration of Authorship

I hereby certify that this material, which I now submit for assessment on the programme of study leading to the award of Ph.D. is entirely my own work, and that I have exercised reasonable care to ensure that the work is original, and does not to the best of my knowledge breach any law of copyright, and has not been taken from the work of others save and to the extent that such work has been cited and acknowledged within the text of my work.

Signed: _____

ID No.: _____

Date: _____

Acknowledgements

I would like to thank my thesis supervisor Dr. Masha Chernyakova, she has always been willing to take the time to discuss in great depth our own research area and many other interesting research areas. Every time we have met, I have been inspired a lot by her great scientific insights. I must also thank Masha for her patience in explaining to me the varying scientific aspects of my thesis. In addition, I enjoyed going to parties in her home with Masha's family, and I will never forget the delicious dishes she prepared for me being a student. It is my great pleasure and honor to get to know Masha during these years, trust this will continue into the future.

In DCU, I would like to thank all of the wonderful staff of School of Physical Sciences, namely Prof. Enda McGlynn, Prof. Greg Hughes, Prof. Colette McDonagh, physics dept secretary Lisa Payton, plus all the staff lectures and graduate students in the School of Physical Sciences. People that I met during conferences and seminars were more than helpful to me, the list would be far too long to name one by one, but I would like to say a big thank you here to all of them.

I would also like to thank my examiners, Prof. Joern Willms and Prof. Eugene Kennedy under which guidance thesis got the much improved current shape.

In DIAS, I would like to thank the staff in the Dublin Institute for Advanced Studies, namely the School of Cosmic Physics Director, Head of the Astronomy & Astrophysics Section, Senior Professor Prof. Luke O'C Drury, Prof. Tom Ray, Prof. Felix Aharonian, who have taken care of me while in the Section. To the IT personnel, I would also like to thank Philippe and Dmitrii, who helped me with my computer issues. My thanks also go out to the very helpful staff members, Anne Grace-Casey and Eileen Flood. Finally, thank you to all the School fellows, post docs and scholars for all their formal and informal discussions both of a scientific and non scientific nature.

The number of people in DIAS and DCU whom I would like to thank is so big, that probably the whole volume of this thesis would not be enough to fit everybody in. I mentioned only briefly very few of them and would like to ask all the others to forgive me their absence in this acknowledgment. I remember all of you and you always will be in my heart.

I would like to voice my gratitude to my Ukrainian advisor Dr. Irina Vavilova at the Main Astronomical Observatory of National Academy of Science of Ukraine for her guidance and continuous support during these years. I want to thank Dr. Ievgen Vovk

at the Max-Planck Institute fur Physics for his encouragement and numerous discussions over skype, in Ireland and Ukraine during my academic career. Thanks to Dr. Mike Hogan for correcting the numerous English mistakes I made during the writing of this thesis.

Last but not least, I can not forget Hilary O'Donnell/Sullivan, during my Ph.D. she was my real local mother, my Irish Mother, who cares about me in DIAS and Dunsink Observatory, providing me a nice possibility to improve my English skills getting involved and meeting with lots of people through the outreach program in Dunsink Observatory.

Finally, and most importantly, this work would not have been possible without the endless support and encouragement from my lovely wife, parents, family and friends.

Contents

Observational and theoretical study of the point sources of very high energy γ-ray emission

Iurii Babyk

Abstract

The study of the sky using the most energetic photons plays a crucial role in detecting and exploring high-energy phenomena in the Universe. Observations conducted over recent years with new ground-based and space-borne gamma-ray instruments reveal that the universe is full of extreme accelerators, i.e., objects with surprisingly high efficiency for acceleration of electrons. In particular such an efficient acceleration is observed in gamma-ray-loud binary (GRLB) systems.

GRLBs are a newly identified class of X-ray binaries in which interaction of an outflow from the compact object with the wind and radiation emitted by a companion star leads to the production of very-high-energy gamma-ray emission. Only five such systems have been firmly detected as persistent or regularly variable TeV gamma-ray emitters. All GRLBs detected in the TeV energy range contain a hot, young star and exhibit variable or periodic emission at multiple wavelengths across the electromagnetic spectrum. Details of the physical mechanism of the high-energy activity of GRLBs are not clear yet. Broad multi-wavelength observations are crucial to reveal the characteristic energies of the relativistic wind and better understanding of the nature of these sources. It looks quite possible that all these systems can be understood within the "hidden pulsar" model, and the observed differences are due to the different sizes of the system.

In my work, I concentrate on the X-ray and gamma-ray emission observed from gamma-ray binaries PSR B1259−63 and LS I +61° 303 with *Suzaku*, *XMM*-Newton, *Swift*, *Chandra* and *Fermi* observatories. In PSR B1259−63, the compact source is a

young 48 ms radio pulsar orbiting Be-type star with period of 3.4 years. During my studies, I have been intensively involved in the analysis of the results of two multi-wavelength campaigns organized in 2010 and 2014 during the periastron passages in this system. These observations reveal complex spectral variability of the source as it passes through the disk of the companion star. In my work, I have tested different theoretical models trying to reproduce the observed behaviour. For LS I $+61^{\circ}$ 303, I have analyzed historical data of *Suzaku*, *Chandra*, *XMM*-Newton, *Swift* and for the first time demonstrated the variability of the source column density along the orbit.

Dedicated to

Princess Kateryna . . .

Chapter 1

From X-ray binaries to gamma-ray binaries

In this chapter, I describe the current knowledge about X-ray binary systems and their parts, namely about neutron stars, pulsars, companion stars, etc. I also overview the multi-wavelength picture of X-ray binary systems. I show how X-ray binaries came to be observed at gamma-ray wavelengths. I give a current review of five gamma-ray binary systems, their observational and theoretical characteristics, and try to answer why these objects are significant astrophysical laboratories giving access to many different physical conditions on a regular timescale. I also discuss the basic ingredients that models of gamma-ray binary systems use including OB-type stars and Be-pulsars. In addition, I show the challenges that these models currently face. For PSR B1259−63, I discuss the main properties of a companion Be-type star and compact object (a neutron star) that orbit with a period of 3.4 yr around the massive Be-type star. I describe the physical processes during interaction between pulsar and star winds, i.e., I review the radiation processes performed in a pulsar-wind-nebula complex, as well as non-thermal emission processes inside binary systems. For the other four objects, since these sources are less well known than PSR B1259−63, I give some general observational results, i.e., a review of X-ray and Gamma-ray observations on different timescales. In Summary, I discuss why these sources are significant for the present understanding of the production of high-energy and very-high-energy emissions, and why I decide to study gamma-ray binary systems.

1.1 X-ray binaries

In the late 1960's - early 1970's, it was hypothesized that the sources visible in the hard X-ray (> 10 keV), may be associated with neutron stars in binary systems (see Fig. 1.1). At the same time, in 1964, [1] pointed to the possibility of experimental observation of black holes, due to the large energy of accretion onto a black hole in a binary system. With a significant accretion rate, which is supported by filling the Roche lobe of the optical star (the Roche lobe is the region surrounding a star in a binary system, in which matter is bound to the star by gravity), an accretion disk around the compact object is formed. Determining the type of compact component in the binary systems remains one of the most pressing problems facing observational galactic X-ray astronomy. Reliable identification of the X-ray object around the optical star is only possible by collecting more information about the coincidence of temporary manifestations of the object in the hard X-ray and optical radiations. Such information can be obtained using simultaneous monitoring of flares, correlation with the X-ray and optical brightness, as well as simultaneous observation of a batch process with the same period value as in X-ray and optical studies.

It should be noted that most X-ray binary stars are strongly variable in the hard spectral range, and temporal variations of flux are very diverse. Observed sources that are characterized by regular periodic changes in flux, possibly including eclipses, identify such objects as binary systems [2]. The periodic processes observed in hard X-ray radiation of binaries, can be caused by the following reasons. The orbital motion of the components may result in periodic changes in the X-ray flux associated with eclipses of ordinary star field radiation. Typical periods lie in the range of ∼1 day for massive binary systems (for example, the system 4U1700-37, for which P = 3.412 d [3, 4]), and ∼2 d for sources as Cen X-3 [5]. The low-mass systems are characterized by lower values of the orbital periods (for example, according to the measurements in the optical range of the orbital period of Sco X-1 is ∼0.787 d [6]). Pulsars are also known with rotational periods in the 1-10 ms range [7–15]. The phases, that characterize the nature of periodic eclipsing, have the form of more or less deep dips with rectangular shape in the case of total eclipses or flattened shape in the case of incomplete eclipses. The width of the dip essentially depends on the inclination of the orbit of a compact component, as well as the distance between the components and the instead of a star. There is the possibility of hard radiation modulation with a period that is equal to the orbit, and not associated with eclipses. Thus, changing the distance between the components can lead to periodic changes in the rate of accretion.

Radio (see Subsec. 1.1.3) and X-ray (see Subsec. 1.1.2) pulsars have different mechanisms of pulse production. The radio pulsars have pulsations with periods of

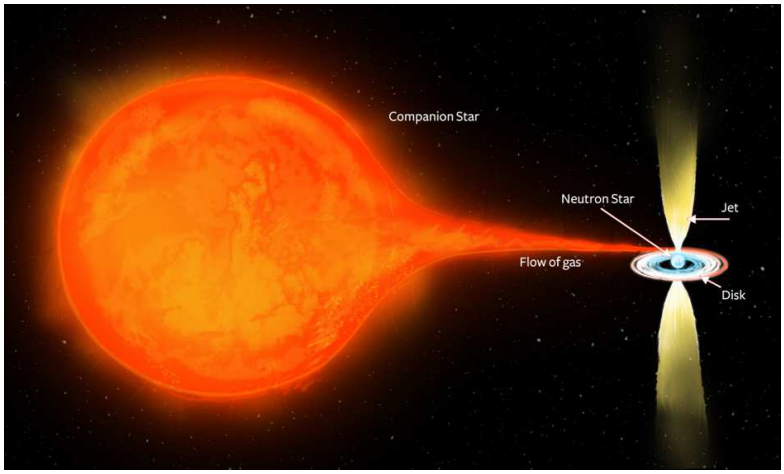

FIGURE 1.1: The binary system PSR J1023+0038. The image is taken from *ICRAR* (http://www.icrar.org/).

milliseconds to seconds [16–18]. All radio pulsars lose angular momentum and slow down. On the contrary, the X-ray pulsars demonstrate spin-down and spin-up behavior. 99% of radio pulsars are isolated objects. They emit their rotational energy in the form of high-energy particles. The X-ray pulsars are members of binary systems. The X-ray pulsars accrete matter consisting relativistic particles from the wind of stars or accretion disks. However, the nature of spin behavior of X-ray pulsars is unclear [19]. One of the possible factors leading to the emergence of periodicities in the hard radiation of binary systems is the precession of the accretion disk. It is believed that the precession results from long-period processes, and periods may exceed the value of the actual orbital periods. Periodic changes of flux can also be caused by the precession of the rotation axis of the components of the binary system. Studying the periodicities of averaged phase profiles in hard X-ray radiation allows us to determine the dynamic parameters of the system, and also allows us to study the exchange of energy and momentum between the system components. The observations in X-rays provide information directly related to the spatial regions in the source, where processes with a large release of energy occur.

The majority of low-mass X-ray binaries do not present as pulsars, i.e., apparently, they contain slowly rotating neutron stars with a relatively weak magnetic field. Here, the "weak" refers to magnetic fields, characterized by the value of B $\sim 10^9$-10^{10} G, that are weak in comparison with the magnetic fields of X-ray and gamma-ray pulsars (B $\sim 10^{11}$ - 10^{14} G) [20]. It can be assumed that these objects must be quite old, since according to the standard scenario, the magnetic moments of the newly born neutron stars must be higher, because the law of conservation of angular momentum in the process of gravitational contraction should cause the rotation of the star to speed up. In the process of evolution, the magnetic field of a neutron star gradually deteriorates, and its rotation is slowed down due to radiation and due to the action of tidal forces if

the neutron star is part of a binary system [20, 21]. Confirmation of such a scenario is the fact that the optical low-mass companions of the binaries that are not pulsars are, as a rule, old stars typically corresponding to spherical populations such as the galactic bulge or globular clusters. At the same time, the optical companions of the majority of X-ray pulsars in binary systems are the hot, young giants located in the galactic arms (disk population) [22, 23].

The temporal X-ray properties of non-pulsar low-mass binaries are very diverse. There are several main groups:

- Bursters, i.e., sources that are characterized by short, sporadic increases in the flux of X-rays such as flares.
- Sources that are characterized by irregular noise variation of X-rays.
- Transients or temporary sources, for which there is some intense increases in X-ray flux, the duration of which is usually from a few hours to days or even months.

In addition to the marked time features, the low-mass binaries with old neutron stars have a number of additional common properties. In particular, their optical companions are dim stars, whose spectra have no features associated with absorption. Such objects have relatively high X-ray luminosity compared with the optical: $L_{\rm X}/L_{\rm opt} \sim 10^2$ - 10^4 (for massive binaries $L_{\rm X}/L_{\rm opt} \sim 10^{-4}$ - 10^1). It is mainly due to a lower X-ray luminosity ($L_X \sim 10^{34}$ erg/s) of low-mass binaries in comparison with the massive objects, where the X-ray luminosity can reach 10^{37} - 10^{38} erg/s. The X-ray spectra of the low-mass binaries are softer than the spectra of X-ray pulsars. Furthermore, periodic X-ray type eclipses are typically not observed in such systems [22]. In our Galaxy, about one hundred low-mass binary systems that do not manifest themselves as X-ray pulsars have been discovered. More than ten of them are in globular clusters, which due to the distribution of stars in the Galaxy suggests a fairly high relative concentration of such systems in globular clusters [24]. Most other systems of this type exist in the galactic bulges, i.e., the spherical population of galactic objects concentrated to the center of the Galaxy [22]. As a result, some researchers consider the galactic bulge as a kind of giant globular supercluster. Many attempts have been made to detect pulsations of low-mass X-ray binaries in the galactic bulge. However, all of them were negative, characterized by the following upper limits: for the ∼3% (the range of fluctuations was $\sim 2{\cdot}10^{-3}$-2 s, [22]), for 1-10% ($\sim$1.6-10^3 s, [25]), ∼ 30% ($\sim 10^2$-$2{\cdot}10^5$ s, [26]).

X-ray sources found in globular clusters have apparently the same nature as the sources of the galactic bulge. They are compact low-mass binary systems containing a neutron star with a weak magnetic field. Such clusters are “enriched” by X-ray sources

[22]. Since the density of objects in a globular cluster is maximum at the center, it has been suggested that X-ray sources are also located near the centers of globular clusters. This assumption was firstly confirmed by the observations of the satellite $SAS3$, which allowed the coordinates of these sources to be determined with high accuracy. The relatively high concentration of X-ray sources in globular clusters is a result of the high concentration of compact objects, especially in the central regions of clusters.

As noted above, many of the low-mass binaries manifest themselves as X-ray bursters, i.e., sources with rather short (from a fraction of a second to several hundred seconds) bursts. There are type 1 and type 2 bursters. Most of the known bursters are sources of type 1, which are characterized by relatively long intervals between bursts (from hours to a day or more), and "softening" of the spectrum [22]. Type 2 bursters are similar to the source MXB 1730-335, and received the name of "Rapid Bursters". These sources are located in globular clusters and generate bursts with the intervals between them from seconds to minutes. The duration of the bursts can vary by two orders of magnitude (from a fraction of a second to tens of seconds). The fluence of bursters is approximately proportional to the waiting time between bursts.

The physical mechanisms leading to the generation of bursters of type 1 and 2 are significantly different. It has been observed that the spectral evolution of some bursters of type 1 are in good agreement with the model that considers the cooling-ray bursters. Today it is a generally accepted theory that type 1 bursters are caused by thermonuclear explosions of accreting matter on the surface of the neutron star [27]. As a result, the released energy is converted to a quasi-stationary X-ray radiation, which is also observed for the majority of sources of type 1 bursters. As for type 2 bursters, they can not be generated due to thermonuclear explosions, because the high frequency of repetition requires a very high rate of accretion during which the significant flux of quasi-stationary X-ray radiation should be observed. However, this flux is not observed from the type 2 bursters. Therefore, the hypothesis has been suggested that the type 2 bursters are associated with various accretion instabilities, i.e., the gravitational energy of the accreting material from collapsed object is a source of energy [28]. The estimated size of the emitting object in this model gives an effective radius of the "black body" of 7-10 km. The estimated luminosity within a typical distance from the source in the region of the galactic center, $\sim$10 kpc, and assuming a mass of the emitting object of $\sim 1.4 M_{\odot}$ gives a value close to the Eddington limit[1]. Thus, the estimated size and mass provide evidence that the radiating object in sources such as X-ray bursters is a neutron star. In addition to the X-ray bursters, the low-mass binary includes objects

[1]The maximum luminosity for which the gravitational force on a fluid element exceeds the radiation pressure force, i.e., the maximum luminosity at which matter can be accreted [10].

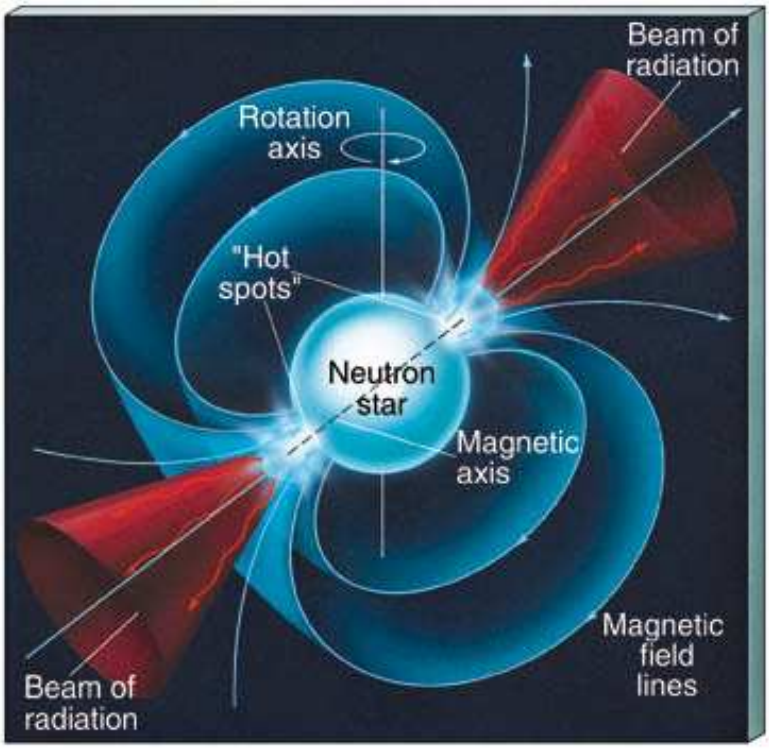

FIGURE 1.2: The schematic view of a neutron star. The image is taken from [31].

that are characterized by extremely irregular variations of flux. One of these objects is the well-known Sco X-1.

It should be noted that the periodic processes in hard X-ray radiation could be observed for a relatively small number of low-mass binary systems with neutron stars. This is because the compact binary systems must have relatively short orbital periods, and in such systems it is difficult to ensure favorable conditions for the full eclipse of the optical component emitting region due to the relatively small size of the relative accretion disk sizes.

1.1.1 Neutron stars

Neutron stars are extremely compact objects (with a radius of about 10 km) with a powerful magnetic field. Due to the fact that they consist almost entirely of neutron matter it is possible to "pack" a mass comparable to the mass of the Sun into such a small, in astronomical terms, region. The existence of neutron stars was predicted in the 1930's by L.Landau immediately after the discovery of the neutron in 1932. Note that all neutron stars whose masses are known with sufficient accuracy (they are members of binary pulsars) have masses in the range of 1.4 to 3.2 solar masses [20, 29, 30].

Neutron stars are one of the most interesting astronomical objects from the physical point of view (see Fig. 1.2). The physics of neutron stars is connected with superfluidity. These sources are important for plasma physics, especially for studying the interaction of plasma with a strong magnetic field and the processes of superstrong magnetic fields. In addition, neutron stars are one of the most important laboratories for tests of general relativity.

In the 1960's radio pulsars were discovered and identified with neutron stars. To date, astronomers have found more than 2,500 of these compact objects[2]. Most of them are radio pulsars, i.e., sources with strictly periodic radio pulses, and the rest are X-ray or gamma-ray sources. What is the actual number of neutron stars in the Galaxy? Astronomers believe that our Galaxy includes millions of such objects. It is quite simple to detect such objects, if the neutron star is a component of a binary system. Such systems are characterized by the accretion onto the surface of a neutron star from the second component of the binary. As a result, there is powerful X-ray radiation that we can detect with spacecraft instruments.

However, neutron stars do not only exist in binary systems. Firstly, isolated neutron stars can be formed as a result of the collapse of the binary system. Isolated neutron stars can also be formed as a result of "natural death", i.e., a supernova explosion, i.e., in the case of an initially single massive star.

The detection of an isolated neutron star is a rather complicated task. It is difficult to detect an object with a diameter of only 10 km, with the thermal radiation of the object, even if it has a higher temperature, and with a distance that is more than one kpc. To see an isolated neutron star at such a large distance can be exclusively achieved only during two stages of its evolution. The most famous is the so-called ejection stage when the radiation of a rapidly rotating neutron star (electromagnetic radiation or wind of relativistic particles) does not allow the substance to fall on its surface, and then we can see the neutron star as a radio pulsar. But, unfortunately, this stage is relatively brief. In addition, the pulsar emits asymmetrically, and the beam can slide past the Earth. For this reason, we do not see more than half of pulsars that are available for us. If a young star has an extremely strong magnetic field, 10^{15} G, then such an object is called a "magnetar" (see Fig. 1.3), and it can be found during detection of soft gamma-ray bursts, and probably also as an X-ray source.

It is much more interesting to see a single neutron star during the accretion stage, which can take up a significant portion of its evolution if the star is not moving with very high speed [32, 33]. During this stage, matter is falling onto its surface without anything opposing it. The various processes that accompany this fall give the possibility

[2]According to the ATNF Pulsar Catalogue, http://www.atnf.csiro.au/research/pulsar/psrcat/

FIGURE 1.3: An image of the magnetar in the yang star cluster Westerlund. The image is taken from wikimedia.org.

of detecting the neutron star. But, where does the matter come from if we are dealing with an isolated neutron star? The answer to this question is not very complicated. We should not forget that space is not a void. All space between the stars is filled with gas and dust. Thus, the interstellar medium could well become a source of matter which accretes onto a neutron star. The idea of the accretion of the interstellar medium into the neutron stars, as well as into the black holes, has been debated by scientists for a long time. Since the nineties, the modern X-ray satellites such as *ROSAT* began to be able to detect such objects [34], the mechanism of energy has begun to attract more and more attention of astrophysicists. Now the new generation of X-ray satellites has detected about one hundred candidates of isolated accreting neutron stars, and these detections require detailed study and analysis, as well as new observations with modern instruments.

Recent calculations show that the brightest sources must be observed during the flight of the neutron star through molecular clouds, since they are characterized by the high density of interstellar matter. Thus, depending on the speed of the star relative to the cloud, as well as its density, the accretion can assume very interesting shapes. For example, if the velocity of the neutron star with respect to its surrounding matter is sufficiently small, e.g. several kilometers per second, and the cloud has a high concentration ($10^2 - 10^4$ cm^{-3}), then we may see the so-called regime of supercritical accretion which forms jet emissions [33].

Another case of accretion onto the neutron star during its contact with the molecular cloud is associated with the fact that the magnetic field (with the rapid rotation) may be able to keep matter from falling for some time [35]. In such circumstances, a

shell can be formed around a neutron star. When the mass of the shell becomes too large, the magnetic field and the rotation will not be able to keep the plasma supported, and it will fall to the surface of the neutron star. Then this process repeats. Thus, such a neutron star becomes a periodic X-ray source. In this case, astronomers are able to see such objects, because the emitted energy is released in a relatively high-power pulse, which is easier to register. Flares can also occur on the surface of the neutron stars. It is another type that associated with thermonuclear reactions. During these flares the matter accumulates on the surface of star. Their power is about 10 times lower than in flares that happen due to a fall of the matter onto the surface (such objects are observed in binaries and are called "bursters", see above for details).

By the way, when the neutron star passes through the dense molecular cloud, an interesting effect can occur (it is somewhat similar to the hysteresis effect), that was described in the 1970s by the Russian astronomer V. Shvartsman [36–38]. During the pulsar stage the neutron star enters into the molecular cloud (ejection), after that this step is replaced by a stage of accretion since the falling matter on the surface of the star "crushes" the pulsar. Then, after the departure of the neutron star from the clouds, the pulsar may not re-appear, since the matter is now so close to the surface that it is not so easy to "scatter", using, for example, a magnetic field. If we could a look at our Galaxy from the side, we would see that the neutron stars that are accreting matter from molecular clouds are mainly distributed in the region at a distance of 5-7 kpc from the center. This is due to the fact that here the density of the interstellar medium has a maximum, as well as the distribution of neutron stars, which has a toroidal shape with a maximum at about the same region of the Galaxy.

How many isolated neutron stars are located around the vicinity of our Sun? According to various estimates, their number amounts to several thousand. But why do we not see them? This is due to the fact that the luminosity of such X-ray sources is low, about 10^{31} erg/s, if the accretion comes from the inter-cloud environment. In the dense molecular cloud the luminosity of an isolated star can reach 10^{36} erg/s. In this case, we must assume that luminosity will depend not only on internal parameters of the interstellar medium and the neutron star, but also on their relative velocity, since luminosity is proportional to υ^{-3} (if speed is decreasing, the luminosity will increase). However, the probability of small velocities, 20-40 km/s and below, is very small. Due to the asymmetry of supernova explosions, the neutron stars must have a very large average speed, 200-300 km/s [36, 37]. It is important to note that such systems have not been discovered yet.

1.1.2 X-ray pulsars in binaries

As noted above, a neutron star with a strong magnetic field ($\sim 10^{11}$-10^{13} G), and a member of a compact relativistic component of the binary system, determines the existence of an astrophysical object like the X-ray pulsar. The model of a rotating neutron star in a binary system located in the accretion phase, provides an explanation of short- and long- period X-ray pulsars [39]. The properties of pulsars are determined by the magnitude of the magnetic field on the surface of a neutron star, by the type of the companion star, the degree of filling of its Roche lobe and the distance between the components of the binary system. Because of conservation of the magnetic flux we expect that neutron stars have magnetic fields which are $(\mathrm{R}_{star}/\mathrm{R}_{ns})^2$ higher than those of normal stars.

A neutron star can accrete matter either by capture of stellar wind of the optical companion, or as a result of the expiration of the donor star through the Roche lobe. At the neutron star, the accretion flows are characterized by a strong magnetic field, which causes the ionized matter to fall along the field lines in the magnetic poles of the neutron star. The discrepancy between the axis of rotation of the neutron star and the axis of the magnetic dipole, as well as the possible asymmetry of radiation areas near the polar caps leads to a pulsed radiation with a period equal to the period of rotation of the neutron star with an intensity proportional to [39–43]

$$L \sim G\frac{M_{\mathrm{X}}M'}{R_{\mathrm{X}}} \simeq \left(1.2\times 10^{36}\mathrm{erg/s}\right)\cdot\left(\frac{\dot{M}}{10^{-10}M_{\odot}\mathrm{yr}^{-1}}\right)\cdot\left(\frac{M_{\mathrm{X}}}{1.4M_{\odot}}\right)\cdot\left(\frac{10\mathrm{km}}{R_{\mathrm{X}}}\right), \quad (1.1)$$

where R_{X} is the radius of the neutron star, M_{X} is the mass of the neutron star, $\dot{M}$ is the time rate of mass loss of the neutron star by accretion, and G is the gravitational constant. The presence of angular momentum from falling matter, as well as the interaction between the incident flux and magnetic field, lead to the change of the moment of a neutron star, which leads to the observed changes in the pulsation period of a few days [44].

The luminosity of an accreting neutron star allows us to obtain an assessment of "black-body" effective temperature T_{eff} of the emitting region using the basis of the law of Stefan-Boltzmann's, $L = S\cdot T_{\mathrm{eff}}^4$. In the case of the typical size of the emitting regions near the polar caps, $S \approx 1$ km^2, Eq. 1.1 gives the value of the effective temperature $kT_{\mathrm{eff}} \sim 3$ keV. The peak of the X-ray spectrum of an accreting pulsar is observed at these energies (in the spectral representation νJ_ν, where J_ν is the spectral flux density, while ν is the frequency of the detected radiation). However, as noted above, the overall emission spectra of the hard X-ray pulsars are non-thermal in nature and in the energy

range from a few to hundreds of keV, significantly harder than predicted by blackbody spectrum with the effective temperature. Thus, the spectrum of the hard X-ray radiation of the typical X-ray pulsar in a binary system can be represented as a combination of the blackbody spectrum with an effective temperature of a few keV and a non-thermal "tail" that can be approximated by a power law with a slope of ~ 1.5. Usually, there is an exponential cut-off or break in the non-thermal spectrum at energies in the range of 5 to 25 keV [19].

The first X-ray pulsar discovered in a binary system, Cen X-3, was detected by the first cosmic X-ray Observatory *Uhuru* [45]. A comprehensive study of this object gave an understanding of the processes of accretion in a binary system, as well as the mechanisms of pulsations in the framework of the concepts discussed above [46–48]. Since then, X-ray pulsars have been intensively studied in a number of space experiments, including orbiting observatories *Ariel*5, *SAS*3, *OSO*8, *Einstein*, *Ginga*, *EXOSAT*, *ROSAT*, *RXTE*, *Swift*, *XMM*-Newton, *Chandra*, etc. Great contributions to the study of X-ray pulsars were made using the Space Observatory Compton (*CGRO*), in experiments using *BATSE* apparatus [49]. Thanks to the detectors, which provide observations in the monitor mode of the entire sky, data were obtained on the evolution of many pulsars over a long (almost 10 years) timescale. The so-called transient pulsars, which are characterized by an extremely unstable intensity, were also investigated. Several new sources of this type were discovered including the famous flaring pulsar GRO J1744-28 [50]. For many pulsars, the optical component was identified. This component is the star, which supplies the matter. In addition, the parameters of the orbits of the components of the binary system were derived. The small moment of inertia of the neutron star makes it possible to measure directly the speed variation of the pulsar (with characteristic times of the day). This allows us to define the nature of the accretion flow in a binary system. In particular, a constant trend in the change of the speed indicates the presence of an accretion disk (accretion fed), while the short-term changes without constant trend are usually associated with accretion of stellar wind (wind fed).

After the new X-ray observatories *RXTE*, *ASCA*, *BeppoSAX*, *Chandra* and *XMM*-Newton were launched in the late 1990s, the list of the detected X-ray pulsars expanded significantly. There are now a few thousand accreting pulsars known, including tens that are called abnormal, the nature of which is not reliably established. Most of the new pulsars in binary systems were discovered in the the Large and Small Magellanic Clouds. Thus, from the total number of the currently known X-ray pulsars only a few are in galaxies, i.e., $M31$ [51, 52] and $M33$ [53], 28 are in the Large and Small Magellanic clouds, and the rest are considered to belong our Galaxy. The range of rotation periods of the magnetic neutron stars in binary systems varies from 2.5 milliseconds to about 3 hours.

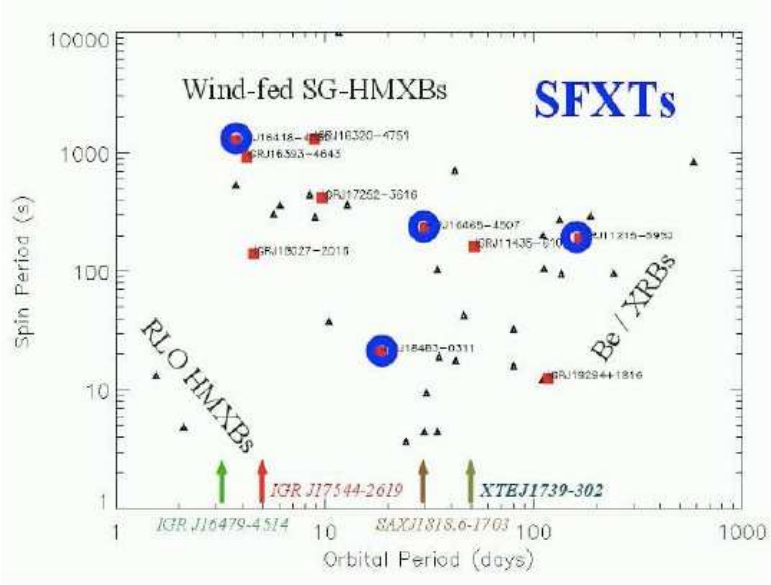

FIGURE 1.4: The Corbet diagram of Galactic pulsars discovered by X-ray missions. Picture taken from [58].

The accreting pulsars in binary systems can be divided into groups depending on the mass of the donor star. There are the so-called low-massive system (M_{comp} $\sim 2.5M_{\odot}$) and an optical system with a large mass companion ($M_{comp} \sim 6M_{\odot}$) [54]. Massive binary systems can be divided into those containing a main sequence Be-type star companion, and to systems with a super giant OB at a later stage of evolution. The systems which include the super giant star may be further divided into objects in which the companion star fills its Roche lobe (accretion disc), and systems in which the accretion is a result of stellar wind effect. In some systems, there may be both these types of mass transfer [55]. Fig. 1.4 shows a diagram of P_{spin} - P_{orb} for those systems in which both pulsation period and orbital period are known. Each of these classes occupies a certain area in the diagram [56, 57].

Systems with OB-type stars. If the star is the supplier of the matter and fills the Roche lobe, then the matter will flow with high angular momentum through the 1-st Lagrangian point and form an accretion disk around the neutron star. Such systems are characterized by short pulsation periods ($P_{spin} \sim 10$ s) and relatively small values of the orbital period ($P_{orb} \sim 4$ d). Following Fig. 1.4, an anti-correlation between the rotation period of the neutron star and the orbital period can be seen for pulsars with accretion disks. Since the accretion through the Lagrange point is highly efficient, they emit constantly and have a fairly high luminosity $\sim 10^{37}$ erg/s. Typical examples of such systems are the known sources Cen X-3, SMC X-1, LMC X-4 [5]. The peculiarity of these objects is a high, relatively constant value of accretion rate indicating the existence of accretion disks in these objects. This is also indicated by optical photometry showing the presence of ellipsoidal variations associated with the distortion of the donor star

by tidal forces and the excess emission arising precisely because of the presence of an accretion disk [59].

The systems in which the accretion comes from the stellar wind are characterized by large values of the orbital period and the pulsation period. They also emit constant radiation but with less intensity ($L \sim 10^{35}$-10^{37} erg/s). Additionally they are characterized by fast (compared with the orbital period) fluctuations in the rotational speed of the neutron star when its acceleration is replaced by deceleration and vice versa [60]. It should be noted that the capture of matter from the high-speed stellar wind by the neutron star is not very effective, so an acceptable accretion rate $\dot{M}$, $\sim 10^{-10} M_{\odot}$ yr^{-1}, is achieved mainly due to the large mass loss rate of the star, i.e. optical companion ($\sim 10^{-6} M_{\odot}$ yr^{-1}). The most famous object in this class is the X-ray pulsar Vela X-1 [49]. Most pulsars with OB-type stars are located in the galactic plane, which corresponds to the fact that massive optical components of the system are short-lived stars and also they typically populate in the disk of the Galaxy.

***Be*-pulsars.** The pulsars with Be-components occupy the third area in the Corbet diagram showing a correlation between the orbital period and the pulsation period. They form the most numerous population (tens of sources) among all types of accreting pulsars in binary systems (it is interesting that almost half of them have been discovered in recent years in the Large and Small Magellanic clouds [61]). The optical companions in such systems are $O-$ or $B-$type stars which remain on the main sequence and, therefore, do not fill their Roche lobe. The high-energy radiation of binaries with $Be-$type stars is usually observed during the transient (temporary) intense flares of activity (outbursts) [62]. Moreover, outbursts typically correspond to the passage of periastron during motion on an eccentric orbit [49]. It is assumed that the X-ray flares are caused by the absorption of the matter onto the neutron star, as a result, the small flares can be explained by the direct accretion of stellar wind [63], while the brightest flares can be explained by assuming the formation of an accretion disk [49]. As can be seen from Fig. 1.4, the Be-pulsars are characterized by a correlation between the orbital period and the rotation period of the neutron star. This correlation may be due to the fact that in the case of, for example, systems with components about the same mass, the system with large orbital period of the neutron star is disposed at a greater distance from the optical component and, as a result, the average accretion rate in such a system will be less [63].

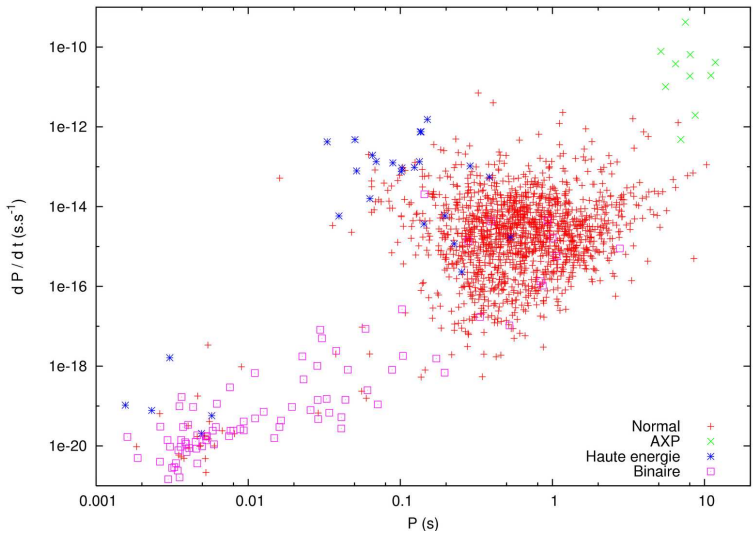

FIGURE 1.5: The diagram characterizes the derivative changes of the rotation period with the rotation period. Red crosses mark pulsars from which gamma-rays are not recorded, blue and green points correspond gamma-ray pulsars, and magenta squares are binary systems. Figure credit [67].

1.1.3 Gamma-ray pulsars

Isolated neutron stars in supernova remnants emit mainly at radio wavelengths [64]. Only some of them are characterized by a hard spectrum extending up to the gamma-ray range (i.e. gamma-ray pulsars) [65]. The first object of this type was discovered in our Galaxy and is known as the pulsar in the Crab Nebula (Crab) [66]. It is assumed that the gamma-ray pulsars are magnetic neutron stars, and the magnetic field has values of $\sim 10^{12}$ - 10^{13} G. At the present time, a couple of hundred gamma-ray pulsars are known[3]. The light curves for the same objects are quite different in different energy bands, which is testified to by the fact that the mechanisms of hard radiation at different energies may not be the same. In particular, in the soft X-ray band, the radiation probably has a thermal nature and is generated near the surface of the neutron star, which is clearly not the case for the gamma range.

Fig. 1.5 shows the pulsar distribution depending on the time period of the neutron stars and the derivative of this period [67]. Until 2008 only 7 pulsars were observed at very high energies ($> 10^{12}$ eV), including the pulsar in the Crab Nebula (see left image of Fig. 1.6). However, all seven gamma-ray pulsars observed at energies > 100 MeV can also be seen at energies above 5 GeV. The results of *EGRET* observations indicate that the light curves of at least four, most statistically robust objects (Crab, Vela, Geminga, PSR B1706-44) have significant changes in their lightcurves at energies above 5 GeV [68]. The double-peaked character of the light curve is transformed into an almost single peaked

[3]https://confluence.slac.stanford.edu/display/GLAMCOG/Public+List+of+LAT-Detected+Gamma-Ray+Pulsars

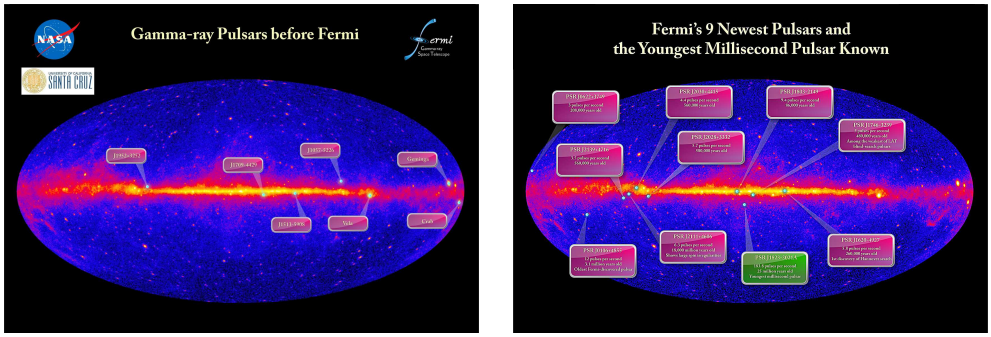

FIGURE 1.6: The distribution of pulsars on gamma-ray sky before (left figure) *Fermi* with the newly discovered pulsars (right figure). The images are taken from the official *Fermi* web-page.

curve. As a result, the amplitude of the first peak in the lightcurve does not completely disappear, but becomes substantially less than the next peak's amplitude. In addition, the lack of gamma-ray data obtained by very-high-energy ground-based instruments from gamma-ray pulsars (except Crab) indicated that their spectra at energies of 10-100 GeV must be steeper [69–73].

Up to now it is not clear where and how the high-energy non-thermal radiation in the pulsar's magnetosphere forms. Since the pulsations in the radiation of gamma-ray pulsars are observed up to energies of ∼10 GeV, there is no doubt that the radiation is generated by charged particles accelerated to ultra-relativistic energies in its magnetosphere. In this case, the Lorentz factor of these particles should be in the range of 10^5-10^7. It is believed that these particles can be accelerated to such high energies in the large-scale electric fields. Such fields arise in the vicinity of the magnetic neutron star, which is, in fact, a natural unipolar inductor [74]. It should be noted, however, that a large electric field is capable of pulling out charges from the surface of the neutron star against the force of gravity [75]. As a result, accumulation of high charge density in the magnetosphere of a neutron star creates a compensating field, which effectively "cuts" the component of the electric field parallel to the magnetic field everywhere, except for a few local areas. It is assumed that the acceleration of charged particles occurs in areas where $\mathbf{E}\cdot\mathbf{B} \sim 0$. These regions are apparently located above the surface of the neutron stars near the polar caps and along the so-called zero charge surface corresponding to the condition when $\omega \cdot \mathbf{B} = 0$ (ω is the angular velocity of the pulsar). Accordingly two classes (models) of high-energy generation in the magnetosphere of the pulsar are discussed; a model of "polar cap" (polar cap) [76, 77] and the model of "outer gaps" (outer gap) [78–80], which give different predictions with respect to the spectral characteristics of hard radiation, as well as on the relation between the number of gamma-ray pulsars, quiet and active in the radio.

There are various versions of the "polar caps" model with differing assessments

of the possibility of free emission of charged particles from the surface of the neutron star [81–83]. This question is sufficiently uncertain, due to the incompleteness of our knowledge about the composition of the surface of the neutron star and the physical processes taking place there. In those models, where there is free emission of particles of any sign from the surface of a neutron star, it is assumed that the surface temperature ($\sim 10^5$ - 10^6 K) is greater than the value at which thermal emission becomes possible. Although the longitudinal (i.e., parallel to the direction of the magnetic field) component of the electric field is zero on the surface of the neutron star, the charge along the opened field lines due to their curvature or relativistic increasing in the inertial system falls over the surface of the neutron star to smaller values compared to corotation charge [74]. As a result of such charge deficiency, the uncompensated longitudinal component of the electric field accelerates particles to the energies corresponding to the Lorentz factor of $\gamma \sim 10^2$ - 10^6. As a result of inverse-Compton scattering of thermal X-ray photons which are emitted from the surface of the neutron star and the bending mechanism, the accelerated particles are able to generate high-energy photons, which form the strong magnetic field of the electron-positron pairs, which gives the rise to the development of electromagnetic cascades. During the formation of the spectrum, the predominant role is played by synchrotron radiation pairs, which are characterized by a very sharp energy cut-off at energies above a few GeV due to the weakness of the process of pair's formation at these energies [76].

The "outer gap" model of the gamma-ray pulsars is based on the existence of a vacuum field in the outer magnetosphere, which can be formed between the last open field of power line and a surface with zero charge ($\mathbf{B} = 0$) in a charge-separated magnetosphere [80, 84, 85]. Such a gap is formed, since the ejection of the charges through the light cylinder along the open field lines of the zero-charge surface can not be replenished from below. It is assumed that the emission of these gaps is connected with the two magnetic poles of neutron stars [78]. A similar pattern can successfully explain the observed spectrum of the pulsar like Vela, but does not reproduce the light curves which are more reliably obtained if the radiation is associated with only one magnetic pole [72, 86].

As a source of accelerated particles consider the electron-positron pairs which form as a result of photon-photon processes. In the young type of pulsars, e.g. such as the Crab, the pair is formed by curvature photons from the primary particles interacting with non-thermal synchrotron X-rays generated by the same pairs. It is assumed that older pulsars such as Vela, in which non-thermal X-ray emission is much weaker, the pair are the result of the interaction of photons that have been affected by inverse-Compton scattering of primary particles with infrared photons. However, this model predicts large fluxes in the TeV range, that are several orders of magnitude greater than current observational limits [84]. Therefore, improved models have been proposed. According to

these models the thermal X-ray radiation generated at the surface of the neutron stars is considered instead of infrared radiation. Thus, the required level of thermal radiation is provided by the fact that a part of the accelerated pairs slow down and heat the surface of the neutron stars [72, 79, 87].

The "outer gap" models predict a cut-off of the spectrum of high-energy radiation at energies about 10 GeV due to cut-off of radiation losses of the spectrum of the primary particles. However, this cut-off is much less dramatic than in the "polar cap" models, since if the high-energy photons emitted in the outer magnetosphere, where the local magnetic field is an order of magnitude weaker than on the surface of a neutron star, the single-photon pair production will not play any role in any forming pairs or in the spectral attenuation. Calculations show that in such cases the spectrum is characterized by a relatively gradual exponential (rather than double-exponential) blockage at high energies. Moreover, the "outer gap" models predict the existence of the radiation component at energies of 1 TeV, making it possible to observe gamma-ray pulsars using ground-based instruments [72, 74].

The "polar cap" and "outer gap" models give significantly different predictions about which pulsars may emit gamma-rays and what is the ratio between the gamma-ray pulsars, "active" and "loud" in the radio band. Thus, the "polar cap" model predicts that all pulsars emit high-energy photons, and the problem of detecting gamma-ray pulsars, thus, is only subject to the sensitivity of the observational instruments. At the same time, the "outer gap" models predict that relatively old pulsars are not capable of supporting the formation of pairs in the outer gap at a level which is sufficient to keep activity in the gamma-ray range. The oldest known gamma-ray pulsar by far is Geminga, which according to [68] is located just at the "border" that separates the pulsars which are visible in the gamma-ray range from those that are not. Conversely, the lack of evidence for the existence of older gamma-ray pulsars than Geminga can serve as a basis for the confirmation or refutation of the models described above [83].

Numerical calculations of the morphology of the radio emission of many pulsars favor the fact that radio emission is formed in the polar regions in the range of tens of stellar radii from the surface of the neutron star [88, 89]. Consequently, in the "polar cap" model a strong correlation is expected between gamma-ray and radio radiation. On the other hand, in the "outer gap" model, the high-energy radiation is directed in the opposite direction relative to the radio, so, in general, according to these models, the pulses in gamma and radio bands should be observed at different times. The various numerical estimations of the ratio between the expected number of gamma-ray pulsars, active and loud in the radio bands, performed in these models show that in the case of the "polar cap" model, the proportion of the gamma-ray pulsars which are loud in the

radio range should be 10-25% of the the total number of the registered sources. At the same time the "outer gap" models give a different ratio, i.e., the number of gamma-ray pulsars which are loud in the radio band should be about 15 times higher than the number of gamma-ray pulsars which are active in the radio range [74].

Thus, there is no reason to give preference to one or another model to explain the mechanisms of generation of high-energy radiation of isolated magnetic neutron stars. Apparently, the critical observations, in terms of the choice of an adequate model, are observations in the gamma-rays range of very high-energy, because exactly for this energy interval the different models predict significantly different behavior of the spectrum and, thus, different estimates of the luminosity. Observations at energies of 10^{10}-10^{11} eV are extremely important to understand the generation mechanisms of high-energy gamma-rays. Such observations became possible after the launch of *Fermi* which has helped to close the gap of our knowledge about the nature of the spectrum of the gamma-ray pulsars in this region of the electromagnetic spectrum.

In contrast to isolated gamma-ray pulsars, in the past few years several high-mass X-ray binaries have been detected as gamma-ray binary systems, causing an intensification of observational and theoretical interest.

1.2 Gamma-ray binaries

The γ-ray binaries are another type of binary system which display gamma-ray emission. Gamma-ray binary systems show a non-thermal spectral energy distribution clearly dominated by the gamma-ray emission and display an emission from radio to very-high-energy gamma-rays. Since the spectral energy distribution is dominated by gamma-ray emission, instead of by the X-ray emission, scientists refer to these sources as γ-ray binaries. This definition is also physically consistent with the fact that the nature of gamma-ray binaries are distinct from X-ray binaries emitting gamma rays. For example, contrary to the X-ray binaries, whose states evolve with time, the X-ray emission from gamma-ray binaries does not show signatures of an accretion disk and their emission is always modulated by the orbital period of the binary system and does not show changes between different states [90].

Typically, binary systems are considered to be thermal sources, in which the gravitational energy of the compact object (neutron star or a black hole) is effectively transferred to X-ray radiation emitted by the accreting hot plasma. However, effective acceleration of particles is possible in gamma-ray binary systems, if a compact source is a radio pulsar (in this case, the system is a compact analogue nebula formed by the

pulsar wind, being in the field of photons emitted by the massive star), or, as a result of acceleration of internal shock waves in the jet, formed near the black hole. Currently only five gamma-ray binaries are known, namely LS I +61° 303, PSR B1259−63, LS 5039, HESS J0632+057, and 1FGL J1018.6-5856. The observational parameters of these binaries (orbit, distance, companion star etc.) are known from optical spectroscopy and radio observations, and are presented in Tab. 1.1. The schematic view of orbits of four binaries is shown in Fig. 1.7.

The nature of the compact source is known only in the case of PSR B1259−63. In this system, the 48 ms pulsar rotates in a highly elliptical orbit around the massive Be-type star SS 283 with an orbital period of 3.4 years (see Fig. 1.8). The OB-type star is characterized by a strong outflow of material from the surface. In the case of Be-type stars, the strong outflow of material comes from the slow equatorial disk. Interaction of the pulsar wind with the wind of the Be-type star leads to the production of a shock wave. The particles that pass the shock wave lose energy due to the synchrotron, bremsstrahlung, and/or inverse-Compton (on photons of Be-type stars) radiation, leading to the formation of the observed broadband spectrum, from radio to TeV range. Contribution to TeV radiation can also provide interaction accelerated by the shock wave from the non-relativistic gas of protons in the disk of the Be-type star. The radio observations show that the disk of SS 283 is inclined with respect to the orbital plane of the system. Thus, the pulsar crosses the equatorial disk of the Be-type star two times per orbit, before and after periastron (see. Fig. 1.8). In 2004, *H.E.S.S.* first detected TeV emission from the system.

The nature of the compact object in the other four systems is unknown. Similarly to PSR B1259−63, they may be radio pulsars in which pulsations are absorbed by the outflowing wind from the surface of the companion star (the distance between the companions in these four systems is ten times less than in the case of PSR B1259−63). In another model, the observed broadband radiation is the result of the interaction of particles accelerated in the jet with the wind of the companion.

LS I +61° 303 is another gamma-ray binary from which very-high-energy emission has been observed. To date, the emission of LS I +61° 303 from radio to very-high-energy is observed. LS I +61° 303 is characterized by variability of flux on the orbital period of 26.490±0.003 days. In addition to the orbital period, this system is variable on the superorbital period at 1667 days [92]. Other parameters of LS I +61° 303 are less well known than for PSR B1259−63 and summarized in Tab. 1.1 [30, 93, 94]. The flux versus orbital and superorbital periods is shown in Fig. 1.9. The radio observations of LS I +61° 303 do not show the trace of the outflow inside the binary orbit due to the free-free absorption of the stellar wind [95]. However, the high-energy outflow has been observed

Table 1.1: Observational parameters of gamma-ray binary systems (see [90] for more details).

System	PSR B1259−63	LS 5039	LS I +61° 303	HESS J0632+057	1FGL J1018.6-5856
Companion	Be	O	Be	B	O
T_* (10^3 K)	33.5	39	22.5	30	38.9
R_* ($R_\odot$)	10	9.3	10	8	10.1
M_* ($M_\odot$)	31	23	12	16	31
Distance (kpc)	2.3	2.9	2	1.6	5.4
Compact object	NS	NS or BH	NS or BH	NS or BH	NS or BH
Orbital period (days)	1237	3.9	26.5	321	16.58
Eccentricity	0.87	0.337	0.537	0.83	-
Inclination (°)	19-35	13-64	10-60	47-80	-
Periastron angle (°)	139	236	40.5	129	-

– the orbital parameters of 1FGL J1018.6-5856 are still unknown.

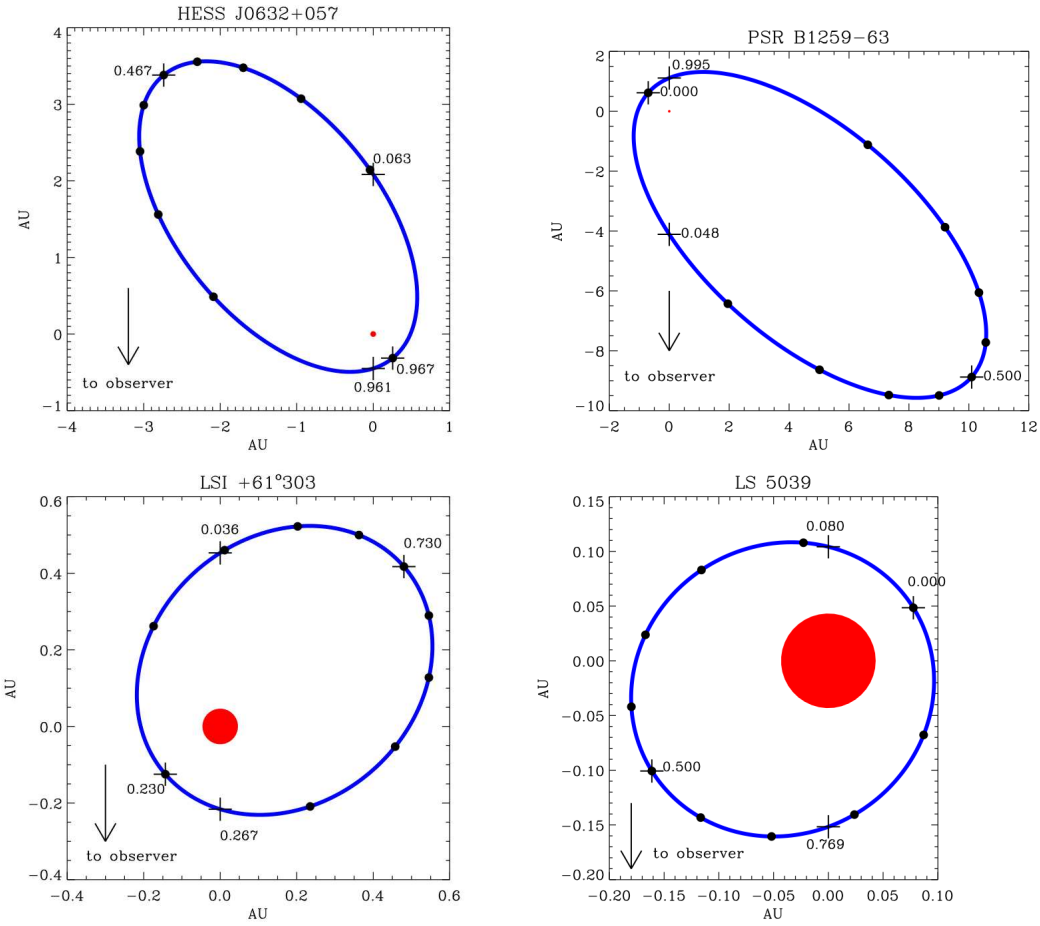

FIGURE 1.7: The view of orbits of the γ-ray binaries. The size of stars is to scale. Crosses mark the phases of apastron/periastron and conjunctions. Dots mark intervals of 0.1 in orbital phase, starting from the periastron. The figures are taken from [90].

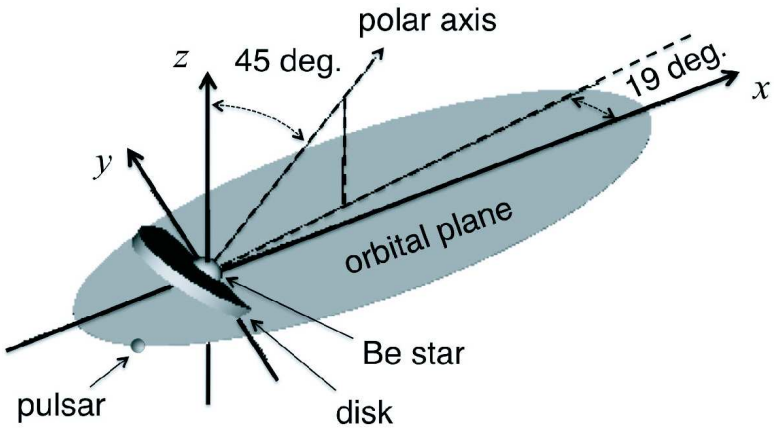

FIGURE 1.8: A schematic view of orbit of PSR B1259−63 (the image is taken from [91]).

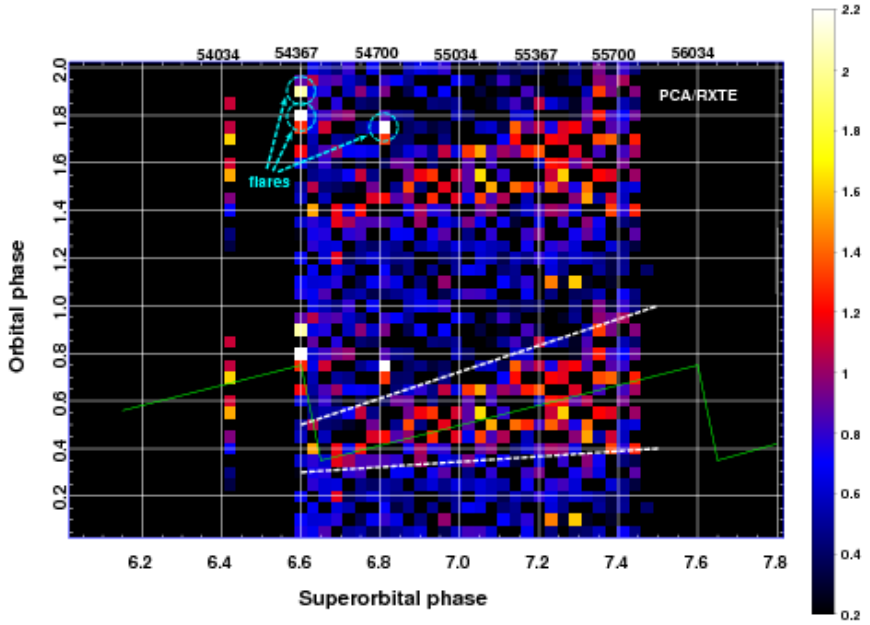

FIGURE 1.9: 3.0 – 20.0 keV flux from LS I +61° 303 versus the orbital and superorbital phases (the flux is given in erg/cm^2/s, and the image is taken from [97]).

at radio wavelengths [96]. These observations showed the variability of the high-energy morphology on the orbital timescale, as well as showing that the outflow of LS I +61° 303 can not be a jet [90, 95]. For a better understanding of the nature of high-energy emission in LS I +61° 303, complementary data in the X-ray and gamma-ray energy ranges are needed.

LS I +61° 303 has been recently observed at X-ray energies by numerous telescopes. All results have indicated the presence of variability on the orbital and superorbital timescales [18, 97–99]. The X-ray spectrum of LS I +61° 303 is well fitted by an absorbed power law model with the hardening of photon index as a function of flux from 1.9 to 1.5. The value of the flux varies, starting from (0.5-3.0) $\times$ 10^{-11} erg/cm^2/s at 1.0 – 10.0 keV energies. Simultaneous observations of LS I +61° 303 at X-ray and gamma-ray energies became possible with the launch of *Fermi* Gamma-ray Mission [100]. To date, we are able to use 8 years of collected data. In the case of X-ray data, the monitoring of X-ray flux was performed using the *Chandra*, *XMM*-Newton, *Suzaku*, *Swift* and *RXTE* satellites [101–103]. Thus, the periodic modulation of both X-ray and gamma-ray emissions were studied. According to the X-ray data, one flare per orbit has been identified. This X-ray flare coincides with the radio one. Moreover, the first year of *Fermi* monitoring has also indicated one flare per orbit [100]. The nature of these flares in different energy bands is unclear. During X-ray monitoring of LS I +61° 303, the drift of the orbital phase of the X-ray flares was found [92]. This drift occurs on the half orbit from $\phi_r \simeq 0.5$ to $\phi_r \simeq 1$ and continues during ∼4.6 years. [92]

concluded that such a drift can not be explained by a precession, since in the case of precession we would be able to observe a flare drift on the full orbit but not just on the half. [104] suggested an alternative theory in which the massive star of LS I +61° 303 has an equatorial disk which is built up and then decays during the superorbital period, i.e. 4.6 years. Although we have the gamma-ray data of LS I +61° 303 performed during last 8 years, the X-ray data have gaps in monitoring of the LS I +61° 303 binary system. It is necessary to study the X-ray and gamma-ray emissions on superorbital timescales using simultaneous monitoring of the system with no gaps in observations. In my thesis, I use the *Swift* data which cover four years to study possible changes in the behavior of the high-energy emissions in LS I +61° 303 binary system (see Chapter 7).

As was mentioned, the nature of X-ray activity is not understood. Two models have been proposed to explain such radio-to-X-ray flare activity. According to the first one, the activity of the source is a result of accretion onto the compact object. According to the second one, the activity is a result of interactions between the pulsar and star winds. A new insight about the nature of the compact object of LS I +61° 303 could be obtained from the study of the system in the hard X-ray energy range. One expects to find a cut-off in the power law spectrum of the binary. A source spectrum with a cut-off at 10.0 – 60.0 keV indicates that the compact source is a neutron star, while a spectrum with a cut-off at about 100 keV corresponds to a black hole [95, 97]. This idea can be checked with *Suzaku* observations (see Chapter 6). The very-high-energy emission in LS I +61° 303 has been recently detected by the $MAGIC$ and $VERITAS$ instruments. Both spectra are consistent with each other within systematic uncertainties. The spectra are well fitted with an absorbed power law model with a photon index of 2.4-2.7 [105–107].

The X-ray source RX J1826.2-1450 was identified with an optical object LS 5039 and was previously identified as a massive X-ray binary system [34]. The object is also characterized as a radio source with a non-thermal spectrum [108]. The radio observations, performed by $VLBI$, found relativistic jets on milliarcsecond angular scales, which allowed LS 5039 to be classified as a microquasar [109]. Recent EVN and $MERLIN$ radio observations confirmed a jet in this system. This jet was classified as an asymmetric two-sided jet extending to $\sim$ 1000 a.u. on the longest jet arm [110]. The object is also a source of gamma-ray radiation at energies above 100 MeV [110–112], and is also associated with a hard gamma-ray source HESS J1826-148, detected at energies above 250 GeV [113].

In the optical bands of the spectrum, the LS 5039 is classified as a star with spectral class of O6.5V((f)) [114, 115], as well as an object with a spectroscopic orbital variability with a period P_{orb} = 4.4267 day, and with an orbital eccentricity e = 0.48±0.06. Additionally, LS 5039 has also been identified as an object with detected

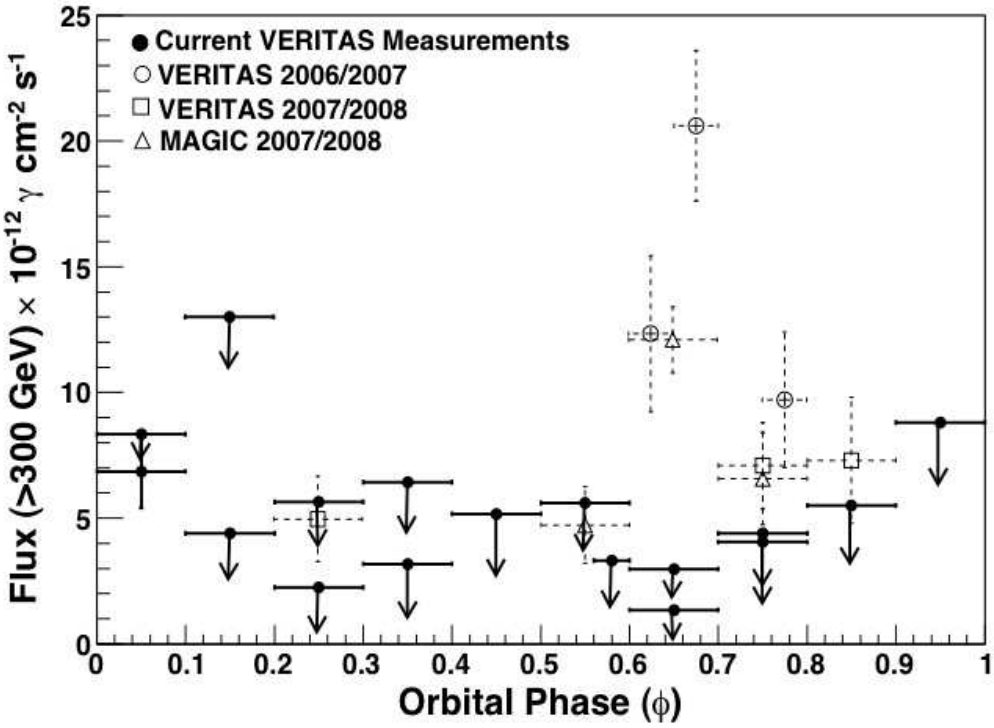

FIGURE 1.10: Observations of LS I +61° 303 at $VERITAS$ and $MAGIC$ wavelengths. The TeV modulation adapted from [107]. Periastron passage is at $\phi = 0.23$.

self linear polarization at the optical radiation of the order of 3%, which is due to the Thomson scattering at the stellar surface [116].

The paper [93] produced new spectroscopic observations. The obtained parameters specified are the spectroscopic orbit with $P = 3.90603 \pm 0.00017$, $e = 0.35 \pm 0.04$, and the half-amplitude of the radial velocity curve of the optical star $K_\upsilon = 19.4 \pm 0.9$ km/s, and the radial velocity the center of mass of the system $\gamma = 17.2 \pm 0.7$ km/s. The corresponding mass function $f_\upsilon(m) = 0.0053 \pm 0.0009\ M_\odot$. The value of $\upsilon_{rot} \sin i$ is estimated from the rotational broadening of the absorption lines as $\upsilon_{rot} \sin i = 113 \pm 8$ km/s. The selected atmospheric models to the observed spectrum of the optical star O6.5V((f)) as well as with a new estimated distance to the system $d = 2.5 \pm 0.1$ kpc give the following parameters for the optical star: $R_\upsilon = 9.3^{+0.7}_{-0.6} R_\odot$, $\log L_\upsilon / L_\odot = 5.26 \pm 0.06$, $m_\upsilon = 22.9^{+3.4}_{-2.9} M_\odot$. Combining these data with the results of analysis of the radial velocity curve of the optical star and assuming the pseudo-synchronization of the axial and orbital rotations of the optical star, the authors of [93] found the orbital inclination of LS 5039 as $i = (24.9 \pm 2.8)$ degrees and the mass of the compact object as $m_x = 3.7^{+1.3}_{-1.0} M_\odot$. This gives reason to believe that the compact object in the system LS 5039 is a black hole. The most recent orbital ephemeris of the LS 5039 system was obtained by [93]. But, due to the big uncertainties in the estimation of the orbital inclination

angle ($13^\circ < i < 64^\circ$) obtained in other works, the nature of the compact object is unclear. Such high uncertainties do not allow an accurate estimate of its mass. If the compact object of LS 5039 is a black hole, then we have to deal with the microquasar scenario. According to this scenario, the non-thermal processes inside LS 5039 happen in a jet as a result of accretion on the compact object.

Recently, LS 5039 has been observed at X-ray energies using the *XMM*-Newton, *Chandra*, *Suzaku* and *RXTE* telescopes. The X-ray spectrum of LS 5039 at 0.5 – 10.0 keV energy range is well fitted with an absorbed power law model with a slope of 1.4-1.6. The flux varies around to 1.0×10^{-11} erg/cm^2/s. Softer spectra and larger fluxes had been also inferred from *RXTE* observations, although background contamination was probably behind these differences. Also, *Chandra* data taken in 2002 and 2005 showed spectra significantly harder than 1.5 [117, 118]. The hard X-ray observations of LS 5039 performed by *INTEGRAL* over the 25.0 – 60.0 keV energy band have measured the flux of the binary as $(3.54 \pm 0.44) \times 10^{-11}$ erg/cm^2/s [119]. Additionally, the flux at the superior conjunction position (the moment when the compact object passes behind the star) was derived as 1.4×10^{-12} erg/cm^2/s. LS 5039 has been also observed by *H.E.S.S.* at TeV wavelengths [113]. These observations confirmed that LS 5039 is a source of very-high-energy gamma-rays as well as that LS 5039 can accelerate high-energy photons above TeV energies. The *H.E.S.S.* observations confirmed a stable modulation of the flux on its orbital period. The maximum modulation occurs around inferior conjunction (the moment when the compact object is located between the star and the observer). It is significant to note that observed orbital modulation in the Galactic binary system was seen at first [120]. The stable orbital modulation indicates that observed high-energy processes in LS 5039 happen nearby the optical star.

In paper [121], a model of LS 5039 as a close binary system containing a young pulsar is considered (it is assumed that the big uncertainty in the mass of the relativistic object allows this possibility). In this model, the gamma-ray emission of LS 5039 is formed as a result of acceleration of particles to relativistic energies in the region where the stellar wind of the massive optical star interacts with the relativistic wind of the young pulsar. According to this model, LS 5039 would behave in a similar manner as the PSR B1259−63 binary system, where the production of gamma-ray emission is a result of interaction between pulsar and stellar winds at the termination shock. This model, as the authors note, needs to be confirmed by further observations.

Currently LS 5039, which contains a very bright optical star ($\sim 10^{39}$ erg/s), is the only system in which the orbital modulation of TeV signal has been detected. The properties of the LS 5039 binary system are summarized in Tab. 1.1. Fig. 1.7 shows the binary orbit of LS 5039. The period of 3.9078±0.0015 d is in agreement with

observations at optical wavelengths. The source spectrum was measured up to 20 TeV, which indicates a high efficiency particle acceleration in the LS 5039 system. The LS 5039 system has also been identified as a gamma-ray source in the *EGRET* survey.

The gamma-ray emission from HESS J0632+057 was discovered in 2004-2005 during *H.E.S.S.* survey of the Galactic plane. [122] concluded that the very-high-energy source in HESS J0632+057 is associated with a massive Be-type star MWC 148, HD259440 = LS VI +05 11. The spectral type is B0pe. The star in HESS J0632+057 is characterized by the equatorial disk. The physical parameters of the equatorial disk in HESS J0632+057 were studied by [123, 124]. First of all, the disk shows an optically-thick nature. Secondly, an inclination of the disk is derived with huge uncertainties and ranges from 47 to between 71 and 90 degrees. Such big uncertainties also give huge uncertainties in mass determination of the compact source. This mass ranges from 1.3 to 7.1 $M_{\odot}$. Therefore, the nature of the compact source is unclear. The effective temperature of MWC 148 is equal to 30000 K. The radius of the star is equal to 6-10 $R_{\odot}$ with a mass of 13-19 $M_{\odot}$. The orbital period of HESS J0632+057 was derived using X-ray data; first results indicated about 315 days [122], while [106] found 321±5 days. The eccentricity of the system is equal to 0.83±0.08, phase of the periastron is equal to 0.967±0.008 (at T = MJD 54857). The distance to this system was derived as 1.1-1.7 kpc [124]. It is interesting to note that HESS J0632+057 is the only binary system observed using ground-based observatories in the two hemispheres: northern and southern.

[122] argued that high-energy emission is variable. These authors searched the pulsed emission from HESS J0632+057 using *Chandra* and *XMM*-Newton instruments. During this monitoring, GeV gamma-ray source 3EG J0632+0521 was identified, and [122] suggested potential association of this source with HESS J0632+057. Later, this source was found in the third *EGRET* catalogue. In the following years, the very-high-energy emission of HESS J0632+057 was observed using *H.E.S.S.*, *MAGIC* and *VERITAS* [125]. Variability of the very-high-energy emission was confirmed. In addition, the high-energy emission is correlated with variability at X-ray energies. The lightcurves of HESS J0632+057 reach a maximum at phase of 0.3 (approximately 100 days after periastron). Until 2010, the TeV emission was not detected with *VERITAS* [106], confirming its variability at very-high-energy. However, in 2010 the gamma-ray signal was observed by *H.E.S.S.*, confirming the TeV variability also [126]. Further analysis of TeV data showed a statistically significant signal ($\sim 6.5\sigma$) of TeV at 0.6-0.9 phase. *Fermi*/LAT do not detect the gamma-ray emission of HESS J0632+057 at MeV-GeV energies [127]. In addition, [123] confirmed the periodic modulation of HESS J0632+057 at optical wavelengths using photometric measurements.

HESS J0632+057 was also monitored at radio wavelengths. The radio instruments $GMRT$ and VLA detected a weak radio signal at the position of HESS J0632+057 [128]. Later, [118, 129] argued about the variability of the radio source in the HESS J0632+057 binary. The observations of HESS J0632+057 performed by $VLBI$ indicate the presence of an extended radio source with a diameter $\sim$ 75 a.u.

Based on the point-like very-high-energy gamma-ray appearance and spectral properties of the source, [122] identified HESS J0632+057 as a new TeV binary system. Moreover, the X-ray observations, i.e. X-ray variability, firmly established the binary nature of HESS J0632+057.

In 2011, the gamma-ray binary system 1FGL J1018.6-5856 was discovered using *Fermi*/LAT observations. Later, the modulation in both radio and gamma-ray ranges was found by [130]. The period of this modulation is 16.58$\pm$0.02 days. [130] identified the source as a gamma-ray binary system with the companion star to be an O6V(f) star. Broadband observations of 1FGL J1018.6-5856 were provided by [131, 132] soon after the discovery. These observations were performed for better understanding of the nature of source features. Unfortunately, these observations were not able to say much about the nature of the compact object of 1FGL J1018.6-5856.

Intensive observations of 1FGL J1018.6-5856 were performed with the *Swift* X-ray Observatory. Using these observations, [132] found that the peak of the X-ray flux corresponds to the gamma-ray maximum at phase 0. In addition, it was found that X-ray flux correlates with spectral hardness. Later, it was concluded that this peak either demonstrates orbit-to-orbit variation, and does not show a persistent property (see e.g., [130]). Using the long baseline of the gamma-ray observations of *Fermi*/LAT, [131] found the period of gamma-ray modulation as 16.531 $\pm$ 0.006 days, that is slightly bigger than the value obtained by [132] using X-ray observations. Thus, X-ray results should be refined. At the present, the baseline of X-ray data is 5 years, as a result, phases of future data can vary significantly.

1.3 Summary

The physical mechanism of the high-energy emission of binaries are not clear. It is possible that binaries detected in the very-high-energy γ-ray band are fundamentally different from the accretion-powered X-ray binary systems. In fact, one of the five gamma-ray binaries known so far, PSR B1259$-$63, is known to be powered by the rotation energy of a young pulsar rather than by accretion. The nature of the companion (black hole or neutron star, accretion or rotation powered) in other systems are not

known yet. Pulsed radio emission from the neutron star in these systems would be absorbed in the wind from the companion star because of the compactness of the binary orbits. It is, therefore, possible that the mechanism of activity of these source is similar to the one at work in the PSR B1259−63 system, where collision of the pulsar wind with the stellar wind produce the accelerated particles and γ-ray emission. Alternatively, it is possible that the observed emission is produced in interaction of the jet from the compact source with the wind of the companion star.

For studying high-energy processes occurring in the gamma-ray binaries comprehensive approaches are required; stellar physics, accretion, magnetohydrodynamics, particle acceleration, radiative and absorption processes, relativity as all these topics play a main role in gamma-ray binaries. In these systems, the shock wave is produced by the interaction of the pulsar wind and enhanced mass outflow from the stellar companion. Although the current population of the gamma-ray binaries is still very limited, these systems have common features in harboring massive OB stellar companions.

In a massive OB-type star environment, the intense photon field provided by the companion star not only plays an important role in the cooling of relativistic electrons but also serves as a perfect target for the production of high-energy gamma-rays. Furthermore the high-energy processes that take place in gamma-ray binaries, such as photon-photon absorption, and the occurrence of electromagnetic cascades, are of great importance to understand the spectral and time properties of the observed emission from these sources. Therefore gamma-ray binaries provide us with an excellent laboratory for the study of the gamma-ray production/emission mechanisms by providing detailed information about the time evolution of the particle spectrum over the orbital period. In addition, gamma-ray binaries provide opportunities for the study of relativistic outflows and particle acceleration. Emergence of such a new class of objects, γ-ray binary systems, brings up new questions on the emission mechanisms, how to accelerate particles up to multi-TeV energies in such a compact object and so on. Gamma-ray binaries have now grown in prominence in high-energy astrophysics. This thesis is focused on a few of these systems.

Chapter 2

Observations and data analysis

This thesis is largely based on the analysis of X-ray and Gamma-ray observations of gamma-ray binaries. This chapter includes an historical review of X-ray observations. I give a general review of the X-ray and Gamma-ray Observatories used in my thesis, the data format, and the analysis tools. I also introduce some technicalities related to the instrumental response files, that will be useful in following chapters. Here, I give the main steps of data analysis that were performed during work with X-ray and Gamma-ray observations. I also discuss how to get the main products (images, lightcurves, spectra, etc) from data. Since the spectral fitting was performed in the `Xspec` environment, I also review the main aspects working with `Xspec`, namely: fitting, models used in the thesis, and estimation of errors (χ^2 and C-statistics, etc). In addition, I review the Monte Carlo simulations that I used in the thesis to improve the errors of measurements. Such error estimations were used in the case of statistically poor spectra, usually for *Swift* data, but sometimes for other data also.

2.1 Atmospheric windows

Our first knowledge about the stars, galaxies, and the Universe as a whole was obtained through a rather narrow "optical window". The nature of astronomical sources can be obtained only through detecting different kinds of radiation coming from them. The Earth's atmosphere is quite opaque; as a result, we are able to "see" only a tiny proportion of all the radiation present in space. Fig. 2.1 illustrates the opacity of Earth's atmosphere for electromagnetic wavelengths. The first transparent window is the optical one. This window lies mainly in the field of visible light, from ultraviolet to infrared. The Earth's atmosphere is completely opaque to radiation whose wavelength is less

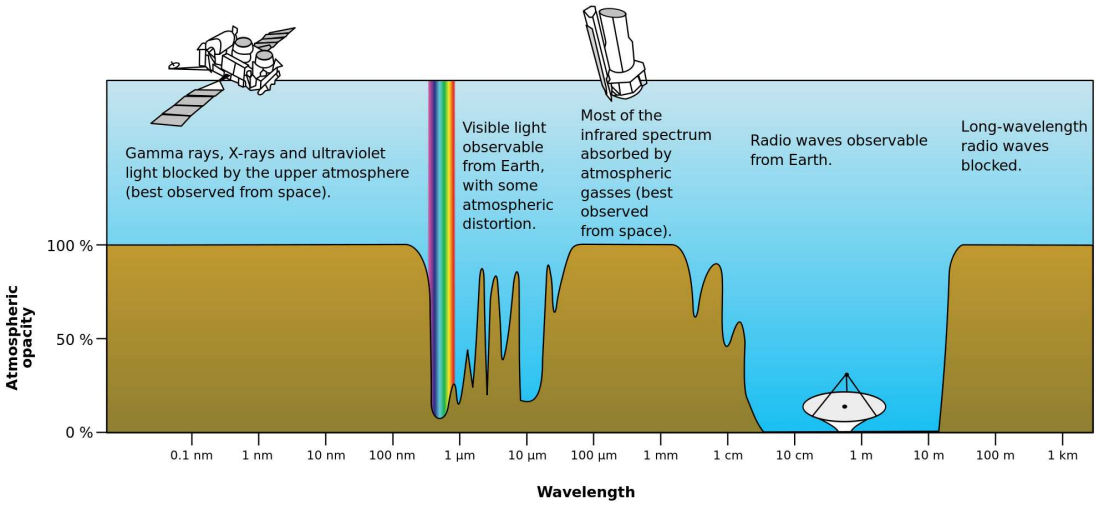

FIGURE 2.1: The opacity of Earth's atmosphere to different types of electromagnetic radiation. Image credit: *NASA* (public domain).

than 2.9×10^{-5} cm. In the far ultraviolet region of the spectrum, spectral lines of many chemical elements are found.

Another transparent window lies in the radio range of the electromagnetic spectrum. The main advantage of radio observations is that the long radio emission wavelengths dramatically reduce requirements for precision manufacturing and maintaining the surface of the reflective telescope mirror. Surface irregularities should be small compared with the wavelength. Therefore, radio telescopes can be made using metal instead of glass. Radio telescopes collect electromagnetic radiation from an area hundreds of times larger than the largest optical telescopes. Another advantage is the transparency of radio observations for all types of clouds in Earth's atmosphere. As a result, monitoring of the sky at radio wavelengths can be carried out in any weather. In addition, interstellar dust is also transparent to radio wavelengths. The disadvantage of radio observations is their low resolution (i.e., the minimum angular distance between two objects that the telescope can detect separately), which causes difficulty in the study of the fine structure of celestial objects. However, astronomers are able to resolve this issue by using very long baseline interferometry (VLBI) [133, 134]. According to this technique, it is possible to observe many radio sources with an angular resolution higher than can be achieved even with the best optical instruments. To date, the European Very Long Baseline Interferometry Network (EVN) is the most sensitive VLBI array on Earth [135].

From the depths of the Universe we receive three other types of electromagnetic radiation: ultraviolet, X-rays, and gamma-rays. Such radiation has become observable

with rocket and space technology [136]. In the following subsection I give a historical review of X-ray astronomy, since in my thesis I use mainly X-ray observations.

2.1.1 Historical review of X-ray astronomy

Observation of cosmic objects at X-ray wavelengths has became possible thanks to the development of rockets and the appearance of satellites. Such satellites are able to launch telescopes beyond the Earth's atmosphere where X-ray photons are absorbed. X-ray photons with energies above a few hundred eV can penetrate through interstellar gas, passing distances comparable to the size of our Milky Way Galaxy with greater or lesser absorption depending on the direction of the source. Photons with energies of a few keV can freely pass through the thickness of the galactic gas. In fact, we can observe X-ray sources located at distances comparable to the size of the Universe [137]. The X-ray and gamma-ray energy ranges generate the greatest flow of X-ray photons.

Since 1962, from the beginning of X-ray astronomy [138, 139], the sensitivity of X-ray telescopes has increased by more than 10 orders of magnitude. X-ray photons are observed from all categories of space objects from planets to normal stars, from ordinary galaxies to quasars, from small groups to the largest clusters of galaxies. As a result of these observations, it became evident that high-energy phenomena play a fundamental role in structure formation, as well as in the chemical and dynamical evolution of cosmic structures of all sizes. X-ray observations have been crucial for developing an understanding of the important aspects of these phenomena. The first evidence of the falling of matter into collapsed objects such as neutron stars or black holes was obtained using X-ray observations. X-ray radiation from the hot plasma of galaxy clusters has shown that the high-temperature component of the Universe is more than two times higher than the content of the "visible" (baryonic) matter. Moreover, due to the appearance of new-improved experimental techniques, such as dispersionless spectroscopy, and/or X-ray telescopes with high resolution, we are able to focus more and more energy from a larger field of view. As a result, it opens for us opportunities for new astronomical discoveries [140].

The first X-ray source detected outside the solar system was Scorpius X-1. During 1966, astrophysicists from USA and England identified more than 30 X-ray sources using rockets and balloons. The first X-ray satellite was launched by NASA in 1970 and was called X-ray Explorer, but later was renamed *Uhuru* [45]. *Uhuru* operated on orbit for two and a half years, and sent a lot of significant scientific information. *Uhuru* detected 339 X-ray sources including the famous source in the constellation Cygnus which later became the first contender in the history of astronomy for the role of the black hole

(Cyg-1). It should be noted that *Uhuru* was not an X-ray telescope, it was an X-ray satellite. *Uhuru* did not have an optical system that could collect and focus the radiation passing through the aperture. The collection of X-ray photons were performed using discharge detectors (similar to a Geiger counter) and a collimator. *Uhuru* was useful to detect point sources only and not suitable in the case of extended objects.

In 1960 Giacconi and Rossi published a paper containing a schematic diagram of the first X-ray telescope with a focusing mirror system [138]. In the case of optical telescopes, the optical photons might be collected at any angle (the angle between perpendicular to the surface of telescope). This not work with X-ray photons since they have higher energy. To resolve this issue, astrophysicists used grazing incidence optics. This is optics where X-ray mirrors have very low angle from the plane of reflection. Such mirrors give the possibility to detect X-ray photons when high-energy particles come almost parallel to the reflecting surface. Later calculations have shown that the X-ray telescope mirrors should be in the form of a tapered tube (see Fig. 2.2). In 1952, Hans Wolter, a German physicist, noted that proper focus of X-ray photons can be achieved using two reflective surfaces. Giacconi and Rossi understood that increasing the sensitivity of the telescope can be achieved with multiple nested mirrors with a single central axis. Wolter found that by using two different types of mirrors it is possible to increase the field of view of an X-ray telescope. It was also found that hyperbolic and parabolic types of surfaces are ideal for such instruments. The parabolic surface suffers from strong coma, but such a surface may still focus, and parabolic surfaces have been used as "light buckets" [141]. There are three types of X-ray telescopes for grazing incidence, which are the Wolter telescopes of type I, II and III. The first two use a combination of paraboloidal and hyperboloidal mirrors, while type III consists of hyperboloidal and ellipsoidal surfaces. The main difference between them is the ratio of focal length to the total system length [141]. The *XMM*-Newton, *Chandra*, *Suzaku* and *Swift* X-ray observatories used type I systems.

The first X-ray telescope was launched in November 1978 and was called High Energy Astronomy Observatory-2 (later renamed as *Einstein*) [66, 142, 143]. *Einstein* operated in the 0.2-20.0 keV energy band with about 5 arcsec resolution. *Einstein* made high-quality spectroscopy of supernova remnants, and discovered a lot of very weak extragalactic X-ray sources. During years 1980-1990, many of X-ray satellites and telescopes were launched, e.g, *ROSAT*, *SAX*, *ASCA* [144], etc. At the end of the 20th century, the new generation of X-ray telescopes were built and lunched to the orbit of Earth. At this time, the third generation of X-ray space telescopes are monitoring the sky. In my thesis, I use all available X-ray data obtained from *XMM*-Newton, *Chandra*, *Suzaku* and *Swift*. Below I describe all these instruments and steps of data reduction

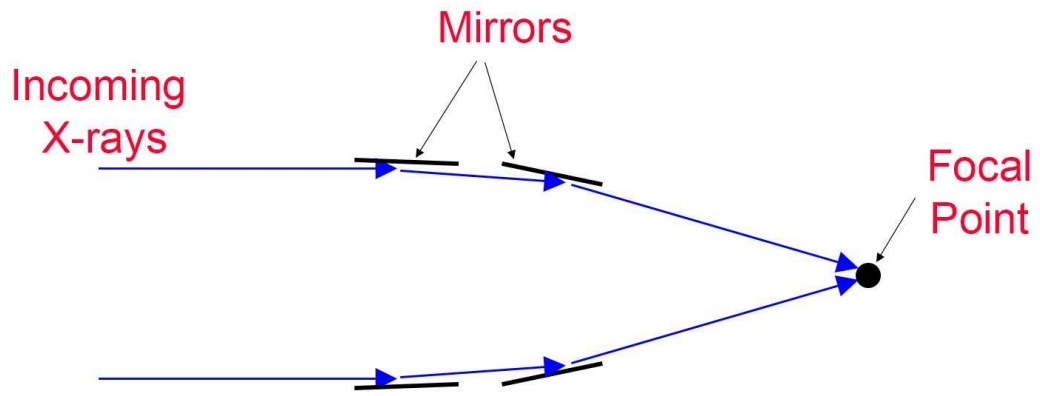

FIGURE 2.2: The diagram of X-ray telescope with one set of mirrors. The image is taken from http://imagine.gsfc.nasa.gov/science/toolbox/xray_telescopes1.html.

and analysis related to this instruments. The following sections on data extractions of main scientific products are written in a more tutorial style for students.

2.2 *XMM*-Newton X-ray Observatory

The X-ray Multi-Mirror Mission (*XMM*-Newton) was launched by the European Space Agency in December 1999 [145, 146]. *XMM*-Newton is named in honor of Sir Issac Newton. To date, it is one of the most popular and successful X-ray astronomy missions. The main aims of the *XMM*-Newton Observatory are accurate observations of faint point and extended sources, and conducting deep surveys of the sky in X-rays, with the possibility to obtain images and spectra of X-ray sources simultaneously [147]. The main characteristics of *XMM*-Newton are reviewed in Tab. 2.1 and shown in Fig. 2.3.

XMM-Newton includes both X-ray and optical/UV telescopes. There are three types of instrument on board *XMM*-Newton:

- The European Photon Imaging Camera (EPIC), for X-ray imaging, X-ray spectroscopy and photometry.
- The Reflection Grating Spectrometer (RGS), for high-resolution X-ray spectroscopy and spectro-photometry.
- The Optical Monitor (OM), for optical/UV imaging and spectroscopy.

The main advantage of these instruments is that they are able to operate simultaneously. There are three EPIC cameras, the two RGC spectrometers, and one optical monitor.

TABLE 2.1: The overview of *XMM*-Newton characteristics (the information is taken from the XMM-Newton Users' Handbook [148]).

Instrument	EPIC MOS	EPIC pn	RGS	OM
Energy band	0.15-12.0 keV	0.15-12.0 keV	0.35-2.5 keV	180-600 nm
Orbital target	5-135 ks	5-135 ks	5-135 ks	5-145 ks
Sensitivity	$\sim 10^{-14}$	$\sim 10^{-14}$	$\sim 8 \times 10^{-5}$	20.7 mag
FOV	30'	30'	$\sim$ 5'	17'
PSF	5"/14"	6"/15"	N/A	1.4"-2.0"
Pixe; size	40 μm (1.1")	150 μm (4.1")	81 μm (9×10^{-3} Å)	0.476513"
Timing resolution	1.75 ms	0.03 ms	0.6 s	0.5 s
Spectral resolution	$\sim$70 eV	$\sim$80 eV	0.04/0.025 Å	180

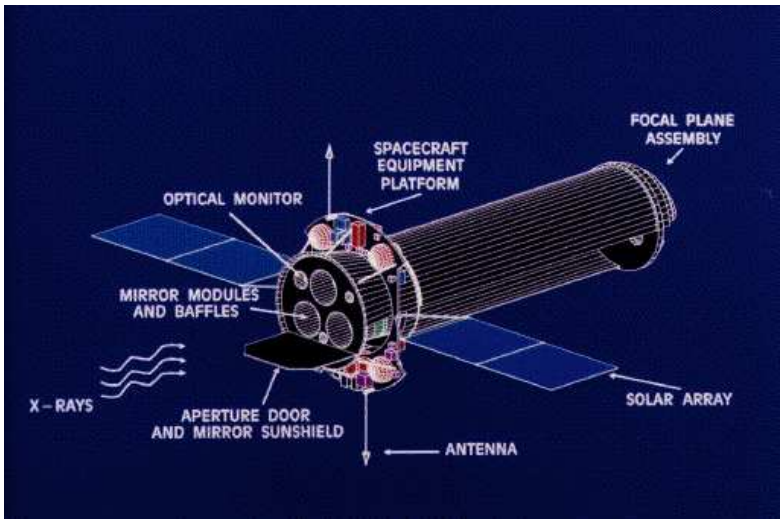

FIGURE 2.3: The *XMM*-Newton X-ray Observatory (*ESA*, 2007).

EPIC cameras consists of three X-ray CCD instruments. Two of them have MOS CCD arrays which are installed behind the telescopes [149]. These instruments are able to perform high quality observations over 30 arcmin FOV (field of view) and in the 0.15-12.0 keV energy band. Fig. 2.4 demonstrates the mirror effective areas according to the response of the different instruments on-board of *XMM*-Newton. The maximum is peaked at about 1.5 keV. One can see that the effective area of the MOS instruments is lower than in the pn camera. The MOS/pn effective area is defined as the part of the surface's effective area, the filter transmission, and the detector quantum efficiency. Since the two MOS cameras include the RGA (Reflection Grating Assemblies) transmission factors, they receive only about half of the incoming radiation, i.e., the incoming radiation is diffracted by RGAs to the direction where RGS is situated [150].

As I mentioned above, approximately half of the X-ray radiation is utilized by

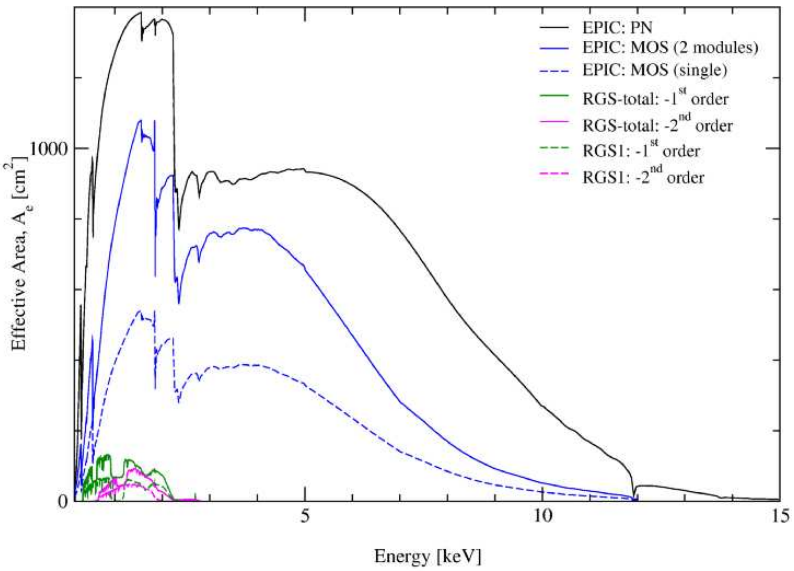

FIGURE 2.4: The effective area of *XMM*-Newton X-ray Observatory (*XMM*-Newton-manual, 2006).

the RGS. Each RGS consists of an array of reflection gratings [151, 152]. This array diffracts the X-ray photons to an array of dedicated charge coupled devices detectors, i.e., CCD. The resolution of RGS instruments is from 5 to 35Å (0.33 to 2.5 keV). Fig. 2.4 demonstrates that the maximum effective area of RGS is close to 15Å (0.83 keV). The RGS includes 182 similar gratings. All these gratings were configured in classical places, where incident and diffracted X-rays lie perpendicularly to the grating grooves [148]. A 2000Å gold coating was used to cover the gratings.

The Optical/UV Monitor Instrument (OM) is a telescope mounted alongside the X-ray mirror modules on the mirror support platform of *XMM*-Newton [153]. The OM covers 170 – 650 nm of the central 17 arcmin square region of X-ray FOV giving possibilities to perform X-ray and optical/ultraviolet observations simultaneously. The Optical Module includes a Telescope Module (TM) and Digital Electronic Module (DEM). The TM includes the telescope detectors and optics while the DEM performs the Instrument Control Unit (ICU) within the spacecraft, commanding of the telescope, and DEM [153]. The FOV of OM is 17×17 arcmin giving to the observer the possibility to define a number of collection windows around the target.

2.2.1 Analysis of *XMM*-Newton X-ray Data

XMM-Newton scientific data are grouped in ODF-files (Observation Data Files) and they have `.fits` format. These *XMM*-Newton observations are freely available after the "proprietary period" which is approximately equal to one year after the observation. Thereafter, the data are publicly available on the official *XMM*-Newton web-page, i.e., http://nxsa.esac.esa.int/nxsa-web/#search/ (or through HEASARC[1] website also). To download data, we should specify the name of the source in which we are interested in the search form and we also need to choose the name of the desired instrument (i.e., *XMM*-Newton). After processing the request, we must go to the `xmmmaster` tab that contains information about the "raw" observations. Understanding whether or not the observation is "empty" is possible by downloading prepared images (we need to mark the flag on "XMM Quicklook Images"), or, alternatively, the easiest way is to just look at the raw exposure time of the observation. An observation with exposure time less than a thousand seconds usually contains bad/poor data. To download the preliminary data from this monitoring it is necessary to put the flag only near "XMM ODF Basic Data" field, as well as the flag near the observational number of interest. After that, we must go on the tab "Data products retrieval", and click on "Create download script". As a result, we will able to see the link clicking on which we download directories with previously marked observations. The downloaded folders contain the ODF directory which includes the results of observation. As we can see, the ODF folder includes a large number of files with "unknown" destination. In fact, there are files recorded in the "useful" satellite format. The first task will be to obtain the so-called "list of events". As a result, we are able to get the following information about the event:

1. Detector number where "event" occurred (i.e., the "coordinates").
2. The energy of the event (in "instrument units", or PI).
3. Event time.
4. Supporting technical information.

The event files are the basis from which to obtain scientific products, such as light curves (if we leave only a temporary variable), images (coordinates) and spectra (energy). Now, I try to describe how to get the event files and scientific data using [148]. First of all, the data in the ODF folders must be unpacked (it can be done using `gunzip *gz` command in Linux).

[1] http://heasarc.nasa.gov/

In this thesis, the *XMM*-Newton data reduction was performed using the Scientific Analysis Software package, namely SAS v.14.0.0 and the latest calibration files. This package contains scripts, tasks, commands and libraries to analyze *XMM*-Newton data. The MOS and pn event files can be obtained after the following steps. The first one is to build the so-called list of calibration files. The *XMM*-Newton telescope is a complicated technological device and requires a lot of additional useful information such as ambient temperature, position of satellite relative to the Earth and Sun, the list of bad detectors, etc. The list of calibration files contains this information. The `cifbuild` task records this information into the list (located in ccf.cif file). Then, the `odfingest` task should be used to create the basic summary file with calibration files, etc. Now we are ready to produce the event files. To produce event files for the MOS and pn detectors the tasks `emproc` and `epproc` can be used. Thus, in the directory with the observation you will find event files with long names. The first four digits of these names show the number of the satellite turnover (orbits) around the Earth (since satellite's launch). Another important parameter specified in the file name is the type of (mode) file (Imaging or Timing). Files of various modes have quite different structure, therefore they will be processed using two different methods. Here, I use data made in Imaging mode, therefore, below I describe data reduction performed in the case of Imaging mode only. It should be noted, that this mode is the most common. In this mode, the two-dimensional spatial information is recorded on the event coordinates including subtraction of background events. Usually, each observation has three event files performed in Imaging mode (one for each camera), but sometimes for MOS only or pn due to the constraints on the telemetry rate [148, 153].

The next step is building an unfiltered image. This step (and not only this one) was performed using the multi-functional `evselect` task, where one of the main aim of this task is filtering event files. `evselect` consists of a number of parameters described below (note that parameters below are the group of parameters needed to build images only, in general the `evselect` has a bigger number of parameters):

- *table* - name of the event file to be used for imaging. This file should contain column EVENTS (See below);
- *withimageset* - parameter, indicating the desire to build an image (if yes);
- *imageset* - the name of the generated image file (output file);
- *xcolumn* and *ycolumn* - the names of the columns that contain information about the two-dimensional coordinates. The most commonly used coordinates are "physical" associated with the satellite, they are the same for all three cameras; or (DETX, DETY) coordinates of the detector associated with each of the cameras,

suitable for "cutting" of the field of view of the satellite, as well as automatic processing of the same spatial region by combining different observation; or (RAWX, RAWY) coordinates, it is coordinates on a separate CCD;

- *imagebinning* specifies the method of partitioning the picture into pixels. Parameter *imageSize* helps with choosing a fixed-size figure, while the angular size of a pixel in the picture is selected depending on the original angular size of picture and its final size in pixels, and set the parameters *ximagesize* and *yimagesize*.

This image can be viewed with specialized software `ds9`[2], an universal viewer of FITS image files. In the window `ds9` program, you can open all three (MOS+pn) images. Here, it is very useful to use *log* option, that displays the "brightness" of images (the number of events per pixel) on a logarithmic scale and *zoom*, that fits the scale of images automatically.

The next step is filtering of event files. There are a few known components of EPIC background [148]. There are backgrounds from (1) photons, i.e., the background from thermal emission at lower energies (<1 keV) and a power law emission at higher energies, solar wind, etc.; (2) particles, i.e., soft proton pollution (flares), cosmic-ray induced, etc.; and (3) electronic noise, i.e., bright pixels, columns, etc. The *XMM-Newton* data filtering can be done with the `evselect` task. In the case of the pn camera, the filtering is performed as

```
evselect table=pn.fits:EVENTS withfilteredset=yes \

expression='(PATTERN <= 4)&&(FLAG == 0)&&(PI in [150:15000])' \

filteredset=pn-filt.fits filtertype=expression keepfilteroutput=yes
```

Here, both options *withfilteredset = yes* and *keepfilteroutput = yes* allow us to obtain the result of filtering in the form of the event file, similar to the original file events. These output events files contain events with the following condition: '(PATTERN <= 12) && (FLAG == 0) && (PI in [200:12000])' for the MOS cameras, and '(PATTERN <= 4) && (FLAG == 0) && (PI in [150:15000])' for the pn camera. The `PATTERN` parameter specifies the number of "multiple" events. This is when a single photon corresponds to more than one event. For example, the electron cloud is produced by one photon and can be in several neighboring detectors, which formally leads to the simultaneous recording of multiple events. Because these events were produced by a

[2] http://ds9.si.edu/site/Download.html

single photon, they should be interpreted as one "fold" (double, triple, quadruple, etc.) event. In order to distinguish "multiple" events from the unit we need to introduce the parameter ‘‘PATTERN’’. In particular, single events correspond to ‘‘PATTERN == 0’’, the double events to ‘‘PATTERN in [1:4]’’. ‘‘PATTERN <= 12’’ condition allocates single, double, triple and quadruple events. The difference between the conditions of selection for MOS(12) and pn(4) cameras is associated with the different calibration of MOS and pn instruments. The FLAG parameter corresponds to the "quality" of the event. Events with "FLAG > 0" (for example, the events near the "hot" pixels or outside the field of view of the instrument) are less suitable for the analysis, in particular for quantitative analysis it is customary to leave only the events with "FLAG $== 0$". PI parameter is an instrumental energy. This value is determined by the amplitude of the signal entering through the processor of the corresponding camera. This parameter is normalized in such a way as to correspond approximately to the photon energy. This leads to the fact that the high energy photons gives some input on events with low PI. This effect is called the redistribution of energy and, as a result, the transition matrix between the PI and the energy of the photon (redistribution matrix function, RMF) must be defined. As a result of numerous calibrations, the "standard" data is getting the events with too small and too large values of PI. For MOS cameras the "recommended interval" of PI is 200-12000 eV, while for pn camera - 150-15000 eV. The next step is building a filtered image. To do this step, I use the evselect task again as shown above. The fv program is an universal viewer of FITS files and can be used to construct the light curves.

The evselect task is used to build the light curve. For this approach, the following number of parameters are required:

- withrateset=yes - "yes" if you need to build a light curve;
- rateset - a name for the light curve (output name);
- maketimecolumn - whether in the column of the light curve the time of arrival of photons;
- makeratecolumn - whether in the light curve the account of the speed;
- timebinsize - the size of a bin in the light curve (in seconds).

Another significant moment of the data reduction is the selection of the region of interest on the filtered image. It was found by the *XMM*-Newton team[3] that 90% of the energy from a point source is contained in a circle with a radius of 30-45 arcsec.

[3]http://www.cosmos.esa.int/web/xmm-newton/documentation

They showed that for the quantitative analysis of the light curve and spectrum of point sources, the optimal range of radius should be about 40-50 arcsec, or 800-1000 in physical units. I select a region of radius 1000 units for the *XMM*-Newton data analysis of binary systems. To build the spectra, we need to use the `evselect` task again but with following parameters:

- `withspectrumset=yes` - whether to create a range of file
- `spectrumset` - the name of the created spectrum (output name)
- `energycolumn` - energy column name (in our case is PI)
- `withspecranges` - indicate whether the channel borders (yes)
- `specchannelmin` - the minimum value of PI
- `specchannelmax` - the maximum value of PI (for MOS camera is 11999, for pn - 20479). It is not recommended to change this value
- `spectralbinsize` - the size of a bin in the PI units (for MOS cameras is 15, for pn - 5). It is not recommended to change this value
- `updateexposure` - update exposure information (necessary for correct calculation of the count rate)

For a quantitative analysis of the spectrum it is necessary to subtract the background events. To do this, we need to select a region without any point sources and nearby the source region (best of all, in the same-CCD). It is necessary that the chosen background region is bigger than the source region. The background spectrum will be normalized to the ratio of scaling factors and the background source. This will (to first approximation, it does not work in the case of extended sources) allow us to subtract the background for the point sources. The output spectrum contains the number of photons PI per bin.

Using the exposure time, it is possible to calculate the count rate in each bin. However, the obtained value is strongly dependent upon the instrument. Namely, the charge redistribution in the surface of the CCD leads to the production of an off-diagonal matrix, in this case, the "physical" energy depends upon the channel number (redistribution matrix function, `RMF`). Such effects as the partial reflection of photons from the mirror, the quantum efficiency of the CCD, the PSF correction, and the presence of out-of-time events, are recorded in a so-called ancillary response function (`ARF`) which contains an effective area as a function of energy. `RMF` and `ARF` files are modeled numerically using the `rmfgen` and `arfgen` tasks, respectively. The `rmfgen` task has the following parameters:

- `format = 'var'` - by default
- `rmfset` - the name of the generated `RMF` file (output name)
- `spectrumset` - the name of used spectrum
- `threshold` - the elements of the matrix with a value less than that set in `threshold` are considered to be zero

The `arfgen` task requires the following parameters:

- `arfset` - the name of the created `ARF` (output name)
- `extendedsource = no` - set to simulate a point source
- `modelee = yes` - "yes" if you need to simulate the PSF to describe the external regions. This is an important parameter since to calculate the correct value of the flux we must model the PSF in the central part
- `psfenergy` - the energy at which the PSF is calculated (5 keV by default)
- `withrmfset = yes` - whether to use a previously created `RMF` (recommended)
- `rmfset` - the name of a previously created `RMF` file
- `spectrumset` - the name of the spectrum
- `withbadpixcorr` - "yes" if you need to make the exception of bad pixels
- `badpixlocation` - the name of the file that specifies the position of the bad pixels. It is possible to take the filtered event file
- `modelootcorr` - whether to correct the out-of-time events

After the production of the source and background spectra, as well as the `RMF` and `ARF`, all these files should be grouped for further analysis. The `grppha` groups these files into one. Thus, the grouped spectra are ready for scientific analysis, i.e., modeling. In my thesis, the analysis of spectra was performed in the `Xspec` environment (details see below).

2.3 *Chandra* X-ray Observatory

The *Chandra* X-ray observatory was launched by shuttle on 23 July 1999 (the orbit is elliptical with a perigee of 10 000 km and an apogee of 140 000 km, the orbital

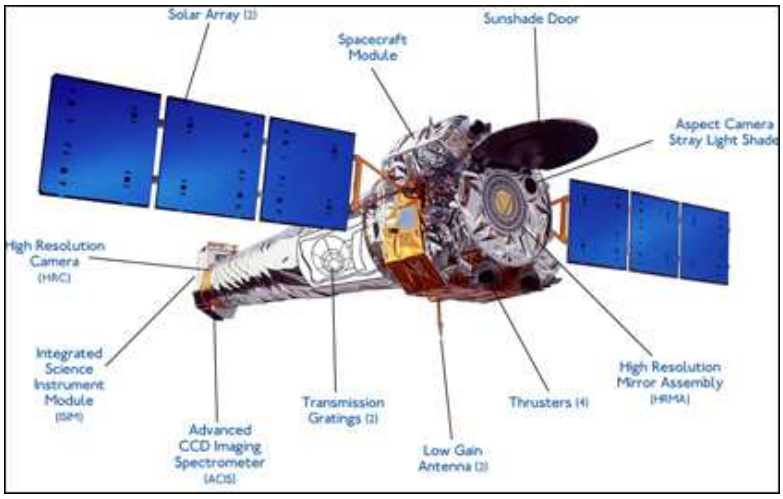

FIGURE 2.5: The *Chandra* X-ray Observatory (*NASA*, 2007).

period is about 64 hours). *Chandra* has the highest resolution (0.492 arcsec) of all past and current X-ray telescopes. The *Chandra* telescope has 4 mirrors of Wolter's type, and includes two instruments on-board: the High Resolution Camera and CCD X-ray spectrometer (Advanced CCD imaging spectrometer, ACIS) [154]. In addition, *Chandra* has two types of arrays for recording high- and low- energy photons (High- and Low-energy transmission grating) [155]. A schematic view of the main parts and units of the observatory is shown in Fig. 2.5. The observatory covers the 0.3 – 10.0 keV energy range, corresponding to soft X-rays. The spatial resolution of ACIS is limited by the size of the pixels. Such a limitation works in both cases for ACIS-S and ACIS-I detectors. It was estimated that about 90% of the encircled energy concentrates within 2 arcsec at 1.49 keV and within 2.5 arcsec at 6.4 keV. No evidence for any differences between the databases obtained by ACIS-S and ACIS-I was found. *Chandra* has better spatial resolution ($<$ 1") than previous X-ray missions and the highest spectral resolution. Thanks to the design, 50% of the energy is concentrated in the area of 0.4 arcsec in the line of sight to the source, and 90% in the area of 0.9 arcsec. The FWHM (full-width-half-maximum) of the on-axis point spread function is 0.5". However, in the case when the point moves more than a few arcmin off-axis the PSF increases rapidly [154, 156].

In my thesis, I used data from the ACIS instrument only. Here, I review the main characteristics of the ACIS instrument. The mirrors of *Chandra* are comprised of 4 pairs of parabolic and hyperbolic mirrors nested into each other. The largest diameter mirror is 1.2 meters across. The focal distance of the telescope is 10 meters. The effective surface area is largest for energies below 2 keV (see Fig. 2.6).

The Integrated Science Instrument Module (ISIM) consists of the Advanced CCD Imaging Spectrometer (ACIS) and High Resolution Camera (HRC). The ACIS spectrometer consists of 10 CCD pixel size 1024×1024. These 10 matrices form 2 arrays with

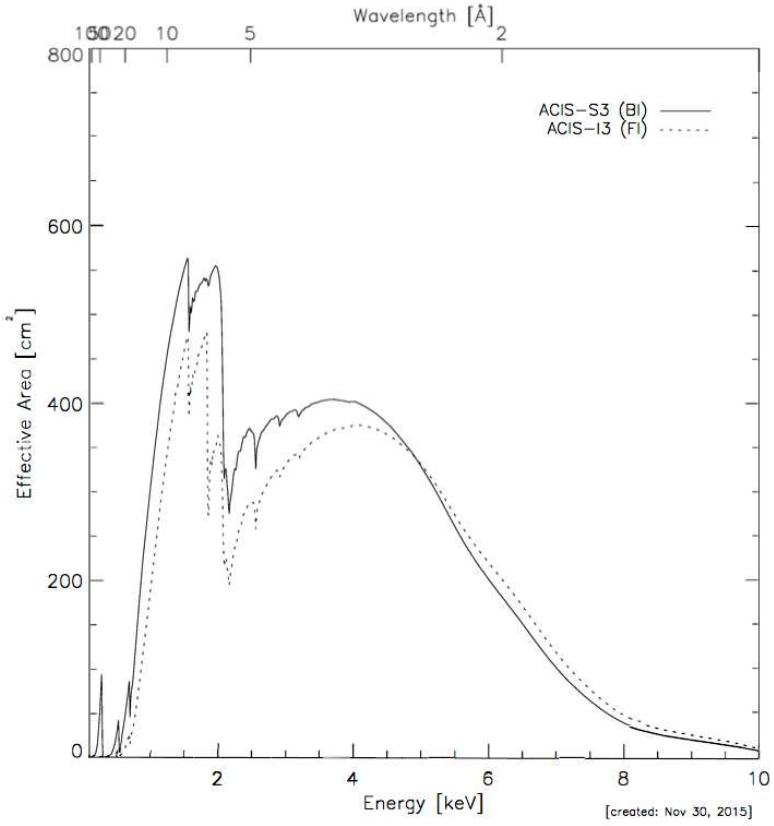

FIGURE 2.6: The effective area of the ACIS instrument in *Chandra* X-ray Observatory (*NASA*, 2007).

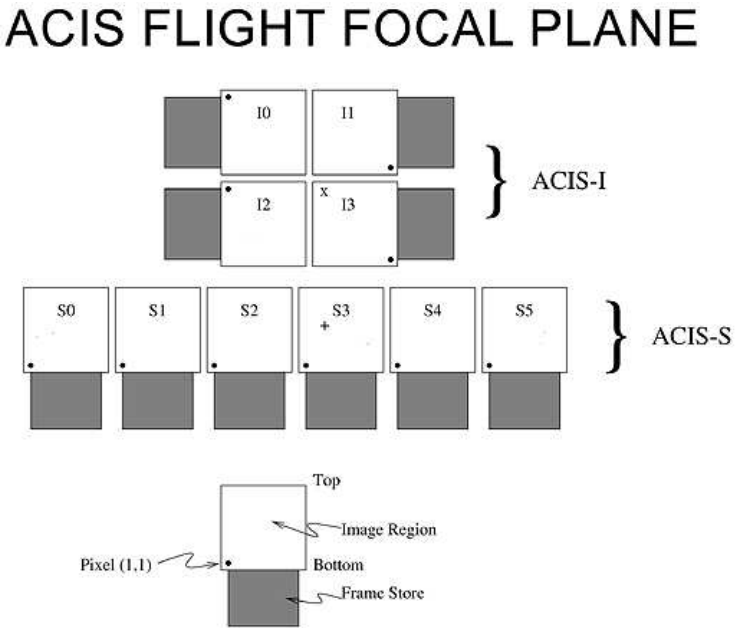

FIGURE 2.7: A schematic view of the *Chandra* ACIS focal plane layout. The "x" at the I3 chip and the "+" at the S3 chip represents the default aiming points for observations with ACIS-I and ACIS-S respectively (*NASA*, 2007).

different fields of view, and size. ACIS-I (I0-I3) has a grid of 2×2 with a field of 16 x 16 arcmin and is used mainly for spectroscopy images, while ACIS-S (S0-S5) has 1×6 grid with a field of 8 x 50 arcmin and is used not only for image spectroscopy, but also for conventional spectroscopy. Pixel size is approximately 24 μm ($\sim$ 0.492 arcsec). The ACIS spectrometer contains two types of CCD matrices with front and back lighting. In the case of front illumination, the X-rays photons fall into the top of the device; in the case of back illumination the streams of photons come from below. Fig. 2.7 shows a schematic view of the ACIS instrument.

2.3.1 Analysis of *Chandra* X-ray Data

In this thesis, the *Chandra* data reduction was performed using the *Chandra* Interactive Analysis of Observations, called `CIAO`. I have used the `CIAO` version 4.6 and calibration database version 4.6.3. A full description of the `CIAO` software package, as well as a guide to data analysis, is available at the main `CIAO` web-page[4]. Also, I used [157] to analyze the ACIS data. `CIAO` includes the `Sherpa` fitting environment [158], the analogue of `Xspec`. The *Chandra* scientific products were analyzed in the same manner as *XMM*-Newton data, i.e. spectral modeling was performed in `Xspec`, and the visualization of images was done using `ds9`. All data are available through the official *Chandra* web-page, i.e., http://cxc.harvard.edu/cda/ (in addition through HEASARC web-page) after the proprietary period (usually one year). All data can be downloaded as `.fits` files and in the same manner as *XMM*-Newton data (see above). The downloaded data have "primary" and "secondary" files, according to folders that you will see in the observational folder. The standard screening and reprocessing data files can be done with the `chandra_repro` task. This task checks the "level 1" data files for the presence of cosmic background events, etc. As a result, this task creates a new folder (the default name is "repro") with "level 2" data files that can immediately be used for data analysis. After defining the region on the CCD, the `specextract` task is able to generate all required files, including the `ARF` and `RMF`. Using this task, it is also possible to subtract the background events. The data were grouped using the `grppha` task. The spectral modeling was performed in the `Xspec` environment.

2.4 *Suzaku* X-ray Observatory

Suzaku is a Japanese X-ray Space Observatory launched on 10 July 2005. The orbit is elliptical with an apogee of 568 km, an orbital period is about 96 min that gives

[4]http://cxc.harvard.edu/ciao/manuals.html

FIGURE 2.8: The image of the *Suzaku* X-ray Observatory.

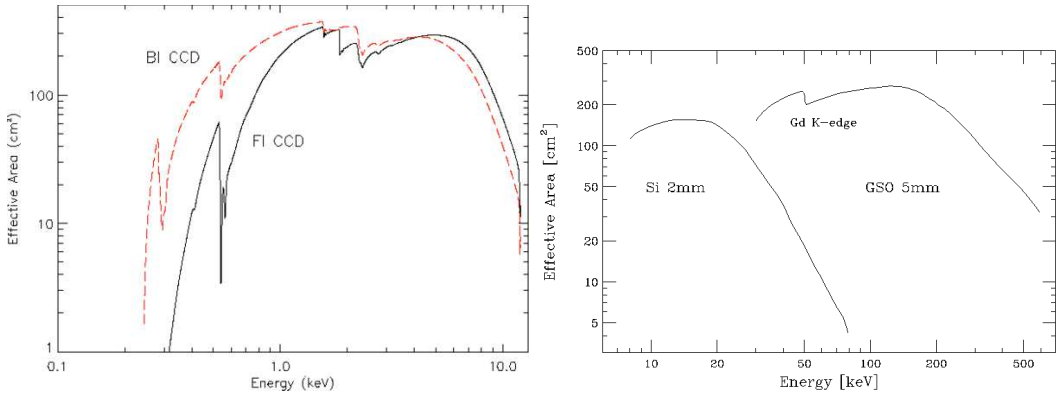

FIGURE 2.9: The total effective area of XIS (left) and HXD (right) *Suzaku* instruments. The images are taken from official *Suzaku* web-page.

$\sim$ 43% of observing efficiency [159]. An image of the *Suzaku* observatory is presented in Fig. 2.8. *Suzaku* consists of 4 main instruments: the XRT (X-ray telescope) [160], XIS (X-ray Imaging Spectrometer) [161], HXD (Hard X-ray Detector) [162, 163] and WAM (Wide-band All-sky Monitor). The main capabilities of *Suzaku*'s instruments are reviewed in Tab. 2.2. The XIS instrument is analogue to ACIS on *Chandra*, and EPIC on *XMM*-Newton. The HXD instrument consists of two detectors, i.e., PIN and GSO. The total effective area as a function of energy for XIS and HXD is shown in Fig. 2.9. The *Suzaku* XIS instrument consists of 4 sets of mirrors. These sets are located in the focal plane of the XRT. Each of them has a CCD with 1024×1024 array. Such a CCD is 25×25 mm in size and covers a 17'.8×17'.8 area of sky.

Note that XIS2 has not operated since 9 November 2006 due to fatal damage [165]. The XIS0 and XIS3 use a front-illuminated CCD, in contrast with XIS1 which uses a back-illuminated CCD. The HXD is a non-imaging instrument including 16 detectors and 20 scintillators. The WAM instrument is a part of the HXD which is mainly used to observe solar flares, gamma-ray bursts, bright X-ray transients, etc.

TABLE 2.2: The log of *Suzaku* characteristics (the information is taken from [164]).

	XRT	XIS	HXD	WAM
FOV	17' at 1.5 keV	17'.8×17'.8	4.°5×4.°5 ($\gtrsim$ 100 keV) 34'×34' ($\lesssim$ 100 keV)	2π (non-pointing)
Eff.area	440 cm^2 at 1.5 keV	330(FI) cm^2 at 1.5 keV 370(BI) cm^2 at 1.5 keV	160 cm^2 at 20 keV 260 cm^2 at 100 keV	800 cm^2 at 100 keV 400 cm^2 at 1 MeV
Bandpass	0.2 - 12.0 keV	0.2 - 12.0 keV	10.0 - 600.0 keV - PIN 10-70 keV - GSO 40-600 keV	50.0 keV - 5.0 MeV
Angular resolution	2' (HPD)			
Time resolution		8 s (normal mode) 7.8 ms (P-sum mode)	61 μs	31.25 ms for GRB 1 s for All-sky-Monitor
Energy resolution		∼130 eV at 6 keV	∼3 keV for PIN $7.6/\sqrt{E_{MeV}}$% for GSO	

2.4.1 Analysis of *Suzaku* X-ray Data

Suzaku data can be downloaded through HEASARC in the same way as for *XMM-*Newton and *Chandra* (or through the http://darts.isas.jaxa.jp/astro/astroquery/, i.e., the official *Suzaku* website). For data reduction and scientific analysis, the `HEASoft` software package v.6.19 as well as the latest calibration files were used. The `aepipeline` tool was used to perform recalibration and rescreening of the XIS and HXD data. I excluded data obtained during passages through the South Atlantic Anomaly[5]. For XIS analysis, I used "cleaned event files". I have re-processed them with standard screening criteria as recommended by the *Suzaku* team[6]. The source region was selected with a radius of 100 arcsec. The `xselect` task performs the data analysis to extract the main scientific products like images, lightcurves and spectra. The response matrices (`RMF`) and ancillary response functions (`ARF`) were generated using `xisrmfgen` and `xissimarfgen`, respectively. The spectra and lightcurves for the three XIS instruments were grouped using `addascaspec` task. The HXD/PIN spectra were extracted using the `hxdpinxbpi` tool. Before extracting PIN spectra the PIN non-X-ray background files compiled by the XIS team were downloaded. Two different non-X-ray background models for the HXD/PIN are available, the *tuned* background[7] and the *quick* background[8]. In this thesis, I use *tuned* files as recommended by *Suzaku* team [164]. The `hxdpinxbpi` tool performs the dead time correction of data as well as taking into account the PIN backgrounds (non-X-ray background (NXB) and cosmic X-ray background (CXB)). The CXB flux is approximately 5% of the total background for HXD/PIN and 0.1% for HXD/GSO instruments. The estimation of CXB assumes uniform emission from a area of 2×2 degree. Source spectra were binned using the `grppha` task, and analyzed using the `Xspec` environment.

2.5 *Swift* X-ray Observatory

The main task of the *Swift* [166] observatory is to observe gamma-ray bursts (GRBs) and their afterflares. The observations of afterflares by the *Swift* observatory are as follows. Monitoring of gamma-ray bursts, called BAT (Burst Alert Telescope) [167], works in the energy range 15-150 keV, and has a wide field of view (about 1.4 sr). As a result, the telescope observes about 100 GRBs per year. When the BAT detects an increase of flux in a certain direction, the telescope commands the satellite to

[5]The *Suzaku* launched in low-Earth orbit, as a result, the high particle flux makes *Suzaku* instruments unusable [164].

[6]http://heasarc.gsfc.nasa.gov/docs/suzaku/analysis/abc/node9.html

[7]ftp://legacy.gsfc.nasa.gov/suzaku/data/background/pinnxb_ver2.0_tuned/

[8]ftp://legacy.gsfc.nasa.gov/suzaku/data/background/pinnxb_ver2.0_quick/

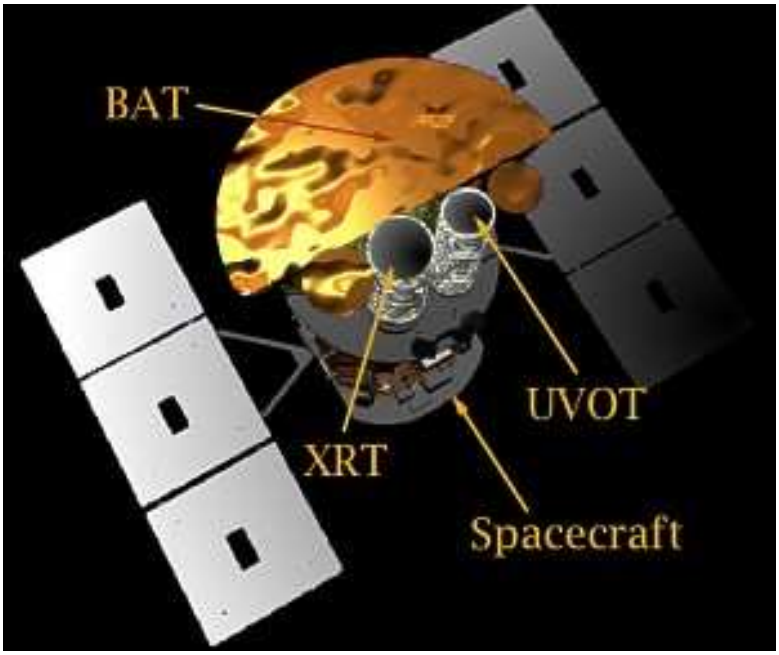

FIGURE 2.10: Schematic view of *Swift* Observatory. Image credit: *NASA* (public domain).

slew the XRT (X-ray Telescope) [168], and the UV/Optical Telescope (UVOT), towards gamma-ray burst (in fact, the observatory is named "Swift" in honor of the very quick bird, catching insects on the fly). Such repositioning from one direction to another takes about 90 seconds, which allows us to observe the afterflare of gamma-ray bursts in the X-ray and ultraviolet-optical bands simultaneously. The requirement that *Swift* be able to reposition so quickly, and with such flexibility, restricts the physical size of the observatory to being quite small, and, as a result, greatly limits the effective area of the telescope (compared to the current telescope observatories, for example, *XMM*-Newton, *Chandra* and *Suzaku*). It is not very important for the analysis of afterflares, because they are quite bright events. On the other hand, the X-ray telescope spends most of its time "resting", since gamma-ray bursts are rare events. Therefore, the auxiliary task of XRT is monitoring the state of quite bright X-ray objects. The XRT uses different operating modes to observe the sources. Depending on the brightness of the source, the X-ray observation can be performed using Imaging mode (IM), Photo-diode mode (PD), Windowed Timing mode (WT), or Photon Counting mode (PC). An image of *Swift* X-ray Observatory is shown in Fig. 2.10.

2.5.1 Analysis of *Swift* X-ray Data

The data are available on the official *Swift* web-page[9] and HEASARC. The data can be downloaded in the same manner as for *XMM*-Newton, *Chandra* or *Suzaku*. The

[9] http://www.swift.ac.uk/swift_portal/

only peculiarity is that we need to select the Swift Master Catalog (and not the Swift XRT Instrument Log). From the data products, it is enough to download "aux" and "xrt" data only. In this thesis, I used the `HEASoft` software package, version 6.19 to reduce and process *Swift* data. The data were reduced with standard procedures using the FTOOLS[10] task `xrtpipeline`. I subtracted the background events in the same manner as for the other missions. I have chosen the background areas as circular regions with the same radius as the source areas. The *Swift* data are usually characterized by a low count rate (about 0.4 counts/sec). With such a low count rate pile-up correction is not necessary [169]. The `ARF` files of *Swift* spectra were generated using `xrtmkarf`, while `RMF` files were downloaded separately for each observation[11] and according to different modes of *Swift* data as well.

2.6 *Fermi* Gamma-ray Observatory

The *Fermi* Space Telescope (see Fig. 2.11) was launched on 11 June 2008. Firstly, this telescope was originally called $GLAST$, but later was renamed to $Fermi$. The two main instruments on board of *Fermi* are LAT (Large Area Telescope) [100, 170] and GBM (GLAST Burst Monitor). The LAT is used for ordinary observations of sources, while GBM is used mainly to observe the gamma-ray bursts. In my thesis I used LAT observations, thus, here I describe how to process the data of LAT only (often written as $Fermi$/LAT). LAT works like a particle detector rather than a usual telescope. LAT consists of 880,000 silicon strips to detect high energy gamma-rays. All these strips are concentrated in a 1.8 meter cube. *Fermi* orbits around Earth detecting gamma rays from cosmic sources. These gamma rays interact firstly with tungsten's highly charged and massive atomic nuclei (electrons and positrons) creating electron-positron pairs. Such pairs can be easily detected by silicon strips. Then, such signals can be transformed to the arrival time of the original gamma-ray photon and its direction as well. Then, these particles transfer through a cesium iodide imaging collimator generating light flashes. The brightness of these light flashes is proportional to the energy of particles [171, 172]. LAT observes the sky in the energy range from 30 MeV to about 1 TeV, however, the common or "normal" energy band of this instrument is 100 MeV – 300 GeV. The analysis of LAT observations performed with energies below 100 MeV is extremely complicated, because such data are characterized by an increasing background. Moreover, problems are also known with the calibration for data analysis of observations made above 300 GeV. *Fermi* was launched specifically to constantly scan the full sky. *Fermi* makes a full rotation around its axis every $\sim$ 1.6 hours, and views the full sky every two turns,

[10] http://heasarc.gsfc.nasa.gov/docs/software
[11] http://www.swift.ac.uk/analysis/xrt/rmfarf.php

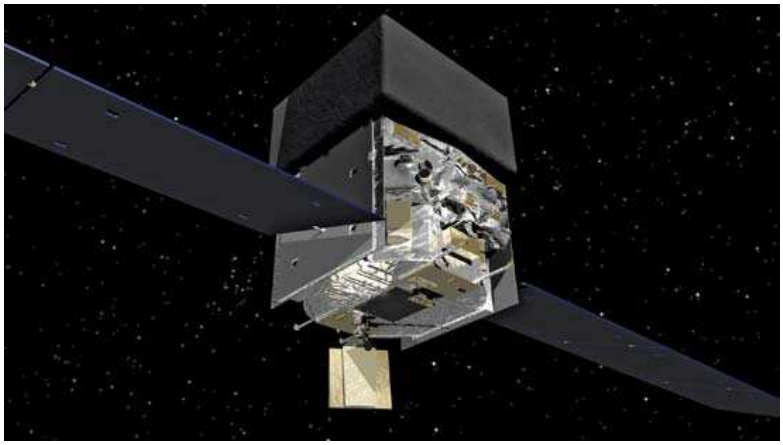

FIGURE 2.11: Schematic view of *Fermi*/LAT Gamma-Ray Observatory (*NASA* credit).

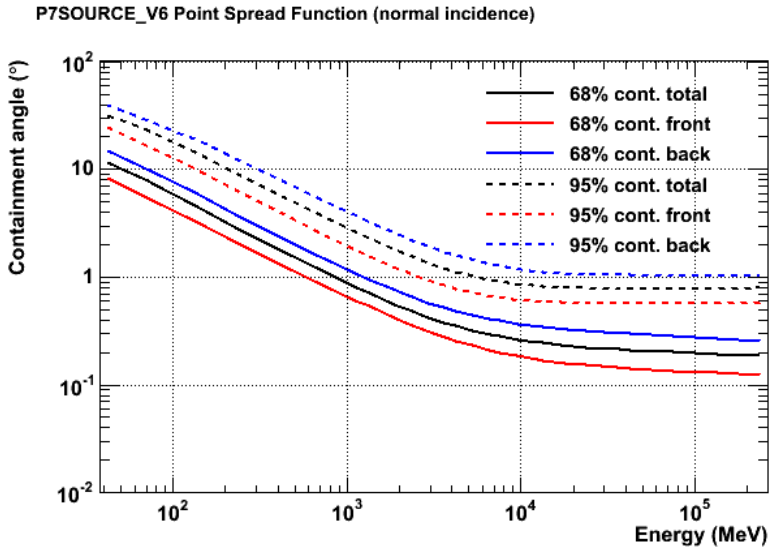

FIGURE 2.12: The point spread function of *Fermi*/LAT as a function of energy (*NASA* credit).

i.e., 3.2 hours [173]. Sometimes *Fermi* can be stopped to observe only one object, but this happens only in extraordinary cases (e.g., observation of the "standard candle" - the pulsar in the Crab Nebula, in September of 2010) [174–176].

The PSF of *Fermi*l is highly dependent on energy as $\theta_{PSF} = 2 * (\mathrm{E}/1\ \mathrm{GeV})^{-0.8}$ degrees (for 95% confidence interval). As a result, the PSF at 100 MeV is equal to 10 degrees, but at 100 GeV is to equal 0.2 degrees only[12]. This should be considered when analyzing the data obtained from *Fermi*l. The PSF of *Fermi*/LAT as a function of energy is presented in Fig. 2.12.

[12]https://www.slac.stanford.edu/exp/glast/wb/test/

2.6.1 Analysis of *Fermi* X-ray Data

The *Fermi* data can be downloaded using the official *Fermi* web-page[13]. For the analysis we need to download a file with the registered events (photon file) and a file containing the position and orientation of the satellite in space (spacecraft file). It should be noted, that if the content of the event file depends on the part of the sky that you selected, the satellite file depends on time only. As a result, if you need to analyze the observation of two objects during the same time period, then the satellite file can be downloaded only once. On the web-page introduced above we need to indicate the name of the source of interest, search radius, observation dates and the energy range. At the bottom of the page we need to indicate that we also want to download the spacecraft data. Then, click on "Start search". On the next page, the server will inform us that the our request has been successfully received. In addition, the server will show a summary of our request and a link where we can download the data. Note, that your summary is useful to keep, at least to remind us what files were downloaded.

In my thesis, the analysis was processed using the *Fermi* Science Tools 09-27-01 software package[14]. The *Fermi* server calls the downloaded files by names, e.g.,

```
L100924055816E0D2F37E91_PH00.fits
L100924055816E0D2F37E91_SC00.fits.
```

I strongly recommend to rename them with short names, e.g. "ph.fits" and "sc.fits". By the way, if you downloaded a lot of data, the *Fermi* server breaks them into smaller files (after I usually rename these files as ph0.fits, ph1.fits, ph2.fits, ph3.fits and so on). I recommend to combine them together into one file, e.g. "ph.fits". Now the data should be filtered. Why is this necessary? It must be performed because not all registered events are the photons from the interested source, there are also cosmic rays and events from other sources. *Fermi* is able to define the events which correspond to the target source. General recommendations for event filters can be found on the official *Fermi* web-page[15]. I used the `gtselect` task to filter the event files. Now we need to consider that the satellite could not work all the time. Disruptions are possible during normal operation. This issue can be solved by choosing the GTI (Good Time Interval). To record the GTI to our data we need to use the `gtmktime` task. To build the image, I used the `gtbin` task indicating the name of the filtered event file, name of the spacecraft file, size of the output image with output name, coordinates of the source, and the image scale. To build the lightcurve and spectrum, the `gtbin` task was used also. We

[13] http://fermi.gsfc.nasa.gov/cgi-bin/ssc/LAT/LATDataQuery.cgi
[14] http://fermi.gsfc.nasa.gov/ssc/data/analysis/software/
[15] http://fermi.gsfc.nasa.gov/

can choose whether to create a lightcurve or spectrum, or image, etc in the "Type of output file" field of `gtbin` task. The visualization of images can be done with `ds9`, while lightcurve can be viewed using the `fv` tool. To perform the spectral analysis I used the `P7SOURCE` and `P7SOURCE_V6` instrument response functions. The zenith angle cut was applied as $< 100°$. It is necessary to reject atmospheric gamma particles associated with Earth's limb. To obtain the spectrum of the source, it is also necessary to provide three files, the catalog of *Fermi* sources where the model for each source observed by *Fermi* is indicated, the model that describes the galactic diffuse emission, and the model that describes the isotropic diffuse component. The latest version of these files are available on the official *Fermi* web-page mentioned above. In my thesis, I used the 2 year catalog [177, 178], the `gal_2yearp7v6_v0.fits` model for the galactic emission, and the `iso_p7v6source.txt` model for the isotropic component [172]. For *Fermi* spectral analysis of binaries I also choose the 0.1-300.0 GeV energy band. According to this energy and PSF, I have extracted the scientific products from circular region of radius $20°$.

2.7 X-ray spectral analysis

The user receives data from the X-ray telescope, which contains information about events (EVENTS), such as coordinates of the position of each event (DETX, DETY), the time of the event (TIME), energy channel events (known as PHA or PI, amplitude analyzer pulses) and the probability of this event. Among other data, the predicted state of the sky in detector coordinates (X,Y), impulse invariant, PHA-adjusted change of events, PI power channel and ENERGY channel, which evaluates energy events and information on chips (ACIS spectrometer) are received also as well as the status of events on separate chips. A display of a specific PI channel in units of energy can be obtained using the response matrix file (`RMF`). For the specific energy of an input photon, there are a number of possible channels of PI which can be activated. The `RMF` file gives the probability that the photon energy is in a certain energy range for a given number of events with a specific PI or PHA values. If the actual spectrum of sources can be provided as a function of energy, $f(E)$, we can get the number of D_{PI} in each channel of the detector PI as

$$D_{PI} = \int_{E=0}^{\infty} f(E)\mathrm{RMF}(PI, E)dE. \tag{2.1}$$

The obvious way to check whether the source spectrum is consistent with the model spectrum is the inverse convolution of the `RMF`. Unfortunately, this convolution is not unique, because it is unstable to small changes of D_{PI}. In addition, `ARF` files must be generated. The `ARF` files take into account additional effects, such as the effective

area of the telescope depending on energy. The modeled spectrum is the convolution of `RMF` and `ARF` files [156]. Comparison and verification of theoretical and observation models can be done using a χ^2-test. The value of χ^2 during simulation looks like

$$\chi^2 = \sum_{j-1}^{N} \frac{[h(x_j - NP(x_j))]^2}{\sigma_j(h)^2}, \tag{2.2}$$

where x_j is the value obtained from spectral binning, $h(x_j)$ is photon frequency, N is overall number of iterations, $P(x_j)$ is probability of obtained value (predicted by model), and $\sigma_j(h)$ is standard deviation depending from observed frequency $h(x_j)$. With enough events per bin, we can rewrite the previous equation as

$$\chi^2 = \sum_{PI=min}^{max} \frac{[D_{PI} - M_{PI}]^2}{D_{PI}}, \tag{2.3}$$

here D_{PI} is the number of observed PI, M_{PI} provides the number of modeled PI. The variations of the model parameters to reduce χ^2 can improve the model. The parameters that give the lowest χ^2 are the best-fit parameters that can be used to describe observational data. If the model describes the observational data so χ^2 corresponds to the χ^2/ν value, where ν is a number of degrees of freedom for spectral modeling (the difference between the number of all spectral channels (i.e. $max - min + 1$) and the number of free parameters of the model).

The physical parameters of spectra such as flux, parameters of the models, etc, can be obtained using the application `Xspec`[16] [179]. `Xspec` is a tool included in the software package HEASOFT. To determine the physical parameters of the source it is necessary to model the spectra of the source. `Xspec` performs modeling using a number of additive, multiplicative models and their combinations. Selecting a model is often a combination of science and art. Below I list a few points that I found useful when selecting a model:

- First of all, at low energies, the absorption of the spectrum of the source is modified, mainly by the interstellar medium. There are several models of absorption. Here, I used the models `phabs` and `wabs` depending on the task. These models include one parameter, the column density of hydrogen atoms [180, 181]. This value can be obtained in two ways. Galactic surveys are suitable for extragalactic sources. For galactic sources, this value is usually an upper limit. Thus, the column density should be determined from the modeling.

[16] http://heasarc.nasa.gov/xanadu/xspec/XspecManual.pdf

- Secondly, it is needed to check the thermal component in the spectrum. Such a component can be easily defined using the emission lines in the spectrum of the object. A non-thermal component is also visible, so the radiation can generally be described as the sum of the thermal and non-thermal components.
- Thirdly, we should start with these simplest models, updating them if it is necessary. For example, the simplest non-thermal model is `powerlaw`, describing a power spectrum (with a fixed spectral index). The simplest thermal model is `bbody`, this model describes the black body radiation. Emission lines phenomenologically might be described, for example, by a `gaussian` model.
- Fourth, there are models that are commonly used for particular class objects.

The *XMM*-Newton, *Chandra*, *Suzaku* and *Swift* spectra were analyzed in `Xspec` version 12.8.2 with an absorbed power law model. In the `Xspec` environment, the simplest power law model is called `power` and is defined as

$$A(E) = KE^{-\alpha}, \tag{2.4}$$

where α is the photon index of power law model.

2.7.1 χ^2- and $C-$ statistics

A maximum likelihood is the standard statistic that is usually used in parameter calculations [182]. The definition of errors of modeled parameters is performed in `Xspec` using two types of statistics, Gaussian and Poisson. Poisson statistics are usually used with statistically poor data, in contrast with Gaussian statistics which can work only with statistically rich data (i.e. data with low and high count rate). Below I describe the mathematical equations of these statistics (see [182–185] for more details). The likelihood for Gaussian data (χ^2 - statistic) is performed in `Xspec` as

$$L = \prod_{j=1}^{N} \frac{1}{\sigma_j \sqrt{2\pi}} \exp\left[\frac{-(x_j - m_j)^2}{2\sigma_j^2}\right]. \tag{2.5}$$

The sense of x_j in the Eq. 2.5 correspond to the indicator of the observed data values, while the σ_j correspond to the errors of these observed values. The sense of m_j correspond to the theoretically predicted data values. The double negative natural logarithm of Eq. 2.5 provides nearby statistic

$$\chi^2 = \sum_{j=1}^{N} \frac{(x_j - m_j)^2}{\sigma_j^2}, \tag{2.6}$$

and referred as the `statistic chi` command in `Xspec` environment.

The likelihood for Poisson data (C - statistic) is performed in `Xspec` as

$$L = \prod_{j=1}^{N} \left((tm_j)^{S_j} \mathrm{e}^{-tm_j} / S_j! \right) . \tag{2.7}$$

The sense of S_j in the Eq. 2.7 correspond to the observed data values. The values of m_j and t correspond to the theoretically predicted data values and exposure times, respectively. The maximum likelihood of the Poisson values can be presented as

$$C = 2 \sum_{j=1}^{N} \left((tm_j) - S_j \ln (tm_j) + \ln (S_j!) \right) . \tag{2.8}$$

The Eq. 2.8 was firstly presented by [183] and modified to give

$$C = 2 \sum_{j=1}^{N} \left((tm_j) - S_j + S_j (\ln (S_j) - \ln (tm_j)) \right) . \tag{2.9}$$

As a result, such statistic is proportional to S^2 if we have to deal with a limit of indicator of data values. The Eq. 2.9 is referred in `Xspec` as the `statistic cstat` command. In my thesis I used both statistics depending on the task.

2.7.2 Parameter measurements

To estimate the pair parameters of source spectra modeled by power law model, I used Monte Carlo simulations and `Xspec`. The main reasons to do such an approach are (1) statistically poor data and (2) correlation between parameters of model (in my case, N_H (hydrogen column density) and Γ (photon index)) and obtained flux. The data with poor statistics have large and non-symmetric error bars in spectral bins. As a result, the uncertainties in the derived flux become also non-symmetric (non-Gaussian) - a fact which is important to take into account in the subsequent analysis. A more significant problem, however, lies in correlations between the model parameters, which complicates an accurate estimation of the uncertainties on the derived values of the flux. To resolve these problems I performed the Monte Carlo simulations to estimate directly the scatter and correlations between the parameters of the spectral model and to compute statistically precise uncertainties on the estimated flux values [186, 187].

As a first step of simulations I sample the N_H - Γ parameter of each observation with `Xspec` to obtain the C-statistic likelihood profile of the fit to the data. The values of likelihood in this profile can be used to determine how probable is a given combination (N_H, Γ) with respect to the best fit values. This probability can be estimated from the

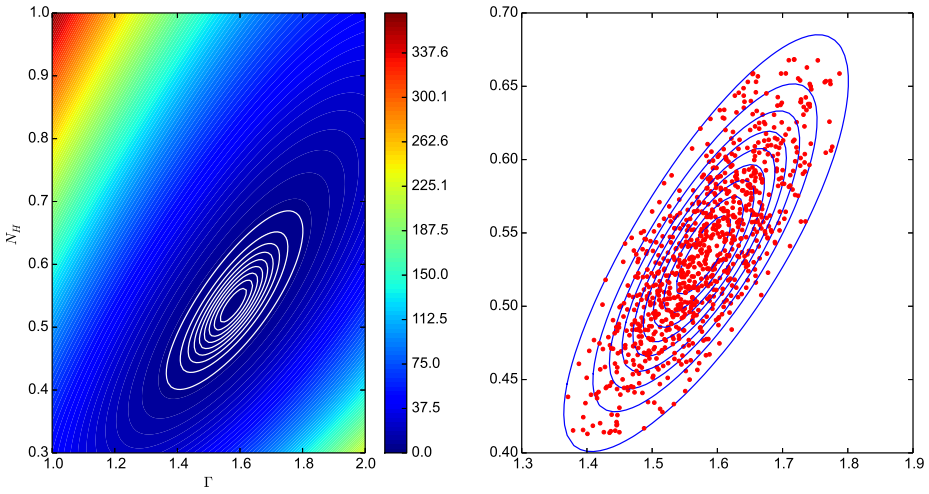

FIGURE 2.13: (left:) The C-statistic likelihood profile on the grid of column density, N_H, and photon index, Γ. (right:) The distribution of the selected test-points in each annulus.

Wilks theorem, determining the -2 log(likelihood) values to be distributed around the minimum as χ^2 with 2 degrees of freedom - as there are two model parameters of interest (N_H and Γ). As an example, the corresponding confidence ranges with 10% step are shown in Fig. 2.13 for one of the analyzed observations.

Next I randomly choose 1000 points in the derived N_H - Γ parameter space according to the probability profile derived at the previous stage (see right image in Fig. 2.13). For each of these pairs, I then compute the corresponding source flux. In this way I obtain the probability distribution of source flux in a given observation, which naturally accounts for the correlations between the latter, N_H and Γ.

To estimate confidence intervals for values of flux, I built an averaged histogram of all obtained fluxes, as shown on the left panel of Fig. 2.14. Using this histogram, I calculated the errors for the values of the flux in such a way, that the interval [F-dF-; F] contains 68 % of all simulated flux values below F and [F; F+dF+] contains 68 % of values above it (see right panel in Fig. 2.14). To do this approach, I used the cumulative distribution function (CDF). The definition of CDF, in the case of random variable X is

$$F(x) = \int_{-\infty}^{x} f(t)dt, \text{for} - \int < x < \int . \tag{2.10}$$

In probability theory and statistics, CDF, evaluated at x is the probability that the defined randomly variable X will take a value less than or equal to x. In other words, $CDF(x) = P(X <= x)$, where P denotes probability. In the case of a continuous distribution, it gives the area under the probability density function from minus infinity to x. In addition, CDF might be used to determine the propagation of variables. The

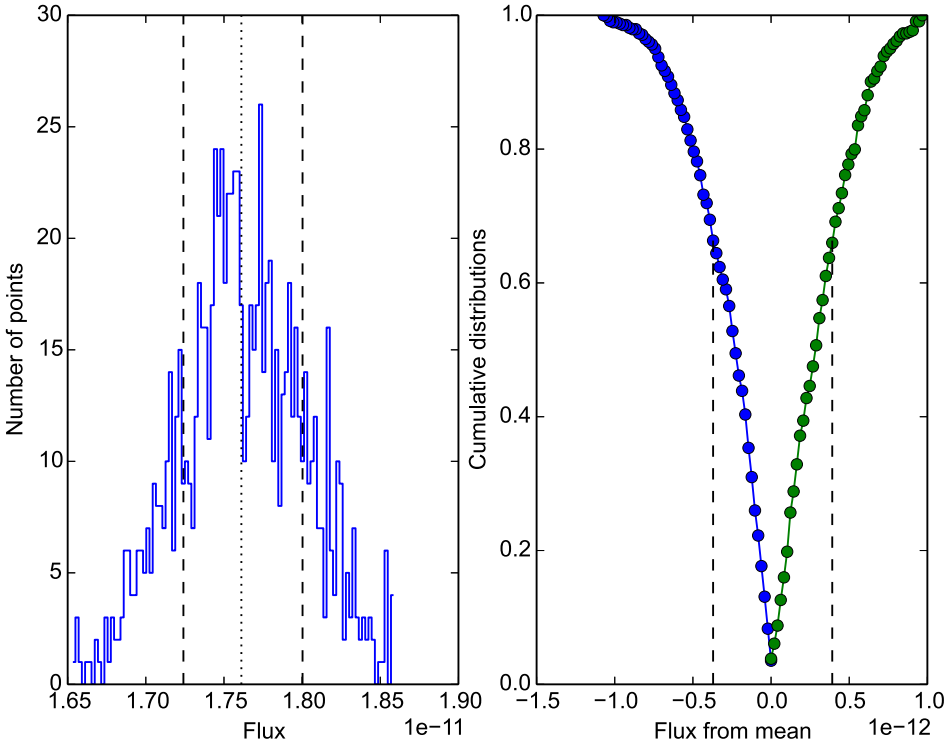

FIGURE 2.14: (left:) The histogram of averaged values of flux. The dotted line corresponds the best-flux value, while two dashed lines correspond the 68 % confidence range of errors. (right:) The cumulative distribution function of flux.

confidence intervals dΓ+ and dΓ- as well as dN_H+ and dN_H- were computed from this distribution in the same way as flux. The error-bars of column density and slope were calculated for 1σ confidence level as well.

The X-ray flux, F, that I was interested here, depends on the number of other parameters, such as the source spectral index (Γ), normalization (A) and the assumed hydrogen column density (N_H). The proper estimation of the uncertainties on the flux thus requires the sampling of the $\Gamma - A - N_H$ parameter space, which is conventionally performed with the help of Monte Carlo simulations (e.g., the Monte Carlo Markov Chain method).

Such simulations typically start from the raw data and propagate the corresponding measurement uncertainties to the value of interest - such as the flux in my case. Development of such simulation can be a complicated enterprise as it requires, in particular, the proper account for the instrument response functions (IRFs). To simplify the analysis and minimize the sources of potential errors, I've built my simulations around `Xspec`, which includes the correct treatment of IRFs. `Xspec` is not capable of doing the MC simulation I needed, but instead can properly sample the fit likelihood in

the $\Gamma - A - N_H$ parameter space. Thus, my method above used this sampled likelihood in a smaller MC simulation, which computed the exact confidence ranges for the X-ray flux values I have obtained at earlier steps.

Chapter 3

High-energy processes in gamma-ray binaries

In this chapter, I review the main high-energy emission mechanisms relevant to gamma-ray binaries. For this, I describe the main theoretical aspects of "leptonic processes", namely: Compton scattering, inverse-Compton scattering, bremsstrahlung, and synchrotron radiation. The initial energy of particles can be changed by cooling, so I describe the equations of cooling for particles and define analytical solutions in some cases. I also discuss possible additional mechanisms of high-energy processes in binary systems, namely: "hadronic processes" (proton-proton collision, photomeson production). For PSR B1259−63, I calculate the energy losses of electrons during inverse-Compton scattering, synchrotron radiation and ionization.

3.1 Compton scattering

Compton scattering is the scattering of a photon by an electron [188–191]. Compton scattering determines the opacity of material to both X-rays and gamma-rays (high-energy). It plays an important role in the atmospheres of neutron stars, in X-ray sources, and in the interior of stars. A special case of Compton scattering in the limit of low-frequency photons and low-energy electrons is Thomson scattering. In the scattering of a photon by an electron at rest, due to the laws of conservation of energy and momentum, the photon loses energy and transfers it to an electron. This phenomenon was experimentally discovered in 1922 by American physicist A. Compton who investigated the scattering of X-rays photons in graphite, and is known as the Compton effect. Due to the scattering of low-frequency photons by ultra-relativistic electrons, the energy of photons increases (many times). This effect is called the inverse-Compton effect.

The inverse-Compton effect is one of the most important mechanisms in the X-ray and gamma-ray spectral range of astronomical objects.

The cross section of Compton scattering (i.e., Klein-Nishina) depends on the parameter $x = (2h\nu/m_e c^2) \cdot \gamma(1 - \mu v/c)$ [189], where ν is the frequency of the photon before scattering, μ is cos of the angle Θ between the directions of propagation of the electron and photon before scattering, v is the velocity of the electron before the scattering, $\gamma = [1 - (v/c)^2]^{-1/2}$ is the Lorentz factor of the electron. In the case of a stationary electron scattering, $x = 2h\nu/m_e c^2$. For the non-relativistic case ($x \ll 1$) the cross section σ is slowly reduced, and $\sigma = \sigma_T(1 - x)$. For the ultra-relativistic case ($x \gg 1$) the cross section decreases rapidly with increasing x as $\sigma = (3/4)\sigma_T \cdot x^{-1}(\ln x + 1/2)$. Thus, for low-frequency photon scattering the cross section is equal to the section of the Thomson scattering of $\sigma_T = (8\pi/3)(e^2/m_e c^2) = 6.65 \cdot 10^{-25} cm^2$. As with Thomson scattering, Compton scattering can lead to noticeable polarization effects. During Compton scattering, the frequency of the photon and the electron energy charge [188, 189, 191]. The frequency of the photon after scattering is

$$\nu' = \nu \frac{1 - \mu \frac{v}{c}}{1 - \mu' \frac{v}{c} + \frac{h\nu}{\gamma m_e c^2}(1 - \cos\alpha)}, \tag{3.1}$$

where μ' is cos of the angle Θ' between the directions of propagation of the photon after scattering and electron before the scattering, and α is the scattering angle (the angle between the directions of propagation of the photon before and after scattering (see Fig. 3.1). In the case of scattering off an electron at rest

$$\nu' = \nu \frac{1}{1 + \frac{h\nu}{m_e c^2}(1 - \cos\alpha)}, \tag{3.2}$$

or

$$\lambda' = \lambda + \frac{h}{m_e c}(1 - \cos\alpha), \tag{3.3}$$

thus, the scattering of the photon at wavelength λ is increased, this increase (proportional to h, and, therefore, having a quantum nature) depends only on the scattering angle [189, 191]. The value of $\lambda_C = h/m_e c = 0.024$ Å is called Compton wavelength. From the equations above it is clear that the change in wavelength of the photon in the scattering on a stationary electron is less than λ and, thus, is substantial only for sufficiently short-wave radiation.

During Compton scattering the photon γ_1 with energy of electron $h\nu_1$ has a low probability for the production of a low-frequency photon γ_2 with energy $h\nu_2 < h\nu_1$: $\gamma_1 + \mathrm{e} \rightarrow \mathrm{e} + \gamma_1 + \gamma_2$. This process is called the double Compton effect. The production of low frequency photons due to the double Compton effect can compete with the inhibitory

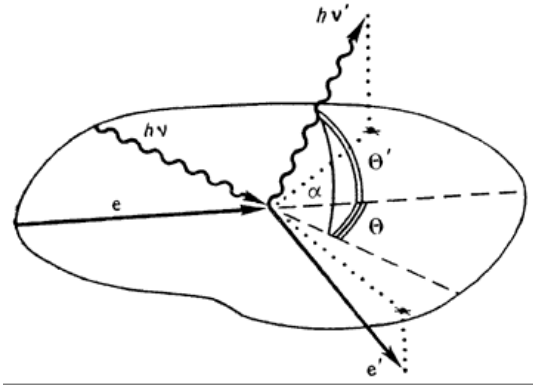

FIGURE 3.1: The Compton scattering geometry. The solid arrows correspond to the direction of movement of the electron before and after scattering, while the wavy arrows correspond to the same for the photon. The image is taken from [189].

process $e + p \rightarrow e + p + \gamma_t$ (see Bremsstrahlung radiation below) only in the extremely tenuous and hot plasma of the early stages of expansion of the Universe, in X-ray and gamma-ray sources. The Compton effect limits the propagation of high-energy photons through matter [189]. As a result of multiple scatterings, the high-energy photon's energy is reduced (the energy being transfered to the electrons), and so it enters the other wavelengths (cooling) and is absorbed due to the photoionization of atoms. The Compton effect determines the length of the path of the high-energy X-ray photons (10 keV $< h\nu <$ 3 MeV) in diffuse astrophysical plasma. Scattering of high-energy photons with $h\nu > 3$ keV by the electron in a hydrogen atom occurs with the same cross section as for a free electron. This is due to the fact that the energy imparted to the electron due to the recoil effect is greater than the binding energy of an electron in a hydrogen atom. In the scattering of low-frequency photons by ultra-relativistic electrons (case of inverse-Compton effect) the maximum probability of scattering of photons occurs when $\mu' \sim 1$ [188, 190–192]. If $h\nu/\gamma m_e c^2 \ll 1$, then the change in frequency of the photon is described by formula

$$\nu' = \nu \frac{1 - \mu \frac{v}{c}}{1 - \mu' \frac{v}{c}}. \tag{3.4}$$

Thus, the scattering of photons by ultra-relativistic electrons, the change of frequency occurs only due to the Doppler effect [191] (the same as in the reflection from the moving wall), and the scattering cross section is Thomson. It is easy to understand, since in this case in the rest frame of the electron classical Thomson scattering occurs. Therefore, the inverse-Compton effect, in contrast to the direct Compton effect, is a purely classical effect (the change of frequency is independent from h). From Eq. 3.4 it follows that the scattering of the electrons motion in the direction corresponding to $\mu' \sim 1$ significantly increases the frequency of the photon $\nu \sim \gamma^2 \nu$. The frequency of photons in scattering by relativistic isotropically distributed electrons should rise in $(4/3)\gamma^2$ times. The same average increase takes place, if the photons of an isotropic

radiation field are scattered by a field of ultra-relativistic electrons. If the electrons have a power law distribution of energy $dN_e = K\varepsilon_e^{-\beta}d\varepsilon_e$ (dN_e is the concentration of relativistic electrons in the energy range from ε_e to $\varepsilon_e + d\varepsilon_e$), then the spectrum of the high-energy radiation, which is formed as a result of the inverse-Compton effect of low-frequency photons, is also a power law. Its intensity is equal to $I_\nu = B\nu^{-s}$ (K and B are constants), where the spectrum index is $s = (\beta - 1)/2$. At very-high-energies, when the parameter x becomes large, the cross section is decreasing, and the increase of the energy of the photons during scattering becomes less than $\sim \gamma^2\nu$. This leads to a deviation of the high-energy spectrum from the power law. Asymptotically the intensity is equal to $I_\nu \sim \nu^{-\beta}\ln(h\nu kT_r/m_e^2c^4)$, where T_r is the temperature of low-frequency photons [189].

The inverse-Compton effect is often considered the primary mechanism in the formation of the hard power law emission spectra in quasars and active nuclei of galaxies [192]. This process is the main reason for the loss of energy by relativistic electrons in an isotropic field of low-frequency radiation (e.g. in the field of the microwave background radiation in the Universe), or radiation field of compact objects (e.g. binaries) [189]. The characteristic time of energy loss in such a field emission is $t \approx (3/4)m_ec/\sigma_T\varepsilon_r\gamma$ [188], i.e., higher the energy of the electron ($\sim \gamma$), and the radiation energy density ε_r. When $\varepsilon_r > H^2/8\pi$, where H is intensity of magnetic field, the energy loss due to the inverse-Compton effect exceeds the losses to synchrotron radiation, as will be shown in the sections below where I compare the losses of electrons for synchrotron and inverse-Compton scattering.

3.2 Synchrotron emission

Synchrotron radiation is the radiation of electromagnetic waves of charged particles (mostly electrons in space), moving at relativistic velocities in the magnetic field **H**. Synchrotron radiation from electrons was first observed in accelerators, i.e., synchrotrons [76, 188, 189, 193]. Magnetic fields bend the trajectory of the motion of the electrons (as a result of the Lorentz force), as a result, the acceleration produces the electromagnetic radiation. This mechanism of radiation is often used to explain the radio, optical and X-ray radiation in a variety of cosmic sources. A similar non-relativistic particle radiation is happening on a regular gyromagnetic frequency $\nu_C = qH/(2\pi mc)$ and its first harmonics (q and m are the charge and mass of the particle at rest). The emission of charged relativistic particles, i.e., particles moving at speeds close to the speed of light, has a number of significant differences from the emission of slow particles. Due to the Doppler effect, the frequency of light emitted by the fast-moving particle in the direction of its movement is greatly increased, and the intensity of the emission

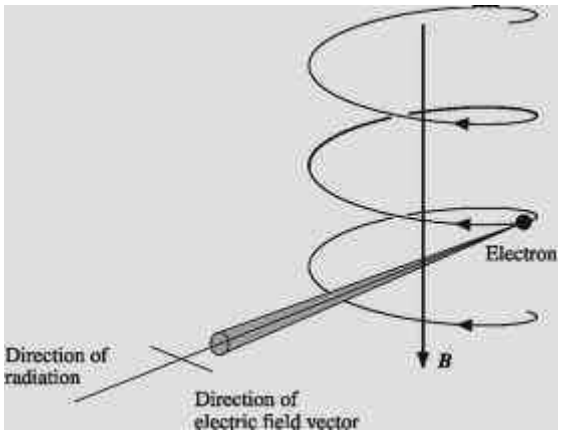

FIGURE 3.2: The schematic view of synchrotron radiation. The image is taken from http://www.astronomyclub.xyz/main-sequence/supernova-remnants.html.

increases at higher harmonics. In relativistic particles with energies $E \gg mc^2$, the radiation at high harmonics has a practically continuous spectrum and is focused into the direction of the instantaneous velocity in a narrow cone with an angle of the solution $\psi \sim mc^2/E$. Moving in the magnetic field, the relativistic electron describes a circle (if it has no velocity component along the field). Rotational speed in its magnetic field **H** is $\nu_H = \frac{eH}{4\pi mc} \cdot \frac{mc^2}{E} = \frac{ecH}{2\pi E}$. Hereafter **H** will mean the field component that is perpendicular to the velocity vector of the particle (i.e., $H_\perp$). The narrow cone, within which lies the electron radiation, is rotated together with the rotation of the vector of instantaneous velocity of the electron (Fig. 3.2). This means that the observer in the plane of the electron orbit sees bursts of radiation at those times when the electron velocity is directed at him. Flares are happening with intervals of $2\pi E/ecH$, the duration of each flare is $\sim (2mc/eH) \cdot (mc^2/E)^2$ [189].

Since the frequency of flares is high enough, the observer observes almost continuous radiation. The total power of synchrotron radiation for one electron per unit frequency, near the frequency ν_m and per unit of solid angle is equal

$$P_\nu = \frac{1.6e^3 H}{4\pi mc^2} = 1.7 \cdot 10^{23} H \left(\frac{\text{erg}}{\text{s} \cdot \text{sterrad} \cdot \text{Hz}} \right), \tag{3.5}$$

where **H** is expressed in erg [189]. At lower frequencies, the radiation is reduced as $\nu^{1/3}$, and at large frequencies, the radiation decreases exponentially $\sim \nu^{1/2} \exp(-0.29\nu/\nu_m)$. For an observer located exactly in the plane of the orbit of the electron, the radiation is linearly polarized with the electrical vector lying in the orbital plane. On a certain angular distance from this plane, the polarization is elliptical with opposite signs on either side of the plane. In addition, the intensity of elliptically polarized radiation is negligible. The system of relativistic electrons in a homogeneous magnetic field gives

linearly polarized synchrotron radiation with electrical vector which is perpendicular to the magnetic field [189].

If all electrons had about the same energy, the emission spectrum of this system would have the maximum at frequency $\nu_m = \frac{eH}{4\pi mc} \cdot \left(\frac{E}{mc^2}\right)^2 = 1.4 \cdot 10^6 H \left(\frac{E}{mc^2}\right)^2$ (Hz). The relativistic electrons have different energies in different cosmic conditions. Usually, the electron energy distribution is approximated by a power law model [76, 188, 189, 193], i.e., the number of electrons, N, in the unit of volume in energy range from E to $E+\Delta E$ as

$$N(E)\Delta E = \frac{K}{E^\gamma} \cdot (mc^2)^{\gamma-1} \cdot \Delta E, \tag{3.6}$$

where K and γ are constants. The synchrotron radiation per unit of volume per unit of solid angle and per unit of frequency range (so-called coefficient of radiation) is given by

$$J_\nu = a(\gamma)\frac{e^3 H}{mc^2}\left(\frac{3eH}{4\pi m^3 c^5} \cdot \frac{1}{\nu}\right)^{(\gamma-1)/2} \cdot K\left(\frac{\text{erg}}{\text{s} \cdot \text{cm}^2 \cdot \text{sterrad} \cdot \text{Hz}}\right), \tag{3.7}$$

where $a(\gamma)$ is a numerical coefficient that depends on γ and varies from 0.1-0.2 within $1.5 < \gamma < 5$. The degree of linear polarization of the radiation is equal to $(\gamma+1)(\gamma+7/3)$. The value of $(\gamma - 1)/2 = \alpha$ is called the spectral index of synchrotron radiation. If the concentration of relativistic electrons is not too large, the radiation intensity is determined by the formula $I_\nu = j_\nu l$, where l is the size of the radiation area. At high concentrations of electrons, the self-absorption of synchrotron radiation must be considered. The ratio between j_ν and coefficient of absorption $\varkappa(\nu)$

$$\frac{J}{\varkappa_\nu} = b(\gamma)\left(\frac{4\pi m^3 c}{3eH}\nu^5\right)^{1/2}, \tag{3.8}$$

where the numerical coefficient $B(\gamma)$ varies from 0.7 to 0.1 at $1.5 < \gamma < 5$. The above relations are valid, if the radiating electrons are in a vacuum. In a sufficiently dense plasma the radiation's character is changing, i.e., the direction of radiation and its intensity decrease sharply. This leads to a cut-off of the spectrum at frequencies of less than $7ecn_e/H$, where n_e is the concentration of electrons in the plasma. But there is a possibility to see synchrotron maser radiation. Synchrotron radiation at radio wavelengths is often called non-thermal because its spectrum differs from the spectrum of thermal radiation [189]. The spectrum of synchrotron radiation can not be characterized by one value of the temperature, as in the case of thermal radiation. If the concentration of relativistic electrons is so high that the self-absorption of synchrotron radiation becomes significant, the spectrum of synchrotron radiation can be characterized by a

frequency-dependent effective temperature, T_e which equals

$$kT_e(\nu) \approx mc^2 \left(\frac{4\pi mc}{eH}\nu^5\right)^{1/2}. \tag{3.9}$$

The synchrotron radiation mechanism is used for the interpretation of objects like our Galaxy and other galaxies, radio, optical and X-ray radiations of the Crab Nebula and other nebulae, supernova remnants, certain kinds of solar radiation, pulsars, quasars, and γ-ray binaries as well [194–197].

3.3 Bremsstrahlung emission

According to the laws of electrodynamics, a charge radiates electromagnetic waves when accelerating or decelerating [189]. In space, the deceleration (or acceleration) of charges can be caused by either attraction or repulsion at the convergence of the electrons and ions, or their centrifugal acceleration during their driving in the external magnetic fields. Bremsstrahlung emission (in an astrophysical sense of the word) usually occurs in ionized gas due to the thermal collisions of electrons and ions. Most of the bremsstrahlung emission can also be called the radiation of free-free transitions, because it can be associated with transitions of electrons from one orbit to another, and it is not accompanied by the capture of an electron by ion. The whole spectrum of electromagnetic waves are radiated at these transitions, including X-rays and radio. The spectrum of bremsstrahlung emission is continuous and terminates at the maximum possible energy which is equal to the initial energy of the electron. The energy of bremsstrahlung emission in units of the plasma volume within a solid angle per unit of frequency in range of time (another word coefficient of radiation) is equal to

$$J_\nu(T) = \frac{16}{3}\left(\frac{\pi}{6}\right)^{1/2}\frac{N_\nu Z^2 e^6}{m_e^2 c^3}\left(\frac{m_e}{kT}\right)^{1/2}\cdot g\cdot e^{-h\nu/kT} n_e n_i = 5.44\cdot 10^{-39}\frac{N_\nu Z^2 g}{\sqrt{T}} e^{-h\nu/kT} n_e n_i \tag{3.10}$$

in units of ergs/(cm^3 s sterrad Hz) [189]. n_ν is the refraction index, Z is the ion charge, n_e and n_i are the concentration of electrons and ions, and g is the so-called Gaunt factor (in optical range $g \approx 1$, and in radio $g \approx$ 6-7). Due to the large mass of the ions, their bremsstrahlung emission is negligible compared with bremsstrahlung emission of electrons. The rate of plasma energy loss by bremsstrahlung is equal to $W = 1.43\cdot 10^{-27} T^{1/2} n_e n_i Z^2$ (erg/cm^3/s). Bremsstrahlung emission is responsible for the radio emission of the solar corona as well as the star' coronas in general, HII regions, planetary nebulae, gas in clusters of galaxies, etc. Bremsstrahlung emission also contributes a significant part of the IR and optical radiations of stars. This mechanism also explains the radiation of certain X-ray sources [188, 189].

3.4 Calculation of losses

In the sections above, I have presented the main high-energy cooling processes of relativistic electrons (positrons) and protons usually considered in high-energy astrophysics. I found that inverse-Compton scattering and synchrotron radiation are the most relevant high-energy leptonic processes in the typical environment of compact binaries. Bremsstrahlung could be relevant in denser environments than those found in binaries. Triplet pair production is unimportant in the cooling except if the system accelerates electrons to PeV energies. Hadronic processes are not favored as the energy budget in protons required to account for the full gamma-ray luminosity should be very high, i.e., 3 or 4 orders of magnitude higher than the power injected in leptons [198]. High-energy gamma rays can be highly absorbed through pair production due to the massive companion star [79, 199]. For the modeling of the high-energy radiation in PSR B1259−63, I will consider inverse-Compton scattering and synchrotron radiation. The result of my modeling is presented in Chapter 5, namely in Section 5.3.

In this section, I estimate the energy losses of electrons during inverse-Compton scattering, synchrotron radiation and ionization. I use the physical parameters of PSR B1259−63 during the calculations below. Here, I try to understand the high-energy processes that might be happening in this binary system. These calculations will be used in Chapter 5 to model the double-peaked light curve of PSR B1259−63.

3.4.1 Electron losses during inverse-Compton scattering

The effect of inverse-Compton scattering of high-energy electrons through a field of photons has been studied in detail by a number of authors. In the description below I mostly follow [188], [200] and [201].

As was discussed above, when the energy of a photon is much smaller than the rest mass energy of an electron, and the electron is scattered without loss of energy, i.e., the outcoming energy of the electron is $\varepsilon_1 \approx \varepsilon_0$, it is known as the Thomson regime. For example, when $\gamma_e = 10^4$ and $\varepsilon_0 = 1$ eV, a γ-ray photon with energy $\varepsilon_1 = 100$ MeV can be produced. In the case when $\varepsilon_0 \gg m_e c^2$, the electron loses almost all its energy so the energy of the scattered photon equal $\varepsilon_1 \sim \gamma_e m_e c^2$. It is known as the Klein-Nishina regime.

The integrated inverse-Compton energy losses of an electron is shown in Fig. 3.3 for the Thomson and Klein-Nishina regimes. The total power lost per electron is given by

$$\frac{dE}{dt} = -\int_{\varepsilon_1} (\varepsilon_1 - \varepsilon_0) n_{ph} \frac{dN}{dt d\varepsilon_1} d\varepsilon_1, \tag{3.11}$$

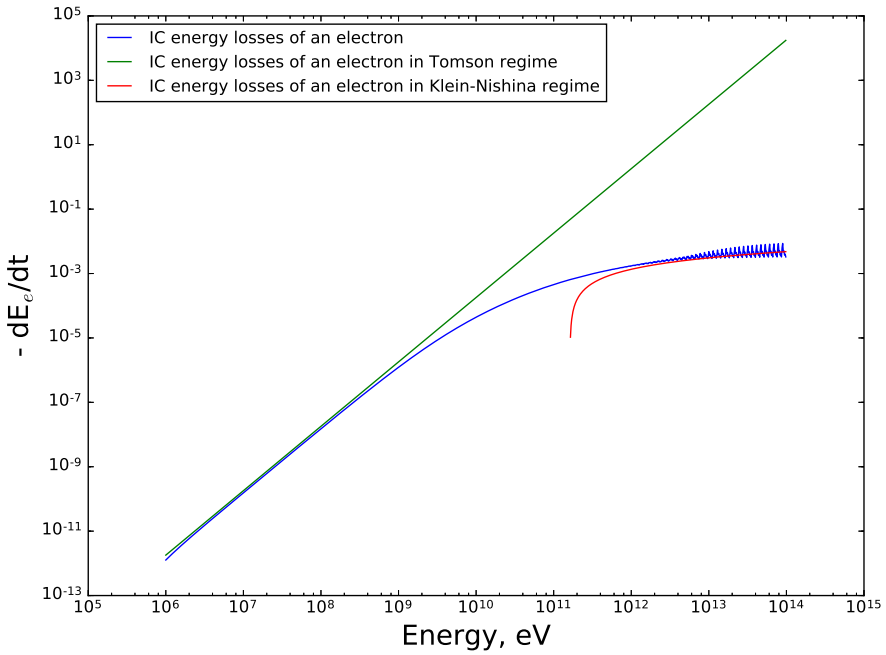

FIGURE 3.3: The numerically integrated inverse-Compton energy losses (Eq. 3.11, blue solid line) of an electron of energy $E_e = \gamma m_e c^2$ bathed in an isotropic gas of photons with a black body energy distribution of effective temperature $T = 34000$ K ($-dE_e/dt$ is calculated in erg/s units). The analytical formula in the Thomson (green solid line) and Klein-Nishina (red solid line) regimes are overplotted for comparison (the analytical equations were obtained from Eq. 3.12 and taken from [188]). The parameters used here are compatible with PSR B1259−63: $T = 34\ 000$ K, $R_* = 6.2{\times}10^{11}$ cm and $d = 10^{13}$ cm at periastron.

where n_{ph} is the density of photons. It is known that Be-type stars emit eV photons. The energy density of photons emitted from a Be-type star as a function of distance to the star is shown in Fig. 3.4. Here, I used the parameters of the Be-type star similar to the companion of the PSR B1259−63. The emission of the star is described by black-body emission. The total flux from the star, namely the total radiation in all directions, is constant. As a result, the flux decreases with distance from the star as $1/R^2$. For more details about the density of Be-type star see Section 5.3 in Chapter 5.

The cooling timescale of inverse-Compton scattering as a function of the electron energy is shown in Fig. 3.5. The resultant cooled spectra of electrons is shown in Fig. 3.6 for 1, 10 and 100 ks after the particle injection.

If the energy of a scattered photon in units of the initial energy of electron is expressed $\varepsilon_0 = \gamma_e m_e c^2 \varepsilon_1$, the total spectrum of the scattered photons (the density of γ-rays scattered per electron, per unit of energy, per unit of time) is given in [188]

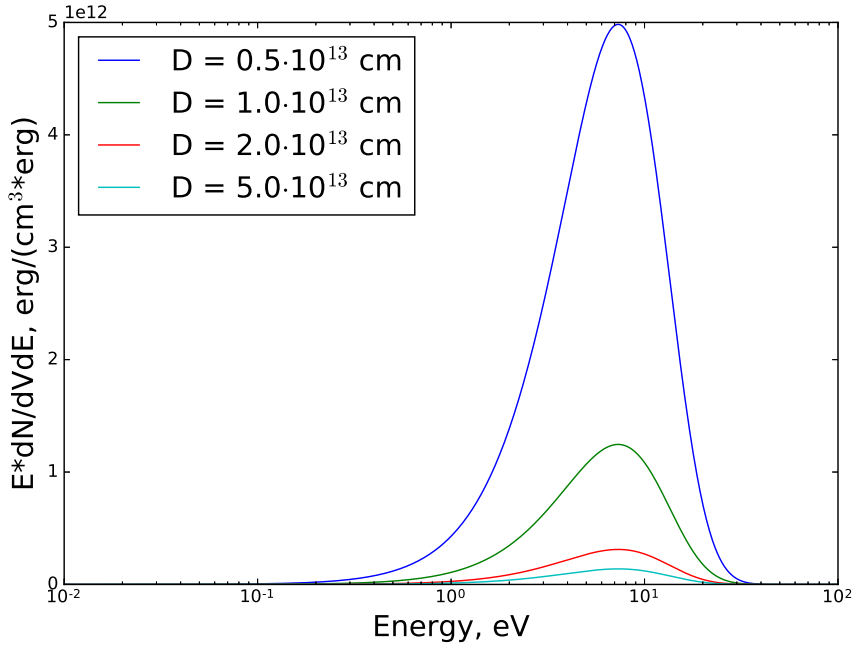

FIGURE 3.4: The distribution of flux density of SS 2883 as a function of distance to star, the $T = 34000$ K and $R_* = 6.2{\times}10^{11}$ cm.

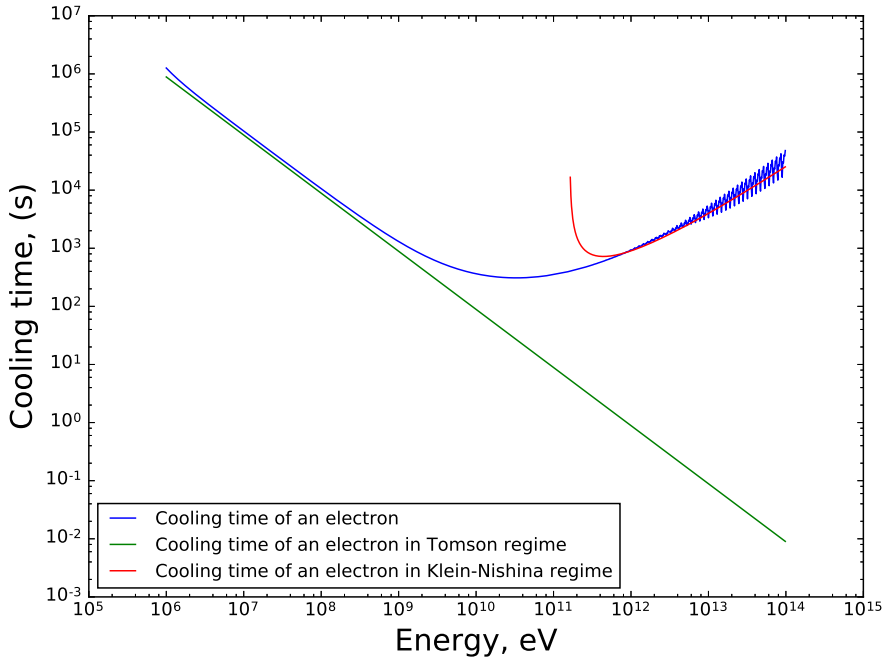

FIGURE 3.5: The cooling timescale of inverse-Compton scattering (solid lines, green in the Thomson limit and red in the Klein-Nishina regime) as a function of the electron energy. The analytical equations for the Thomson and Klein-Nishina regimes were obtained from Eq. 3.12 and taken from [188]. The parameters used here are compatible with PSR B1259−63: $T = 34\,000$ K, $R_* = 10\ M_\odot$ and $d = 10^{13}$ cm at periastron.

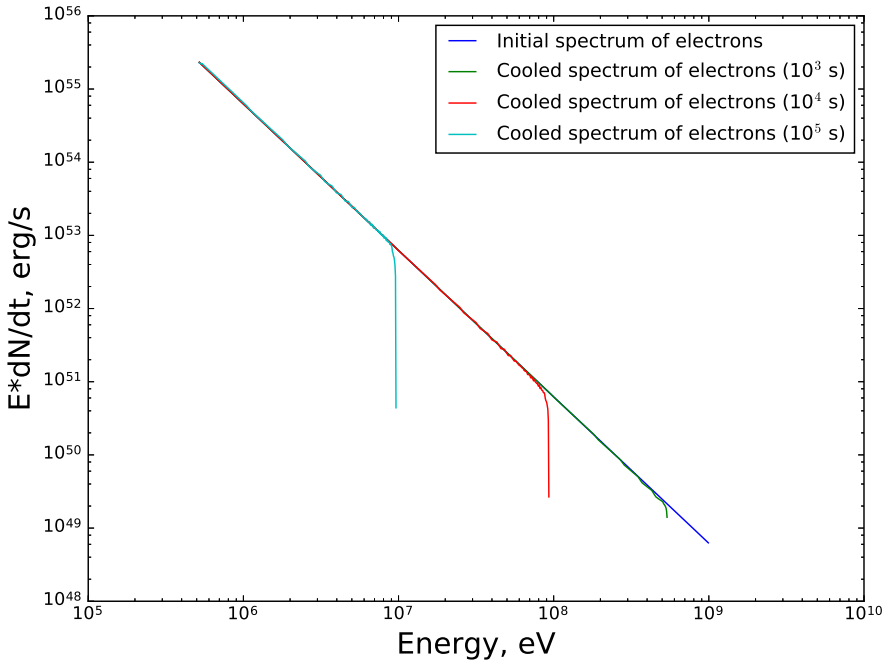

FIGURE 3.6: The cooled spectra of electrons during inverse-Compton scattering at 1, 10 and 100 ks after the particle injection.

(including the Klein-Nishina regime)

$$\frac{dN_{\gamma,\epsilon}}{dtd\varepsilon_1} = \frac{2\pi r_0^2 mc^3}{\gamma}\frac{n(\varepsilon_0)d\varepsilon_0}{\varepsilon_0} \times \left[2q\ln q + (1+2q)(1-q) + \frac{1}{2}\frac{(\Gamma_{\varepsilon_0}q)^2}{1+\Gamma_{\varepsilon_0}q}(1-q)\right], \quad (3.12)$$

here $\Gamma_{\varepsilon_0} = 4\varepsilon_0\gamma/m_ec^2$, and $q = \varepsilon_1/\Gamma_{\varepsilon_0}(1-\varepsilon_1)$. The dimensionless parameter Γ_{ε_0}, determines the domain of the scattering, where Thomson corresponds to $\Gamma_{\varepsilon_0} \ll 1$. In the Thomson limit also, $\varepsilon_1 \ll 1$ and the last term in the brackets in Eq. 3.12 is negligible.

3.4.2 Electron losses during synchrotron radiation

Synchrotron emission was studied intensively in [200]. According to this paper, the energy distribution of synchrotron radiation can be expressed as

$$\frac{dN_\gamma}{dtdE_\gamma} = \frac{\sqrt{3}}{2\pi}\frac{e^3B}{m_ec^2\hbar E_\gamma}F\left(\frac{E_\gamma}{E_c}\right). \quad (3.13)$$

In Eq. 3.13, the parameter $F(x) = x\int_x^\infty K_{5/3}(\tau)d\tau$, while the parameter $E_c = \frac{3e\hbar B\gamma^2}{2m_ec}$. In the case when $B_\perp = B\sin\Theta$, where Θ is the angle between $\mathbf{B}$ and υ, the previous equation can be written as

$$G(x) = \int \sin\theta F\left(\frac{x}{\sin\theta}\right)\frac{d\Omega}{4\pi} = \frac{1}{2}\int_0^\pi F\left(\frac{x}{\sin\theta}\right)\sin^2\theta d\theta \quad (3.14)$$

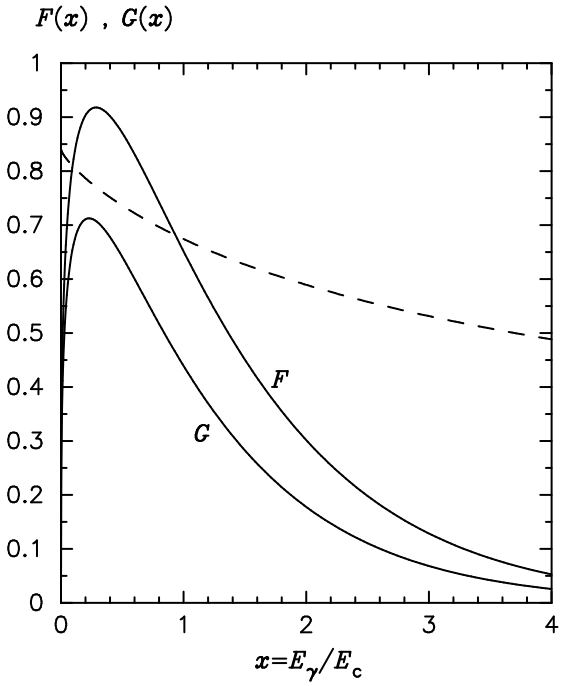

FIGURE 3.7: The function of emissivity for the synchrotron radiation $F(x)$ and $G(x)$. The dashed line corresponds the ratio $G(x)/F(x)$. The graph is taken from [200].

The equation mentioned above can be defined as a single integral. For this, [200] changed the order of integration

$$G(x) = x \int_x^{\infty} K_{5/3}(\xi) \sqrt{1 - \frac{x^2}{\xi^2}} d\xi, \tag{3.15}$$

and using Bessel functions this can be modified as

$$G(x) = \frac{x}{20}[(8 + 3x^2)(k_{1/3})^2 + x k_{2/3}(2k_{1/3} - 3x k_{2/3})], \tag{3.16}$$

here, the coefficient $k_{1/3}$ is equal to $K_{1/3}(x/2)$, while coefficient $k_{2/3}$ is equal $K_{2/3}(x/2)$. The distribution of $F(x)$ and $G(x)$ as well as the function of $G(x)/F(x)$ are presented in Fig. 3.7. This distribution was obtained by [200]. They concluded that their approximation, for $F(x) \approx 2.15x^{1/3}(1 + 3.06x)^{1/6} \times \frac{1+0.884x^{2/3}+0.471x^{4/3}}{1+1.64x^{2/3}+0.974x^{4/3}} e^{-x}$, provides very good accuracy, even better than 0.2% over the entire range of variable parameter x.

The total power lost per electron for synchrotron radiation was calculated in the same way as for inverse-Compton scattering, i.e., using Eq. 3.11, and shown in Fig. 3.8. The cooling timescale of synchrotron radiation as a function of the electron energy and magnetic field is shown in Fig. 3.9.

The resultant cooled spectra of electrons are shown in Fig. 3.10 at 1, 100 and 10000 ks after the particle injection.

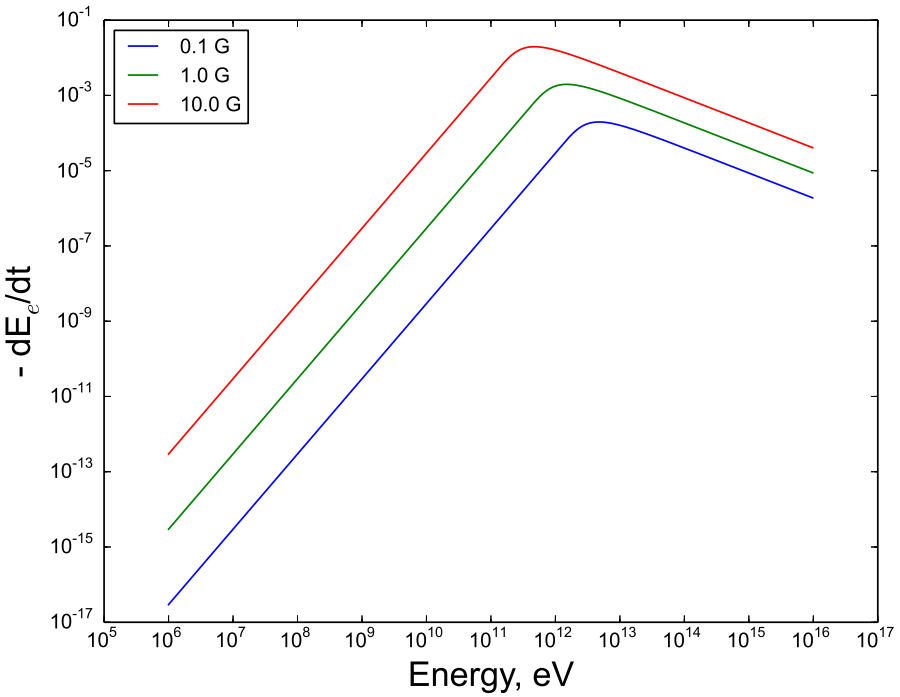

FIGURE 3.8: The numerically integrated function of synchrotron energy losses (see Eq. 3.11) of an electron of energy $E_e = \gamma m_e c^2$ versus magnetic field ($-dE_e/dt$ is calculated in erg/s units). The energy distribution of synchrotron emission was described using equations 3.13. The parameters used here are compatible with PSR B1259−63: $T = 34\,000$ K, $R_* = 6.2{\times}10^{11}$ cm and $d = 10^{13}$ cm at periastron.

3.4.3 Energy losses of electrons during ionization

In addition, I estimated the energy losses of electrons during ionization. I used the method suggested by [202], where the authors determined the energy losses of cosmic-rays in the interstellar medium. According to their approximation, the spectrum of the cosmic-ray component k is proportional to the inverse of the energy loss function, determined as

$$L_k(E) = -\frac{1}{n(H_2)}\left(\frac{dE}{dl}\right), \tag{3.17}$$

where, l is the path length, while $n(H_2)$ is the density where we study the electrons propagation (in my case it is the density of equatorial disc around Be-type star). [202] considered the energy losses with H_2 only (i.e., clouds of molecular hydrogen). The column density of hydrogen $N(H_2)$ is

$$N(H_2) = \int n(H_2)dl, \tag{3.18}$$

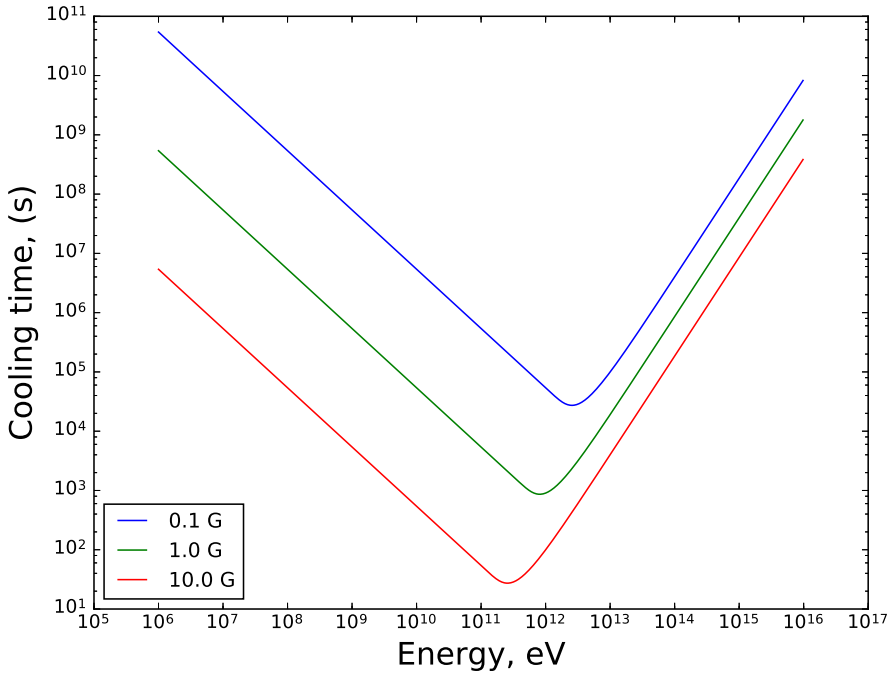

FIGURE 3.9: The cooling timescale of synchrotron radiation as a function of energy and magnetic field. The parameters used here are compatible with PSR B1259−63: $T = 34\,000$ K, $R_* = 6.2{\times}10^{11}$ cm and $d = 10^{13}$ cm at periastron.

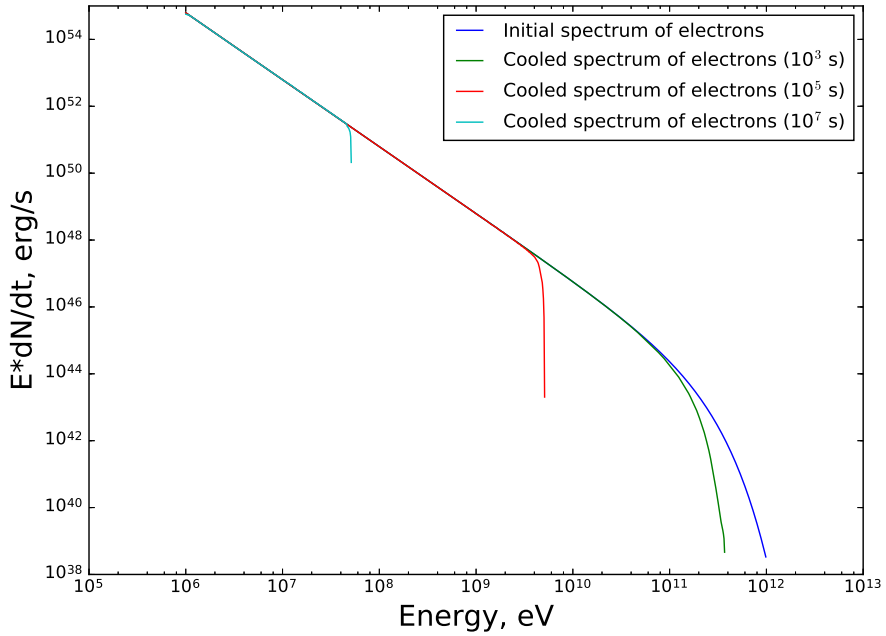

FIGURE 3.10: The cooled, synchrotron spectra for electrons at 1, 100 and 10000 ks after particle injection.

as a result, it is possible to re-write the function of energy losses (Eq. 3.17) in the following form

$$L_k(E) = -\frac{dE}{dN(H_2)}. \tag{3.19}$$

Then, from Eqs. 3.17, 3.18 and 3.19 the energy losses can be defined as

$$N(H_2) = -\int_{E_0}^{E} dE/L_k(E) = n(H_2)[R_k(E_0) - R_k(E)], \tag{3.20}$$

here, $R_k(E)$ is a range, which can be expressed as

$$R_k(E) = \int_{E}^{0} dl = \int_{0}^{E} \frac{dE}{-dE/dl} = \frac{1}{n(H_2)} \int_{0}^{E} \frac{dE}{L_k(E)}. \tag{3.21}$$

Conservation of the number of particles, in our case electrons, can be defined from the equation

$$j_k(E, N)dE = j(E_0, 0)dE_0, \tag{3.22}$$

where dE_0 is a variation of the particle's initial energy, which corresponds to variation dE of its energy at depth $N(H_2)$ and is presented as

$$\frac{dE}{L_k(E)} = \frac{dE_0}{L_k(E, 0)}, \tag{3.23}$$

As a result, the relationship between an initial spectrum $j_k(E_0, 0)$ and cooled spectrum $j_k(E, N)$ at depth $N(H_2)$ can be found from

$$j_k(E, N) = j_k(E_0, 0)\frac{dE}{dE_0} = j_k(E_0, 0)\frac{L_k(E, 0)}{L_k(E)}. \tag{3.24}$$

The Eq. 3.24 and energy loss function for electrons colliding with H_2 (taken from Fig. 3.11) were used.

3.4.4 Results of calculations

The relationship between cooling time and energy of electrons during inverse-Compton scattering, synchrotron radiation and ionization is shown in Fig. 3.12. The energy loss rate of electrons was evaluated in the range of medium column densities, typically suggested in hydrodynamic simulations of the disks around the Be-type stars [203]. In the case of the 1.0 – 10.0 keV lightcurve, as shown in Fig. 3.12, the energy losses of electrons produced by ionization below a density of 10^{10} cm^{-3} can be neglected. On the other hand, for higher densities this energy loss should be considered. For densities

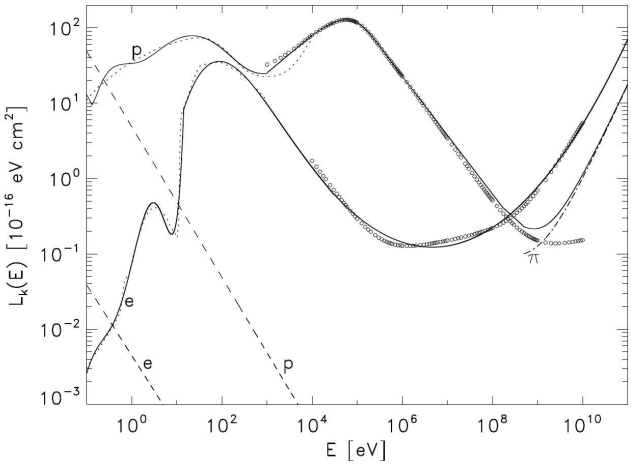

FIGURE 3.11: The image is taken from [202] and describes the energy loss functions $L_e(E)$ and $L_p(E)$ for electrons and protons. The dashed lines correspond to Coulomb losses. The dash-dotted line corresponds to the energy loss by pion production.

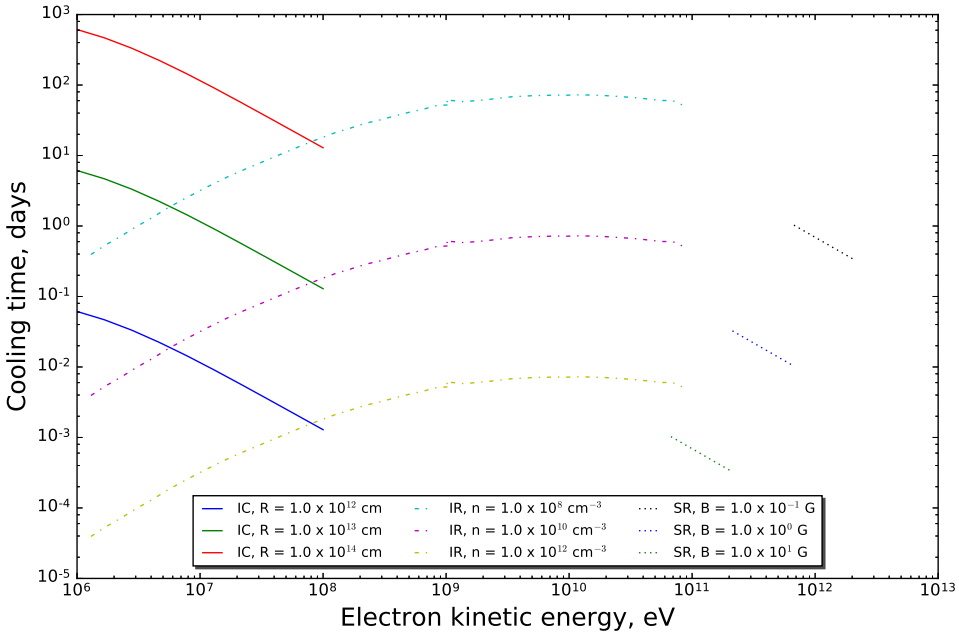

FIGURE 3.12: The relationships between cooling time and energy of electrons for inverse-Compton scattering, synchrotron and ionization energy losses. The calculations were only performed to get the 1.0 - 10.0 keV flux of PSR B1259−63.

higher than 10^{12} cm^{-3} energy losses produced by inverse-Compton scattering can be neglected.

Chapter 4

X-ray and Gamma-ray observations of PSR B1259−63

In this chapter, I report on the X-ray (*XMM*-Newton, *Suzaku*, *Chandra* and *Swift*) and Gamma-ray (*Fermi*/LAT) observations of PSR B1259−63. I use historical data of PSR B1259−63 that were downloaded from the `HEASARC` archive. Here, I use the *XMM*-Newton data that cover observations during four periastron passages, the *Chandra* observations as well *Suzaku* that were achieved for the last two periastron passages, and the *Swift* observations of PSR B1259−63 performed during the last three periastron passages. It is significant to note that some results described below and in the following Chapter 5 were obtained during my participation in the project work: "Gamma-ray emitting binaries", sponsored by International Space Science Institute (Switzerland). An interpretation of the results of this data analysis is given in the following Chapter 5.

4.1 The *XMM*-Newton observations

PSR B1259−63 was observed by *XMM*-Newton 16 times during last four periastron passages. These data were already presented by others in [99, 204]. Here, I reanalyzed them [**205, 206**] using the latest version of SAS software (v.14.0.0). The observational log of the *XMM*-Newton data is presented in Tab. 4.1. The table consists of the reference name, date of observation in MJD (Modified Julian Day), time relative to periastron passage, orbital phase, and exposure time for each observation. The negative/positive value of τ in Tab. 4.1 corresponds the number of days before/after the date of periastron. *XMM*-Newton performed the PSR B1259−63 X1 – X5 observations in 2000 (2000 October 17), the X6 – X10 observations in 2004 (2004 March 7), the X11 – X13 in 2007 (2007 July 27), and the X14 – X16 in 2010-2011 (2010 December 14).

TABLE 4.1: The log of *XMM*-Newton observations of PSR B1259−63 performed during last four periastron passages.

Ref	Date	MJD	τ, days	ϕ, deg	Exp. time, ks
X1	2001-01-12	51921.73	87.2	320.8	11.3
X2	2001-07-11	52101.31	266.7	342.9	11.6
X3	2002-07-11	52467.24	−604.1	0.5	41.0
X4	2003-01-29	52668.27	−403.1	9.31	11.0
X5	2003-07-17	52837.53	−233.9	19.5	11.0
X6	2004-01-24	53028.79	−42.6	57.4	9.7
X7	2004-02-10	53045.43	−25.0	73.4	5.2
X8	2004-02-16	53051.39	−20.0	83.1	7.7
X9	2004-02-18	53052.02	−18.4	86.5	5.2
X10	2004-02-20	53055.82	−15.6	93.2	6.9
X11	2007-07-08	54289.32	−19.2	86.14	9.34
X12	2007-07-16	54297.47	−11.6	112.26	36.54
X13	2007-08-17	54329.48	21.1	278.57	6.35
X14	2011-01-06	55567.71	22.0	86.14	13.49
X15	2011-02-02	55594.82	49.6	112.26	13.58
X16	2011-03-04	55624.21	79.3	278.57	8.10

All 16 *XMM*-Newton observations were performed using the European Photon Imaging Cameras (EPIC) MOS1, MOS2 [207] and pn [208] detectors. The X1-X5 data were observed in the full frame mode, the X6 – X16 data in the small-window mode including a medium filter. The X6 – X16 data were observed using all three cameras, MOS1,2 + pn, in the case of X1 – X5 observations only MOS data available.

In the case of MOS observations, a circular area with a 25 arcsec radius was selected to extract the event lists for spectral analysis, while for the pn data, the circular region with a 45 arcsec radius was chosen. For more details related to the data reduction and analysis see Sec. 2.2. The standard cleaning and filtering of event lists were performed as recommended by the *XMM*-Newton team. According to this recommendation, the lightcurve of each observation was built above 10 keV. Then, all these lightcurves were checked for the presence of extremely high time intervals. All time intervals with count rate higher than 1 counts per second for pn data, and 0.35 counts per second for MOS data were deleted. In X12 – X13 observations, the soft proton flares were detected. Thus, the first 1000 s of X12 data as well as the last 2000 s of X13 data were removed. To perform a background subtraction, the circular regions with the same radii as chosen for the source events and located nearby source regions were built. To increase statistics of spectra, the MOS1,2 + pn were fitted simultaneously.

The PSR B1259−63 spectral analysis was done with the `Xspec` software package. A simple power law with a photoelectric absorption was used to model the obtained spectra. This model describes the data well. No line features were found. The energy range at which the spectral analysis was performed was chosen as 0.5 – 10.0 keV. The best-fit

TABLE 4.2: The best-fit results of the spectral analysis of PSR B1259−63 *XMM*-Newton data.

Ref	F(1-10 keV), 10^{-11} erg cm^{-2} s^{-1}	Γ	N_H, 10^{22} cm^{-2}	χ^2/(d.o.f.)
X1	$0.85^{+0.03}_{-0.03}$	1.51 ± 0.03	0.45 ± 0.02	0.97/(341)
X2	$0.28^{+0.02}_{-0.02}$	1.36 ± 0.07	0.39 ± 0.04	1.02/(122)
X3	$0.10^{+0.05}_{-0.05}$	1.69 ± 0.04	0.29 ± 0.02	0.88/(207)
X4	$0.18^{+0.01}_{-0.01}$	1.82 ± 0.07	0.36 ± 0.03	1.01/(109)
X5	$0.10^{+0.01}_{-0.01}$	1.80 ± 0.08	0.32 ± 0.04	0.80/(62)
X6	$0.25^{+0.02}_{-0.02}$	1.41 ± 0.06	0.35 ± 0.03	0.96/(151)
X7	$0.40^{+0.02}_{-0.02}$	1.20 ± 0.04	0.28 ± 0.03	0.95/(154)
X8	$1.26^{+0.03}_{-0.03}$	1.31 ± 0.02	0.47 ± 0.01	1.12/(614)
X9	$2.43^{+0.04}_{-0.04}$	1.39 ± 0.02	0.43 ± 0.01	1.07/(737)
X10	$1.68^{+0.04}_{-0.04}$	1.47 ± 0.02	0.45 ± 0.01	0.88/(772)
X11	$2.76^{+0.04}_{-0.04}$	1.59 ± 0.01	0.48 ± 0.01	0.94/(1575)
X12	$2.54^{+0.02}_{-0.02}$	1.53 ± 0.01	0.48 ± 0.01	1.10/(2543)
X13	$3.40^{+0.04}_{-0.04}$	1.65 ± 0.01	0.48 ± 0.01	1.03/(1595)
X14	$3.25^{+0.01}_{-0.02}$	1.71 ± 0.01	0.48 ± 0.04	1.09/(2029)
X15	$1.61^{+0.02}_{-0.01}$	1.45 ± 0.01	0.44 ± 0.01	0.97/(1453)
X16	$1.13^{+0.02}_{-0.01}$	1.37 ± 0.02	0.42 ± 0.01	1.00/(851)

parameters of the spectral analysis of the *XMM*-Newton data are shown in Tab. 4.2. The error bars are given at the 1σ confidence level. The systematic uncertainties are not included into presented errors.

A first look at the obtained results shows a strong correlation between the variation of column density values and the period when pulsar enters/leaves the disk of Be-type star. Too small values of column density at X2 - X5 correspond to observations when the pulsar is located outside the disk, and/or, in some cases, close to apastron. The value of N_H during these observations is less by a factor of about 1.5 than in the observations X8 - X16 and X1 as well (see Fig. 4.1). As a result, the hydrogen column density began to grow starting from $\sim$ 25 days before the moment when the pulsar crosses the periastron and continues about 90 days after.

It is also seen that slope of the spectrum in the power law model is lower (i.e. spectra are harder) at the moment of periastron passage. It is significant to note that photon index anti-correlates with X-ray flux. Neither model, i.e. synchrotron or inverse-Compton radiations of shock-accelerated electrons, can describe this feature well.

4.2 The *Chandra* observations

PSR B1259−63 was observed by *Chandra* 14 times during monitoring campaigns in 2007, 2010 and 2014, see Tab. 4.3. The archived data are only available for 9 observations. These data were already presented in a series of recent papers [204, 209, 210].

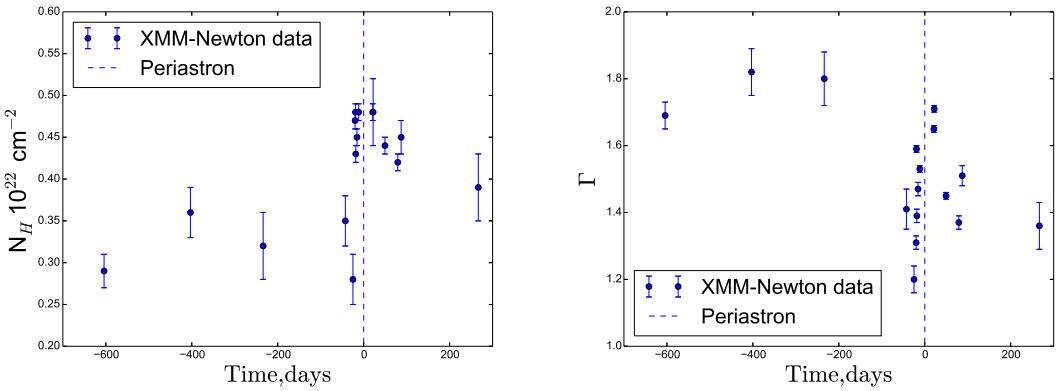

FIGURE 4.1: The behavior of column density, N_H, (left image) and photon index, Γ, (right image) as a function of time, τ.

TABLE 4.3: The log of PSR B1259−63 *Chandra* observations.

Ref	Data	MJD	τ, days	ϕ, deg	Exp. time, ks
Ch1	2007-07-28	54309	1	187.61	4.68
Ch2	2007-08-06	54318	10	248.87	4.67
Ch3	2007-08-24	54337	29	289.56	3.15
Ch4	2007-09-18	54362	54	308.83	7.12
Ch5	2009-05-14	54965	667	182.43	28.28
Ch6	2011-12-17	55912	370	169.82	62.04
Ch7	2013-05-19	56431	886	192.28	62.10
Ch8	2014-02-08	56695	1150	211.22	32.06
Ch9	2014-02-09	56696	1151	221.01	28.54

I reanalyzed these data with the latest version of software, CIAO v.4.6.

The FAINT mode and *HETG* grating were used to perform all *Chandra* observations. The data reduction and analysis were performed as described in Subsec. 2.3.1. The `wavdetect` task was applied to detect and remove all point sources in the field of view of PSR B1259−63. The pile-up cleaning was performed according to the data analysis manual (see http://cxc.harvard.edu/toolkit/pimms.jsp). A circular area with a 3 arcsec radius was selected to extract the event lists for spectral analysis. A region with the same size and nearby source was chosen to contribute background. I used the `specextract` task to extract the spectra of PSR B1259−63 and `RMF` and `ARF` files as well. The event lists were filtered at 0.5 – 10.0 keV energy band.

An absorbed power law model was used to fit spectra of PSR B1259−63 binary system. The best-fitting parameters are shown in Tab. 4.4. The 0.5 – 10.0 keV spectra were analyzed with `Xspec`. The uncertainties of parameters are given at the 1σ confidence level. The Ch1 and Ch2 spectra have very poor statistics, thus the values of hydrogen column density for both cases were fixed at $0.48 \times 10^{22}\mathrm{cm}^{-2}$ that is consistent with the averaged value defined with the *XMM*-Newton observations. The orbital

TABLE 4.4: The results of modeling of the PSR B1259−63 *Chandra* spectra.

Ref	F(1-10 keV), 10^{-11} erg cm^{-2} s^{-1}	Γ	N_H, 10^{22} cm^{-2}	χ^2/(d.o.f.)
Ch1	1.24±0.07	1.65±0.07	0.48±0.01	16/(30)
Ch2	0.93±0.11	1.46±0.09	0.48±0.01	23/(22)
Ch3	3.59±0.07	1.47±0.03	0.48±0.02	187/(196)
Ch4	1.43±0.03	1.48±0.04	0.48±0.02	193/(200)
Ch5	0.14±0.01	1.51±0.10	0.15±0.01	20/(30)
Ch6	0.25±0.04	1.39±0.05	0.29±0.03	76/(87)
Ch7	0.14±0.05	1.68±0.06	0.31±0.03	146/(169)
Ch8	0.15±0.04	1.50±0.04	0.42±0.03	140/(104)
Ch9	0.15±0.04	1.51±0.05	0.43±0.04	102/(100)

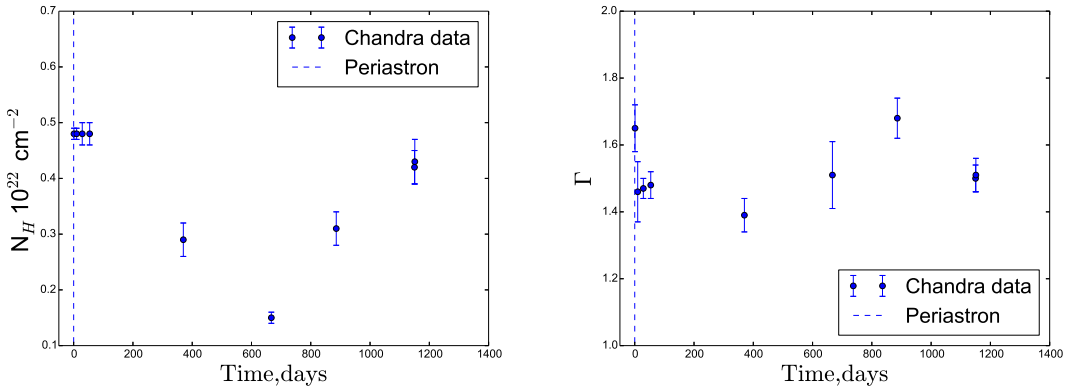

FIGURE 4.2: The behavior of column density, N_H, (left image) and photon index, Γ, (right image) as a function of time, τ.

evolution of the column density and photon index is shown in Fig. 4.2.

4.3 The *Suzaku* observations

The PSR B1259−63 binary system was observed by *Suzaku* 11 times during 2007 and 2010 periastron passages. These data were already presented by [165]. Here, I reanalyzed all available data with latest version of software and calibration libraries [**205**, **206**]. The total exposure time of 11 observations equal about $\simeq$ 300 ks. The list of the *Suzaku* observations is given in Tab. 4.5. The *Suzaku* PSR B1259−63 observations were performed with both X-ray Imaging Spectrometer (XIS) at 0.3 – 12.0 keV [161] and Hard X-ray Detector (HXD) at 13.0 – 600.0 keV [163].

The normal full frame mode of XIS was operated to observe the emission of PSR B1259−63. The frame time of this mode is 8 s. The XIS includes four CCDs including XIS2 that do not operate at this moment. These CCDs are front- and back-illuminated. In my thesis, I use front-illuminated CCDs only since they are characterized

TABLE 4.5: The log of *Suzaku* PSR B1259−63 observations.

Ref	Date	MJD	τ, days	ϕ, deg	Exp. time, ks
Sz1	2007-07-07	54288.6	-19.3	84.6	21.9
Sz2	2007-07-09	54290.7	-17.2	88.1	19.5
Sz3	2007-07-11	54292.6	-15.3	95.8	22.7
Sz4	2007-07-13	54294.7	-13.2	102.2	22.9
Sz5	2007-07-23	54304.3	-3.6	149.6	19.7
Sz6	2007-08-03	54315.3	7.4	230.0	24.0
Sz7	2007-08-18	54330.1	22.2	279.6	20.5
Sz8	2007-09-05	54348.2	40.3	300.4	18.3
Sz9	2011-01-05	55566.8	22	99.6	90.0
Sz10	2011-01-24	55585.6	41	121.0	40.3
Sz11	2011-02-02	55594.2	49	126.5	21.5

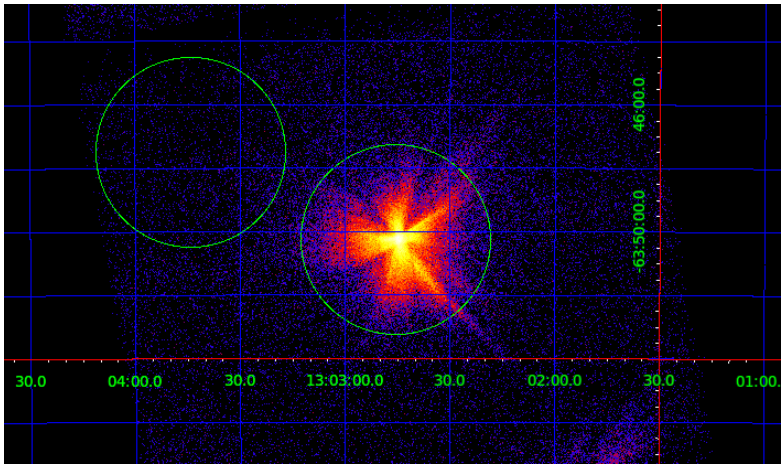

FIGURE 4.3: The *Suzaku* PSR B1259−63 XIS image with a grid of coordinates.

bigger effective areas at energies higher 15 keV. I used the `addascaspec` task to combine the XIS0 and XIS3 spectra. The HXD observations were performed in the normal mode also.

At 10 arcmin away from the PSR B1259−63, the FOV of the XIS instrument contains another X-ray source. This source was separately observed by *Suzaku*. Previously, this source was identified as an accretion-powered pulsar and got name as 2RXP J130159.6−635806 (hereafter 2RXP J1301) [211]. This pulsar is characterized by a high spin period of $\sim$ 700 s. The emission of this object should be assumed during spectral analysis of PSR B1259−63 that was done in the following analysis.

The source event lists were centered on the PSR B1259−63 and extracted from circular areas with 3 arcmin radius. The background event lists were extracted from the circular areas with the same size. The data were filtered at 0.5 – 10.0 keV energy band for XIS, and at 15.0 – 50.0 keV for HXD/PIN. The spectra were binned with 100 counts for the XIS spectra, and 1000 counts for the PIN spectra. The power law model

TABLE 4.6: The results of PSR B1259−63 *Suzaku* XIS spectral fitting.

Ref	N_H, 10^{22} cm^{-2}	Γ	F(1-10 keV), 10^{-11} erg cm^{-2} s^{-1}	χ^2/(d.o.f.)
Sz1	0.50 ± 0.02	1.64 ± 0.02	25.8 ± 0.03	1.06/(354)
Sz2	0.51 ± 0.03	1.58 ± 0.03	26.7 ± 0.03	1.04/(309)
Sz3	0.51 ± 0.03	1.35 ± 0.03	21.6 ± 0.03	1.19/(272)
Sz4	0.52 ± 0.03	1.44 ± 0.03	23.1 ± 0.03	1.30/(298)
Sz5	0.50 ± 0.03	1.83 ± 0.03	19.0 ± 0.02	0.85/(249)
Sz6	0.52 ± 0.03	1.73 ± 0.03	12.9 ± 0.02	0.92/(205)
Sz7	0.50 ± 0.02	1.69 ± 0.02	34.4 ± 0.04	1.01/(402)
Sz8	0.46 ± 0.03	1.57 ± 0.03	22.7 ± 0.03	1.12/(253)
Sz9	0.54 ± 0.01	1.78 ± 0.01	2.84 ± 0.01	1.06/(1568)
Sz10	0.49 ± 0.01	1.54 ± 0.01	1.68 ± 0.02	0.97/(546)
Sz11	0.46 ± 0.02	1.46 ± 0.02	1.47 ± 0.02	1.04/(84)

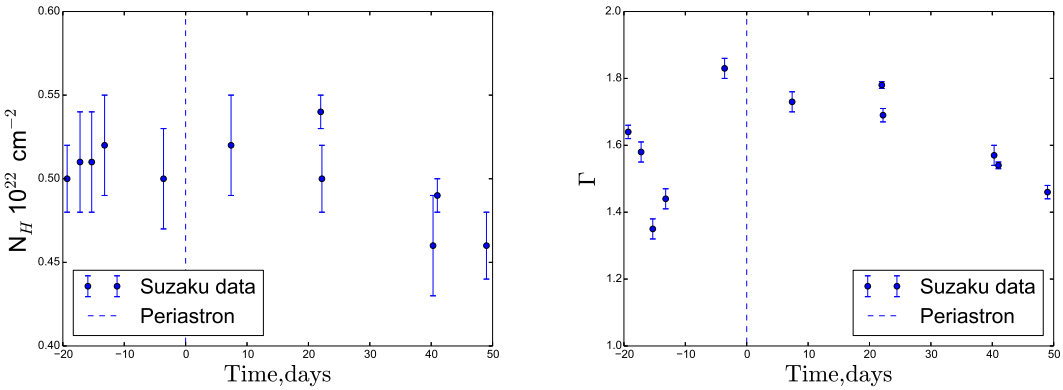

FIGURE 4.4: The distribution of the hydrogen column density, N_H, (left image) and photon index, Γ, (right image) as a function of time, τ.

with an absorption model was used to fit the XIS spectra. The results of the fitting of PSR B1259−63 *Suzaku* spectra are shown in Tab. 4.6. The Sz9 – Sz11 *Suzaku* X-ray spectra are shown in Fig. 4.5.

The hydrogen column density (N_H) values are found in a narrow band (0.46 - 0.54) $\times$ 10^{22} cm^{-2}, while the slopes in a wide band 1.35 – 1.83. No evidence was found for any emission lines. The absorbed power law model shows an acceptable fit to the *Suzaku* spectra except Sz3 and Sz4. The χ^2 values of these modeled spectra are 1.3 for 298 d.o.f. and 1.29 for 272 d.o.f. respectively. [165] has argued this feature, hard power law, might be explained by the spectral steepening. Below I describe this feature in detail using the HXD/PIN data according to [165] arguing.

In Fig. 4.4, the best-fit values of Γ and N_H are shown as a function of time, τ. The roughly constant values of N_H are consistent with the values obtained by *XMM*-Newton and *Chandra* data during the disk passages. On the contrary, the power law index demonstrates changes over the periastron passage. The significant declination of the photon index was observed at the moment when pulsar enters through equatorial

TABLE 4.7: The log of 2RXP J1301 observations performed by *XMM*-Newton and *Suzaku* telescopes.

ObsID(Ref)	Date	τ, days	Exp. time, ks
0653640401(rSz9)	06-01-2011	22	19.91
905007020(rSz10)	25-01-2011	40	10.13
0653640501(rSz11)	02-02-2011	49	26.28

disk firstly. Such declination was observed with *XMM*-Newton data in 2004 at phase -20 days.

4.3.1 Broadband spectra of PSR B1259−63 *Suzaku* observations

The broadband X-ray spectrum of PSR B1259−63 was created by combining the XIS and HXD/PIN spectra. The HXD/PIN spectra were created using the standard steps as described in Subsec. 2.4.1. The HXD/PIN instrument is non-imaging, so we are not able to subtract hard X-ray emission from 2RXP J1301 directly from the image. However, we are able to take into account the 2RXP J1301 emission assuming the known shape of hard X-ray spectrum of 2RXP J1301 from recent observations performed other X-ray telescopes (see details below). Note that CXB (cosmic X-ray background) and NXB (non-X-ray background) backgrounds were subtracted. However, the NXB as well as CXB does not have strong effect on the full emission. Thus, the main contribution to the systematic uncertainties of the HXD/PIN PSR B1259−63 spectrum is the hard X-ray HXD/PIN flux of 2RXP J1301.

The amount of 2RXP J1301 spectrum in hard spectrum of PSR B1259−63 was found using following steps. Firstly, I used three 2RXP J1301 observations performed by *XMM*-Newton and *Suzaku* that were obtained at the same period with Sz9 - Sz11. The list of these three observations of 2RXP J1301 is shown in Tab. 4.7. The source spectra were extracted with circular regions within radius of 3 arcmin. The background spectra were made from the regions with the same radius and without any source inside. Extracting spectra were made in the same way as for PSR B1259−63 and as described in Subsec. 2.4.1.

[165] suggested the model below to fit the spectra of 2RXP J1301. The form of this model has been usually used to describe the spectrum of accretion-powered pulsars [212]

$$F(\epsilon) = \begin{cases} K\epsilon^{-s} & \epsilon \leq \epsilon_{\rm c} \\ K\epsilon^{-s}\exp\left(-(\epsilon-\epsilon_{\rm c})/\epsilon_{\rm f}\right) & \epsilon > \epsilon_{\rm c}, \end{cases} \tag{4.1}$$

here K is the normalization parameter, ϵ_c is the cut-off energy in keV, and ϵ_f is the folding energy in keV. In the `Xspec` environment, the model described above is called a high

TABLE 4.8: The best-fit parameters of an absorbed power law model of 2RXP J1301 *Suzaku* spectra.

Ref	N_H, 10^{22} cm^{-2}	Γ	F(1-10 keV), 10^{-11} erg cm^{-2} s^{-1}	χ^2/(d.o.f.)
rSz1	2.78±0.27	1.20±0.10	3.20±0.11	1.09/(192)
rSz2	2.77±0.25	1.18±0.09	3.24±0.11	0.91/(250)
rSz3	2.69±0.22	1.19±0.08	3.64±0.10	0.95/(315)
rSz4	2.91±0.23	1.20±0.08	3.84±0.11	1.10/(334)
rSz5	2.77±0.23	1.18±0.09	3.27±0.10	1.02/(267)
rSz6	2.88±0.26	1.28±0.09	2.64±0.09	1.03/(267)
rSz7	2.71±0.25	1.17±0.09	3.14±0.10	1.05/(270)
rSz8	3.03±0.30	1.26±0.10	3.07±0.12	1.00/(225)
rSz9	2.27±0.11	0.89±0.05	2.40±0.02	1.29/(84)
rSz10	2.30±0.05	1.10±0.02	2.09±0.02	1.50/(107)
rSz11	2.45±0.12	0.90±0.05	2.63±0.01	1.13/(124)

energy cut-off model, and marked as `highecut`. These three observations were combined and fitted by `constant*wabs*highecut*powerlaw` model in `Xspec` environment. I got the following best-fit parameters: $N_H = 2.30\pm0.08 \times 10^{22}$ cm^{-2}, $\epsilon_c = 4.50\pm0.26$ keV, $\epsilon_f = 17.58\pm1.29$ keV, and $\Gamma = 0.94\pm0.04$. This fit is statistically unacceptable with a reduced $\chi^2 = 1.37$ for 327 d.o.f. However, the obtained parameters are in good agreement with theory of non-cyclotron pulsars, according to this theory, the accretion-powered pulsars characterized by the following measurements, $\epsilon_c = 4$ - 15 keV, and the $\epsilon_f = 10$ - 30 keV [41].

In previous results obtained by [165], they got the following parameters: $\epsilon_c = 4.4\pm0.3$ keV, and the $\epsilon_f = 14.1\pm1.2$ keV for the Sz3 and Sz4 observations only, that are consistent with my results. The flux of 2RXP J1301 was found in 1.0 - 10.0 keV band as 2.31×10^{-11} erg cm^{-2} s^{-1}. In addition, I fitted the 2RXP J1301 spectra of 11 observations by an absorbed power law model. The rSz1 – rSz8, rSz10 data were taken from the field of view *Suzaku* observations of PSR B1259−63, while rSz9 and rSz11 were taken from separate *XMM*-Newton observations of 2RXP J1301. This model gave a statistically acceptable fit for rSz1 – rSz8 data (see Tab. 4.8).

The combined spectra of 2RXP J1301 and PSR B1259−63 obtained by different instruments were fitted by the two component model. The XIS spectra of PSR B1259−63 and 2RXP J1301 were taken at 0.5 – 10.0 keV energy band, while PIN spectra at 15.0 – 50.0 keV. The first component of the used model is a power law, and describes the PSR B1259−63 spectra, while the second model is Eq.(4.1) model was used to fit 2RXP J1301 data. Firstly, such a fitting model was applied for three *Suzaku* observations, Sz9 – Sz11. I applied this approach only to Sz9 – Sz11. In Fig. 4.5 the spectra of PSR B1259−63 and 2RXP J1301 (Sz9 - Sz11, and rSz9 - rSz11), and the HXD/PIN

TABLE 4.9: The result of the best-fitting XIS+PIN spectra of PSR B1259−63 and 2RXP J1301.

Ref	N_H, 10^{22} cm^{-2}	Γ	χ^2/(d.o.f.)
Sz9	0.55±0.006	1.78±0.006	1.11/(1668)
Sz10	0.50±0.01	1.56±0.01	1.13/(663)
Sz11	0.44±0.025	1.45±0.02	1.21/(212)

TABLE 4.10: The result of modeling of the *Suzaku* XIS+PIN spectrum of PSR B1259−63 and 2RXP J1301 at 0.5 – 50.0 keV energy band. The best-fitting parameters of *NuStar* spectrum was used to model the shape of 2RXP J1301.

Ref	N_H, 10^{22} cm^{-2}	Γ	χ^2/(d.o.f.)
Sz1	0.54±0.01	1.68±0.014	1.21/(554)
Sz2	0.54±0.02	1.60±0.015	1.17/(514)
Sz3	0.56±0.02	1.40±0.015	1.42/(518)
Sz4	0.56±0.02	1.48±0.015	1.51/(573)
Sz5	0.53±0.02	1.85±0.02	1.27/(461)
Sz6	0.53±0.02	1.73±0.02	1.22/(407)
Sz7	0.51±0.01	1.71±0.01	1.18/(659)
Sz8	0.45±0.02	1.55±0.017	1.28/(439)
Sz9	0.54±0.01	1.77±0.005	1.13/(1667)
Sz10	0.48±0.01	1.53±0.01	1.01/(662)
Sz11	0.41±0.02	1.42±0.02	1.65/(211)

spectra as the sum of both sources are shown together with the best-fit model. The previously obtained best-fit parameters of the soft X-ray spectra of 2RXP J1301 were frozen during finding of X-ray flux of 2RXP J1301 in PIN spectra. Thus, the two-component model with fixed spectral shape shows an acceptable fit to each observation. The best-fit parameters for PSR B1259−63 using the power law model are shown in Tab. 4.9.

The *NuStar* 2RXP J1301 spectrum performed at 2.0 – 80.0 keV energies was used to check my previous results with *XMM*-Newton data. This spectrum was taken from [213]. The model Eq.(4.1) was used to fit to 2RXP J1301 spectrum by these authors as well. They got the following best-fitting parameters: $N_H = 2.55 \times 10^{22}$ cm^{-2} (was frozen), $\epsilon_c = 6.64\pm0.51$ keV, $\epsilon_f = 15.54\pm1.18$ keV, and $\Gamma = 1.24\pm0.10$ with reduced $\chi^2 = 1.03$ for 780 d.o.f. My results are consistent with their's. Then, I fitted the broadband spectra of PSR B1259−63 and 2RXP J1301 by an absorbed power law model. The best-fit parameters of PSR B1259−63 for Sz1 - Sz11 are shown in Tab. 4.10.

I have found the photon index to be in a wide range 1.42 – 1.85 for Sz1 - Sz11 data. On the contrary, the hydrogen column density varies from epoch to epoch as (0.41 - 0.56) $\times 10^{22}$ cm^{-2}. Acceptable fits were achieved in the case of three epochs, Sz2, Sz7 and Sz10. The subtraction of the 2RXP J1301 emission at hard energies is difficult to account the deficit of X-ray flux of PSR B1259−63.

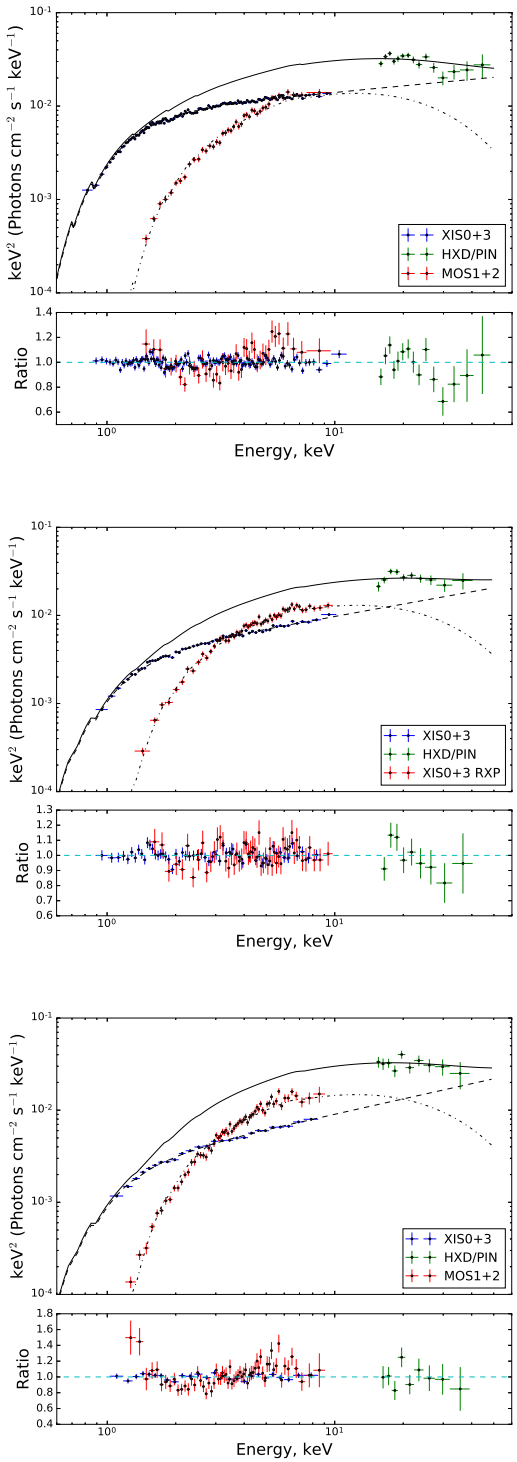

FIGURE 4.5: The *Suzaku* XIS (blue crosses) and HXD/PIN spectra (green crosses) for Sz9 (top), Sz10 (middle) and Sz11 (bottom) observations. The HXD/PIN spectrum is split into the two components through joint fitting: PSR B1259−63 with power law model (blue line), and 2RXP J1301 with cut-off power law model (red line). Green line corresponds the sum of both models. 2RXP J1301 was in the field of view only during Sz10 observation (red crosses). For the reconstruction of PSR B1259−63 PIN spectrum for Sz9 and Sz11 observations the simultaneous *XMM*-Newton spectra (red crosses on the top and bottom pictures) were used.

In addition, [165] fitted the 2RXP J1301 combined Sz3+Sz4 spectrum only. They used an absorbed broken power law model to get better accuracy of fitting. They found the following best-fit parameters: $\Gamma_1 = 1.25^{+0.02}_{-0.04}$ and $\Gamma_2 = 1.66^{+0.05}_{-0.04}$, $\varepsilon_{br} = 4.5^{+0.5}_{-0.2}$ keV. Note, that these authors applied the broken power law model also to rest the combined spectra, Sz1+Sz2, Sz5+Sz6 and Sz7+Sz8 but they did not find any evidence of a spectral break. I checked this model against the Sz9 - Sz11 spectra, and did not find any spectral break either.

4.4 The *Swift* observations

The PSR B1259−63 gamma-ray binary system was observed by *Swift* 45 times during the last four periastron passages. All observations were performed in photon mode with a 500 × 500 pixel window size (see details in Tab. 4.11). These data were already presented in recent papers [99, 204]. The *Swift* observatory [166] gives a great opportunity to monitor the PSR B1259−63 X-ray emission on very different timescales.

All *Swift* PSR B1259−63 observations were performed in Photon Counting (PC) and Windowed Timing (WT) modes. The source event lists were extracted from a circular areas with a radius from 5 – 30 pixels in PC mode and 25 pixels in WT mode (note the size of pixel is 2.6 arcsec). The wide range of radius in PC mode depends on the count rate [214]. The background event lists were extracted from an annulus within 60 – 110 pixels in both modes. The pile-up cleaning was not necessary since all observations have low count rate. The `RMF` files were downloaded from the official *Swift* web-page. I used the following spectral redistribution matrix

```
swxpc0to12s0_20010101v010.rmf
swxpc0to12s6_20010101v010.rmf
swxpc0to12s6_20070901v011.rmf
swxpc0to12s6_20010101v013.rmf
```

for the Sw1 – Sw3 observations, Sw4, Sw5, Sw10 – Sw12 observations, and Sw6 – Sw9, and Sw13 – Sw41, respectively.

The spectra were extracted in the same manner as described in Subsec. 2.5.1. The spectra were grouped with 1 count per bin using the latest version of `FTOOLS` and `grppha`. The spectral analysis was performed at 1.0 – 10.0 keV energy band to resolve issues with the calibration uncertainties at low energies[1].

The poor quality of the *Swift* spectra does not allow us to get both best-fitting

[1] http://www.swift.ac.uk/analysis/xrt/digest_cal.php

TABLE 4.11: The log of *Swift* PSR B1259−63 observations.

Ref	ObsID	Date	MJD	$t - t_p$, days	Exp. time, s	XRT count rate, cts s^{-1}	XRT mode
Sw1	00030966001	2007-07-07	54288.6	-20.003	84.1	2.72	PC
Sw2	00030966002	2007-07-09	54290.6	-18.563	88.3	5.13	PC
Sw3	00030966003	2007-07-11	54292.3	-16.524	92.6	4.56	PC
Sw4	00030966004	2007-07-13	54294.7	-14.783	99.5	4.34	PC
Sw5	00030966005	2010-08-06	55414.3	-131.04	210.6	2.98	PC
Sw6	00030966011	2010-11-20	55520.2	-25.874	255.2	3.87	PC
Sw7	00030966012	2010-11-25	55525.6	-19.095	264.5	4.18	PC
Sw8	00030966013	2010-11-30	55530.5	-14.629	276.5	3.36	PC
Sw9	00030966014	2010-12-14	55544.6	-1.886	355.6	4.30	PC
Sw10	00030966015	2011-01-19	55580.7	35.775	117.0	3.98	PC
Sw11	00030966016	2011-01-20	55581.0	36.099	117.2	4.17	PC
Sw12	00030966017	2011-01-22	55583.7	38.741	119.5	4.13	PC
Sw13	00030966018	2014-04-20	56767.2	-14.561	1171.2	0.36	PC
Sw14	00080099001	2014-04-20	56767.9	-14.249	1740.6	0.44	PC
Sw15	00030966019	2014-04-27	56774.9	-6.779	4015.7	0.29	PC
Sw16	00030966020	2014-05-04	56781.9	0.224	4075.6	0.22	PC
Sw17	00030966021	2014-05-06	56783.9	2.158	1470.9	0.20	PC
Sw18	00030966022	2014-05-07	56784.1	2.352	2404.9	0.19	PC
Sw19	00030966023	2014-05-09	56786.1	4.419	1475.9	0.16	PC
Sw20	00030966024	2014-05-17	56794.6	12.863	179.8	0.44	PC
Sw21	00030966025	2014-05-19	56796.8	15.109	1987.8	0.61	PC
Sw22	00030966026	2014-05-22	56799.4	17.699	2877.3	1.00	WT
Sw23	00030966027	2014-05-25	56802.5	20.761	2925.1	0.74	WT
Sw24	00030966028	2014-05-28	56805.7	23.958	2991.7	0.65	WT
Sw25	00030966029	2014-06-02	56810.9	29.189	1504.4	0.51	WT
Sw26	00030966030	2014-06-03	56811.1	29.327	970.0	0.12	WT
Sw27	00030966032	2014-06-07	56815.1	33.360	2696.4	0.44	WT
Sw28	00030966033	2014-06-11	56819.3	37.558	3983.2	0.54	WT
Sw29	00030966035	2014-06-12	56820.5	38.726	999.6	0.54	WT
Sw30	00030966036	2014-06-13	56821.8	40.114	2036.3	0.51	WT
Sw31	00030966037	2014-06-14	56822.8	41.114	1834.4	0.49	WT
Sw32	00030966038	2014-06-15	56823.3	41.551	767.3	0.44	WT
Sw33	00030966039	2014-06-16	56824.6	42.848	2026.2	0.48	WT
Sw34	00030966041	2014-06-18	56826.2	44.524	981.5	0.50	WT
Sw35	00030966043	2014-06-25	56833.3	51.605	3284.0	0.28	PC
Sw36	00030966044	2014-06-26	56834.5	52.776	1513.4	0.27	PC
Sw37	00030966047	2014-06-27	56835.4	53.678	2559.7	0.25	PC
Sw38	00030966048	2014-07-02	56840.4	58.711	2964.3	0.26	PC
Sw39	00030966049	2014-07-06	56844.7	63.023	3264.0	0.20	PC
Sw40	00030966050	2014-07-07	56845.2	63.519	3785.9	0.17	PC
Sw41	00030966051	2014-07-08	56846.6	64.853	3965.7	0.18	PC

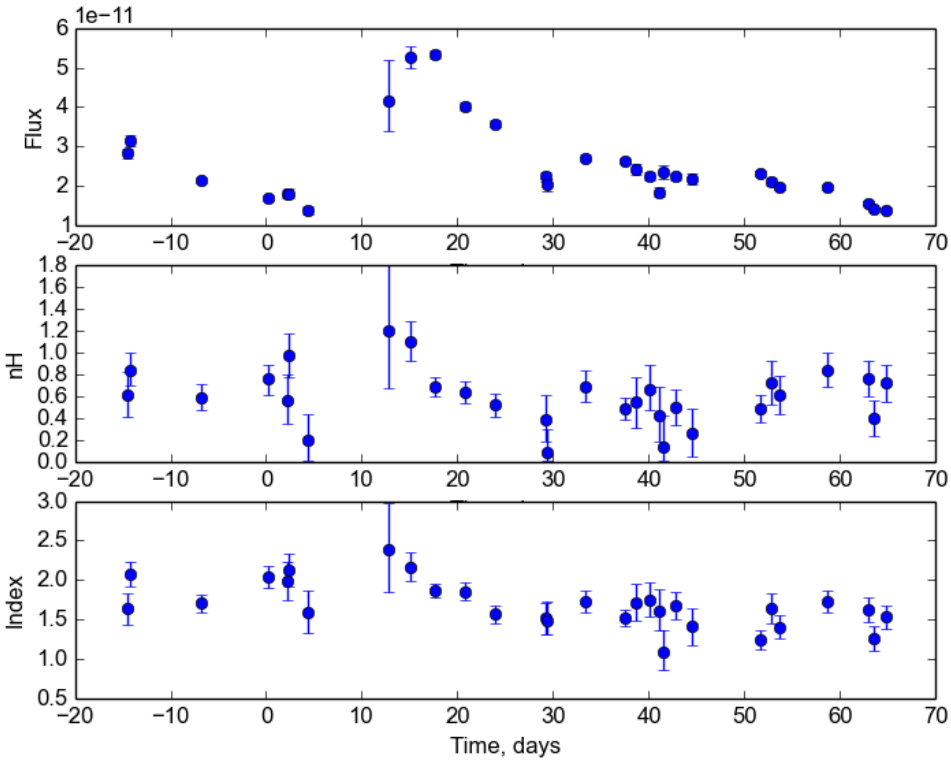

FIGURE 4.6: The distribution of unabsorbed flux measured at 2.0 – 10.0 keV (top panel), column density (middle panel) and photon index (bottom panel) in the *Swift* data. The unabsorbed flux of the PSR B1259−63 is given in units of 10^{-11} cm^{-2} s^{-1}, while the column density, N_H, is given in units of 10^{22} cm^{-2}.

parameters. Thus, I performed the Monte Carlo method and used `Xspec` to get statistically significant results. The full description of the MC method was given in Sec. 2.7. The `Xspec` requires C-statistics in the case of poor spectra. The corrected spectral parameters including X-ray flux at 1.0 – 10.0 keV (absorbed and unabsorbed) and their corrected errors for 1σ confidence level are summarized in Tab. 4.12 and Appendix A. Appendix A includes the averaged histograms as well as cumulative distribution of errors for each *Swift* observation. The distribution of an unabsorbed flux as well as the column density and photon index for the Sw13 – Sw41 observations (2014 periastron passage only) is shown in Fig. 4.6.

It is clearly seen that the power law index starts to be soft, 1.8, corresponding to a few months before the periastron. Then, the photon index starts to be harder a month before periastron, 1.5, and X-ray flux increases. When flux is going to its maximum, the spectrum starts to be harder than 1.5. The spectrum began softer, lower than 1.7, when pulsar leaves periastron and enters the equatorial disk for the second time.

TABLE 4.12: The best-fit parameters of *Swift* PSR B1259−63 spectra.

Ref	$t-t_p$, days	F_{un}(1-10 keV), 10^{-11} erg cm^{-2} s^{-1}	N_H, 10^{22} cm^{-2}	Γ	F_{abs}(1-10 keV), 10^{-11} erg cm^{-2} s^{-1}	C-stat
Sw1	-20.003	$2.58^{+0.31}_{-0.32}$	0.53 ± 0.06	1.65 ± 0.10	$1.15^{+0.19}_{-0.28}$	332.5
Sw2	-18.563	$2.49^{+0.21}_{-0.22}$	0.52 ± 0.05	1.56 ± 0.07	$1.31^{+0.29}_{-0.11}$	163.8
Sw3	-16.524	$2.39^{+0.31}_{-0.32}$	0.49 ± 0.05	1.35 ± 0.08	$1.22^{+0.21}_{-0.14}$	411.0
Sw4	-14.783	$2.41^{+0.21}_{-0.32}$	0.56 ± 0.07	1.57 ± 0.08	$1.31^{+0.16}_{-0.38}$	421.0
Sw5	-131.04	$0.17^{+0.01}_{-0.02}$	0.45 ± 0.03	1.8 ± 0.09	$1.13^{+0.09}_{-0.08}$	128.3
Sw6	-25.874	$0.69^{+0.08}_{-0.16}$	0.51 ± 0.03	0.99 ± 0.23	$1.25^{+0.08}_{-0.11}$	312.6
Sw7	-19.095	$1.53^{+0.12}_{-0.11}$	0.53 ± 0.05	1.33 ± 0.08	$1.30^{+0.39}_{-0.38}$	215.48
Sw8	-14.629	$2.60^{+0.12}_{-0.16}$	0.51 ± 0.07	1.37 ± 0.06	$1.10^{+0.29}_{-0.16}$	612.73
Sw9	-1.886	$1.72^{+0.11}_{-0.08}$	0.58 ± 0.09	1.56 ± 0.05	$1.09^{+0.33}_{-0.10}$	247.9
Sw10	35.775	$2.31^{+0.08}_{-0.11}$	0.54 ± 0.08	1.51 ± 0.06	$1.14^{+0.19}_{-0.09}$	236.1
Sw11	36.099	$2.19^{+0.09}_{-0.10}$	0.65 ± 0.10	1.48 ± 0.06	$1.18^{+0.65}_{-0.18}$	424.7
Sw12	38.741	$2.02^{+0.12}_{-0.05}$	0.75 ± 0.16	1.44 ± 0.06	$1.20^{+0.21}_{-0.21}$	323.2
Sw13	-14.561	$2.83^{+0.12}_{-0.13}$	0.61±0.20	1.64±0.20	$2.42^{+0.13}_{-0.28}$	189.95
Sw14	-14.249	$3.14^{+0.14}_{-0.13}$	0.97±0.20	2.52±0.20	$2.38^{+0.09}_{-0.18}$	260.99
Sw15	-6.779	$2.14^{+0.06}_{-0.06}$	0.59±0.11	1.71±0.12	$1.84^{+0.06}_{-0.11}$	376.91
Sw16	0.224	$1.70^{+0.07}_{-0.06}$	0.75±0.13	2.04±0.14	$1.32^{+0.05}_{-0.09}$	295.15
Sw17	2.158	$1.79^{+0.12}_{-0.12}$	0.57±0.23	2.00±0.24	$1.46^{+0.09}_{-0.22}$	147.61
Sw18	2.352	$1.80^{+0.12}_{-0.11}$	0.97±0.20	2.12±0.21	$1.30^{+0.08}_{-0.15}$	213.93
Sw19	4.419	$1.37^{+0.10}_{-0.10}$	0.20±0.24	1.60±0.26	$1.28^{+0.05}_{-0.26}$	120.14
Sw20	12.863	$4.14^{+1.04}_{-0.73}$	0.61±0.76	1.50±0.70	$2.38^{+0.13}_{-1.21}$	47.14
Sw21	15.109	$5.26^{+0.27}_{-0.29}$	1.10±0.18	2.16±0.18	$3.67^{+0.20}_{-0.41}$	237.50
Sw22	17.699	$5.33^{+0.12}_{-0.12}$	0.69±0.10	1.86±0.10	$4.38^{+0.12}_{-0.21}$	457.72
Sw23	20.761	$4.01^{+0.10}_{-0.11}$	0.63±0.10	1.86±0.10	$3.33^{+0.10}_{-0.19}$	403.67
Sw24	23.958	$3.57^{+0.09}_{-0.09}$	0.51±0.12	1.56±0.12	$3.15^{+0.13}_{-0.20}$	413.16
Sw25	29.189	$2.23^{+0.12}_{-0.11}$	0.39±0.20	1.52±0.20	$2.03^{+0.09}_{-0.24}$	214.99
Sw26	29.327	$2.02^{+0.14}_{-0.15}$	0.80±0.21	1.49±0.23	$1.96^{+0.07}_{-0.37}$	220.49
Sw27	33.360	$2.71^{+0.09}_{-0.09}$	0.69±0.14	1.72±0.14	$2.27^{+0.10}_{-0.20}$	338.63
Sw28	37.558	$2.64^{+0.07}_{-0.06}$	0.49±0.10	1.52±0.10	$2.36^{+0.06}_{-0.13}$	355.16
Sw29	38.726	$2.42^{+0.15}_{-0.14}$	0.55±0.24	1.72±0.24	$2.08^{+0.15}_{-0.38}$	191.01
Sw30	40.114	$2.25^{+0.11}_{-0.11}$	0.68±0.21	1.75±0.21	$1.87^{+0.14}_{-0.27}$	237.73
Sw31	41.114	$1.84^{+0.12}_{-0.11}$	0.43±0.24	1.62±0.26	$1.64^{+0.10}_{-0.27}$	201.54
Sw32	41.551	$2.35^{+0.17}_{-0.18}$	0.15±0.28	1.10±0.25	$2.28^{+0.22}_{-0.49}$	127.01
Sw33	42.848	$2.24^{+0.09}_{-0.10}$	0.49±0.18	1.67±0.17	$1.95^{+0.13}_{-0.15}$	281.04
Sw34	44.524	$2.18^{+0.14}_{-0.15}$	0.25±0.22	1.41±0.23	$2.04^{+0.09}_{-0.36}$	180.19
Sw35	51.605	$2.32^{+0.06}_{-0.07}$	0.49±0.12	1.23±0.12	$2.12^{+0.07}_{-0.14}$	371.76
Sw36	52.776	$2.10^{+0.10}_{-0.10}$	0.73±0.20	1.64±0.20	$1.76^{+0.08}_{-0.24}$	210.88
Sw37	53.678	$1.96^{+0.07}_{-0.07}$	0.61±0.16	1.41±0.15	$1.72^{+0.09}_{-0.16}$	267.29
Sw38	58.711	$1.96^{+0.07}_{-0.06}$	0.83±0.16	1.72±0.15	$1.59^{+0.06}_{-0.14}$	327.19
Sw39	63.023	$1.56^{+0.06}_{-0.05}$	0.75±0.18	1.61±0.15	$1.30^{+0.04}_{-0.13}$	262.48
Sw40	63.519	$1.41^{+0.05}_{-0.05}$	0.39±0.16	1.26±0.15	$1.30^{+0.05}_{-0.12}$	256.06
Sw41	64.853	$1.39^{+0.05}_{-0.04}$	0.71±0.18	1.52±0.15	$1.19^{+0.07}_{-0.09}$	271.68

4.5 The *Fermi*/LAT observations

In my thesis, I used the gamma-ray observations of *Fermi*/LAT for two tasks, namely to obtain the long-term GeV spectrum and light curve of PSR B1259−63, and also to get the spectrum of PSR B1259−63 during the period of the GeV-flare which was discovered by *Fermi*/LAT during 2010-11 periastron monitoring campaign.

For the first task, I analyzed data that covers the 2008 August 4 and 2015 March 19. This period covers the time during which the pulsar locates near apastron until the passage when the pulsar enters through the dense equatorial disk of the Be-type star. For the second task, I analyzed data that covers a period of one month from 30 December 2010, exactly when the GeV-flare was found.

To analyze the data, a catalog was used to describe all spectra of each point source detected on the sky. The data analysis was performed according to [215]. The slope of the PSR B1259−63 spectrum was fixed at 2.86. The Galactic diffuse background, normalizations of PSR B1259−63 as well as the variable sources found in 2FGL catalog were free during modeling. From the *Fermi*/LAT data, the spectra and light curves of PSR B1259−63 were extracted.

The spectrum of the GeV-flare is shown in Fig. 4.7. This flare occurred after the periastron passage and also after the post-periastron transit of the equatorial disk of the Be-type star by the pulsar. The GeV spectrum of PSR B1259−63 as well the flare part of spectrum were used for interpretation of full PSR B1259−63 spectrum (see Fig. 5.7) and described in following Chapter 5. The orbital *Fermi* lightcurve is shown in Fig. 5.1.

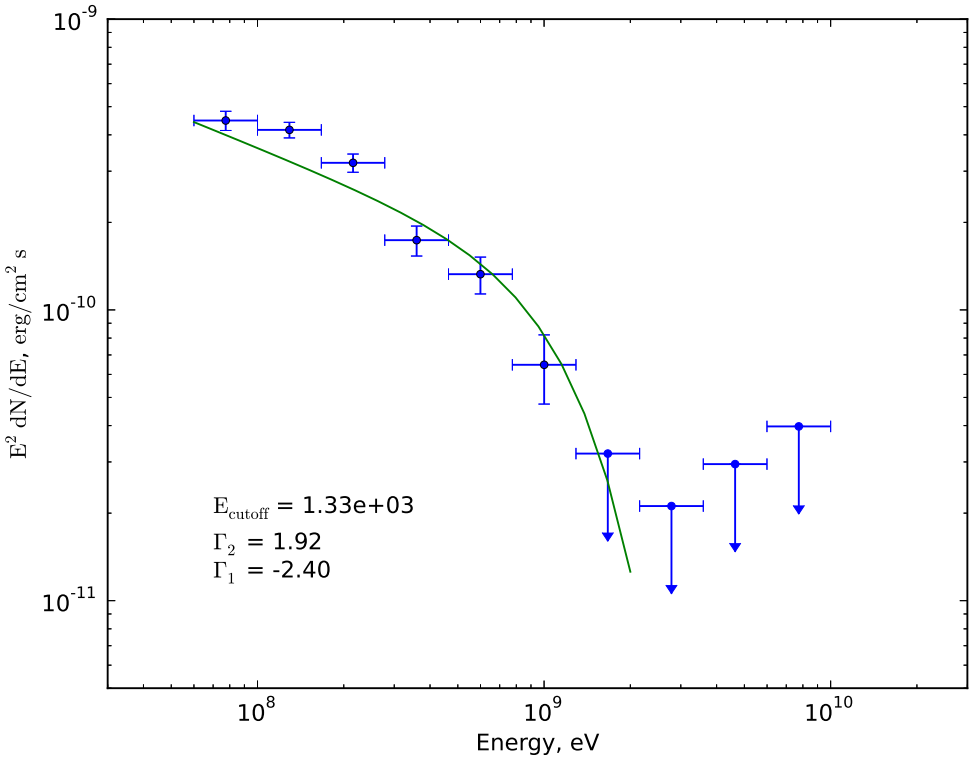

FIGURE 4.7: The spectrum of PSR B1259−63 during GeV flare observed by *Fermi*/LAT Gamma-Ray Observatory with exponential cut-off model (the $E_{cut-off}$ on figure is given in GeV unit).

Chapter 5

Interpretation of results of PSR B1259−63

In this chapter, I present the results of data analysis of PSR B1259−63 using analyzed data made in previous Chapter 4. Here, I give the grouped results of multi-wavelength observations, the physical interpretation of the orbital lightcurves and the main results obtained from multiwavelength monitoring of PSR B1259−63. Using *Swift* data from the 2014 periastron passage I try to investigate the nature of emission in PSR B1259−63, namely I try to model the double-peaked lightcurve in X-ray using inverse-Compton scattering and synchrotron radiation. To define the emission mechanism in PSR B1259−63, I search the short variability of lightcurves. In addition, I present a possible explanation of the nature of the GeV-flare.

5.1 The orbital lightcurves

The orbital lightcurve of PSR B1259−63 is shown in Fig. 5.1. The figure includes all available multiwavelength observations. The X-ray flux in the middle panel was obtained at 1.0 – 10.0 keV energy band. The *Swift* results in 2014 are measurements obtained in this thesis and published in [**206**], the newest *NuStar* data were analyzed in 2014 and published in [**205**] as well. All *XMM*-Newton, *Suzaku* and *Chandra* data points were taken from [99, 204] and [**205, 206**]. The radio, optical, and high-energy lightcurves of PSR B1259−63 are shown in Fig. 5.1 for comparison. The TeV lightcurves of the *H.E.S.S.* observations were obtained for three periastron passages for the energies 1 TeV and higher. The TeV data were taken from [216–218], and the TeV flux is given in 10^{-12} cm^{-2} s^{-1}. The *ATCA* radio observations of PSR B1259−63 were taken from [219–221]. The optical data for last two periastron passages are taken from [222]. The

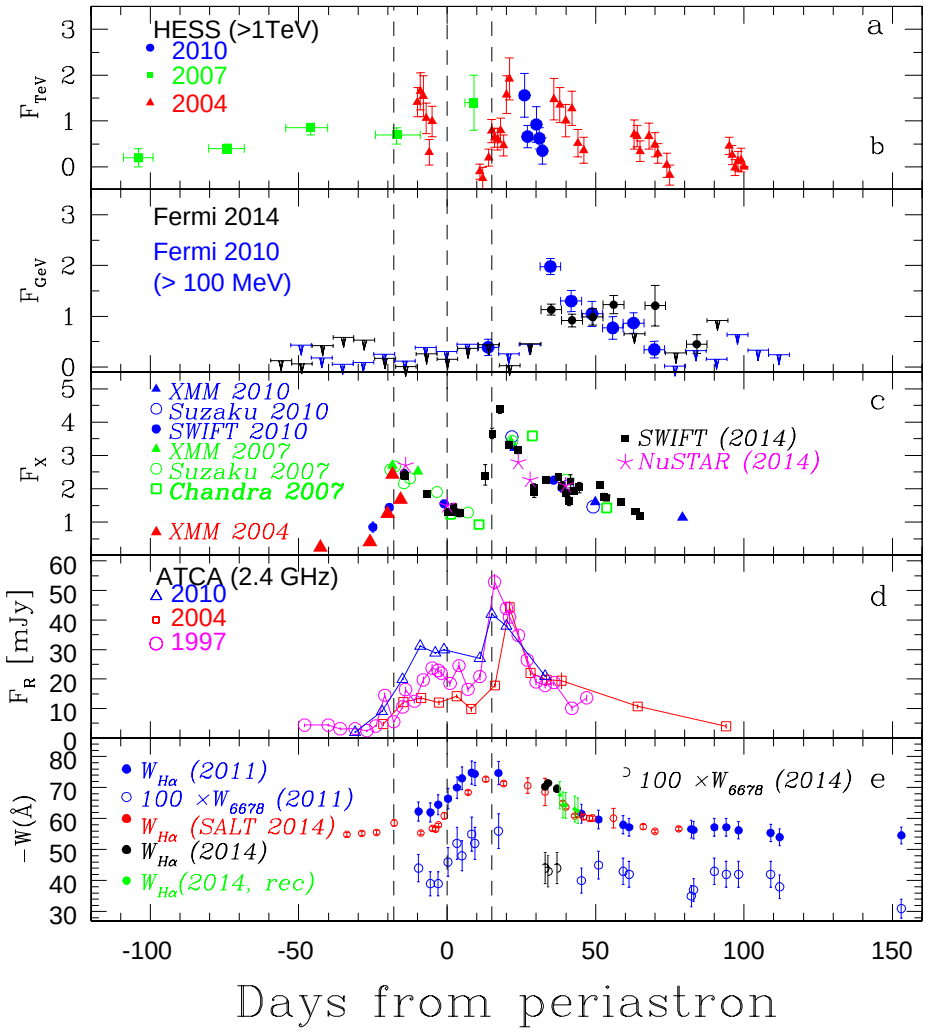

FIGURE 5.1: The multiwavelength orbital lightcurves of PSR B1259−63 around periastron for several passages. The image is taken from [**206**]. See text for full explanation.

dashed line in the middle corresponds to the moment of the periastron, while the other two lines show the moments of starting/ending of the pulsed emission.

Panel (b) demonstrates the *Fermi*/LAT flux measurements in the $E > 100$ MeV energy range for the 2010 and 2014 periastron passages. The GeV flux is given in 10^{-6} cm^{-2} s^{-1} units. The data points of *Fermi*/LAT lightcurve were created with a significance higher than 2σ. The time binning was selected to be 7 days for the period of the GeV-flare and 14 days otherwise. The upper limits on the figure correspond to the 95 % confidence limit. The results of these GeV observations performed by *Fermi* are published in [**206**], [215].

Panel (c) in Fig. 5.1 demonstrates the X-ray lightcurve of the system obtained from the analysis of X-ray data in previous results and which were reanalyzed in this thesis as described in Chapter 4. The data points correspond to the X-ray fluxes from

2004, 2007, 2010 and 2014 periastron passages. The flux is given in 10^{-11} erg cm^{-2} s^{-1}. It is significant to note that the typical errors of the X-ray data points are smaller than the size of the symbols. It is seen that all X-ray data obtained for different periastron passages demonstrate a good intercalibration.

The PSR B1259−63 binary system was observed in radio wavelength (2.4 GHz) by the *ATCA* observatory in 1997, 2004 and 2010 periastron passages. The radio flux densities are measured in mJy and shown on panel (d) in Fig. 5.1. The optical lines of Hα (filled circles) and He I λ6678 (open circles) of PSR B1259−63 were observed also. The evolution of the equivalent width of these lines is shown on the panel (e) in Fig. 5.1.

Since X-ray observations performed at different periastron passages show nearly the same results in measurements of the X-ray flux, it can be concluded that the X-ray lightcurve of PSR B1259−63 is stable. Using this stability, we are able to use all data simultaneously to model the properties of X-ray flux over orbital motion. The analysis of the X-ray lightcurve show the sharp rise of X-ray flux by a factor 4 during 9 days when the pulsar crosses the Be-type star disk firstly. After these 9 days, the flux is going down during the period when the pulsar goes close to periastron. Then, the X-ray flux increases by a factor 5 during 3 days, or in 1.5 times higher than the X-ray flux when pulsar crosses disk firstly. At this moment, the pulsar crosses the equatorial disk of Be-type star in second time. Then, the X-ray flux decreases smoothly.

5.2 Fast variability in the lightcurve

It is known that PSR B1259−63 is a variable source. Additionally to orbital variability, there is a daily variability during periastron passage. [95] explained the fast variability due to the presence of the dense clumps inside the stellar wind. Such an idea was used in my thesis also. The daily timescale variability of PSR B1259−63 was also suggested by [223]. Recently, [99] studied the short variability of PSR B1259−63 using the X-ray lightcurves. An hour-scale variability was found but only during the period when the pulsar enters through the disk. According to recent researches, the lightcurves of PSR B1259−63 can be fitted by a constant function. The flux variations of this fit might indicate the variability of the source. These variations indicate the characteristics of the disk also. The scale of variability is proportional to the size of emitting regions. These regions should be smaller in the disk. However, big density bubbles can also be inside the equatorial disk of Be-type star.

Unfortunately, the *Suzaku*, *XMM*-Newton and *Chandra* data are not suitable to study the variability of PSR B1259−63 on daily timescales due to the too short exposure time. On the contrary, the *Swift* data performed in 2014 cover 3 months observations. These data were used to investigate the short timescale variability. In 2014, the *Swift*

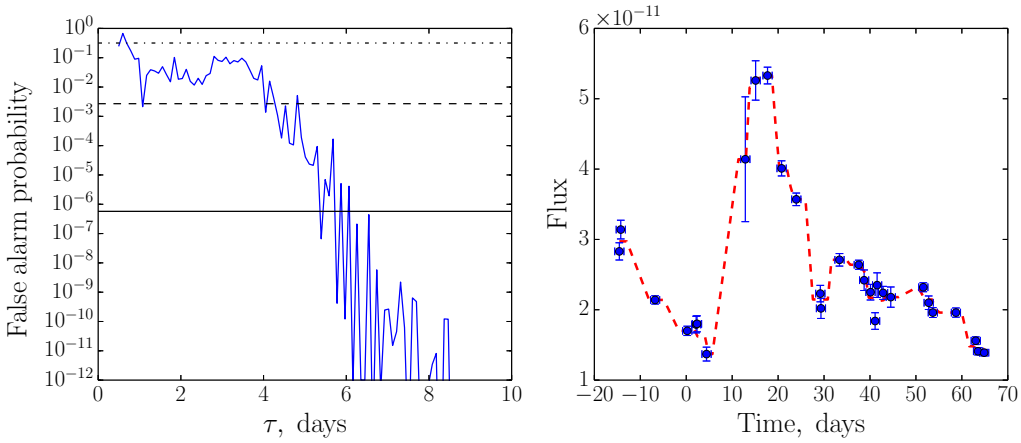

FIGURE 5.2: (left:) The probability of the variability in the PSR B1259−63 lightcurve. The horizontal lines correspond the 1, 3 and 5σ confidence levels from the top. (right:) The 1.0 – 10.0 keV lightcurve of PSR B1259−63 and its averaged lightcurve (the units of flux is erg/cm^2/s).

observations have 10 – 30 ks of averaged exposure time and made approximately each day.

In oder to study the variability of PSR B1259−63 on short timescale, the method previously suggested and used by [224–226] was applied. To find the variability of PSR B1259−63 on the timescale τ, I first created an averaged light curve, using τ as the averaging scale. This averaged light curve contains $n_{av} = (T_{max} - T_{min})/\tau$ time bins. Then I computed the difference of the original and the averaged light curves, which then can be quantified in terms of the χ^2 with $n_{orig} - n_{av}$ degrees of freedom. These χ^2 values I converted to a probability. A zero value of χ^2 means that the averaged lightcurve is close to the original one. In contrast, the huge χ^2 will indicate the significant variability. This procedure was repeated for τ within 0.5 – 10.0 days band. The resulting scan is presented in Fig. 5.2.

It is seen that the variability of the PSR B1259−63 starts to be significant above $\tau \approx 4$ days. This time was chosen as a moment when false alarm probability curve passes the 3σ confidence limit. False alarm probability represents the odds for the null-hypothesis to be the real reflection of the data. The null-hypothesis in this case is the absence of variability, so the false alarm value of p shows the chances of getting a given value of χ^2 if the source flux is actually constant. It is also seen the crossing of 3σ line near 1 day (τ). Since the probability at this point increased back so quickly, it is difficult to conclude that the lightcurve of PSR B1259−63 has variability on the timescale of one day, I conclude that it might be just fluctuation. Moreover, evidence of the variability of the source on a timescale of several days was also reported in some *ROSAT* [227] and *Suzaku* [165] observations.

5.3 The modeling of the X-ray double-peaked lightcurve

As a result of the interaction between the wind of Be-type star and the pulsar wind, strong shock waves will be formed. The electrons of the pulsar wind will be accelerated at the front of strong shocks. Additionally, the magnetic field of the pulsar wind will be compressed by the shock. In such an environment, the accelerated electrons radiate the inverse-Compton and synchrotron emissions due to the motion of these relativistic electrons in the photon field of the Be-type star and in the magnetic field of the pulsar. Such motion produces multi-wavelength radiation. In my model, the broadband emission of the PSR B1259−63 binary system is produced by the electrons.

In my model, I tried to model the inverse-Compton emission of relativistic electrons in the PSR B1259−63. For this, I used two components of the PSR B1259−63 system, namely the pulsar and the Be-type star. It is known that the pulsar emits high-energy electrons, while the star emits mainly eV photons. In Fig. 5.3 the energy density of photons emitted from the Be-type star as a function of distance to the star is shown. Here, I have used the parameters of a star similar to the companion of the PSR B1259−63. The emission of the star is described by black-body emission. The flux decreases with distance from the star as $1/R^2$. Since the radiation of the Be-type star largely dominates over the emission of its equatorial disk, I did not take disk radiation into account.

Additionally, the behavior of the energy density of the Be-type star in PSR B1259−63 as a function of temperature and radius of the star is shown in Fig. 5.4.

To describe the initial spectrum of electrons, a power law model with an exponential cut-off was used

$$\frac{dN_e}{dE_e} = E_e^{-\Gamma} \exp\left(-\frac{E_e}{E_{cut-off}}\right), \tag{5.1}$$

where $\Gamma = 2$, $E_{cut} = 10^{11}$ eV, and E_e was taken in the 10^6-10^9 eV energy band.

To calculate the scattered inverse-Compton and synchrotron emissions, I used Eq. 3.12 and 3.13. To make the model closer resemble the data, I assumed that the accelaration of the relativistic particles, emitted by the pulsar, happens more efficiently during the moments of its passage through the Be-type star disk. So, I modeled two injections of electrons during periods when the pulsar crosses the virtual disk of the Be-type star, namely 18 days before and after periastron. These electrons lose energy with a rate given by Eq. 3.11. As a result, each time when the pulsar enters into the disk, one can see an X-ray flare. To test the model, I used *Swift* data obtained during 2014 periastron passage. Fig. 5.5 presents the modeled lightcurve of the X-ray flux (1.0 - 10.0 keV energy band) together with the *Swift* 2014 observations as a function of days relative to the periastron passage.

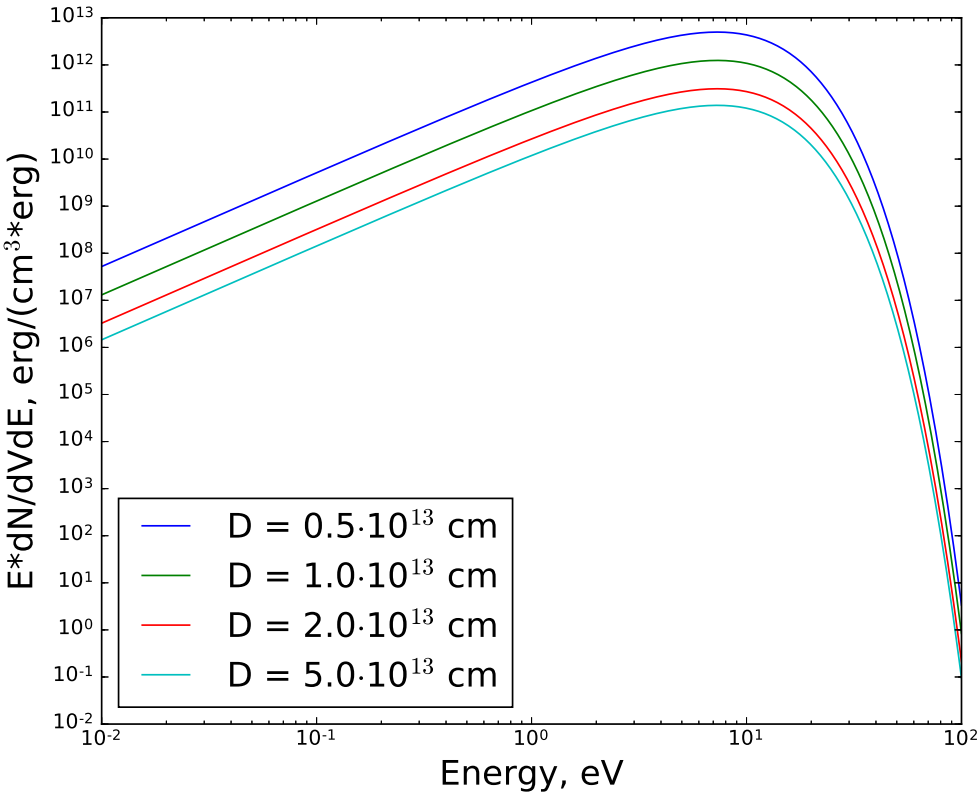

FIGURE 5.3: The distribution of flux density from SS 2883 as a function of distance to star, the $T = 34000$ K and $R_* = 6.2{\times}10^{11}$ cm.

The high-energy emission from the system is produced by the energetic electrons, accelerated by the pulsar. In the presence of the intense background photon field from the neighboring main-sequence stellar companion these electrons will efficiently lose their energy via the inverse-Compton scattering of these low-energy photons. Naturally, one can expect that the process of acceleration is enhanced during the passages of the pulsar through the companion's equatorial disk, accompanied in the jump-like growth in the amount of the electrons available for acceleration.

In this vein, my model attempts to reproduce the overall emission from the system via the sum of three components - persistent emission from the pulsar (Main component in Fig. 5.5) and two temporary components, associated with the injection of the additional electron populations during the disk crossings, ± 18 days before and after periastron (Flare components 1 and 2 in Fig. 5.5). The persistent component evolves with time as the pulsar gets closer/further away from the star and is subject to denser/rarefied background photon field. The two injected electron populations are short-lived, quickly cooling down due to the proximity of the pulsar and companion star.

In the model above, I have assumed that the Lorentz factor of the relativistic

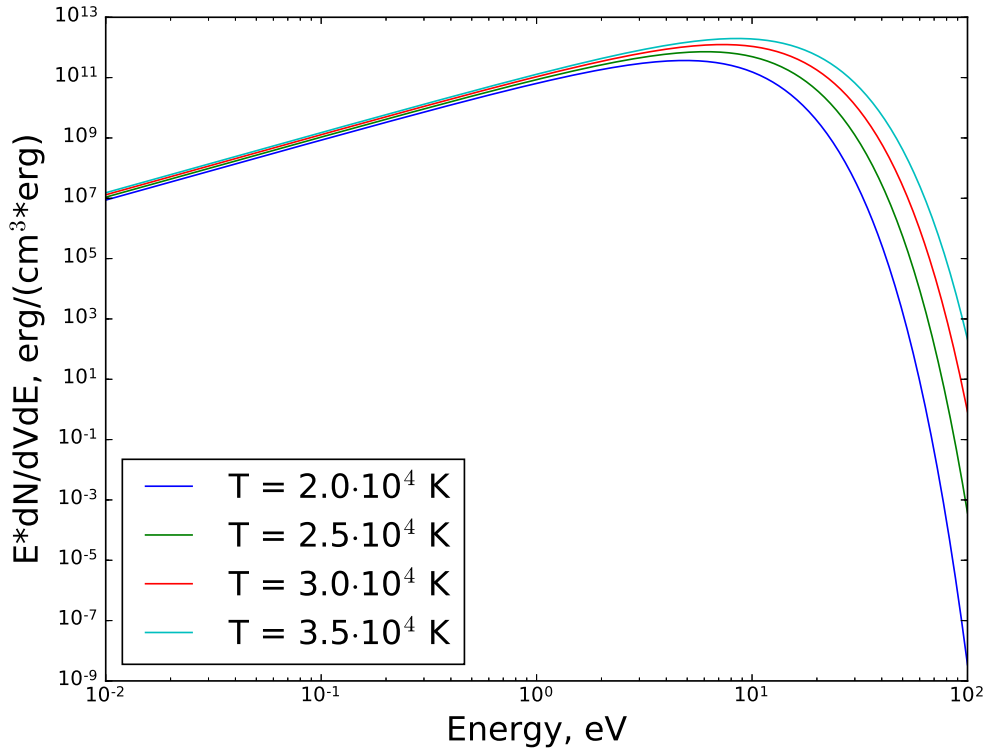

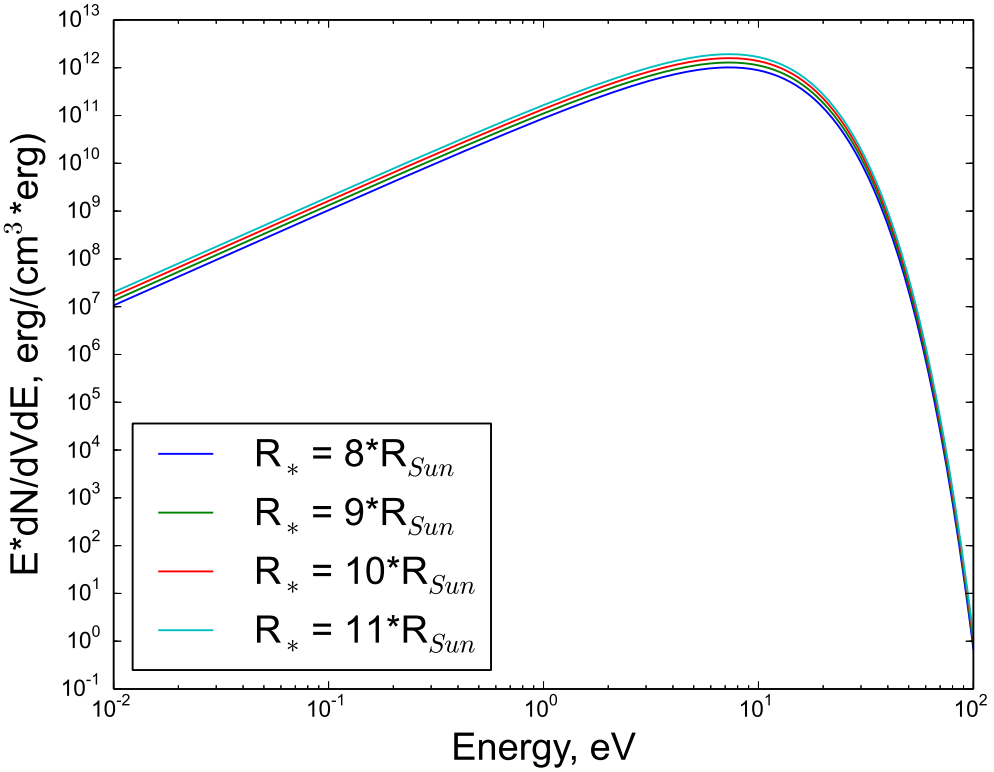

FIGURE 5.4: (top:) The flux density of SS 2883 as a function of different star temperature, the $d = 1{\times}10^{13}$ cm and $R_* = 6.2{\times}10^{11}$ cm. (bottom:) The flux density of SS 2883 as a function of different star radius for $d = 1{\times}10^{13}$ cm and $T = 34000$ K.

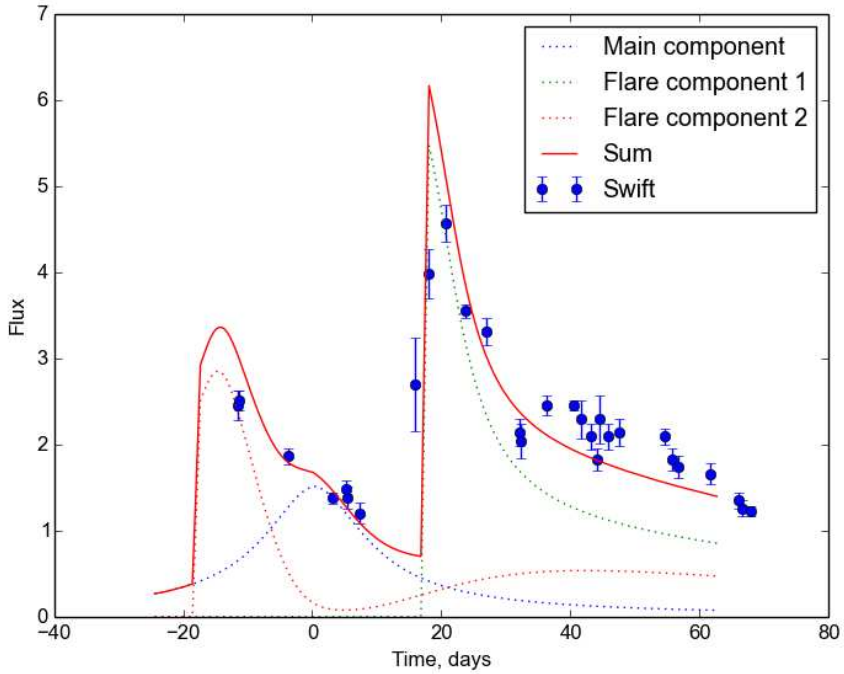

FIGURE 5.5: The modeled double-peaked lightcurve of PSR B1259−63 with the real *Swift* data points in the case of inverse-Compton scattering. The flux is given in 10^{-11} erg/cm^2/s units.

electrons producing the observed X-ray emission is rather mild, $\gamma \sim$ 10-100. In this case, inverse-Compton losses dominate over synchrotron radiation (see Fig. 5.6). Note that the synchrotron emission from electrons with Lorentz factor of about 10^5 will also produce X-ray emission in the 1.0 – 10.0 keV energy range.

The detailed shape of the lightcurve is not fully described by the model, however, it still gives a reasonable description of the data. This suggests that the observed X-ray emission can be indeed explained by the inverse-Compton radiation of the relativistic electrons. The observed excess of the X-ray emission above the model happens during the time of the GeV-flare and can be explained by the additional component resulting from the synchrotron cooling of the injected electrons with Lorentz factor $\gamma \gtrsim 10^5$ (see Sec. 5.4 for details).

5.4 Explanation of the GeV flare in PSR B1259−63

In 2010, an unpredictable and puzzling GeV flare was discovered by *Fermi*/LAT [215]. *Fermi* observations of PSR B1259−63 were performed in the 0.1 – 10.0 GeV energy band and detected a flaring activity in 2010 and 2014 passages. This flare activity was unexpected since these flares were detected after the pulsar's periastron passage and

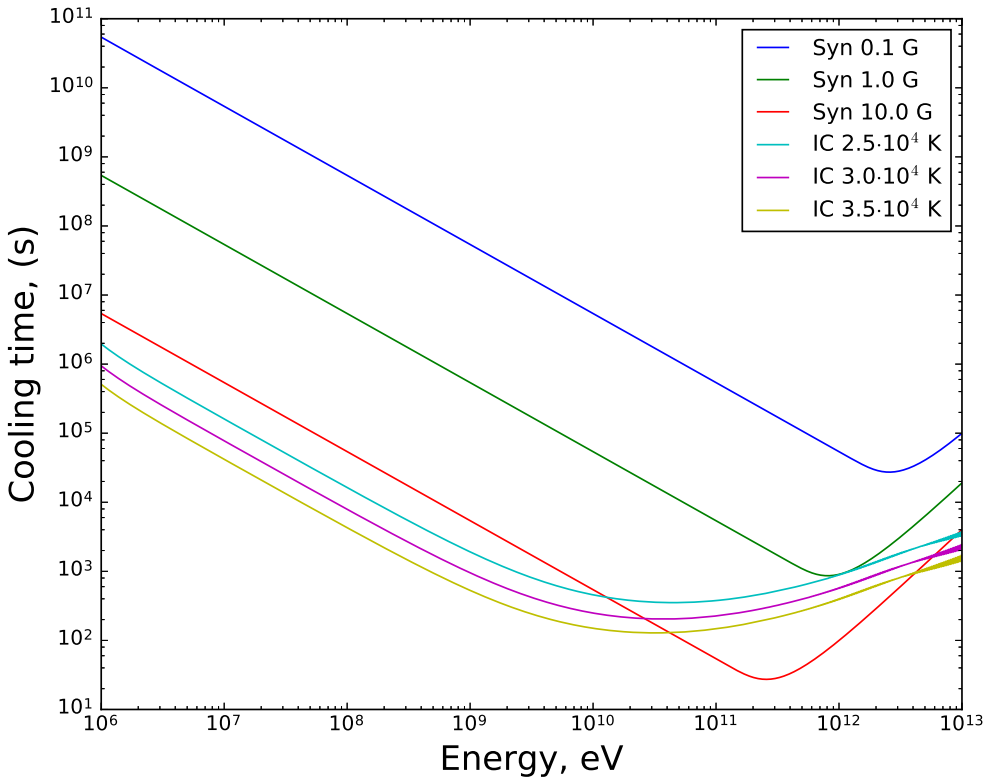

FIGURE 5.6: The cooling time of PSR B1259−63 in the case of inverse-Compton scattering and synchrotron radiation as a function of temperature, magnetic field and energy of electrons.

outside the equatorial disk. The spectrum of the GeV flare discovered in 2010 is shown in Fig. 4.7. The flare is surprising since the output binary power in the 0.1 – 10.0 GeV energy range was close to the maximum of the spin-down luminosity of the pulsar, 8×10^{35} erg s^{-1}. This maximum was derived theoretically, taking isotropic emission into account (see [215]). Firstly, the GeV flaring activity of PSR B1259−63 was not coincident with any other energies of electromagnetic spectrum. However, the optical observations of PSR B1259−63 during the periastron passage and the pre-/post- periastron periods indicate that the equivalent width of the Hα line decreases during the GeV flare [**206**]. The disruption of the equatorial disk during the moment when the pulsar goes through the disk is a common interpretation of such decrease [228].

5.4.1 Evolution of the Be-type star disk mass and size based on the optical observations

It is easy to determine the evolution of the size and mass of the equatorial disk through the periastron passage period using the $W_{\mathrm{H}\alpha}$ observations at multiple wavelengths. A simple model to calculate the ratio between the projected radius of equatorial disk (e.g., effective radius at which half of the Hα emission derives) and the radius of Be-type star companion, R_{disk}/R_*, as well as the density of the stellar disk was described by [228]. Such measurements can be derived using the effective temperature of the massive companion, T_{eff}, angle of disk inclination, i_{disk}, and $W_{\mathrm{H}\alpha}$ as entering parameters.

Due to the disruption and due to the gravitational influence, the equatorial disk of the Be-type star in PSR B1259−63 should be greatly truncated at the moment of periastron passage. The gravitational influence of the pulsars on the disk was observed by [229] for a sample of Be binary systems using optical data. The disruption of the disk was intensively studied by [230, 231] using hydrodynamical simulations. They argued that such disruption in PSR B1259−63 might be the result of the pulsar wind ram pressure. The truncation length increases quickly after periastron. Therefore, **[205, 206]** used the orbital solution of [232], a mass of Be-type star in PSR B1259−63 of 31 $M_{\odot}$ obtained by [233], and the typical mass of neutron star of 1.4 $M_{\odot}$ to derive the binary separation distance, r, as a function of time. Our collaboration derived the separation length in a wide range, $24.8R_* < r <$203.3 R_* (other parameters are well described in **[205]** and references). To estimate the total mass of the disk, **[205]** used an axisymmetric, isothermal density profile as

$$\rho(r,z) = \rho_0 \left(\frac{R_*}{r}\right)^n \exp\left[-1/2\left(\frac{z}{H(r)}\right)^2\right]. \tag{5.2}$$

According to [229], a typical radial density exponent of Be-type star disks is $n = 3$. The typical height of the Be-type star disk is

$$H(r) = H_0 \left(\frac{r}{R_*}\right)^{\beta}, \tag{5.3}$$

where

$$H_0 = \frac{a}{V_{crit}} R_*; \qquad a = \sqrt{\frac{kT}{\mu m_H}}, \tag{5.4}$$

here, the parameter β is equal to 1.5 in the case of an isothermal disk [234, 235]. The total disk mass can be measured using the integration of the density profile out to the truncated radius starting from the equatorial surface of stellar companion **[205]**.

Of course, such measurements of disk features are not realistic since they were derived taking isothermal and axisymmetric disk properties into account, which is not

correct. The real disk shape as well as the real thermal profile produce uncertainties in the estimated mass. [222] discussed these and other possible effects in their work. The assumed truncation radius in the model above is an additional source of error. The assumed distance within which the pulsar becomes eclipsed by the disk is 42.2 stellar radius that is higher than distance from star to the pulsar at periastron. This distance was derived taking 90° inclination between the pulsar orbit and the disk. As a result of an overestimated radius, the disk mass within periastron passage period is also higher. The radius of the equatorial disk can be instead at the effective Roche lobe radius of star, as a result, a lower disk mass can be obtained. Both over- and under- estimated masses are consistent with the model suggested in [**205, 206**].

According to this model, the PSR B1259−63 optical data indicates the growing of the disk during the period when the pulsar crosses the periastron passage. The disk disruption by the pulsar might be the reason of the growing of disk mass. According to [236], the energy dissipation rate extends a maximum value within periastron passage period. Such an effect is observed over the stellar surface and in binary systems with a very eccentric orbits. Thus, an increasing of stellar activity at such orbital phase is promoted. Moreover, recent observations of Be-type stars have been indicated about the possibility to expose disk outbursts near moment of periastron passage [237, 238]. Thus, the applied idea about the growing the equatorial disk around stellar companion of PSR B1259−63 is not so extraordinary.

The optical lightcurves of PSR B1259−63 binary system in Fig. 5.1 indicate that the equivalent width of the $H\alpha$ line remains permanent during the periastron passage until the moment of the GeV flare. Then, it falls quickly at the time of GeV flare pointing to the fact that the stellar disk mass declined by a factor 5 (from $2 \times 10^{-8} M_{\odot}$ to $4 \times 10^{-9} M_{\odot}$) within 5 days after the flare [**206**]. Recent results made by [210, 239] using *Chandra* observations favor the idea of [**206**] about disk disruption. These observations display the variable extended emission of PSR B1259−63. This variability can be explained as an emission that came from the clump of the disk that moves away from the system.

5.4.2 High-energy consequences of the Be-type star disk disruption

The broadband spectrum of PSR B1259−63 is shown in Fig. 5.7. The spectrum is extracted for the flare and pre-flare periods. The *H.E.S.S.* spectrum during flare period was already published in [215]. The pre-flare and GeV-flare spectra of PSR B1259−63 were made by *Fermi*/LAT as described in Sec. 4.5. This broadband spectra was used in [**206**] to explain the nature of the GeV-flare using the synchrotron model argued in [**205**]. According to this model, the tough perturbation of the equatorial disk in

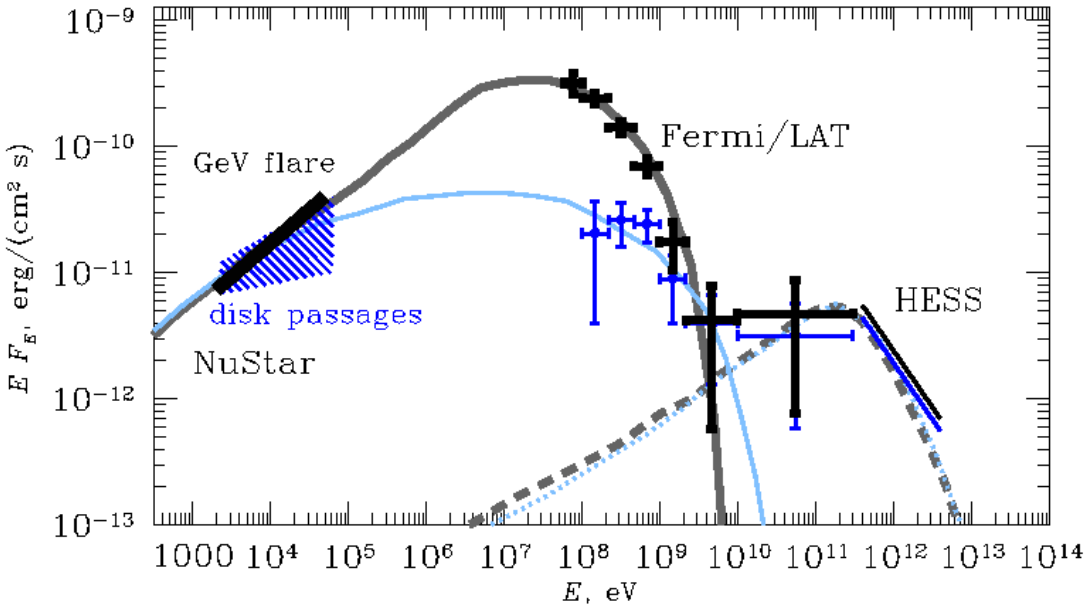

FIGURE 5.7: The broadband spectrum of the PSR B1259−63 during both flare (black crosses) and pre-flare states (blue crosses) modeled by two spectra taken from [**206**], [215] and obtained for the synchrotron (solid lines) and inverse-Compton (dashed and dotted lines) emissions during the GeV flare (grey) and during the pre-flare states of the periastron passages (light blue).

Be-type star eliminates the normal contact surface between the pulsar wind and the Be-type star outflow. Thus, these perturbations lead to the production of clumps from the dense disk. As a result, the contact surface obtains an irregular geometry. The pulsar wind transferred all its power inside the binary system. Thus, the source luminosity increases up to $\sim 70\%$ and 50% of the spin-down power of the pulsar during 2010 and 2014 periastron passages [**206**], [215]. [215] argued that the GeV flare in PSR B1259−63 produced by 100 TeV electrons

$$E_{e,flare} \simeq 10^2 \left[\frac{B_{pw}}{1\ \mathrm{G}}\right]^{-1/2} \left[\frac{\nu}{1\ \mathrm{GHz}}\right]^{1/2}\ \mathrm{TeV} \tag{5.5}$$

taking that magnetic field in the pulsar wind is $B_{pw} \sim 1$ G at distances 10^{13} cm into account.

The low-energy tail of the electron distribution $dN/dE \sim E^{-2}$ is formed by the synchrotron cooling of the particles with 100 TeV energy. As a result, we find that the synchrotron spectrum has a slope $dN_\gamma/dE \sim E^{-1.5}$. This slope is consistent with the photon index of the X-ray spectrum after the flare state (see Fig. 4.6). Such a photon index indicates that the X-ray power is lower than the GeV power by a factor 3. Taking into account that the TeV luminosity of inverse-Compton emission is comparable to the X-ray luminosity, it is argued that no TeV range of the GeV flare is expected to be detectable. The flat shape of the X-ray-to-GeV spectrum of the persistent component of

PSR B1259−63 can be explained by both synchrotron and inverse-Compton emissions depending on the Lorentz factors associated with the accelerated electrons of the Be-type star wind (see, e.g., [**206**], [215]). The inverse-Compton model, however, has an advantage as it can better explain the X-ray orbital lightcurve, see Section 5.3.

Chapter 6

X-ray observations of LS I +61° 303

In this chapter, I use all publicly-available X-ray observations made by *Suzaku*, *XMM*-Newton, *Chandra* and *Swift* to perform a spectral and timing analysis of LS I +61° 303. I use the results of the X-ray analysis to study the distribution of several physical parameters of LS I +61° 303 over orbital and superorbital timescales. A graphical representation of the orbital position of *Suzaku*, *Chandra* and *XMM*-Newton observations is given in Fig. 6.1. The main analysis was performed with *Swift* data that cover observations during 4.5 years. An interpretation of the results of this data analysis is given in the following Chapter 7.

6.1 The *Suzaku* observations

The spectral and timing analysis of the X-ray emission of LS I +61° 303 along the orbit gives significant information about radiation processes in this gamma-ray source. In this section, I present non-published observational data of LS I +61° 303 made by *Suzaku* in 2009. There are three long $\sim$ 40, 60, 70 ks observations (see for details Tab. 6.1), which provides one observation of LS I +61° 303 in periastron and two more in apastron.

For the XIS data, I performed full XIS reprocessing and screening data as discussed in Subsec. 2.4.1. The source photons were extracted from the circle area with a radius of 3 arcmin. The background photons were taken from the circle with the same radius and in the same field of view near the source region.

For the HXD/PIN data, I used standard event reprocessing and screening criteria according to Sec.7.5.1 of *Suzaku* ABC Guide analysis, the HXD background is distributed

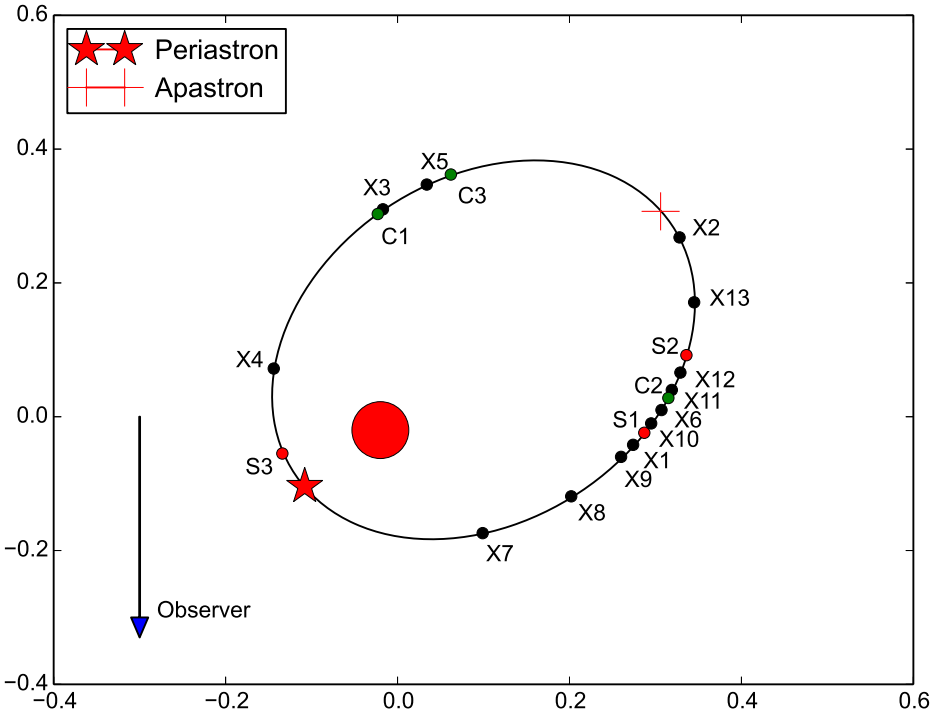

FIGURE 6.1: Orbital geometry of LS I +61° 303 adapted from [94], along with the positions of *Suzaku* (S1-3), *Chandra* (C1-3) and *XMM*-Newton (X1-13) observations.

TABLE 6.1: The list of *Suzaku* observations. ϕ and Φ are orbital and superorbital phases correspondingly.

Ods. date	ObsID	Ref	MJD	Exp. time ks	ϕ	Φ
22-01-2009	403015010	S1	54853.951	40.5	0.562	0.8912
25-01-2009	403016010	S2	54856.696	61.0	0.666	0.8928
10-02-2009	403017010	S3	54872.184	68.6	0.251	0.9021

in the form of simulated event files tailored to each observation. The `tuned` background files were chosen to determine the HXD/PIN non-X-ray Background (NXB). To extract source spectra of LS I +61° 303, I used the `hxdpinxbpi` tool.

6.1.1 Timing analysis

The background-subtracted lightcurves obtained from a combination of the XIS detectors are shown in Fig. 6.2 for all three *Suzaku* observations with their hardness ratio (HR). The lightcurves correspond to two parts of the orbit (S1 and S2 observations correspond to the apastron, while the S3 observation corresponds to the periastron).

The orbital and superorbital phases are calculated with periods of 26.496 and 1667 days [92], respectively, and shown in Tab. 6.1. The reference epoch T_0 (JD2443366.775-JD2400000.5 = JD43366.275) was taken from [92, 240].

S1 and S2 lightcurves show flux modulation, ranging from a maximum rate of about 2.5 counts s^{-1} down to 0.3 counts s^{-1} in a few hours. The hardness ratio maps are smoothly modulated in the case of S2, while the HR of S1 is strongly modulated, displaying a wave-like shape, with three minima (around 20, 40 and 60 ks) and four maxima (around 5, 30, 50 and 80 ks). The lightcurve of periastron (S3) do not show any modulation, ranging from a maximum rate about 0.7 counts s^{-1} down to 0.3 counts s^{-1}. In order to find the most accurate period possible that represents all of the data in the observation, I used a technique called a power spectrum analysis. A power spectrum analysis determines what period or periods best fit the entire data set. The power spectrum plots the likelihood that a frequency is present in the data (represented by "power" on the vertical axis) as a function of frequency (on the horizontal axis) [241, 242]. The two power spectra that correspond to apastron and periastron are shown on the right panel of Fig. 6.3.

Plotting HR versus source intensity (see top image in Fig. 6.3), I have found a significant feature, namely the S1 case indicates that the source is harder when it is brighter that is in agreement with the result obtained by [243].

6.1.2 Spectral analysis

For spectral fitting, I used a single-power law model with photoelectric absorption. This model provides a good fit for all three XIS *Suzaku* observations, see Tab. 6.2 and Fig. 6.4. In contrast, I found that for the PIN spectra of S1 and S2 observations, the standard calibration factor of 1.15 is too small (2.7 for S1 and 3.3 for S2). I have investigated the too large normalization of HXD/PIN compared with XIS. The too large normalization is probably due to the underestimation of the non-X-ray background (not due to the celestial behavior unfortunately). According to the *Suzaku* team, this is because the S1 and S2 observations in the corresponding week were performed during the unfortunate situations[1], namely: (1) too many noise events in the lower energy part by the high temperature of HXD; (2) telemetry saturation by (1) and the dead-time reached close to 50% (typically the dead-time is $< 10\%$); (3) almost no earth occultation data. To generate the HXD/PIN non-X-ray background data, clean earth-occultation data are needed. Usually, only ~ 1 week is not a big problem, since the background is generated using the 1-month data. Also, with (1), I can normally analyze the data by excluding the lower energy part (e.g., < 20 keV). However, the week including S1 and S2

[1]See calibration documentation on the http://www.astro.isas.jaxa.jp/suzaku/caldb/doc/

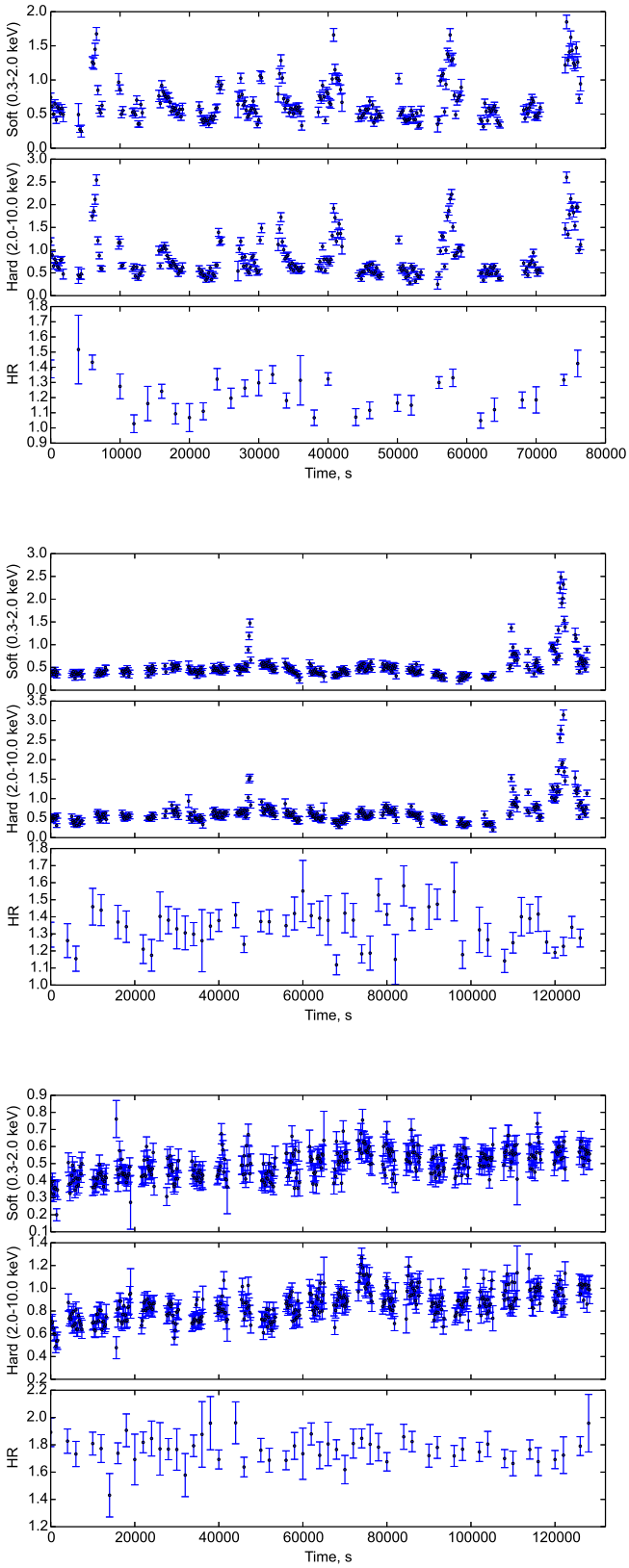

FIGURE 6.2: The *Suzaku* lightcurves of LS I +61° 303 in two energy bands (soft = 0.3-2.0 keV, hard = 2.0-10.0 keV) together with their hardness ratio (HR = hard/soft) for all three observations (from top to bottom, S1, S2, S3). Bin time is 200 s for soft and hard ranges and 2 ks for HR.

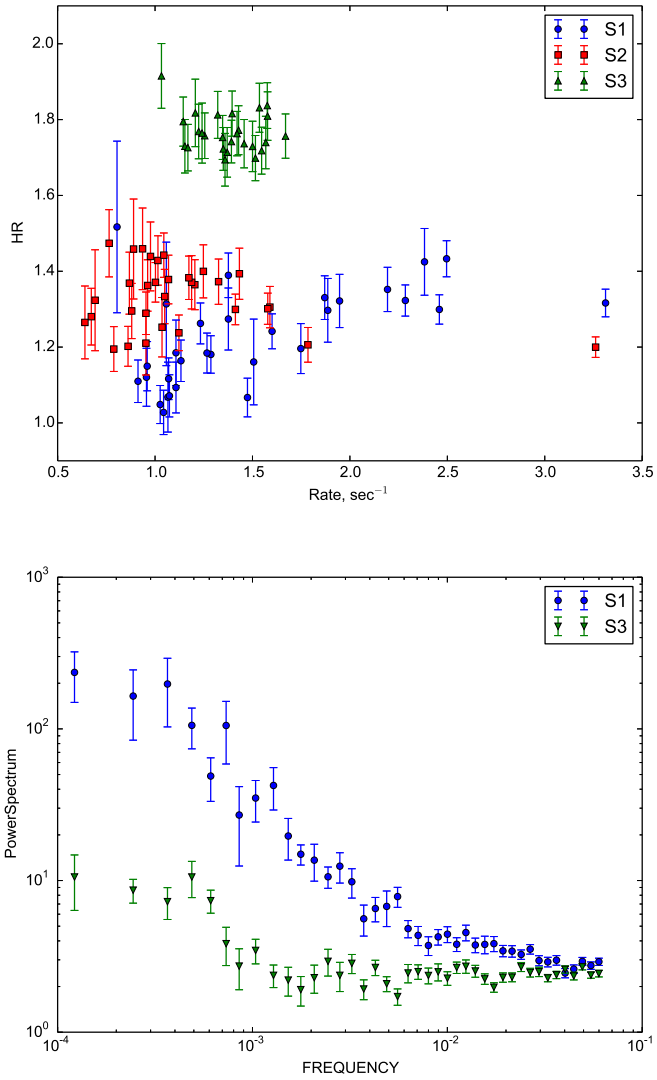

FIGURE 6.3: (top:) HRs versus intensity plot for the all three *Suzaku* observations with a bin time 1 ks for S1 and S2, and 2 ks for S3. Count rates are taken from full energy range 0.3-10.0 keV, while the HRs are defined as ratio between hard and soft energy bands. (bottom:) The S1 and S3 power spectra of LS I +61° 303 (the power spectrum is given in ph^2 unit, and frequency is given in Hz unit). The time bin of power spectrum is 1 ks.

suffered from too many noisy events resulting in too much dead-time. This is very rare (once per year, when the detector damage reached event thresholds on-board) and not well treated in the current background generation. As a result, I only used XIS spectra.

Absorption column densities and photon indexes for S1 and S2 are consistent with results of *XMM*-Newton and *Chandra* observations [243–245]. For the S3 case (near periastron), I got a higher value of the column density and a lower value of the photon index. This value of the column density is in agreement with the results obtained by *Chandra* in spring 2006 [246]. The spectral shape varies from 1.63 near the periastron to around 1.80 near the apastron, while the column density changes from 0.67 to 0.53,

TABLE 6.2: The *Suzaku* results of spectral fitting with an absorbed power law model.

Ref	N_H 10^{22} cm^{-2}	Γ	F(1-10 keV) 10^{-11} erg/cm^2/s	χ^2	RMS
S1	0.53±0.01	1.85±0.01	1.17±0.01	1.08/(379)	0.656
S1a	0.507±0.02	1.91±0.026	0.76±0.08	1.01/(456)	
S1b	0.566±0.02	1.82±0.022	2.08±0.02	0.94/(533)	
S2	0.53±0.01	1.80±0.02	0.91±0.01	1.01/(441)	0.570
S2a	0.56±0.02	1.82±0.02	0.74±0.01	0.96/(770)	
S2b	0.52±0.02	1.82±0.03	1.83±0.02	0.94/(399)	
S3	0.67±0.01	1.63±0.01	1.20±0.01	1.03/(569)	0.176

respectively. I derived the root-mean-square (RMS) variability for each lightcurve as

$$\mathrm{RMS} = \sqrt{\frac{\sum(x_i - < x >)^2}{N}}, \tag{6.1}$$

see Tab. 6.2.

The X-ray flux in 1.0 - 10.0 keV energy band changes only slightly, from (1.20±0.01) × 10^{-11} erg cm^{-2} s^{-1} near the periastron to (0.91±0.01) × 10^{-11} erg cm^{-2} s^{-1} near the apastron. I plotted combined XIS spectra corresponding apastron and periastron moments on the top panel of Fig. 6.5. The difference between the distribution of N_H and Γ are shown in the bottom panel of Fig. 6.5.

To compare the spectral shape of the source in and out the "flares", I split the S1 observation into two parts with the total count rates below (S1a) and above (S1b) 1.8 count/s, respectively. Spectral characteristics of S1a and S1b turned out quite different indeed, see Tab. 6.2 and top panel of Fig. 6.6. The obtained spectra of S1a and S1b are shown in Fig. 6.7. Similarly, I split below and above 1.7 count/s the S2 observation and I don't find notable changes of spectral index (see bottom panel of Fig. 6.6). The variation of the column density is 1σ level only, see Tab. 6.2.

6.2 The *XMM*-Newton observations

LS I +61° 303 was observed 13 times by *XMM*-Newton. These data were already presented in [99, 243, 245]. Here I reanalyzed them using the latest version of the analysis software. Similar to the analysis of *Suzaku* data, source spectra were extracted from a circular area with 3 arcmin radius, while the background spectrum was obtained from the regions with the same radius. Spectra were rebinned at least to have 30 counts per bin. The list of observations, reference names, exposition time, as well as the orbital and superorbital phases of the *XMM*-Newton data are given in Tab. 6.3.

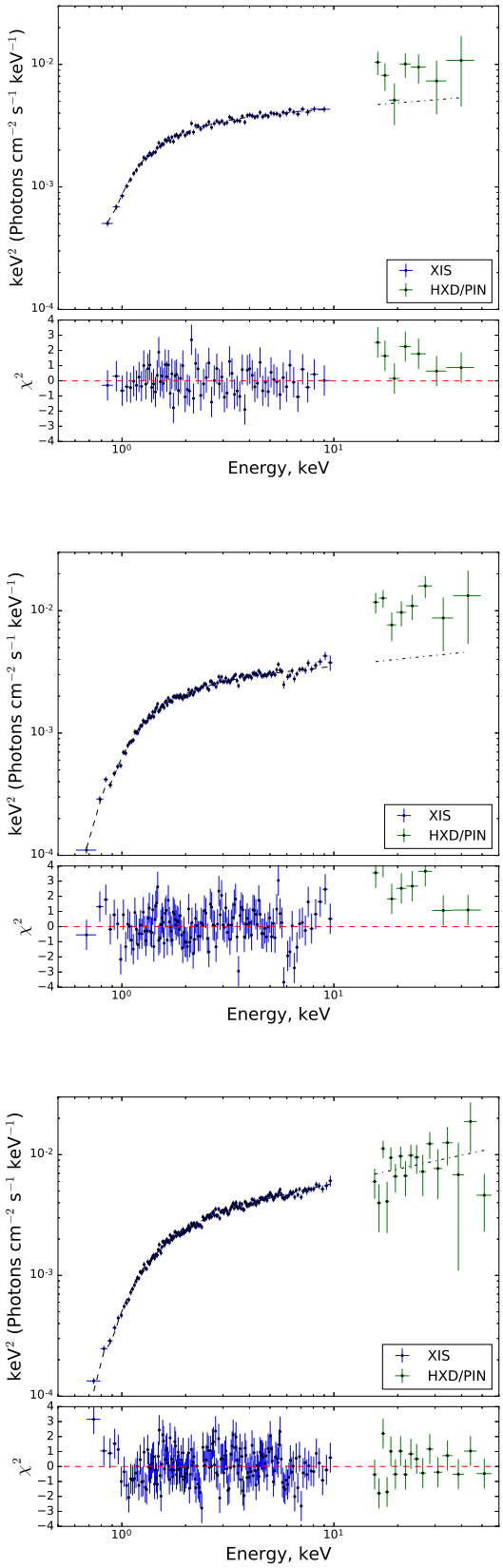

FIGURE 6.4: The fitted *Suzaku* spectra of LS I +61° 303 in two energy bands (XIS, PIN) for all three observations (from top to bottom, S1, S2, S3).

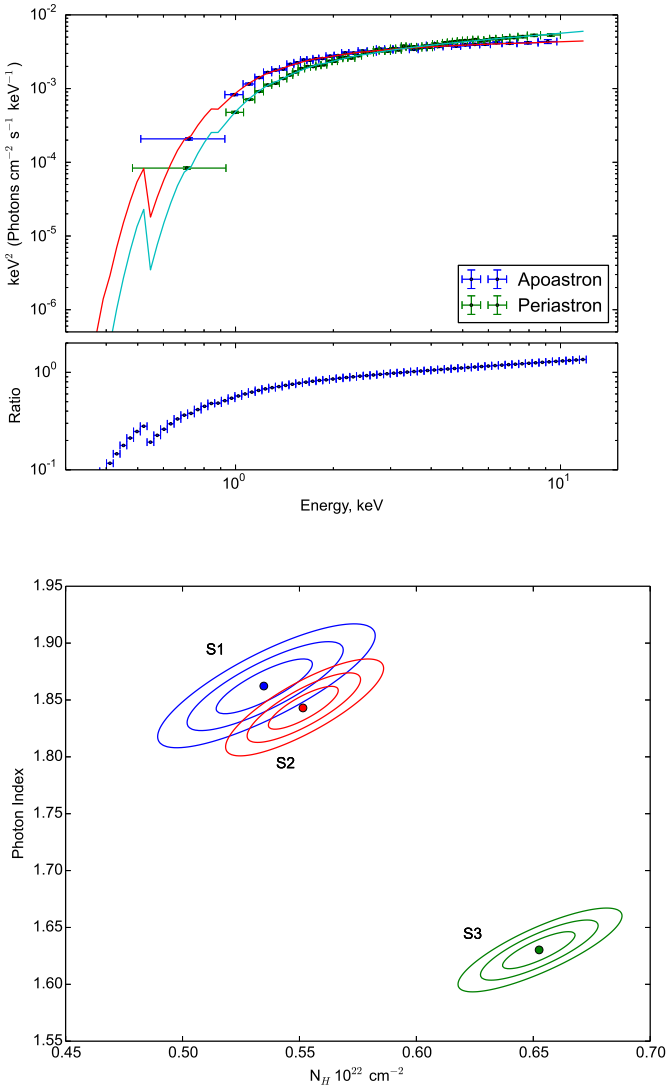

FIGURE 6.5: (top:) The combined XIS *Suzaku* spectra of LS I +61° 303 during periastron and apastron. (bottom:) The 1,2 and 3σ distributions of column density, N_H, and photon index, Γ, for LS I +61° 303.

6.2.1 Timing analysis

For the timing analysis presented here, I have used the longest *XMM*-Newton observation, X6. The background cleaned X6 PN lightcurve in two energy bands (soft and hard, soft = 0.3-2.0 keV, hard = 2.0-10.0 keV) are shown in Fig. 6.8 together with hardness ratio (HR). Both lightcurves demonstrate a smooth modulation, the maximum rate corresponds to approximately 1 counts per second while the minimum corresponds to about 0.1 counts per second. The hardness ratio exhibits a constant value of about 1 for the first 15-18 ks, and then a sharp decrease to 0.8 in a few hundred seconds. Then, HR shows a smooth modulation with two peaks near 25 and 38 ks and one minimum around 32 ks.

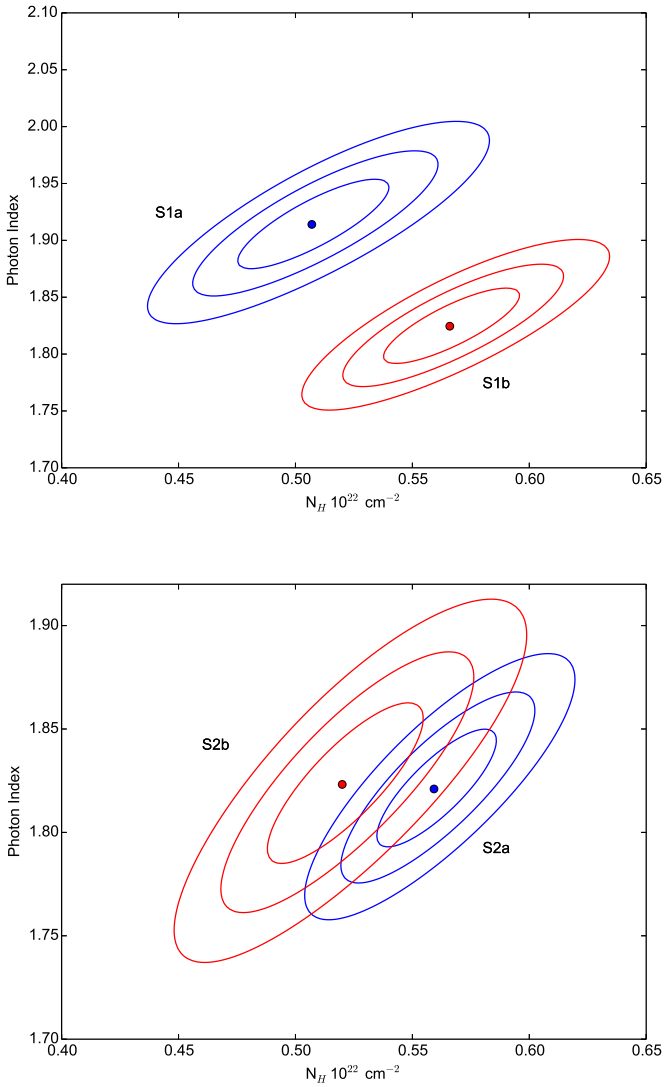

FIGURE 6.6: 1, 2 and 3σ confidence contour plots of the column density N_H versus photon spectral index Γ for a power law fit to S1a and S1b observations (top panel) and S2a and S2b (bottom panel).

To estimate the RMS in a more-correct way, I performed the Monte Carlo simulations for all *XMM*-Newton lightcurves (see in Fig. 6.9). 1000 test lightcurves were created for each *XMM*-Newton lightcurve and compared with original one. The simulated lightcurves were generated in the range of errors of observed lightcurves. Then, the RMS values were calculated using Eq. 6.1 and shown in Tab. 6.3. Here, I only show the simulated lightcurve for the X6 observation (see Fig. 6.9), all other simulated lightcurves are presented in Appendix B. These RMS values I used in Fig. 7.1 to investigate the orbital evolution of LS I +61° 303.

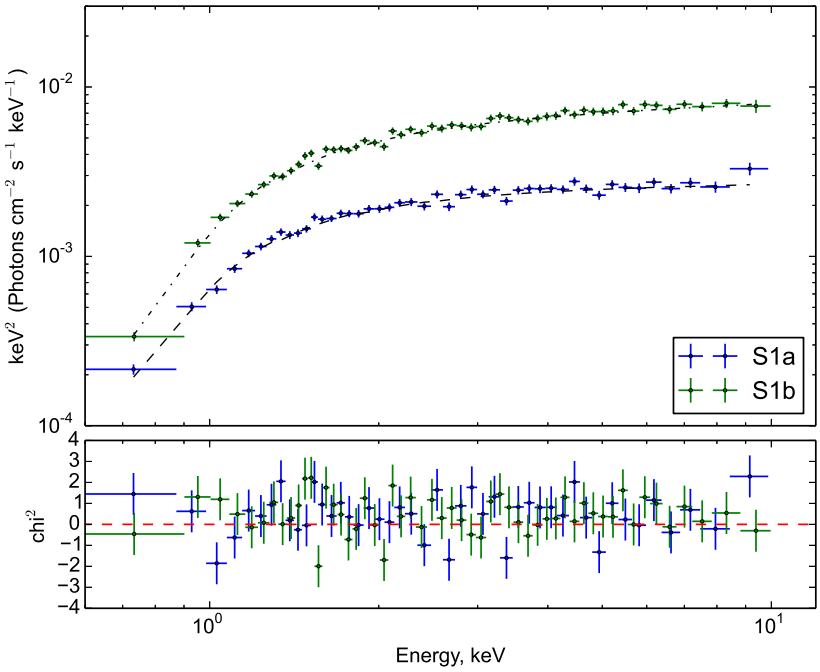

FIGURE 6.7: The spectra of S1a and S1b fitted by the power law model.

TABLE 6.3: The list of *XMM*-Newton observations.

ObsID	Ref	MJD	ϕ	Φ	Exp.time ks	RMS
0112430101	X1	52310.072	0.552	0.3652	6.40	0.127±0.019
0112430102	X2	52315.461	0.756	0.3684	6.40	0.649±0.007
0112430103	X3	52322.179	0.009	0.3724	6.40	0.385±0.008
0112430201	X4	52326.639	0.178	0.3751	7.49	0.223±0.012
0112430401	X5	52533.099	0.970	0.4990	6.46	0.095±0.018
0207260101	X6	53397.736	0.602	0.0176	50.41	0.598±0.005
0505980801	X7	54347.075	0.432	0.5871	17.41	0.284±0.011
0505980901	X8	54349.063	0.507	0.5883	13.41	0.177±0.011
0505981001	X9	54350.092	0.546	0.5890	18.55	0.249±0.007
0505981101	X10	54351.060	0.582	0.5895	17.41	0.327±0.006
0505981201	X11	54352.060	0.620	0.5901	15.01	0.141±0.014
0505981301	X12	54353.058	0.658	0.5907	16.87	0.087±0.012
0505981401	X13	54354.060	0.703	0.5913	14.51	0.274±0.007

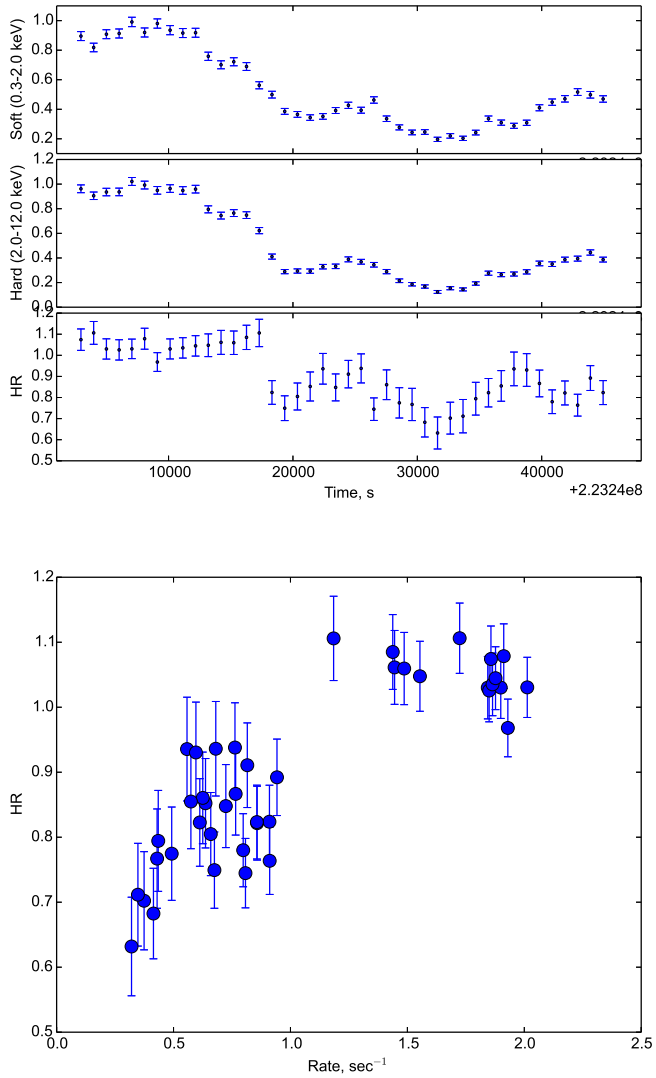

FIGURE 6.8: (top:) The *XMM*-Newton lightcurves of LS I +61° 303 in the soft and hard energy bands with their hardness ratio. Time bin is 1 ks. (bottom:) The distribution between HR and count rate in the full energy band (0.3 - 12.0 keV) for X6 PN observation. Time bin is 1 ks.

6.2.2 Spectral analysis

All *XMM*-Newton spectra of LS I +61° 303 binary system were fitted using a simple power law model with a photoelectric absorption. The hydrogen column density, N_H, and power law photon index, Γ, were free parameters during modeling. The best-fitting parameters of the modeled spectra are summarized in Tab. 6.4.

In addition to the spectral fitting of all *XMM*-Newton spectra, the X6 observation was fitted separately, similar to S1 and S2. I extracted the two spectra for the X6 observation by splitting the observation into two parts. One part of X6 corresponds to the data where the value of count rate is equal 1.2 s^{-1} or lower (X6a). The hardness rate

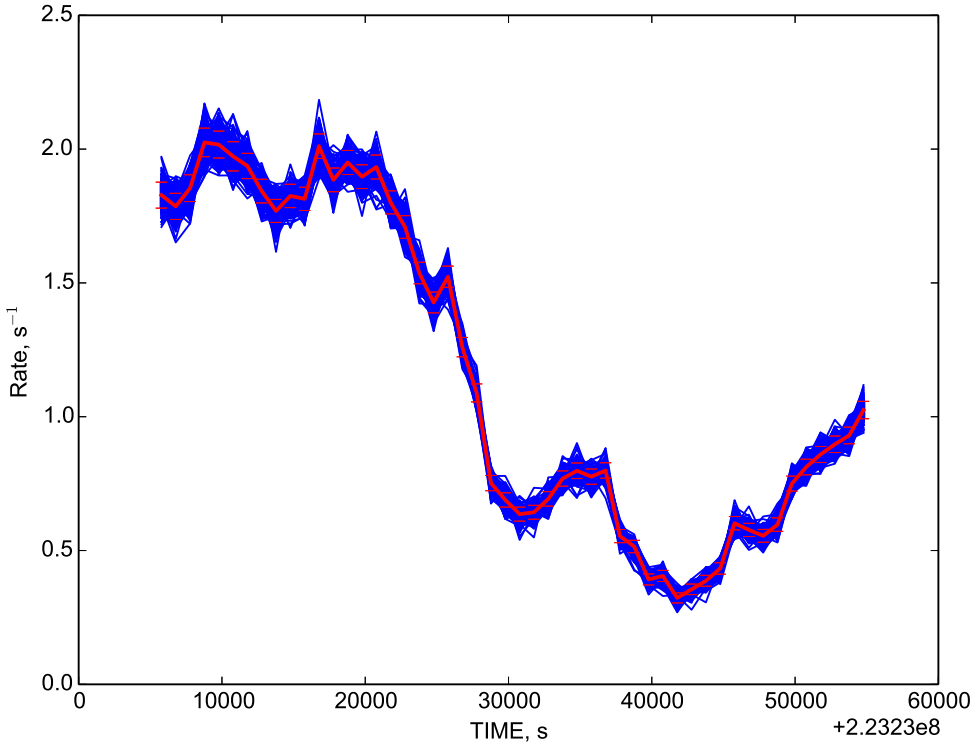

FIGURE 6.9: The simulated lightcurves of the X6 observation of LS I +61° 303 with observed lightcurve.

of these parts is completely different (see bottom panel in Fig. 6.8). The second part of X6 corresponds to the data where the count rate is higher than 1.2 s^{-1}. A power law model with photoelectric absorption gives acceptable fits for both cases (see Fig. 6.11). The values of the hydrogen column density for X6a and X6b are consistent. The best-fitting parameters of these modeled spectra are shown in Tab. 6.4. It is significant to note that the same analysis performed for other *XMM*-Newton data did now show any evidence of presence of significant changes in hardness plots. The distribution of hydrogen column density and power law photon index is presented on the top panel in Fig. 6.10.

6.3 The *Swift* observations

The *Swift* observatory gives a great opportunity to monitor LS I +61° 303 on very different timescales. In this work, I used data which cover more than 4 years of observations of LS I +61° 303 between 2010 and 2014. The data reduction was performed according to the Subsec. 2.5.1. After initial cleaning of events, I have 164 available observations. I have extracted spectra of LS I +61° 303 for PC and WT modes

TABLE 6.4: Best-fitting parameters of the spectral analysis of *XMM*-Newton LS I +61° 303 observations.

Ref	N_H 10^{22} cm^{-2}	Γ	F(1-10 keV) 10^{-11} erg/cm^2/s	χ^2/(d.o.f.)
X1	0.50±0.02	1.54±0.03	1.56±0.03	1.04/(253)
X2	0.52±0.02	1.49±0.03	1.44±0.02	1.05/(223)
X3	0.61±0.04	1.83±0.07	0.75±0.03	0.97/(95)
X4	0.48±0.06	1.53±0.09	0.51±0.02	1.00/(87)
X5	0.63±0.02	1.60±0.03	1.44±0.05	0.91/(251)
X6	0.50±0.01	1.62±0.01	0.94±0.01	1.10/(1074)
X6a	0.47±0.01	1.73±0.02	0.49±0.01	1.02/(223)
X6b	0.53±0.01	1.60±0.02	1.43±0.01	1.12/(289)
X7	0.49±0.01	1.82±0.02	0.82±0.09	1.04/(357)
X8	0.47±0.01	1.60±0.02	0.85±0.01	1.07/(348)
X9	0.49±0.01	1.60±0.02	0.90±0.01	1.25/(505)
X10	0.49±0.01	1.62±0.02	0.90±0.01	0.97/(500)
X11	0.52±0.01	1.52±0.01	1.59±0.02	1.12/(634)
X12	0.51±0.01	1.54±0.02	1.29±0.01	1.05/(513)
X13	0.50±0.01	1.59±0.02	0.86±0.01	1.08/(376)

from circle regions with radii from 5 to 30 pixels (talking into account the value of count rate) and 25 pixels, respectively. The background spectra were taken over the annuli regions around source regions. The spectra were grouped to have at least 1 count bin^{-1} using `grppha` tool. The spectral analysis was performed using Monte Carlo method described in Subsec. 2.7.2, the spectra were fitted in 0.5 - 10.0 keV energy band. The errors correspond to a 1σ confidence level. In Tab. 6.5, I show a list of available data with obtained results of spectral analysis of the *Swift* data.

6.4 The *Chandra* observations

During monitoring campaign, the LS I +61° 303 was observed by *Chandra* X-ray Observatory only 3 times (see Tab. 6.6).

For the data analysis, I used the steps described in Subsec. 2.3.1. The source spectra were extracted from circle area with a radius of 0.15 arcmin, while the background spectra were extracted from the region with no source and with the same radius as source area. The fitting of spectra was performed using absorbed power law model. The results of fitting are given in Tab. 6.7.

TABLE 6.5: The results of *Swift* data analysis of LS I +61° 303.

ObsID	MJD d	ϕ	Φ	N_H 10^{22} cm^{-2}	Γ	$F_{un_{1-10keV}}$ 10^{-11} erg/cm^2/s	$F_{abs_{1-10keV}}$ 10^{-11} erg/cm^2/s	$F_{un_{2-10keV}}$ 10^{-11} erg/cm^2/s
00036093001	53980.340	0.591	0.3671	0.57±0.06	1.58±0.09	2.06±0.05	1.80±0.06	1.62±0.06
00036093002	53983.903	0.726	0.3693	0.63±0.21	1.73±0.26	1.67±0.11	1.39±0.12	1.25±0.12
00036093003	53989.040	0.92	0.3723	0.64±0.10	1.46±0.13	1.03±0.03	0.91±0.04	0.85±0.05
00036093004	53991.403	0.009	0.3738	0.91±0.12	1.69±0.13	1.62±0.05	1.30±0.06	1.25±0.05
00036093005	53993.331	0.082	0.3749	0.59±0.07	1.64±0.10	1.53±0.04	1.32±0.05	1.20±0.05
00036093006	53995.273	0.155	0.3761	0.48±0.12	1.54±0.17	0.74±0.03	0.65±0.04	0.59±0.04
00036093007	53997.412	0.236	0.3774	0.68±0.16	1.79±0.21	0.99±0.05	0.82±0.06	0.74±0.06
00036093008	54060.081	0.601	0.415	0.78±0.11	1.55±0.12	1.82±0.05	1.53±0.07	1.45±0.07
00036093009	54061.145	0.641	0.4156	0.59±0.07	1.61±0.11	1.57±0.05	1.35±0.05	1.22±0.05
00036093010	54062.084	0.676	0.4162	0.60±0.09	1.56±0.10	2.31±0.06	2.01±0.07	1.82±0.07
00036093011	54063.158	0.717	0.4168	0.67±0.08	1.68±0.11	2.20±0.06	1.86±0.07	1.69±0.08
00036093012	54068.260	0.909	0.4199	0.47±0.18	1.68±0.27	0.91±0.07	0.80±0.08	0.69±0.08
00036093013	54069.263	0.947	0.4205	0.55±0.11	1.62±0.15	1.64±0.07	1.42±0.08	1.28±0.08
00036093016	54074.155	0.132	0.4234	0.30±0.13	1.50±0.24	0.79±0.06	0.73±0.07	0.63±0.08
00036093017	54076.158	0.208	0.4246	0.54±0.17	1.66±0.25	0.47±0.03	0.40±0.03	0.36±0.07
00036093018	54078.517	0.297	0.4260	0.50±0.09	1.82±0.16	1.30±0.05	1.12±0.06	0.95±0.07
00036093019	54080.036	0.354	0.4269	0.33±0.15	1.16±0.23	0.95±0.07	0.89±0.08	0.82±0.09
00036093020	54082.043	0.43	0.4281	0.44±0.18	1.43±0.24	1.17±0.09	1.05±0.10	0.94±0.09
00036093021	54083.049	0.468	0.4287	0.40±0.22	1.30±0.32	1.22±0.11	1.12±0.15	1.01±0.12
00036093022	54085.057	0.543	0.4299	0.87±0.16	1.86±0.20	2.02±0.10	1.58±0.09	1.01±0.12
00036093023	54087.261	0.627	0.4313	0.46±0.09	1.25±0.12	2.32±0.08	2.12±0.09	1.94±0.08
00036093025	54091.009	0.768	0.4335	0.68±0.24	1.57±0.29	1.80±0.12	1.52±0.15	1.42±0.14
00036093026	54093.436	0.86	0.4350	0.54±0.09	1.35±0.11	2.07±0.06	1.87±0.08	1.74±0.08
00036093027	54298.156	0.586	0.5578	0.53±0.04	1.43±0.06	1.79±0.03	1.61±0.03	1.47±0.04
00036093028	54354.589	0.716	0.5916	0.94±0.17	2.02±0.19	0.97±0.05	0.73±0.04	0.67±0.05
00036093029	54355.599	0.754	0.5922	0.71±0.16	1.45±0.17	1.17±0.05	1.00±0.07	0.94±0.07
00036093030	54356.597	0.792	0.5928	0.82±0.13	1.50±0.14	1.70±0.06	1.43±0.06	1.37±0.07
00036093031	54357.600	0.83	0.5934	0.61±0.10	1.54±0.15	1.67±0.07	1.44±0.09	1.33±0.08
00036093032	54358.134	0.85	0.5938	0.65±0.06	1.52±0.08	1.75±0.04	1.51±0.04	1.40±0.04
00036093034	54362.010	0.996	0.5961	0.40±0.13	1.38±0.19	1.23±0.07	1.13±0.09	1.01±0.08
00036093035	54363.018	0.034	0.5967	0.72±0.14	1.62±0.18	1.15±0.05	0.96±0.06	0.89±0.06
00036093036	54365.490	0.127	0.5982	0.96±0.21	1.78±0.23	1.31±0.07	1.02±0.07	0.97±0.07
00036093037	54382.506	0.77	0.6084	0.63±0.08	1.56±0.11	2.00±0.06	1.73±0.07	1.59±0.07
00036093038	54383.375	0.802	0.6089	0.65±0.11	1.56±0.14	2.22±0.08	1.90±0.10	1.79±0.11
00036093039	54384.312	0.838	0.6095	0.66±0.14	1.69±0.18	1.45±0.07	1.22±0.09	1.10±0.09
00036093041	54405.136	0.624	0.6220	0.39±0.14	1.65±0.24	0.70±0.05	0.62±0.06	0.52±0.06
00036093043	54408.264	0.742	0.6238	0.47±0.12	1.45±0.18	1.21±0.06	1.08±0.08	0.98±0.09
00036093044	54410.281	0.818	0.6250	0.53±0.15	1.25±0.19	1.20±0.07	1.09±0.08	1.02±0.09
00036093048	54723.430	0.637	0.8129	0.84±0.19	1.87±0.21	0.82±0.04	0.64±0.04	0.60±0.04
00036093052	54728.039	0.811	0.8157	1.35±0.71	1.24±0.48	0.91±0.09	0.71±0.10	0.75±0.09
00036093054	54730.859	0.917	0.8173	0.81±0.40	1.29±0.35	1.23±0.10	1.04±0.12	1.02±0.11
00036093055	54730.986	0.922	0.8174	0.65±0.10	1.45±0.12	1.39±0.05	1.21±0.06	1.12±0.05
00036093056	54734.916	0.07	0.8198	0.97±0.42	1.82±0.37	0.79±0.08	0.58±0.06	0.56±0.05
00036093057	54735.050	0.075	0.8199	0.12±0.10	0.92±0.34	0.72±0.08	0.68±0.09	0.63±0.09
00036093058	54735.921	0.108	0.8204	0.45±0.18	1.64±0.24	0.67±0.04	0.58±0.05	0.51±0.05
00036093059	54736.926	0.146	0.8210	0.31±0.24	2.15±0.50	0.46±0.06	0.37±0.06	0.28±0.06
00036093060	54737.001	0.149	0.8210	0.15±0.15	1.22±0.27	0.65±0.05	0.62±0.06	0.55±0.07
00036093061	54739.067	0.227	0.8223	0.42±0.11	1.44±0.16	0.90±0.04	0.81±0.05	0.74±0.05
00036093062	54744.561	0.434	0.8256	0.58±0.09	1.76±0.13	0.91±0.03	0.77±0.04	0.67±0.04
00036093063	54750.666	0.665	0.8292	0.16±0.11	1.21±0.21	0.58±0.05	0.56±0.06	0.52±0.06
00036093064	54754.082	0.793	0.8313	0.25±0.24	0.67±0.34	0.81±0.12	0.77±0.13	0.74±0.14
00036093065	54761.709	0.081	0.8358	0.84±0.24	1.84±0.29	1.19±0.08	0.94±0.09	0.86±0.09
00036093066	54768.001	0.319	0.8396	0.67±0.20	1.70±0.25	1.23±0.08	1.02±0.09	0.93±0.09
00036093067	54775.354	0.596	0.8440	0.53±0.10	1.56±0.16	2.13±0.09	1.87±0.11	1.70±0.12
00036093068	54781.103	0.813	0.8475	0.97±0.54	1.48±0.49	0.82±0.09	0.62±0.10	0.63±0.10
00036093070	54803.015	0.64	0.8606	1.03±0.51	2.39±0.66	0.95±0.25	0.55±0.09	0.63±0.11
00036093071	54810.106	0.908	0.8649	0.28±0.24	0.97±0.32	1.02±0.11	0.96±0.14	0.90±0.14
00036093072	54812.105	0.983	0.8661	0.31±0.30	1.06±0.39	1.20±0.11	1.12±0.19	1.04±0.19
00036093073	54817.725	0.195	0.8695	0.55±0.11	1.31±0.13	1.11±0.04	0.99±0.05	0.93±0.05
00036093074	54827.240	0.555	0.8752	0.73±0.22	2.15±0.35	0.72±0.06	0.54±0.06	0.47±0.06
00036093075	55119.061	0.568	0.0502	0.60±0.11	1.71±0.18	1.19±0.05	1.02±0.06	0.89±0.06
00036093076	55120.328	0.616	0.0510	0.69±0.13	1.92±0.18	1.11±0.05	0.89±0.05	0.78±0.05
00036093078	55122.340	0.692	0.0522	0.54±0.26	1.40±0.32	0.72±0.06	0.62±0.07	0.58±0.07
00036093080	55124.347	0.768	0.0534	0.63±0.22	1.74±0.30	0.73±0.06	0.61±0.06	0.53±0.07
00036093081	55130.303	0.993	0.0570	0.80±0.30	1.46±0.32	1.45±0.12	1.21±0.13	1.12±0.15
00036093082	55137.050	0.247	0.0610	0.91±0.41	1.74±0.40	1.40±0.13	1.06±0.10	0.95±0.12
00036093083	55144.008	0.51	0.0652	0.42±0.20	1.04±0.24	2.36±0.17	2.19±0.20	2.03±0.20
00036093084	55146.349	0.598	0.0666	0.63±0.14	1.63±0.17	1.93±0.09	1.65±0.10	1.53±0.11
00036093086	55148.304	0.672	0.0678	0.39±0.13	1.61±0.21	0.83±0.05	0.76±0.07	0.65±0.05
00036093087	55149.305	0.71	0.0684	0.32±0.14	1.24±0.22	0.67±0.05	0.62±0.06	0.55±0.06
00036093088	55150.311	0.748	0.0690	0.51±0.12	1.70±0.19	0.88±0.05	0.76±0.05	0.68±0.07
00036093090	55158.192	0.045	0.0737	0.35±0.23	1.00±0.30	1.09±0.11	1.01±0.13	0.95±0.14
00036093091	55164.089	0.268	0.0772	0.78±0.32	1.80±0.37	0.69±0.07	0.53±0.06	0.49±0.06
00036093092	55172.870	0.599	0.0825	0.22±0.15	1.16±0.24	1.07±0.10	1.02±0.10	0.93±0.11
00036093093	55179.505	0.85	0.0865	0.51±0.31	1.18±0.31	0.85±0.07	0.76±0.08	0.72±0.09
00036093095	55193.200	0.366	0.0947	0.64±0.28	1.42±0.32	1.20±0.09	1.03±0.12	0.99±0.11
00036093096	55200.826	0.654	0.0993	0.38±0.20	1.60±0.37	0.59±0.07	0.52±0.08	0.44±0.09

TABLE 6.5: Continued.

00036093100	55476.344	0.053	0.2645	1.14±0.49	1.48±0.46	0.88±0.09	0.68±0.09	0.68±0.09
00036093101	55481.302	0.24	0.2675	0.73±0.23	1.40±0.24	1.54±0.08	1.32±0.10	1.29±0.10
00036093103	55483.387	0.319	0.2688	0.40±0.10	1.39±0.15	1.55±0.07	1.42±0.08	1.36±0.09
00036093104	55484.390	0.356	0.2694	0.66±0.13	1.47±0.16	2.14±0.08	1.85±0.10	1.77±0.09
00036093105	55485.273	0.39	0.2699	0.54±0.12	1.28±0.15	1.88±0.08	1.69±0.09	1.68±0.10
00036093106	55486.341	0.43	0.2705	0.85±0.12	1.80±0.15	2.15±0.08	1.72±0.08	1.74±0.08
00036093107	55491.754	0.634	0.2738	0.57±0.13	1.52±0.18	2.20±0.10	1.92±0.12	1.96±0.13
00036093109	55505.522	0.154	0.2820	0.36±0.33	1.04±0.59	0.80±0.11	0.67±0.12	0.68±0.12
00036093110	55512.412	0.414	0.2862	0.77±0.29	1.44±0.30	1.21±0.08	1.02±0.09	1.02±0.09
00036093111	55518.699	0.651	0.29	0.54±0.13	1.51±0.17	2.09±0.11	1.84±0.10	1.80±0.12
00036093112	55528.204	0.01	0.2957	0.70±0.33	0.55±0.45	0.40±0.06	0.38±0.07	0.38±0.07
00036093113	55540.198	0.463	0.3028	0.58±0.18	1.67±0.26	1.85±0.13	1.57±0.16	1.57±0.17
00036093114	55547.554	0.74	0.3073	1.01±0.25	2.06±0.28	3.68±0.29	2.61±0.19	2.61±0.21
00036093116	55561.059	0.25	0.3154	0.38±0.18	1.17±0.24	1.28±0.10	1.19±0.11	1.13±0.12
00036093117	55568.892	0.546	0.3201	0.65±0.15	1.57±0.19	2.19±0.11	1.87±0.13	1.86±0.12
00036093118	55575.177	0.783	0.3238	0.84±0.15	1.68±0.16	3.05±0.12	2.47±0.14	2.51±0.14
00036093120	55589.111	0.309	0.3322	0.84±0.34	1.77±0.38	1.18±0.10	0.91±0.11	0.90±0.11
00036093121	55835.822	0.62	0.4802	1.01±0.27	1.65±0.26	2.38±0.13	1.86±0.13	1.82±0.12
00036093122	55842.647	0.878	0.4843	0.87±0.28	1.76±0.32	1.70±0.14	1.33±0.12	1.35±0.14
00036093124	55856.576	0.403	0.4926	0.49±0.27	1.64±0.43	0.54±0.06	0.46±0.08	0.46±0.08
00036093126	55870.207	0.918	0.5008	0.76±0.24	1.53±0.26	1.58±0.10	1.31±0.12	1.26±0.12
00036093127	55877.820	0.205	0.5054	0.87±0.29	2.13±0.34	1.16±0.12	0.83±0.08	0.82±0.09
00036093128	55884.247	0.448	0.5092	0.02±0.02	1.01±0.43	0.69±0.10	0.67±0.12	0.62±0.09
00036093129	55891.257	0.712	0.5134	0.84±0.18	1.57±0.20	3.01±0.15	2.48±0.18	2.54±0.20
00036093130	55897.353	0.942	0.5171	0.67±0.15	1.70±0.20	2.01±0.10	1.68±0.12	1.72±0.13
00036093131	55907.394	0.321	0.5231	0.89±0.26	1.64±0.27	2.08±0.13	1.66±0.14	1.66±0.15
00036093135	55914.151	0.576	0.5272	0.84±0.24	1.86±0.28	0.93±0.06	0.71±0.06	0.71±0.06
00036093136	55915.150	0.614	0.5278	0.72±0.15	1.92±0.21	1.01±0.05	0.81±0.05	0.81±0.06
00036093137	55917.149	0.689	0.5290	0.77±0.13	1.67±0.17	1.53±0.06	1.27±0.08	1.25±0.08
00036093138	55918.150	0.727	0.5296	0.77±0.13	1.72±0.16	1.70±0.06	1.40±0.07	1.39±0.08
00036093139	55919.094	0.763	0.5301	0.76±0.12	1.68±0.15	2.01±0.08	1.67±0.09	1.68±0.09
00036093140	55920.156	0.803	0.5308	0.21±0.20	0.81±0.80	0.64±0.14	0.56±0.16	0.56±0.16
00036093143	55923.111	0.914	0.5326	0.74±0.17	1.76±0.22	1.00±0.05	0.81±0.06	0.81±0.06
00036093146	55926.098	0.027	0.5343	0.86±0.21	1.76±0.24	1.09±0.06	0.87±0.07	0.87±0.07
00036093148	55937.271	0.449	0.5410	0.44±0.21	1.51±0.28	0.99±0.08	0.88±0.09	0.88±0.11
00036093149	55940.133	0.557	0.5428	0.90±0.27	1.85±0.30	1.13±0.09	0.86±0.07	0.89±0.09
00036093150	55941.076	0.592	0.5433	0.92±0.21	2.08±0.26	1.01±0.07	0.74±0.05	0.76±0.06
00036093151	55942.082	0.63	0.5439	0.78±0.20	1.43±0.20	1.66±0.08	1.41±0.09	1.37±0.09
00036093153	55944.086	0.706	0.5451	0.62±0.15	1.28±0.17	1.92±0.09	1.71±0.11	1.78±0.13
00036093154	55946.087	0.782	0.5463	1.16±0.25	1.79±0.22	1.68±0.10	1.26±0.08	1.25±0.07
00036093155	55947.153	0.822	0.5470	0.50±0.33	0.92±0.32	1.49±0.13	1.36±0.16	1.36±0.16
00036093156	55954.257	0.09	0.5512	1.03±0.27	2.02±0.30	1.03±0.09	0.74±0.06	0.74±0.06
00036093157	56206.594	0.613	0.7026	0.42±0.25	2.20±0.51	0.35±0.05	0.28±0.05	0.27±0.06
00036093159	56219.105	0.086	0.7101	0.95±0.49	2.52±0.68	1.23±0.36	0.67±0.11	0.68±0.14
00036093160	56227.665	0.409	0.7152	0.33±0.23	1.73±0.60	0.87±0.13	0.69±0.15	0.66±0.13
00036093161	56234.475	0.666	0.7193	0.66±0.20	2.06±0.32	0.88±0.07	0.69±0.07	0.65±0.06
00036093163	56248.149	0.182	0.7275	1.04±0.34	1.91±0.34	1.57±0.15	1.13±0.11	1.14±0.12
00036093164	56255.424	0.456	0.7319	0.59±0.18	1.26±0.21	2.52±0.12	2.25±0.17	2.24±0.17
00036093165	56262.107	0.709	0.7359	0.21±0.20	1.08±0.41	0.71±0.10	0.66±0.12	0.63±0.11
00036093166	56269.277	0.979	0.7402	0.75±0.18	1.64±0.24	1.94±0.11	1.61±0.12	1.61±0.13
00036093168	56270.203	0.014	0.7408	0.61±0.17	1.63±0.24	1.48±0.08	1.26±0.10	1.19±0.10
00036093169	56272.202	0.09	0.7420	0.58±0.21	1.53±0.29	1.09±0.08	0.94±0.10	0.97±0.12
00036093170	56273.150	0.125	0.7425	0.69±0.25	1.63±0.31	0.83±0.06	0.69±0.07	0.63±0.06
00036093171	56275.147	0.201	0.7437	0.53±0.20	1.38±0.27	0.94±0.06	0.83±0.08	0.81±0.09
00036093172	56276.208	0.241	0.7444	0.49±0.24	1.24±0.26	1.17±0.08	1.06±0.09	1.05±0.09
00036093173	56278.143	0.314	0.7455	0.61±0.18	1.69±0.24	1.16±0.07	0.98±0.08	0.95±0.08
00036093174	56279.153	0.352	0.7461	1.00±0.25	2.17±0.29	1.03±0.09	0.71±0.06	0.70±0.05
00036093175	56283.088	0.5	0.7485	0.96±0.23	2.23±0.27	1.72±0.12	1.20±0.08	1.18±0.08
00036093176	56290.360	0.775	0.7529	0.77±0.23	1.58±0.26	1.17±0.07	0.97±0.09	1.02±0.11
00036093178	56304.130	0.295	0.7611	0.60±0.14	1.62±0.19	2.08±0.11	1.79±0.11	1.73±0.12
00036093180	56320.163	0.9	0.7707	0.63±0.14	1.64±0.18	1.86±0.09	1.58±0.11	1.62±0.12
00036093181	56584.674	0.883	0.9294	0.82±0.42	1.30±0.42	0.74±0.08	0.67±0.11	0.68±0.12
00036093183	56598.885	0.419	0.9379	0.66±0.23	1.70±0.29	1.36±0.10	1.13±0.11	1.17±0.13
00036093184	56605.621	0.673	0.9420	0.82±0.26	1.91±0.32	1.74±0.14	1.33±0.12	1.31±0.14
00036093186	56619.157	0.184	0.9501	0.38±0.19	1.34±0.29	0.64±0.06	0.58±0.07	0.58±0.08
00036093187	56620.220	0.224	0.9507	0.29±0.28	0.74±0.40	0.77±0.11	0.73±0.13	0.72±0.14
00036093188	56621.220	0.262	0.9513	0.97±0.35	1.55±0.32	1.10±0.07	0.86±0.07	0.85±0.08
00036093189	56622.225	0.3	0.9519	0.72±0.23	1.78±0.27	1.27±0.09	1.03±0.09	1.01±0.09
00036093190	56623.222	0.338	0.9525	0.61±0.18	1.42±0.22	1.45±0.09	1.28±0.12	1.27±0.11
00036093191	56624.226	0.376	0.9531	0.55±0.17	1.38±0.20	1.86±0.11	1.65±0.13	1.64±0.13
00036093192	56625.225	0.413	0.9537	0.48±0.19	1.60±0.29	0.85±0.07	0.74±0.08	0.71±0.07
00036093193	56626.228	0.451	0.9543	0.38±0.15	1.27±0.21	1.30±0.09	1.20±0.09	1.13±0.10
00036093194	56627.232	0.489	0.9549	0.62±0.16	1.58±0.20	1.52±0.08	1.31±0.09	1.25±0.09
00036093195	56633.325	0.719	0.9586	0.01±0.00	1.45±0.32	0.88±0.20	0.74±0.27	0.77±0.12
00036093197	56640.865	0.004	0.9631	0.48±0.25	1.46±0.36	0.96±0.11	0.84±0.13	0.82±0.12
00036093198	56647.924	0.27	0.9674	0.50±0.21	1.46±0.29	0.98±0.07	0.86±0.09	0.87±0.11
00036093199	56654.723	0.527	0.9714	0.86±0.26	1.60±0.26	2.44±0.16	1.97±0.17	1.95±0.18
00036093200	56661.394	0.778	0.9754	0.16±0.15	0.67±0.48	1.06±0.18	0.99±0.17	0.99±0.17
00036093201	56668.733	0.055	0.9798	0.73±0.32	1.16±0.30	1.27±0.10	1.12±0.13	1.12±0.13
00036093202	56675.328	0.304	0.9838	1.24±0.45	2.13±0.41	1.33±0.21	0.84±0.07	0.81±0.07
00036093203	56934.372	0.081	0.1392	0.41±0.38	1.11±0.43	0.93±0.10	0.83±0.14	0.83±0.12
00036093207	56950.302	0.682	0.1487	0.45±0.21	1.99±0.38	0.48±0.05	0.41±0.06	0.38±0.06
00036093210	56952.360	0.76	0.1500	0.88±0.48	2.00±0.51	0.91±0.14	0.62±0.08	0.62±0.08
00036093211	56953.291	0.795	0.1505	0.78±0.37	1.72±0.38	0.82±0.08	0.65±0.08	0.65±0.08
00036093214	56969.268	0.398	0.1601	0.47±0.18	1.24±0.21	2.19±0.14	1.99±0.16	1.94±0.18
00036093215	56975.210	0.622	0.1637	0.64±0.16	1.33±0.18	2.77±0.13	2.45±0.15	2.40±0.15
00036093216	56976.270	0.662	0.1643	0.82±0.22	1.66±0.24	2.14±0.11	1.74±0.12	1.78±0.14
00036093217	56983.251	0.926	0.1685	1.56±0.75	2.08±0.58	0.91±0.22	0.50±0.06	0.51±0.06

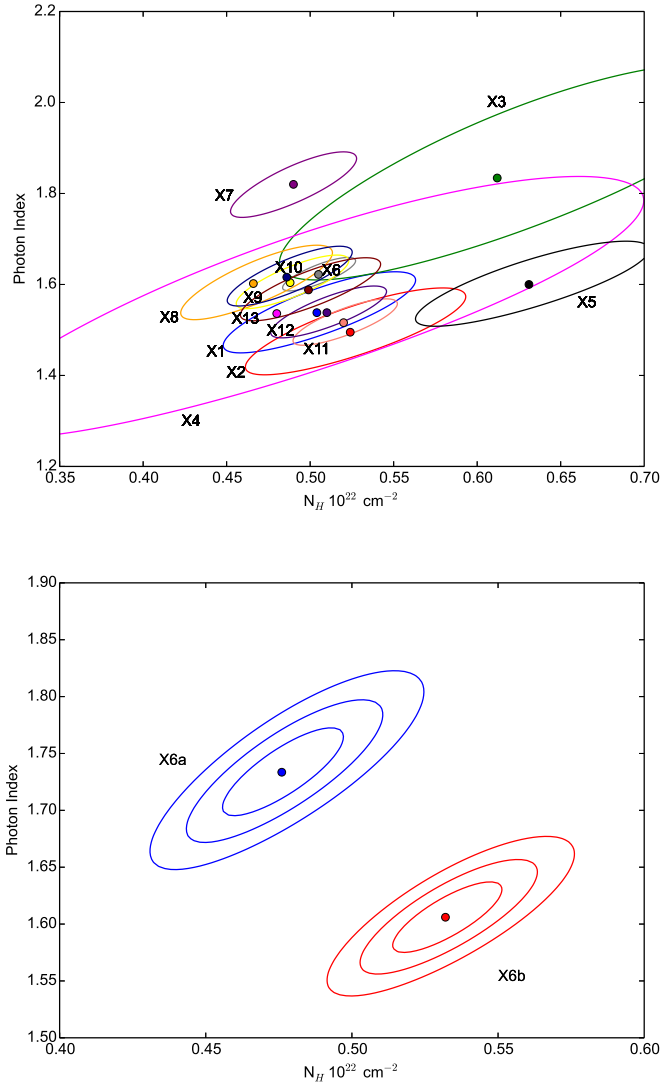

FIGURE 6.10: (top:) The distribution of column density, N_H, and photon index, Γ, of the LS I +61° 303 for *XMM*-Newton observations (3σ contours only). (right:) The grid of hydrogen column density and photon index of the splitted X6 observations (1,2,3 confidence contours).

TABLE 6.6: The log of *Chandra* data of LS I +61° 303.

Data	ObsID	Ref	MJD d	Instr.	Exp.time ks	ϕ	Φ
07-04-2006	6585	C1	53832.922	ACIS-I	49.73	0.027	0.2787
25-10-2006	8273	C2	54033.925	ACIS-I	20.03	0.613	0.3993
14-11-2008	10052	C3	54784.460	ACIS-S	95.67	0.940	0.8495

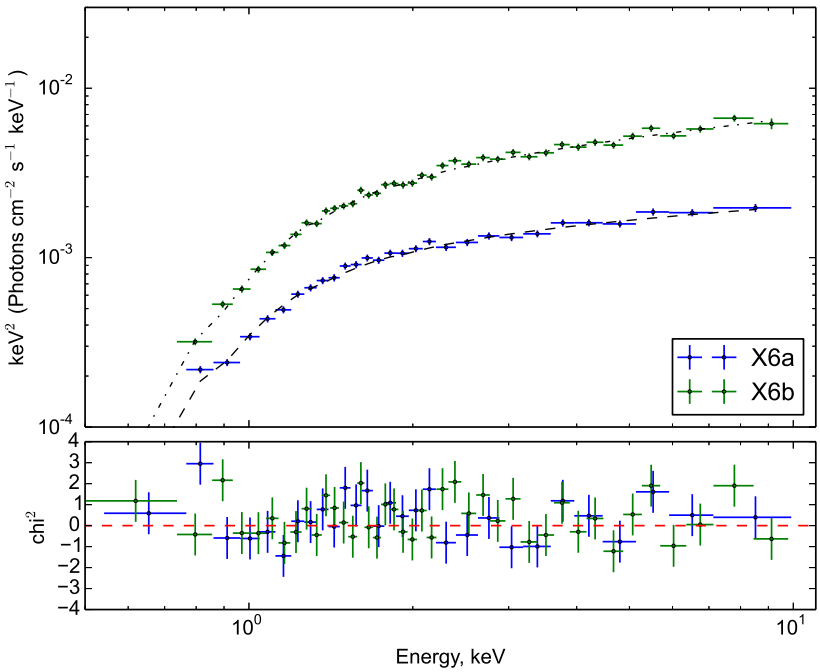

FIGURE 6.11: The X6a and X6b spectra of LS I +61° 303 fitted by absorbed power law model.

TABLE 6.7: The best fit parameters of *Chandra* data of LS I +61° 303.

Ref	N_H 10^{22} cm^{-2}	Γ 10^{-11} erg/cm^2/s	F(1-10 keV)	χ^2/(d.o.f.)
C1	0.59±0.03	1.16±0.03	0.58±0.02	1.21/(173)
C2	0.63±0.02	1.59±0.02	2.23±0.03	0.99/(333)
C3	0.64±0.01	1.80±0.01	0.81±0.01	1.11/(387)

Chapter 7

Interpretation of results of LS I +61° 303

In this chapter, I present results of X-ray monitoring of LS I +61° 303 to explore the orbital and superorbital variability of different physical parameters of the binary system. I show the distribution of absorbed flux, photon index and column density over the orbital and superorbital timescales. In addition, I search the fast variability of lightcurves of LS I +61° 303. The distribution of N_H over orbital phase was used to predict the physical conditions of Be-type star disk of the source. In this chapter, I report an investigation based on the analysis of the monitoring of the LS I +61° 303, mainly with *Swift* and other X-ray data discussed in Chapter 6.

7.1 The modulation of X-ray flare

A study of the orbital modulation of the X-ray signal was missing until intensive monitoring of the source on many orbit (year) timescales by X-ray observatories. A multi-year monitoring campaign was performed by *Swift*. As a result, the orbit-to-orbit variations of X-ray emission from the source were established. The orbital X-ray light curve of the source is characterized by a single flare, whose origin is not well understood. [92] shows that the orbital phase of the periodic X-ray flare drifts on a superorbital timescale by half an orbit from $\phi \simeq 0.5$ to $\phi \simeq 1.0$. Such a drift can not be explained by simple precession, where one expects a drift during a full orbit (from 0 to 1). But such a drift might be explained by the possibility that the equatorial disk of Be-type star in the system can be build up and can decay on the superorbital timescale [92]. A new insight about the nature of superorbital periodicity/variability might be given by the investigation of the changes in the behavior of the X-ray emission during this timescale.

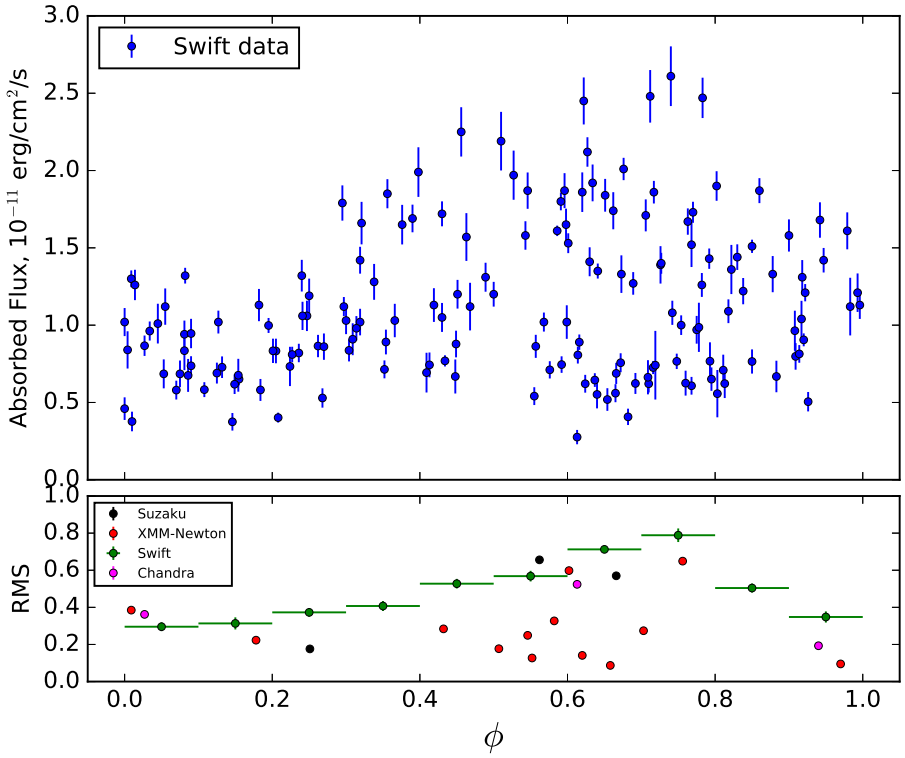

FIGURE 7.1: (top:) The distribution of absorbed flux over orbital phase. (bottom:) The distribution of RMS values of lightcurves obtained for separate *XMM*-Newton, *Suzaku*, *Swift* and *Chandra* observations.

The analysis of X-ray data was performed in Chapter 6. First of all, I use *Swift* data to image the distribution of absorbed flux over orbital phase. Fig. 7.1 shows the 1.0 - 10.0 keV flux from the LS I +61° 303 as a function of the orbital phase. It is readily seen that the scattering of the flux is minimal at periastron and maximal at apastron. This is probably linked to the change of the compact object environment as it moves along the orbit. Close to periastron the compact object is embedded into the smooth dense region of the Be star disk, while closer to the apastron the compact object moves in the outskirts of the disk, where one can expect to find more clumpy structure, which would lead to the higher variability of the flux. Then, I grouped the *Swift* observations within 0.1 orbital phase band, and found the RMS for their grouped lightcurves (green points with error bars in bottom panel in Fig. 7.1). Additionally, I added RMS values which were calculated as described in previous Chapter for separate lightcurves made by *XMM*-Newton and *Suzaku* to check inhomogeneity of the environment along the orbit. From Fig. 7.1, it is seen that the RMS datapoints are consistent with the distributed absorbed flux over orbital phase.

Secondly, I checked the variability of flux, photon index and absorption of LS I +61° 303 over orbital and superorbital phases for grouped *Swift* data. I split all

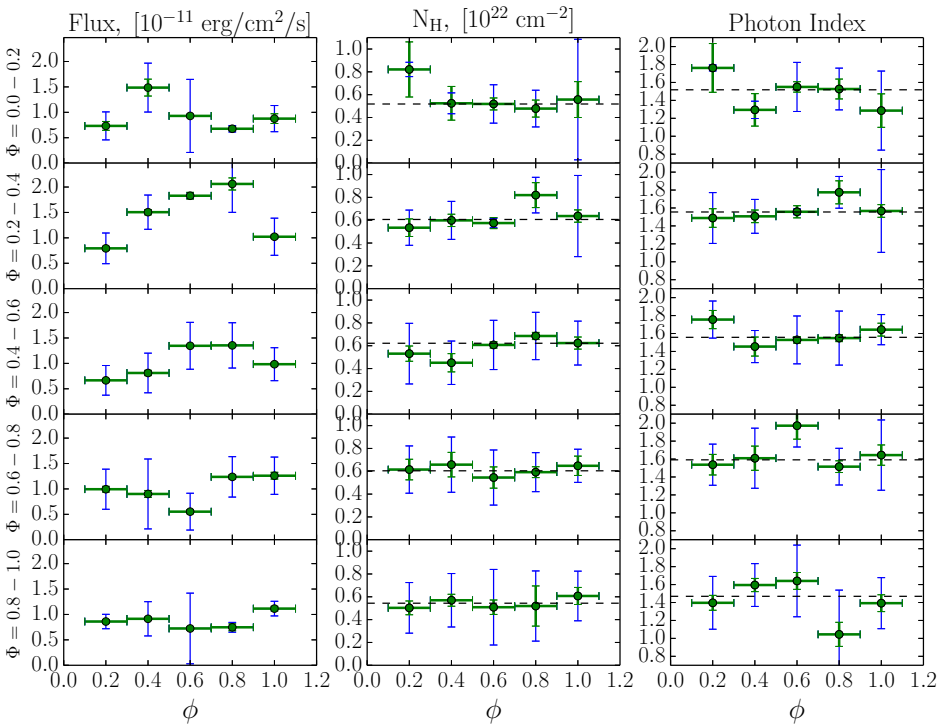

FIGURE 7.2: The *Swift* distribution of flux, photon index, Γ, and absorption, N_H, of LS I +61° 303 over orbital and superorbital phases. The green errorbars correspond the errors estimated using Monte Carlo simulations as described in Subsec. 2.7.2, while the blue errorbars correspond errors estimated from RMS function.

observations within 0.2 range of orbital/superorbital phases and found the values of flux, photon index and column density using Monte Carlo simulations as described in Sec. 2.7. The best-fit parameters of grouped spectra are presented in Tab. 7.1. Note that each point in Fig. 7.2 is a combination of several closely spaced observations. Green error bars correspond to the 1σ errors of the spectral fit. Blue error bars were calculated taking into account the spread of spectral parameters of the individual observations, i.e., the root-mean-square function for each light curve. To calculate it I have used the following definition of $RMS = \sqrt{\frac{\sum(f_i - \langle f \rangle)^2}{N}}$, where N is the full number of time bins in the light curve, and $\langle f \rangle = \Sigma(f_i \delta f_i^{-2})/\Sigma(\delta f_i^{-2})$ is the weighted mean of the flux with the error of δf_i for each time bin t_i with a flux f_i.

One can see that in agreement with previous findings [97, 247] the flux is maximal during the 0.2-0.4 superorbital phase, with a peak becoming wider and moving from orbital phase $\phi \sim 0.4$ at superorbital phase $\Phi = 0.$ – 0.2 to orbital phase $\phi \sim 0.8$ at superorbital phase $\Phi = 0.4$ – 0.6. During the superorbital phases $\Phi = 0.6$ – 0.0 the peak disappears, or become too narrow to be detected with such wide bins. On the contrary, the values of column density and photon index are consistent with a constant value, the same for all orbital and superorbital phases (the averaged value of column density is

TABLE 7.1: The results of modeling of combined *Swift* spectra of LS I +61° 303 over orbital, ϕ, and superorbital, Φ, phases.

ϕ	Φ	F(1-10 keV) 10^{-11} erg/cm^2/s	N_H 10^{22} cm^2	Γ	C-stat
0.9-1.1	0.8-1.0	1.10±0.05	0.57±0.07	1.34±0.09	430.59
0.7-0.9	0.8-1.0	0.76±0.11	0.53±0.16	1.03±0.17	40.85
0.5-0.7	0.8-1.0	0.96±0.05	0.56±0.06	1.61±0.09	443.49
0.3-0.5	0.8-1.0	1.02±0.04	0.58±0.05	1.60±0.07	447.50
0.1-0.3	0.8-1.0	0.86±0.04	0.49±0.06	1.32±0.08	456.51
0.9-1.1	0.6-0.8	1.21±0.10	0.65±0.11	1.64±0.14	278.36
0.7-0.9	0.6-0.8	1.38±0.05	0.60±0.04	1.53±0.06	567.83
0.5-0.7	0.6-0.8	0.72±0.06	0.59±0.10	1.92±0.14	259.80
0.3-0.5	0.6-0.8	1.17±0.07	0.62±0.10	1.57±0.13	302.90
0.1-0.3	0.6-0.8	1.08±0.06	0.59±0.09	1.50±0.11	308.01
0.9-1.1	0.4-0.6	1.05±0.04	0.64±0.05	1.63±0.07	496.82
0.7-0.9	0.4-0.6	1.47±0.04	0.69±0.03	1.54±0.04	779.84
0.5-0.7	0.4-0.6	1.48±0.03	0.60±0.03	1.50±0.04	751.13
0.3-0.5	0.4-0.6	0.97±0.05	0.45±0.07	1.37±0.11	370.88
0.1-0.3	0.4-0.6	0.81±0.04	0.57±0.06	1.73±0.10	363.72
0.9-1.1	0.2-0.4	1.07±0.03	0.67±0.06	1.53±0.07	585.57
0.7-0.9	0.2-0.4	2.18±0.10	0.83±0.11	1.78±0.13	300.87
0.5-0.7	0.2-0.4	1.83±0.09	0.57±0.05	1.55±0.07	496.80
0.3-0.5	0.2-0.4	1.54±0.06	0.62±0.05	1.50±0.07	524.51
0.1-0.3	0.2-0.4	0.87±0.04	0.55±0.07	1.48±0.10	361.02
0.9-1.1	0.0-0.2	0.89±0.10	0.61±0.16	1.28±0.18	203.16
0.7-0.9	0.0-0.2	0.68±0.04	0.46±0.07	1.49±0.11	350.51
0.5-0.7	0.0-0.2	1.22±0.02	0.55±0.04	1.55±0.06	584.85
0.3-0.5	0.0-0.2	1.51±0.13	0.61±0.14	1.36±0.17	243.86
0.1-0.3	0.0-0.2	0.79±0.07	0.79±0.23	1.71±0.28	136.53

equal to $\langle N_H \rangle = 0.55 \pm 0.01$, RMS = 0.24; the averaged value of spectral index is equal to $\langle \Gamma \rangle = 1.54 \pm 0.02$, RMS = 0.32). The evolution of the source X-ray flux with the orbital phase shows X-ray emission along all the phases, although with a difference of a factor 3 in the flux level between two states, with a "high" state preferentially found in the phase range 0.4 – 1.0.

7.2 The variability of LS I +61° 303 lightcurve

I tried to find the fast variability of the system that was previously suggested by [223], similar to PSR B1259−63 (see Chapter 5). I used *Swift* data to search the fast variability in LS I +61° 303 lightcurve. These data provide the lightcurve coverage in about 10-30 ks time bins, separated by $\sim$ 0.1 d time intervals. The result of this search is shown in Fig. 7.3. This figure shows that the variability of the source starts to be significant above $\tau \approx 1.5$ days, where the false alarm probability curve crosses

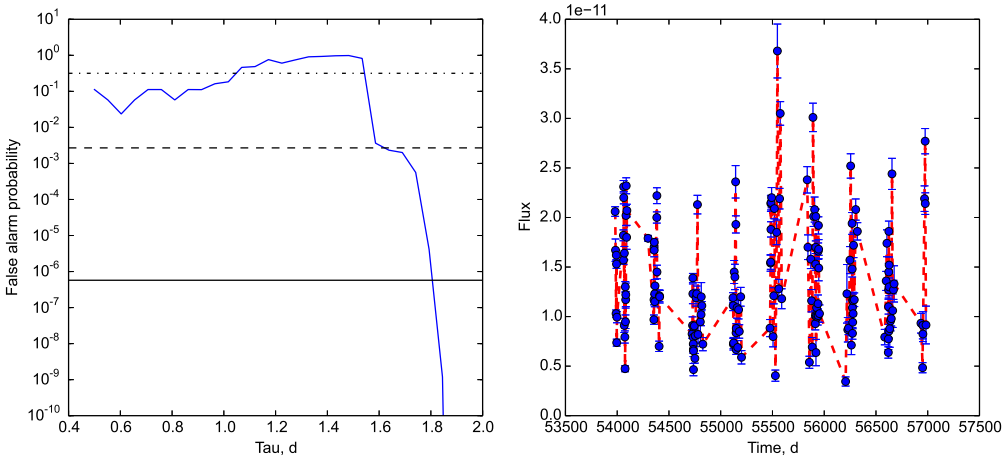

FIGURE 7.3: (left:) The probability of the variability in the LS I +61° 303 lightcurve from the *Swift*. The 1, 3 and 5 σ confidence levels are plotted with the dot-dashed, dashed and solid black lines correspondingly. (right:) The lightcurve of LS I +61° 303 over the 4 observational years period in the 1.0 – 10.0 keV band, shown together with its averaged version.

the 3σ significance limit. Thus, my analysis doesn't reveal any statistically significant variability on shorter then a day timescale.

7.3 The variability of hydrogen column density of LS I +61° 303

The physical properties of the disk can play a crucial role in the understanding of the mechanisms of keV-TeV photons production. The gradual build-up and decay of the disk can lead to the significantly different physical conditions of LS I +61° 303 at the same orbital phase.

The distribution of hydrogen column density (N_H) in LS I +61° 303 observed by *XMM*-Newton, *Chandra* and *Suzaku* is shown in Fig. 7.4. The fit to the constant function gives a value of $N_H = 0.48 \times 10^{22}\mathrm{cm}^{-2}$ with a $\chi^2 = 458.6$ for 18 degrees of freedom, which means that this hypothesis can be rejected at the 19.6σ level. Within the simplest model, the observed value of column density at each orbital/superorbital phase is given by the integration of the smooth Be-type star disk density profile along the line of sight to the observer. The presence of clumps in the wind and/or the regions with highly or partially ionized hydrogen can, however, significantly modify the predictions for the observed values of column density. In order to describe the available set of the data, the model previously used by [248] was adopted. In this model the neutral hydrogen disk

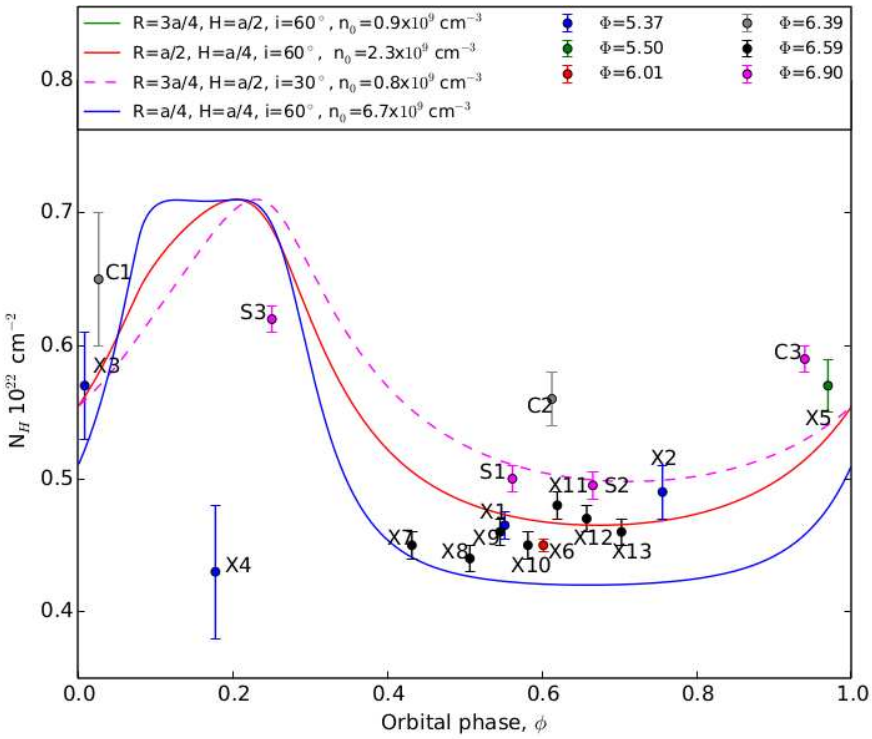

FIGURE 7.4: The points correspond to *Chandra*, *XMM*-Newton and *Suzaku* measurements of N_H at different orbital/superorbital phases. Lines illustrate the column density behaviour predicted by the Eq. (7.1) for different size of the disk.

has an exponential density profile characteristic of an isothermal atmosphere

$$n_D = n_0 \exp(-r/r_D - h/h_D). \tag{7.1}$$

In such a simple case one can expect to see a maximum of the column density when the compact object of the LS I +61° 303 crosses the periastron if an observer looks at the system in the direction perpendicular to the disk, or when the compact object passes the superior conjunction, if an observer is located in the orbital plane. Fig. 7.4 shows the orbital evolution of column density of LS I +61° 303 for different parameters of the disk. The contribution of the galactic N_H to the total N_H value was chosen to be equal to $N_{Hgal} = 0.42 \times 10^{22}$ cm^{-2}. The solid lines correspond to the case of inclination $i = 60°$, and the dashed one to the case of $i = 30°$. As expected the orbital position of the maximum column density shifts toward the phase of periastron, $\phi = 0.275$ with the decrease of the inclination of the observer.

Despite the quite extensive observations of the source during the last few years the available data are not sufficient to answer the question about N_H orbital variability. Indeed, only *XMM*-Newton and *Chandra* observations are able to provide us with the good values of N_H, and these observations cover only small parts of the orbit at any given superorbital phase. The combination of the data from substantially different

superorbital phases would be misleading, as the disk density/size can vary drastically due to described above continuous build-up/decay processes, which can blur the N_H variability even if it is present at every superorbital phase. Unfortunately, the current data does not allow us to distinguish between these hypotheses as well as to check if N_H is following a regular profile, expected in the case of a disk with steady (or slowly varying on superorbital time scale) profile. The X-ray observations along one orbit are thus crucial for the understanding of the properties of Be-type star disk and the physical mechanisms operating in this system.

Chapter 8

Conclusions and future prospects

In this thesis, I have reported the results of X-ray and Gamma-ray observations of PSR B1259−63 during its 2010 and 2014 periastron passages, as well as X-ray observations of LS I +61° 303. In my work, I have obtained the following results:

1. Detailed analysis of X-ray observations of several PSR B1259−63 periastron passages, demonstrated the stability of the source orbital light curve over long-year timescales. This allowed me to use old and new data simultaneously in the analysis of the orbital light curve;

2. I used the inverse-Compton scattering and synchrotron radiation mechanisms to model the X-ray double-peaked lightcurve of PSR B1259−63 and demonstrated that the inverse-Compton radiation of the relativistic electrons explains the data reasonably well before the GeV flare;

3. The GeV flare of PSR B1259−63, that was discovered in 2010 and confirmed in 2014 by *Fermi*/LAT, gives evidence of an additional component present during the time of the GeV flare. The perturbation of the equatorial disk leads to a situation when the pulsar is surrounded by the clumps and releases all its power inside the system. Synchrotron cooling of the injected electrons provides additional X-rays, and corrects the developed model to fit the data during the GeV flare as well;

4. I obtained the daily variability of PSR B1259−63 and LS I +61° 303. In the case of PSR B1259−63, the variability of the source starts to be significant above $\tau \approx 4$ days, corresponding to rise/decay time scales of the main flares in the light curve. Thus, my analysis disfavours the daily variability of PSR B1259−63, suggesting

that its light curve is rather smooth. In the case of LS I +61° 303, the variability of the source starts to be significant above $\tau \approx 1.5$ days, and I don't confirm variability on the seconds-timescale previously reported by, e.g., [101];

5. In my thesis, I present the previously unpublished *Suzaku* spectra of LS I +61° 303. These data presents evidence of the variability of column density of LS I +61° 303 over orbital/superorbital phases. It is significant to note that the N_H variability versus orbital phase of LS I +61° 303 was never presented before. Systematic analysis of all available X-ray data allow to propose that the the column density has a two-peak structure along the orbit with peaks during periastron and superior conjunction passages. Unfortunately, the observations of the superior conjunction and the periastron passage have never been performed during the same orbital/superorbital phases, so that future observations are needed to test this hypothesis.

It is significant to note that during my PhD I analyzed in total 260 X-ray observations and 8 years GeV observations for PSR B1259−63 and LS I +61° 303 (see Fig. 8.1).

In future, I plan to describe the double-peaked lightcurve of PSR B1259−63 with a more detailed model. First of all, I plan to add the influence of the disk of SS 2883 and to model the emission from the relativistic particles from the pulsar wind taking into account the variability of the physical conditions along the shock wave. To research the unpredicted post-periastron GeV flare, an additional optical and TeV observations are required. This information will be hopefully provided with new future multi-wavelength observations of PSR B1259−63.

For a deeper understanding of the variability of N_H over orbital/superorbital phases, we need more X-ray observations. X-ray observations along one orbit are thus crucial for the understanding of the properties of Be-type star disk and the physical mechanisms operating in this system. Thus, my collaborators and I have submitted observational proposals to observe LS I +61° 303 with *XMM*-Newton and *Chandra* facilities.

In future it will be also interesting to compare the $H\alpha$ variability of LS I +61° 303 in detail with the variation in X-rays and γ-rays. It would be interesting to research the discontinuity in the periodicity of the GeV γ-rays emission at periastron, the possible relationship of its disappearance with the variation of the emission around apastron, and finally the possible relationship between GeV and radio emission.

I plan to research in details the multiwavelength properties of other γ-ray loud binary systems. I will also try to find more such systems looking into the correlation

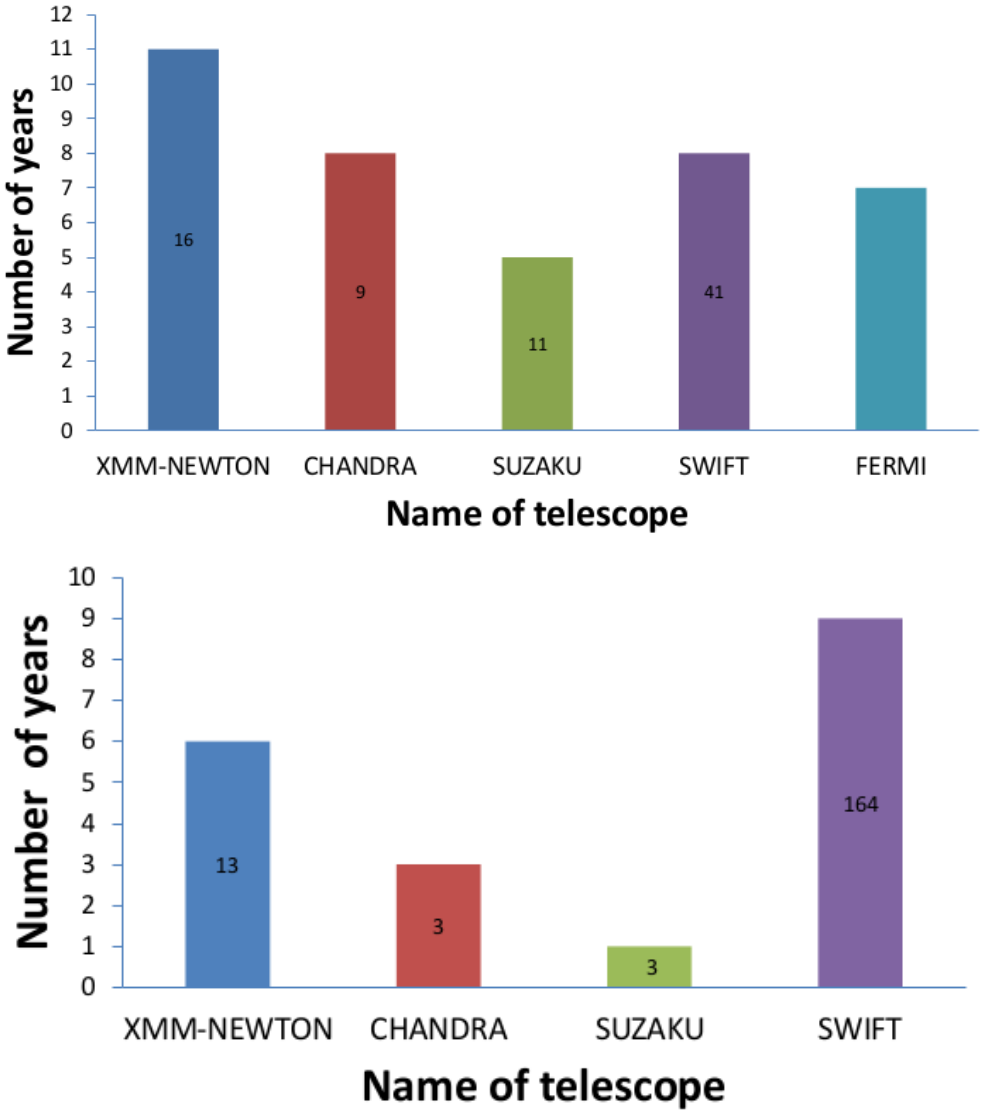

FIGURE 8.1: The graph of all analyzed data in my thesis for PSR B1259−63 (top) and LS I +61° 303 (bottom). The value on bars corresponds to the number of observations.

between the GeV sky and distribution of the O-/Be-type stars.

Coauthor statements

1. M. Chernyakova, A. A. Abdo, A. Neronov, M. V. McSwain, J. Moldon, M. Ribo, J. M. Paredes, I. Sushch, M. de Naurois, U. Schwanke, Y. Uchiyama, K. Wood, S. Johnston, S. Chaty, A. Coleiro, D. Malyshev, and **Iu. Babyk**. Multiwavelength observations of the binary system PSR B1259-63/LS 2883 around the 2010-2011 periastron passage. MNRAS, Vol. 439, PP. 432-445, 2014. During the text of thesis this paper is referred as [**205**].

2. M. Chernyakova, A. Neronov, B. van Soelen, P. Callanan, L. O'Shaughnessy, **Iu. Babyk**, S. Tsygankov, I. Vovk, R. Krivonos, J. A. Tomsick, D. Malyshev, J. Li, K. Wood, D. Torres, S. Zhang, P. Kretschmar, M. V. McSwain, D. Buckley, and C. Koen. Multi-wavelength Observations of the Binary System PSR B1259−63/LS 2883 around the 2014 Periastron Passage. MNRAS, Vol. 454, PP. 1358, 2015. During the text of thesis this paper is referred as [**206**].

3. M. Chernyakova, **Iu. Babyk**, D. Malyshev, I. Vovk, S. Tsygankov, H. Takahashi. Study of orbital and superorbital variability of LS I +61° 303 with X-ray data. (submitted to MNRAS, 2016).

4. N. Chkheidze, **Iu. Babyk**. Nonthermal emission model of isolated X-ray pulsar RX J0420.0-5022. Advances in Astronomy and Space Physics, Vol. 3, PP. 32-37, 2013, [196].

5. N. Chkheidze, **Iu. Babyk**. Synchrotron emission model of gamma-ray pulsar PSR J2021+3651. New Astronomy, Vol. 35, PP. 27-31, 2015, [197].

Appendix A

Monte Carlo simulations of PSR B1259−63 spectra

Here, I present the averaged histograms of unabsorbed flux of PSR B1259−63 and their cumulative distributions of errors for *Swift* (Sw1-41) and *Suzaku* data (Sz1-3) according to calculations performed in Subsec. 2.7.2.

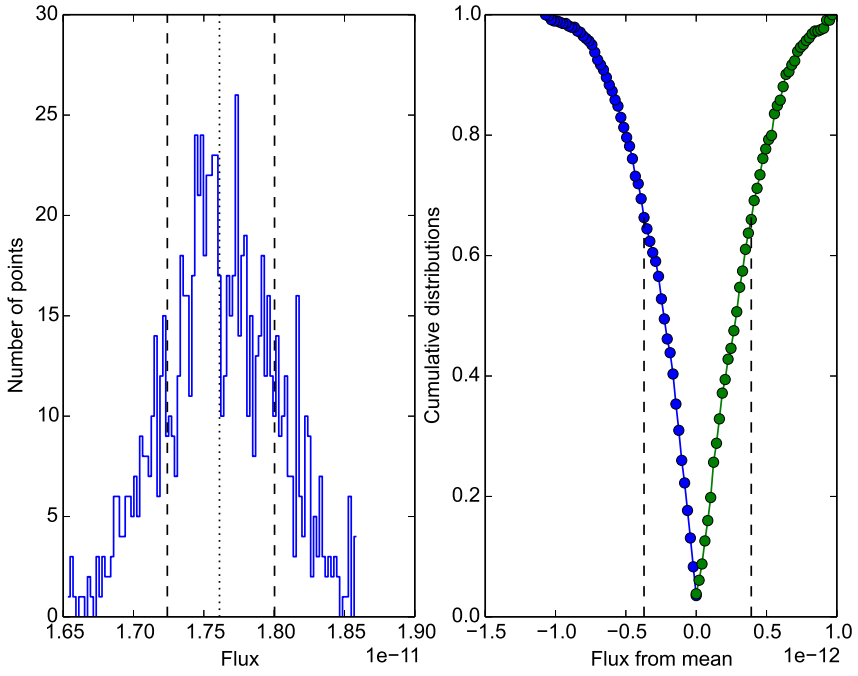

Sw1

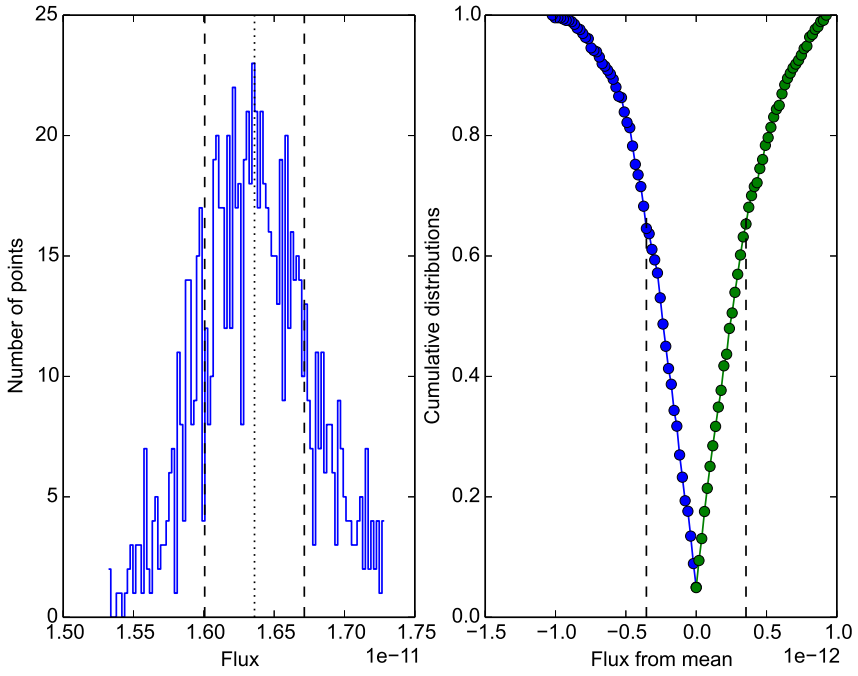
Number of points
Flux
1e−11
Cumulative distributions
Flux from mean
1e−12

Sw2

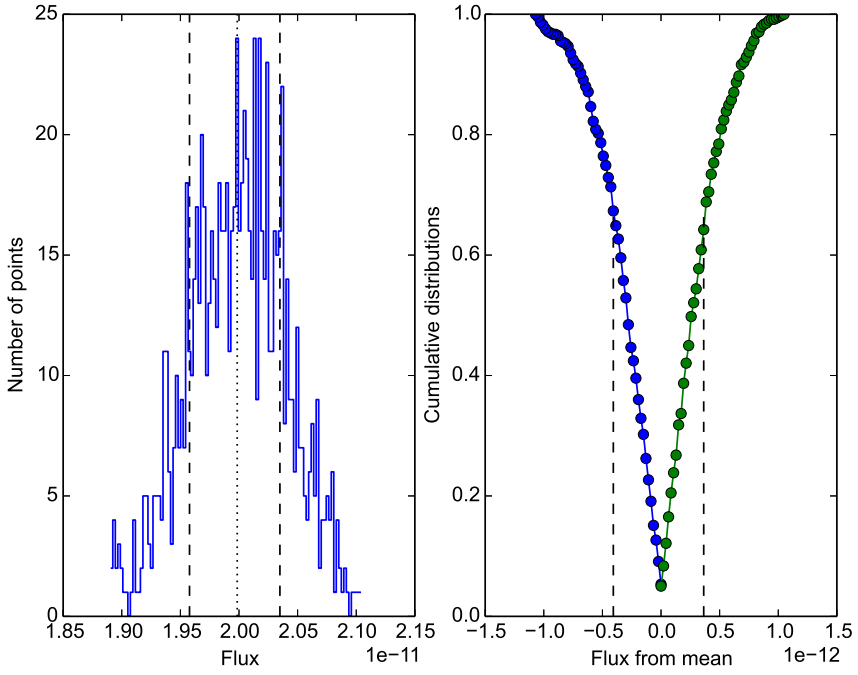
Number of points
Flux
1e−11
Cumulative distributions
Flux from mean
1e−12

Sw3

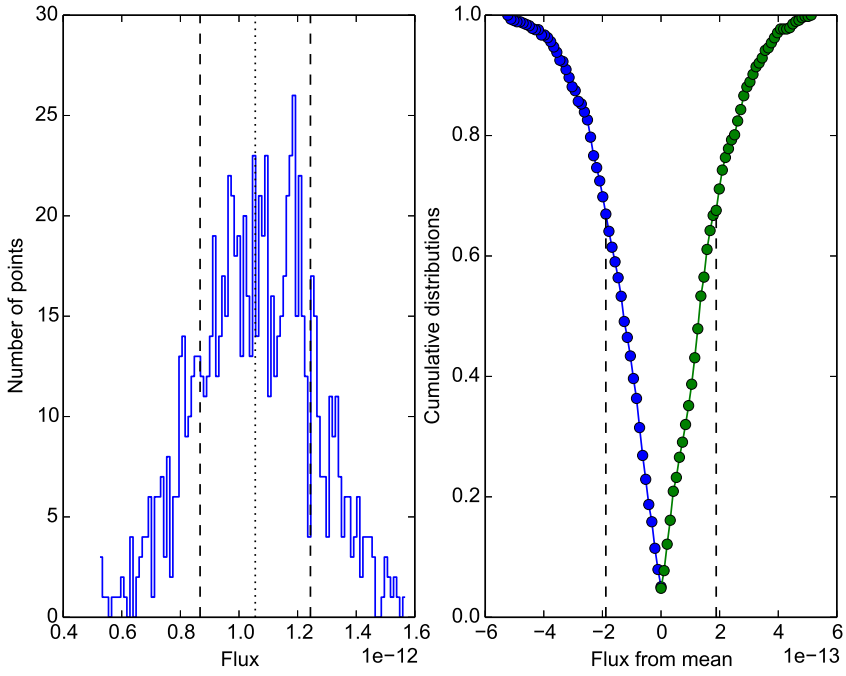
Number of points
Flux
1e−12
Cumulative distributions
Flux from mean
1e−13

Sw4

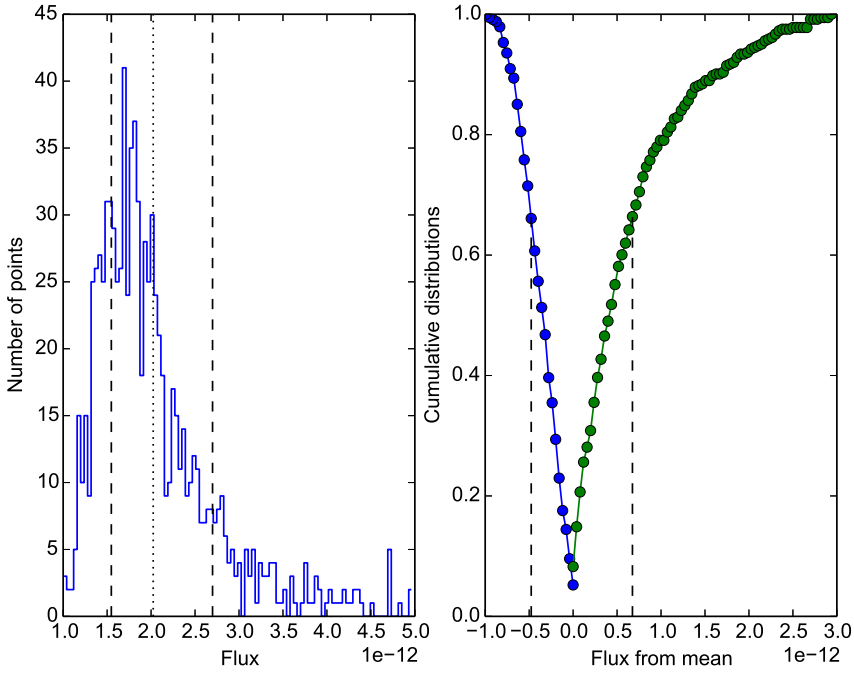
Number of points
Flux
1e−12
Cumulative distributions
Flux from mean
1e−12

Sw5

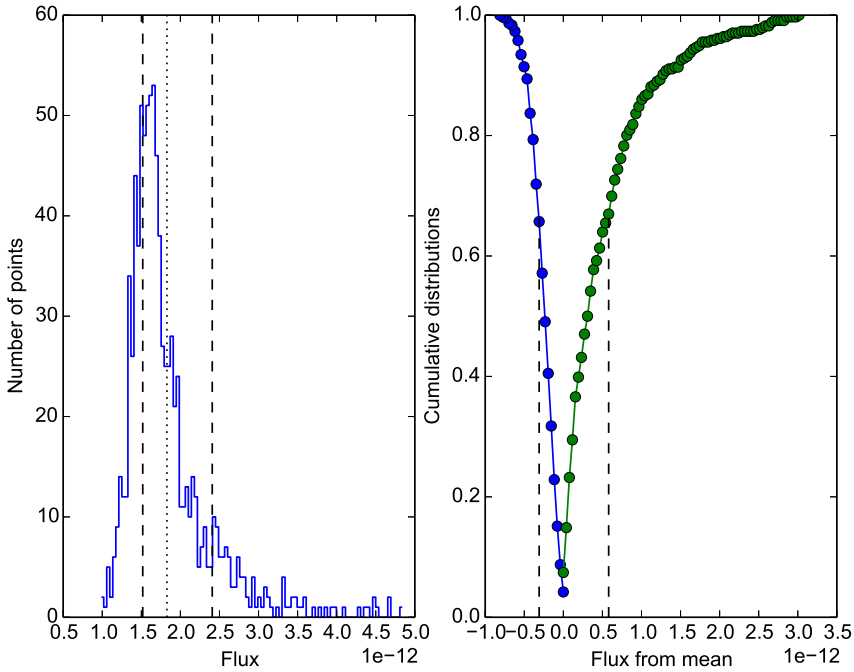
Number of points
Flux
1e−12
Cumulative distributions
Flux from mean
1e−12

Sw6

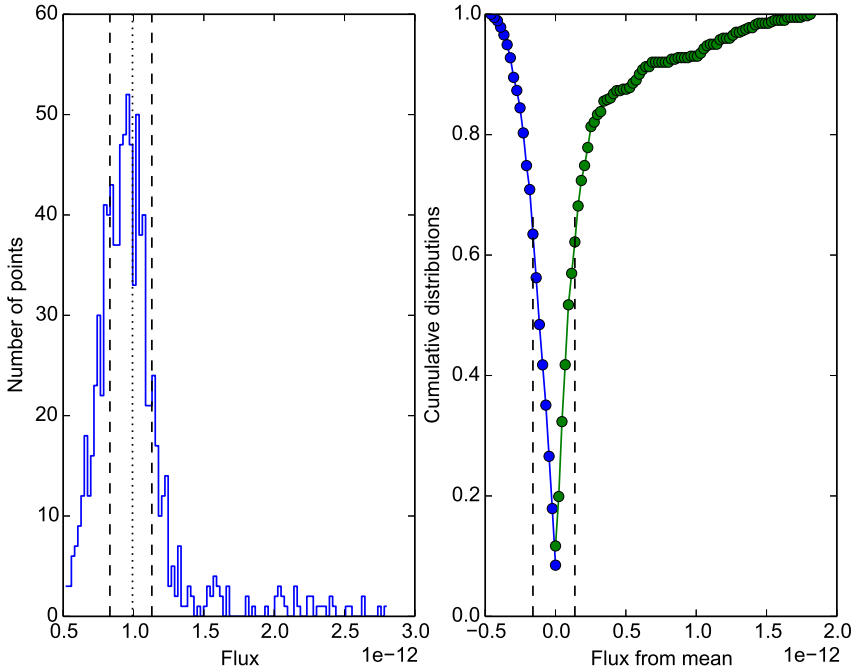
Number of points
Flux
1e−12
Cumulative distributions
Flux from mean
1e−12

Sw7

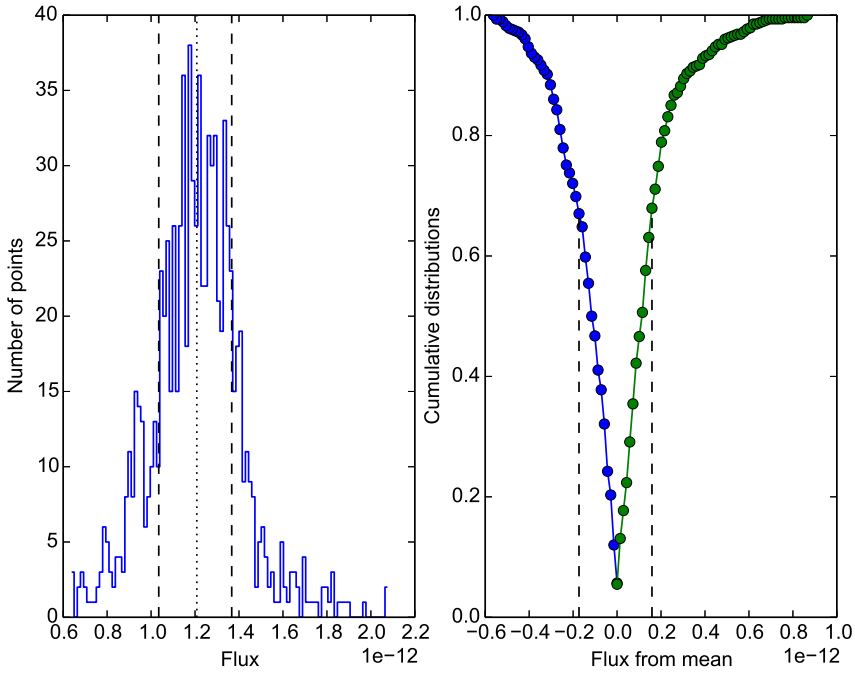
Number of points
Flux
1e−12
Cumulative distributions
Flux from mean
1e−12

Sw8

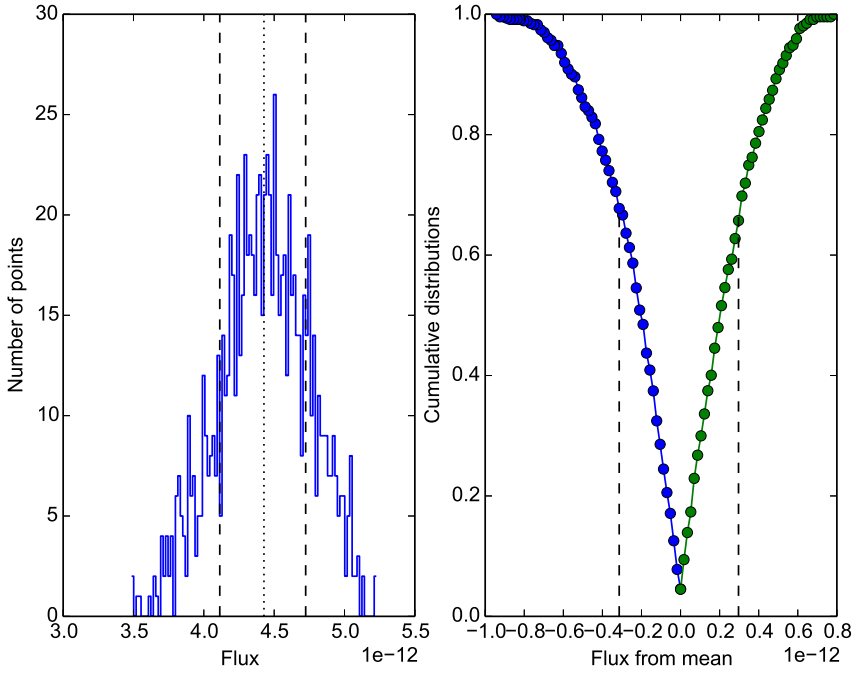
Number of points
Flux
1e−12
Cumulative distributions
Flux from mean
1e−12

Sw9

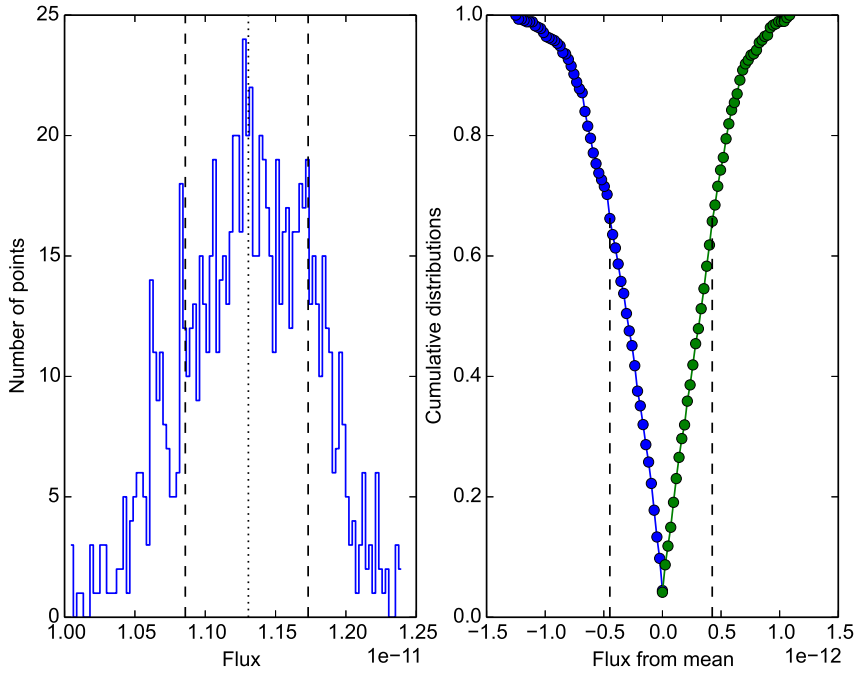
Number of points
Flux
1e−11
Cumulative distributions
Flux from mean
1e−12

Sw10

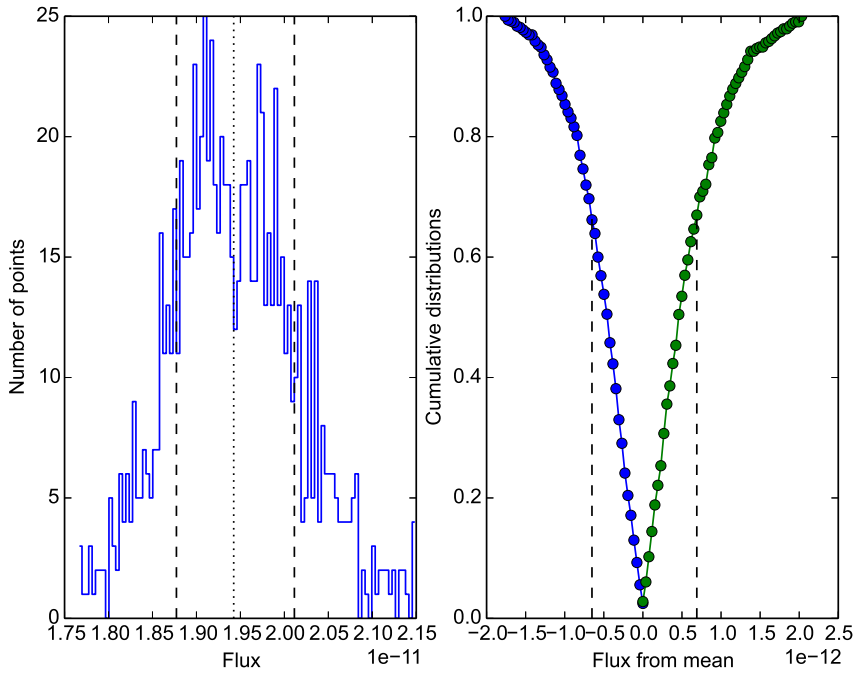
Number of points
Flux
1e−11
Cumulative distributions
Flux from mean
1e−12

Sw11

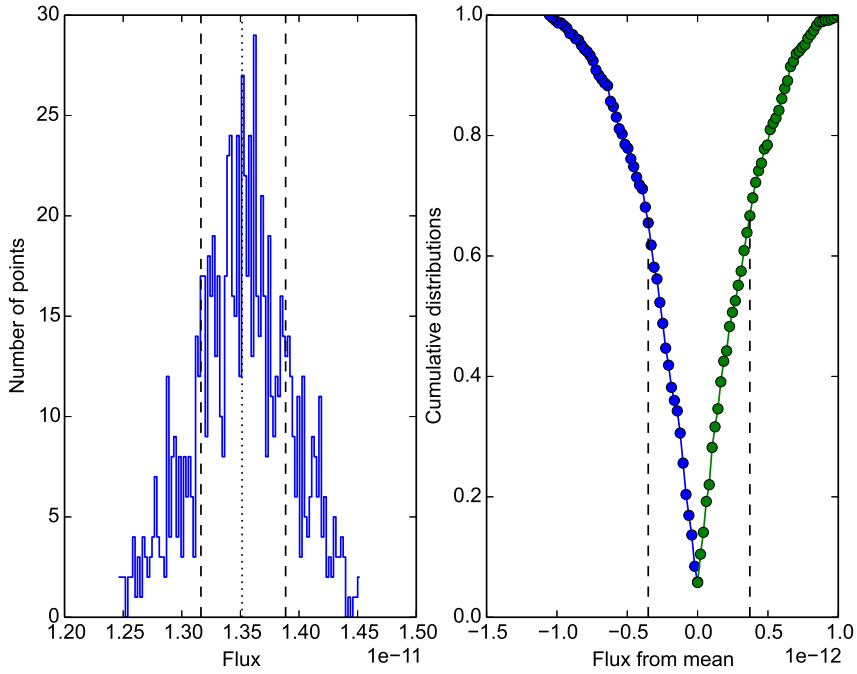
Number of points
Flux
1e−11
Cumulative distributions
Flux from mean
1e−12

Sw12

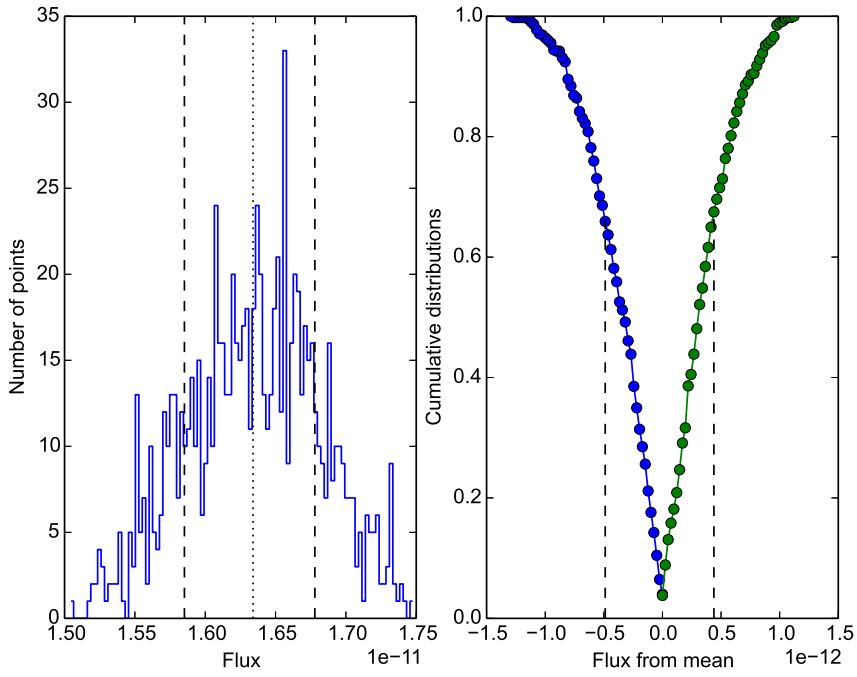
Number of points
Flux
1e−11
Cumulative distributions
Flux from mean
1e−12

Sw13

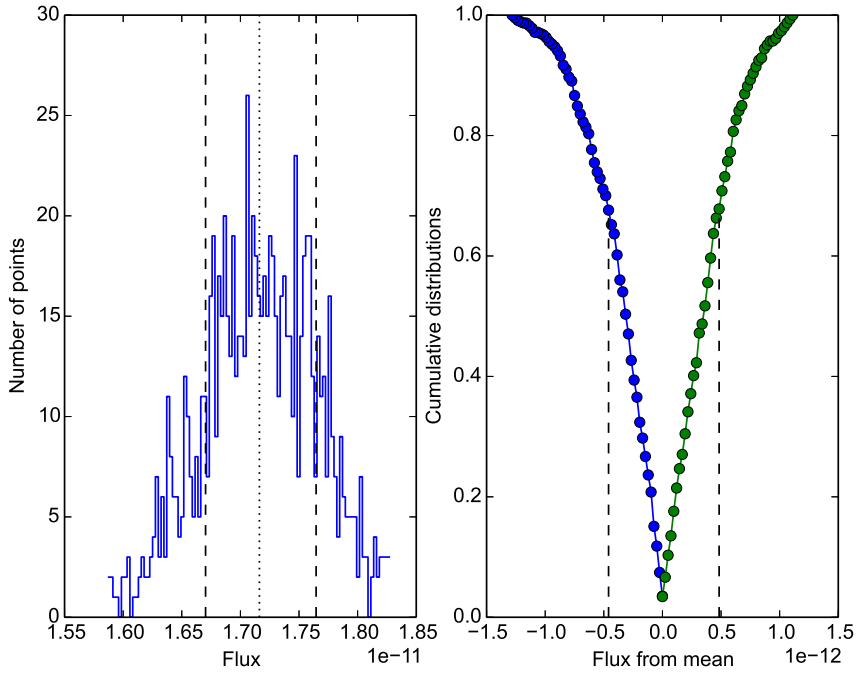
Number of points
Flux
1e−11
Cumulative distributions
Flux from mean
1e−12

Sw14

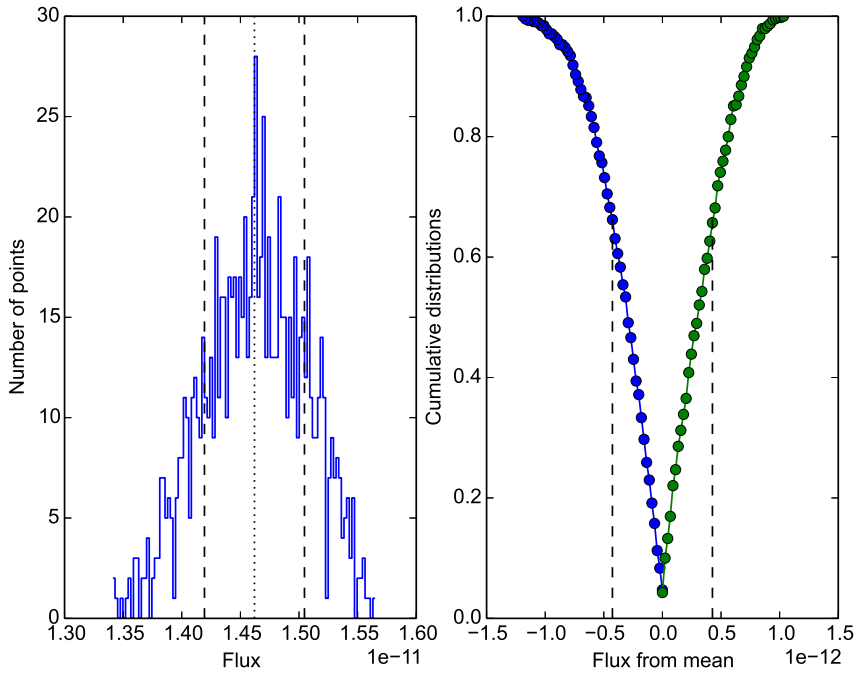
Number of points
Flux
1e−11
Cumulative distributions
Flux from mean
1e−12

Sw15

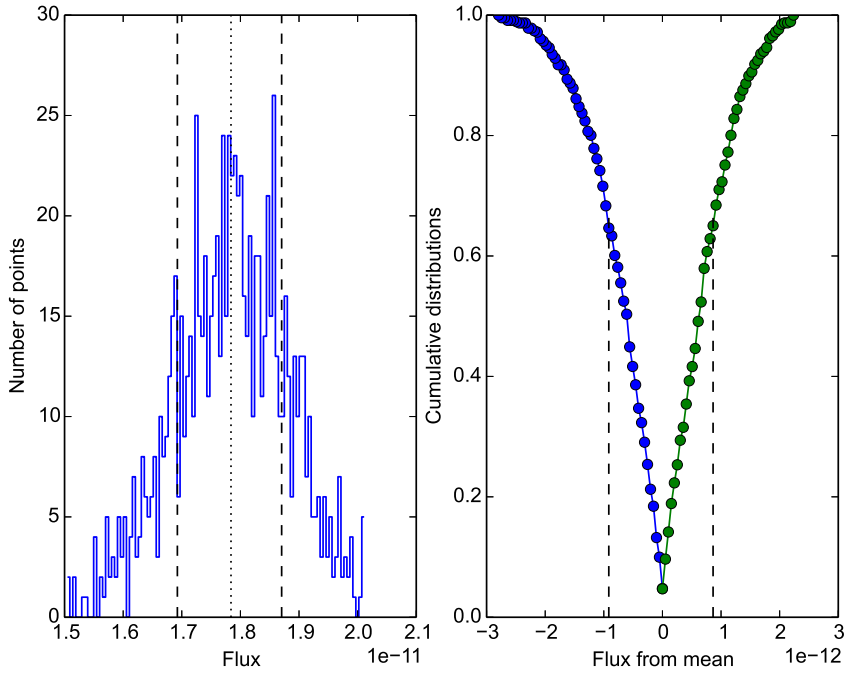
Number of points
Flux
1e−11
Cumulative distributions
Flux from mean
1e−12

Sw16

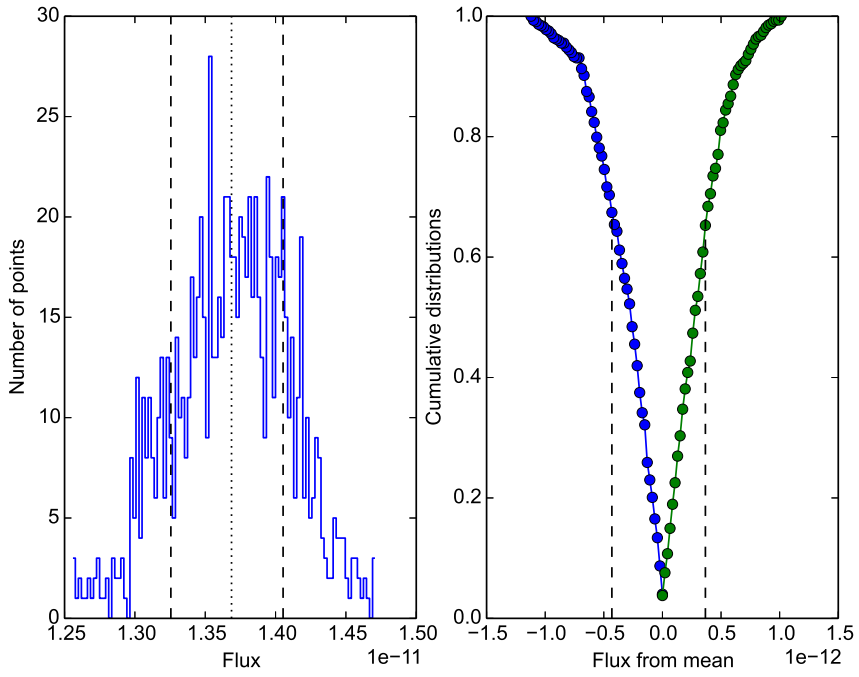
Number of points
Flux
1e−11
Cumulative distributions
Flux from mean
1e−12

Sw17

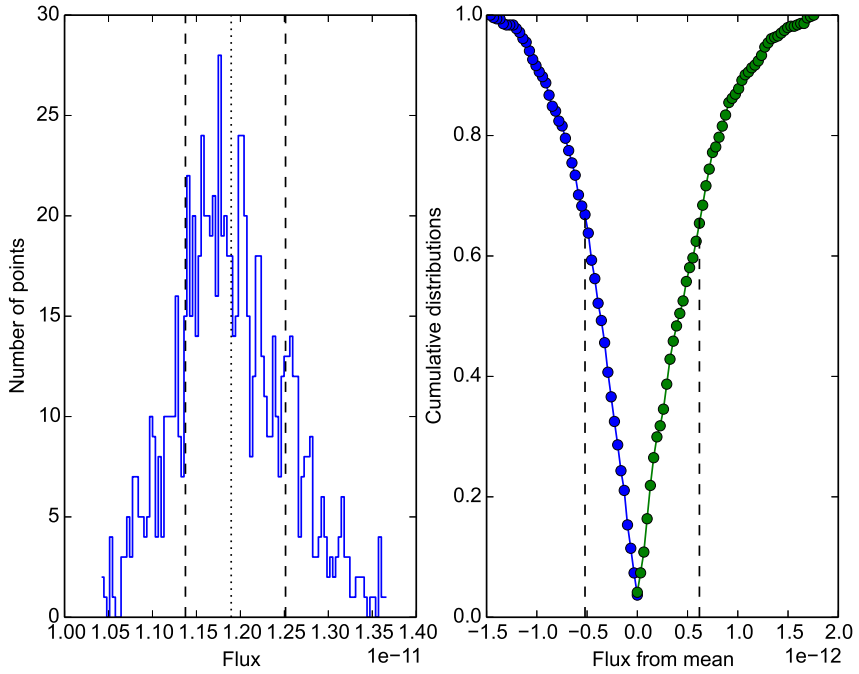
Number of points
Flux
1e−11
Cumulative distributions
Flux from mean
1e−12

Sw18

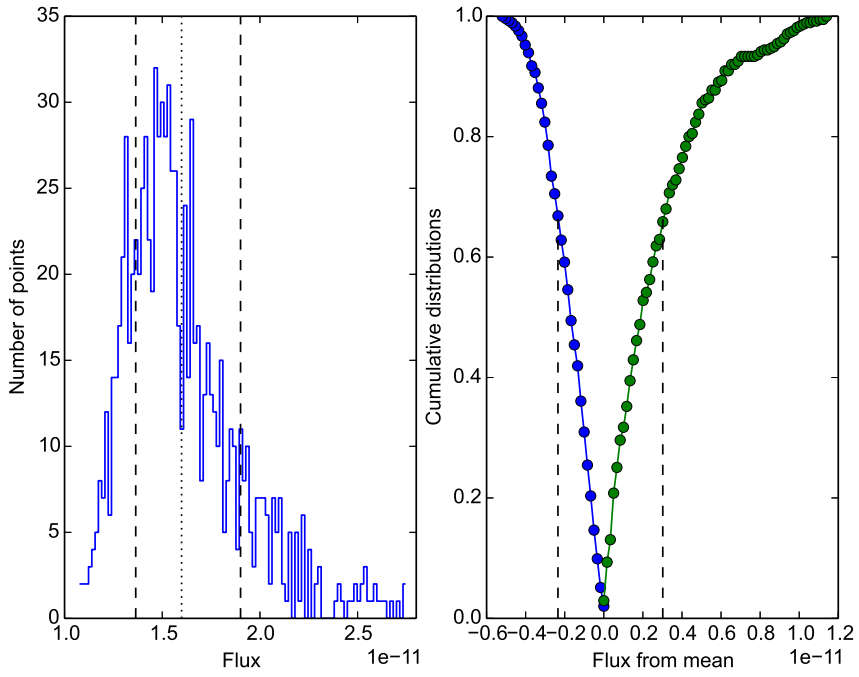
Number of points
Flux
1e−11
Cumulative distributions
Flux from mean
1e−11

Sw19

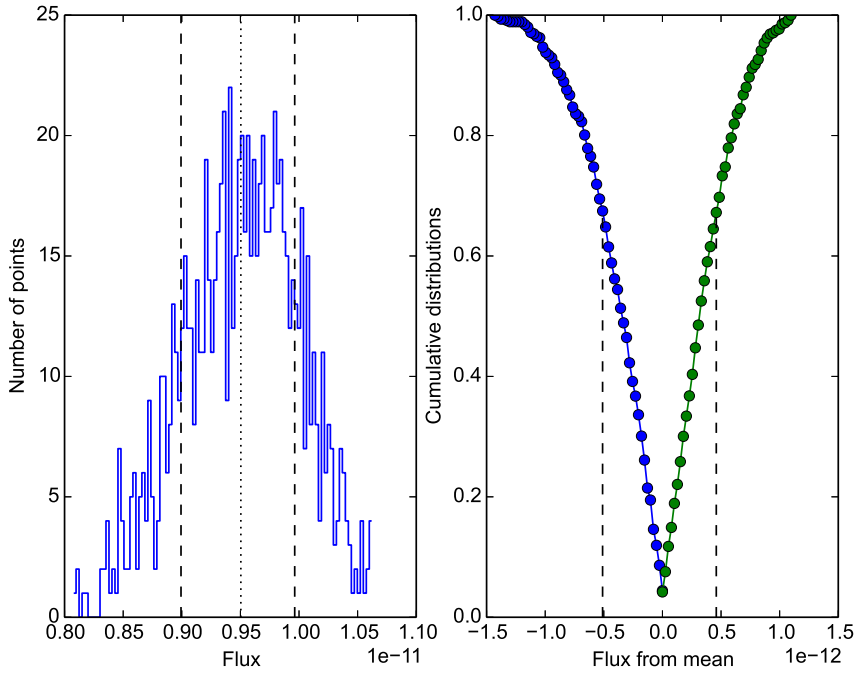
Number of points
Flux
1e−11
Cumulative distributions
Flux from mean
1e−12

Sw20

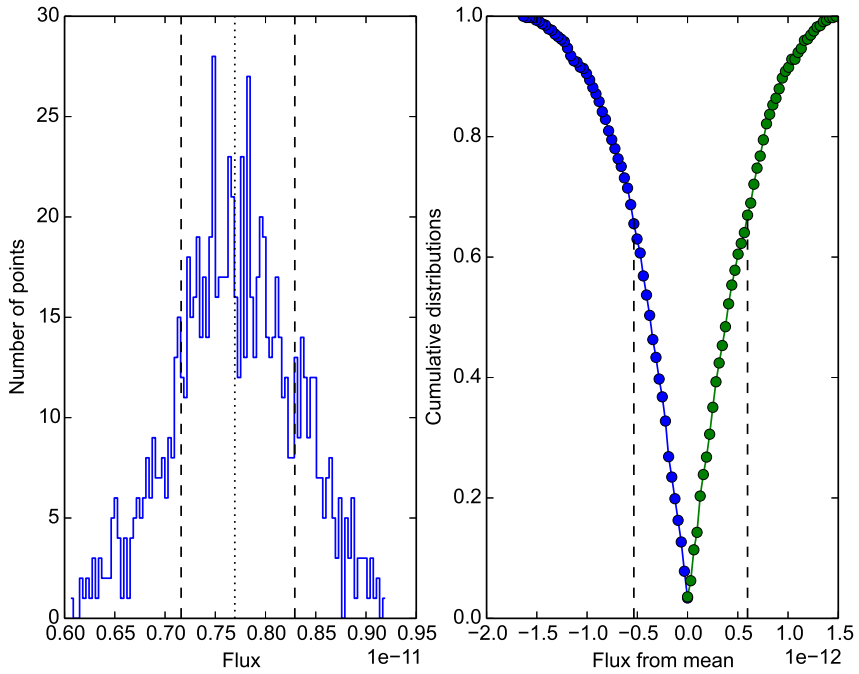
Number of points
Flux
1e−11
Cumulative distributions
Flux from mean
1e−12

Sw21

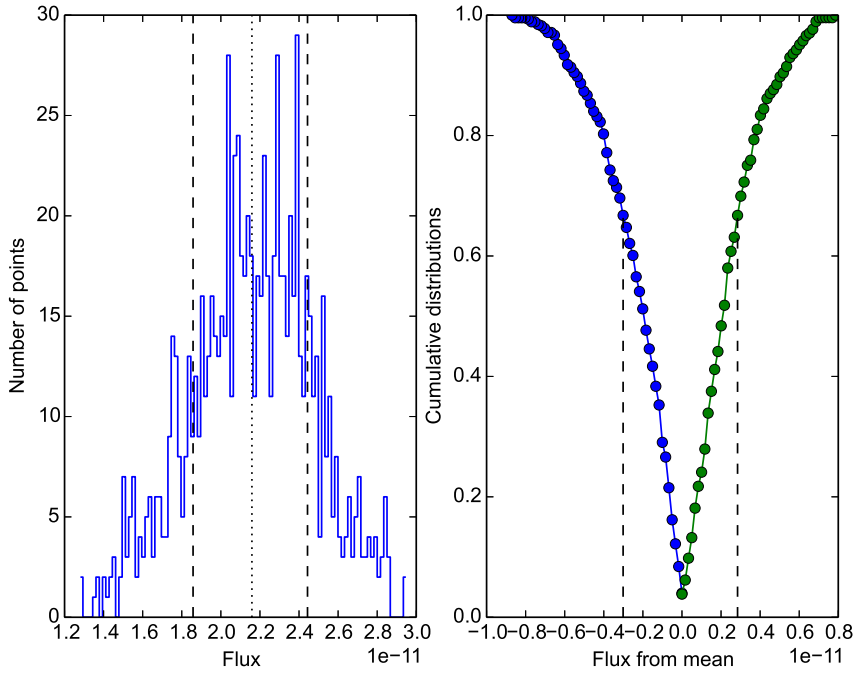
Number of points
Flux
1e−11
Cumulative distributions
Flux from mean
1e−11

Sw22

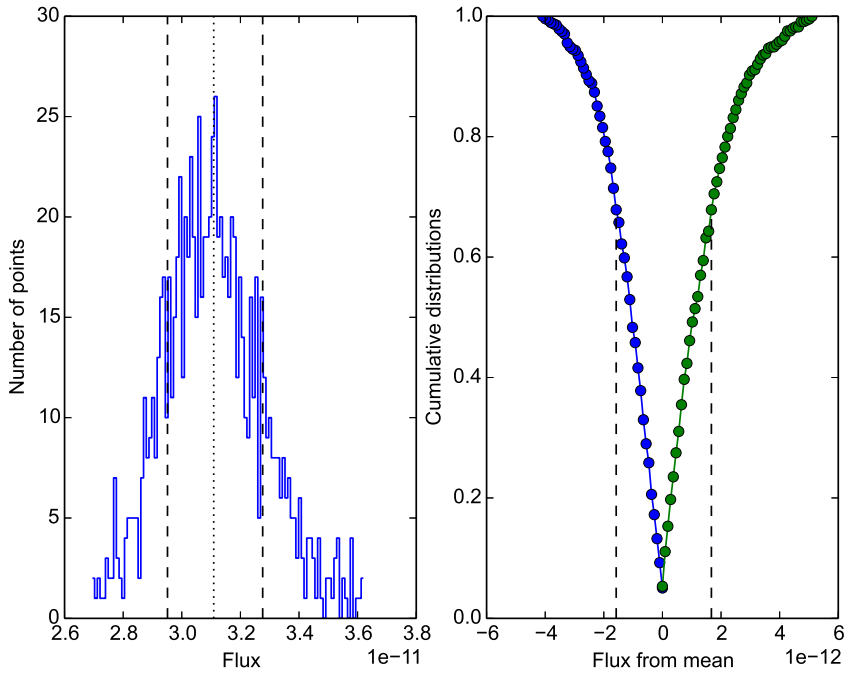
Number of points
Flux
1e−11
Cumulative distributions
Flux from mean
1e−12

Sw23

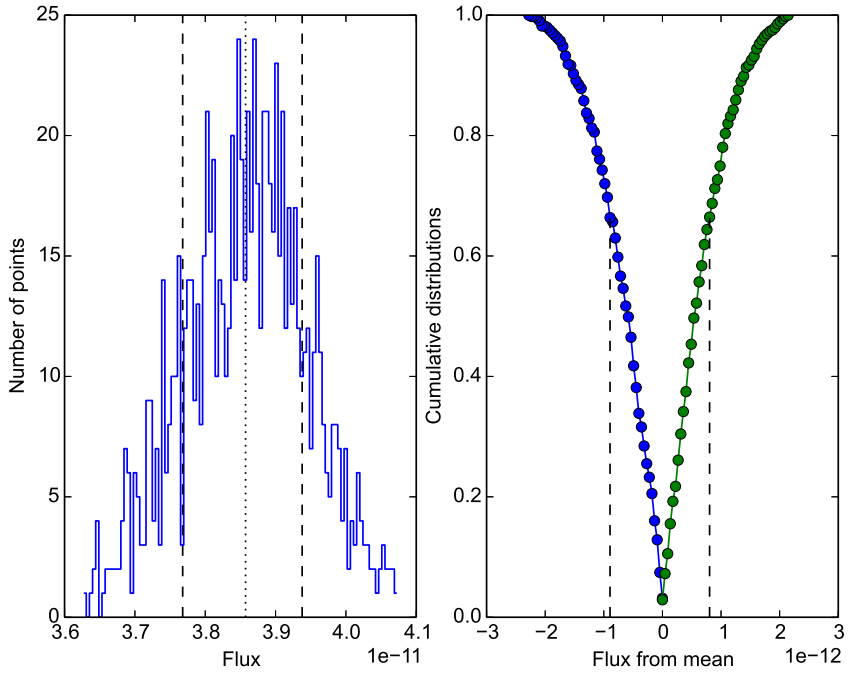
Number of points
Flux
1e−11
Cumulative distributions
Flux from mean
1e−12

Sw24

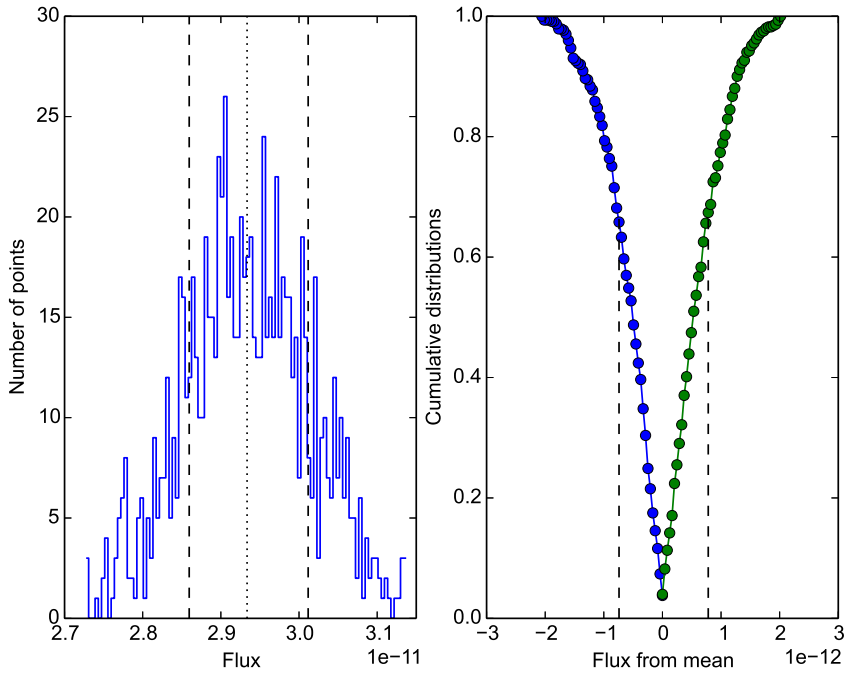
Number of points
Flux
1e−11
Cumulative distributions
Flux from mean
1e−12

Sw25

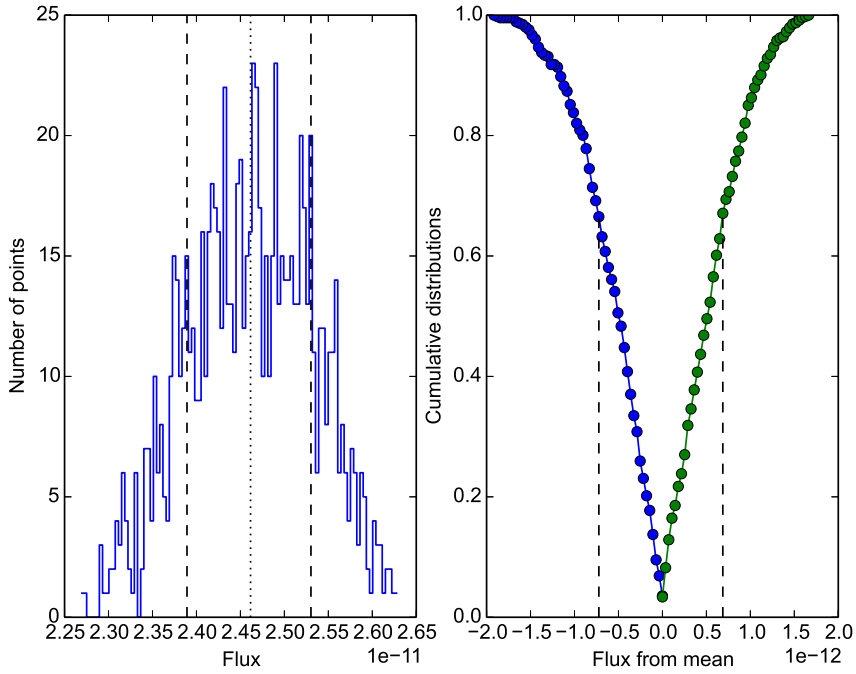
Number of points
Flux
1e−11
Cumulative distributions
Flux from mean
1e−12

Sw26

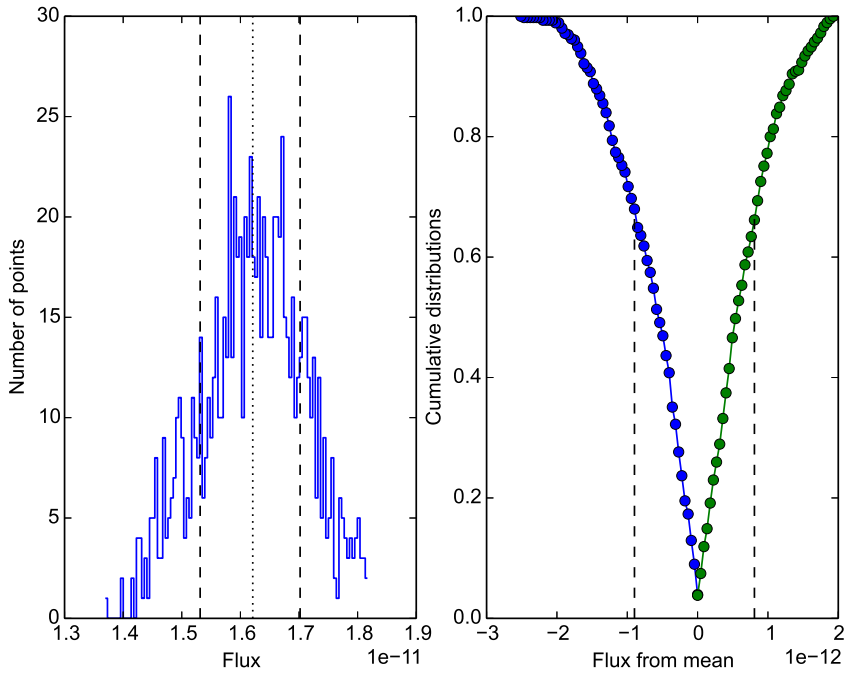
Number of points
Flux
1e−11
Cumulative distributions
Flux from mean
1e−12

Sw27

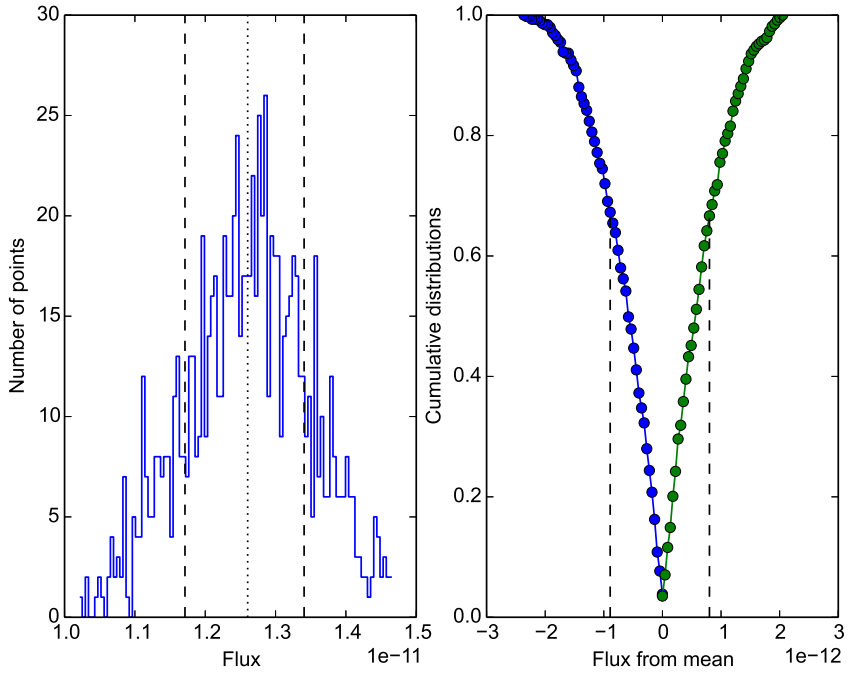
Number of points
Flux
1e−11
Cumulative distributions
Flux from mean
1e−12

Sw28

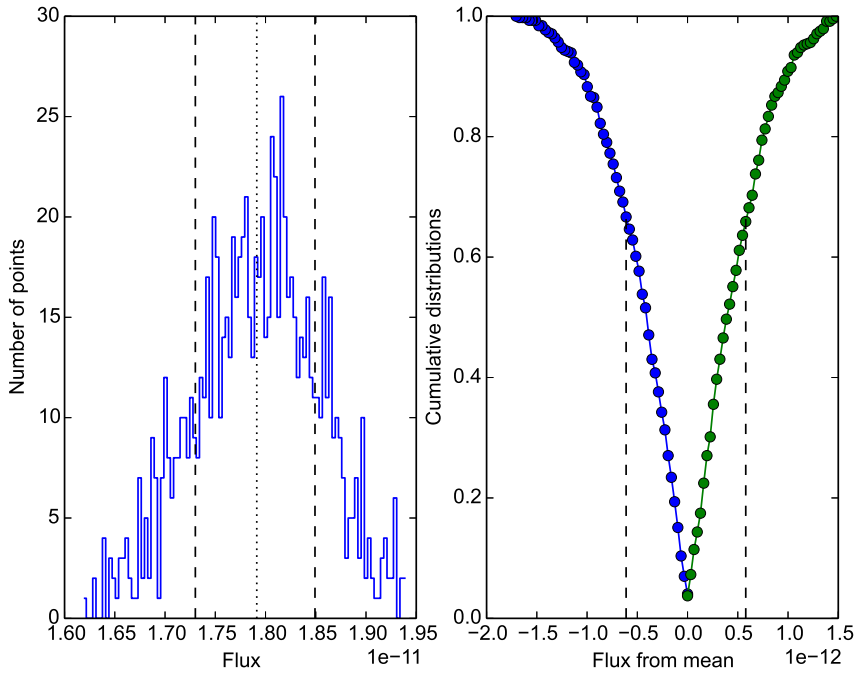
Number of points
Flux
1e−11
Cumulative distributions
Flux from mean
1e−12

Sw29

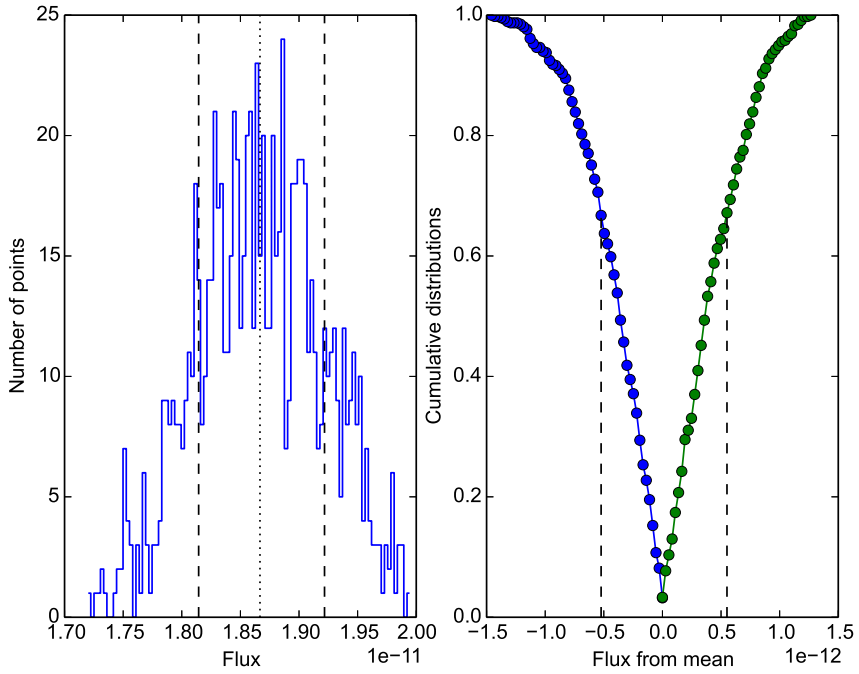
Number of points
Flux
1e−11
Cumulative distributions
Flux from mean
1e−12

Sw30

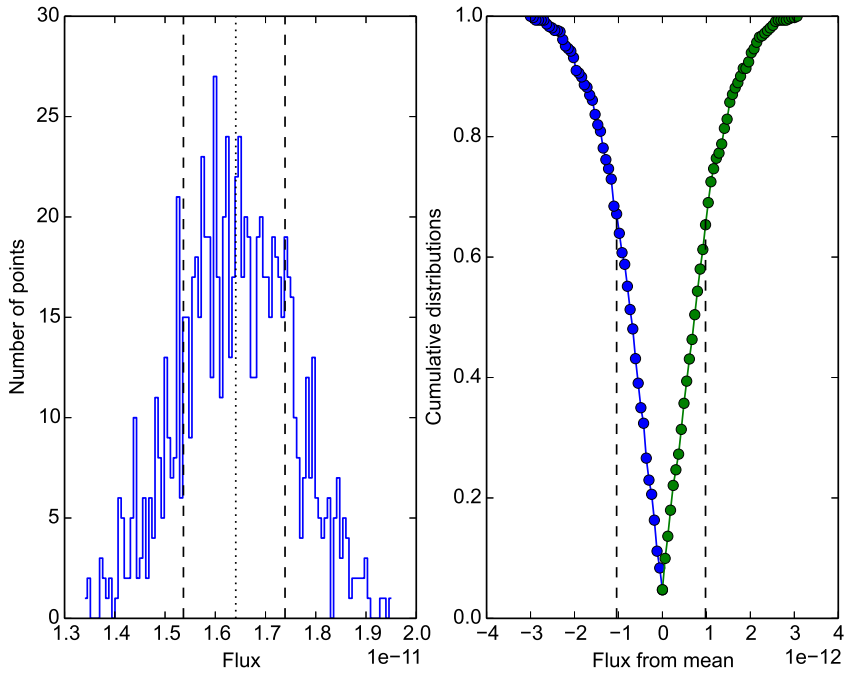
Number of points
Flux
1e−11
Cumulative distributions
Flux from mean
1e−12

Sw31

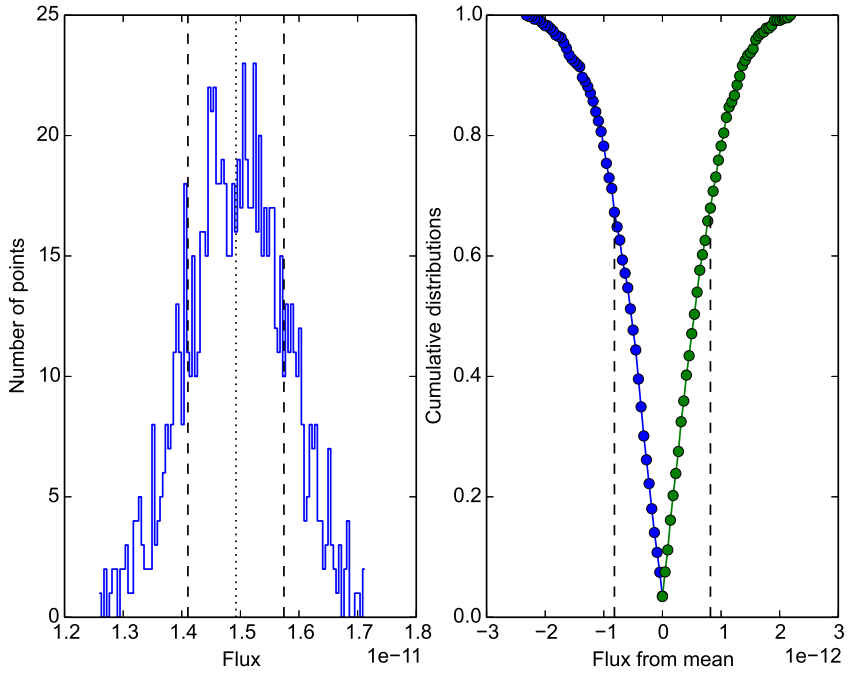
Number of points
Flux
1e−11
Cumulative distributions
Flux from mean
1e−12

Sw32

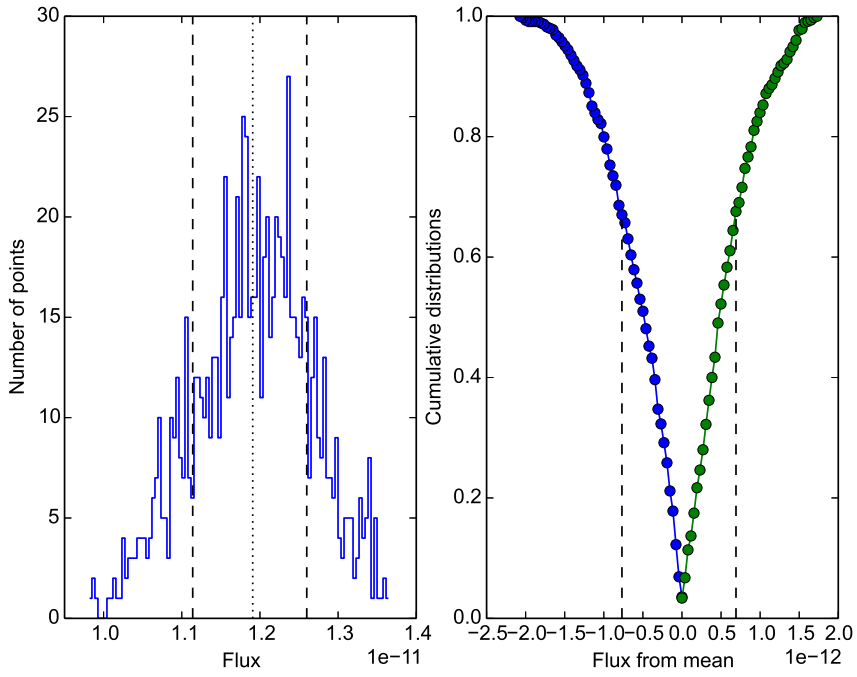
Number of points
Flux
1e−11
Cumulative distributions
Flux from mean
1e−12

Sw33

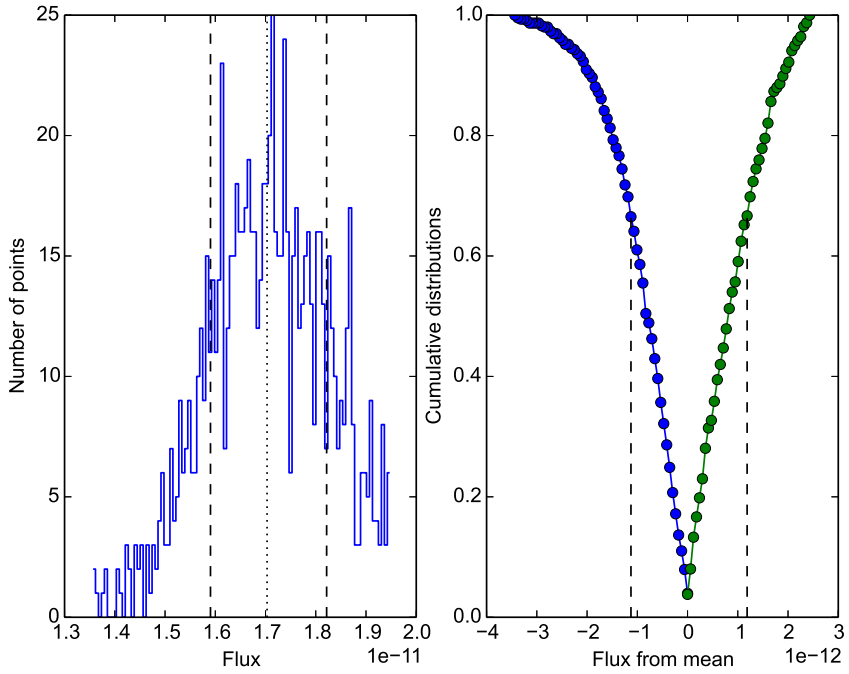
Number of points
Flux
1e−11
Cumulative distributions
Flux from mean
1e−12

Sw34

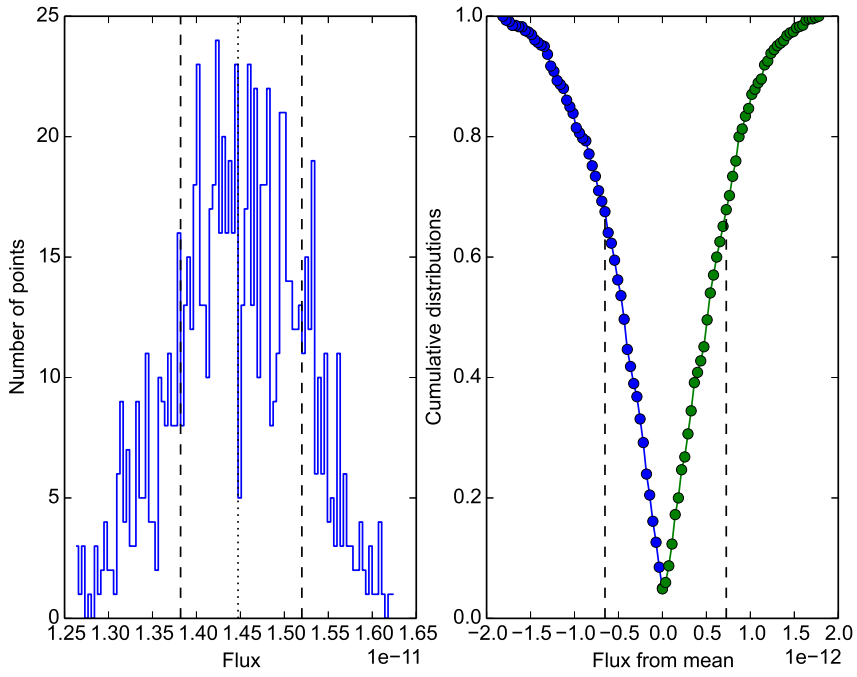
Number of points
Flux
1e−11
Cumulative distributions
Flux from mean
1e−12

Sw35

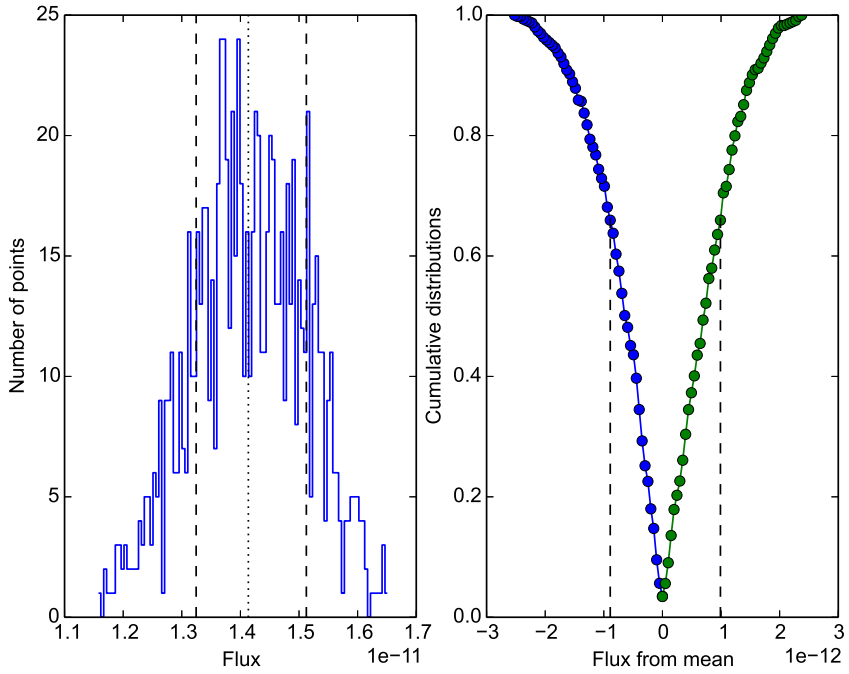
Number of points
Flux
1e−11
Cumulative distributions
Flux from mean
1e−12

Sw36

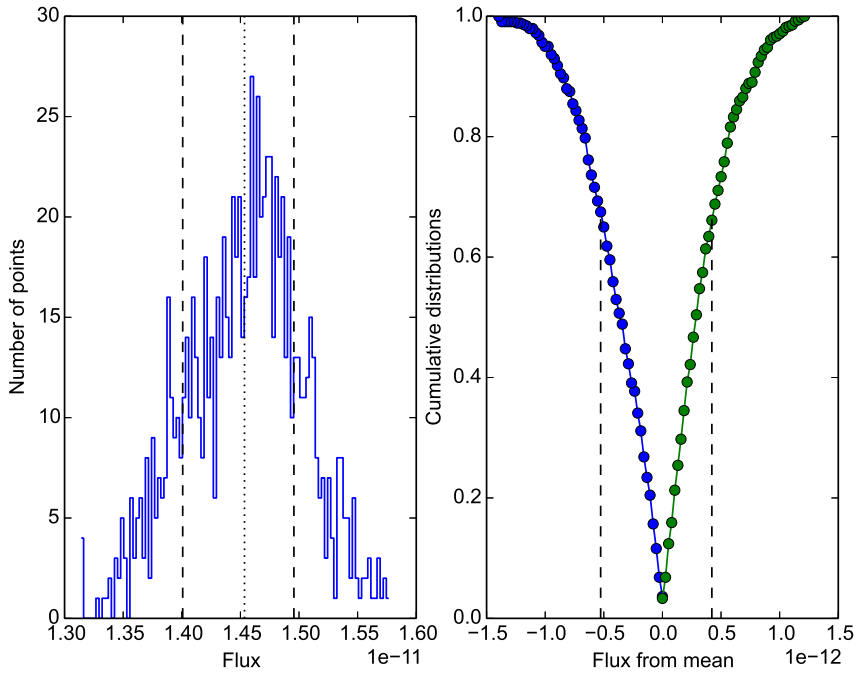
Number of points
Flux
1e−11
Cumulative distributions
Flux from mean
1e−12

Sw37

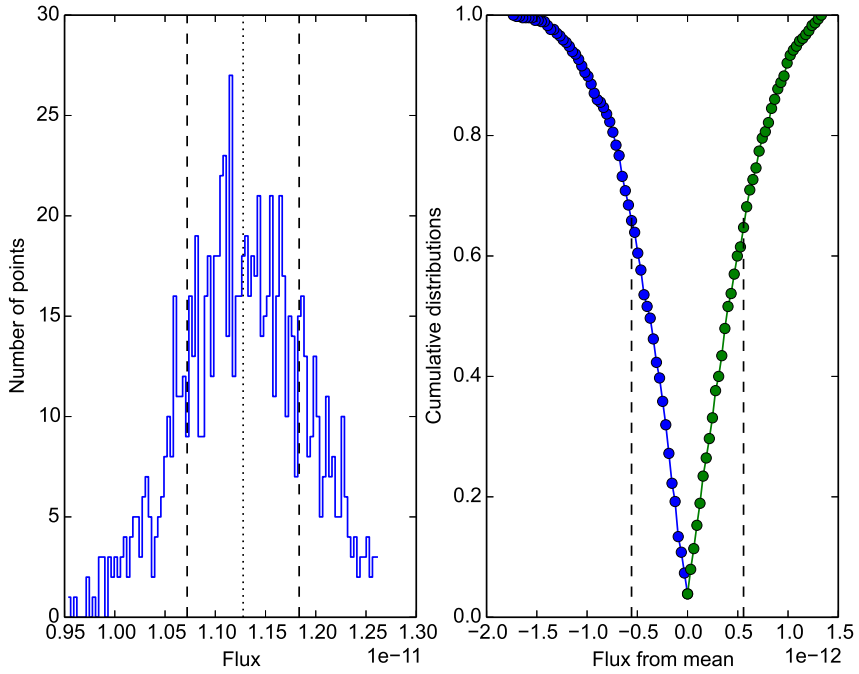
Number of points
Flux
1e−11
Cumulative distributions
Flux from mean
1e−12

Sw38

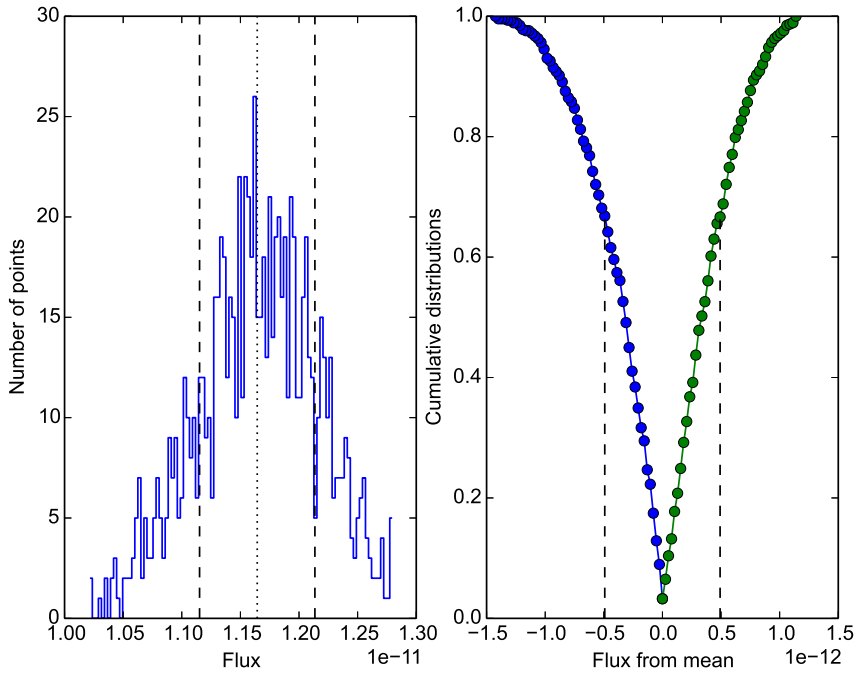
Number of points
Flux
1e−11
Cumulative distributions
Flux from mean
1e−12

Sw39

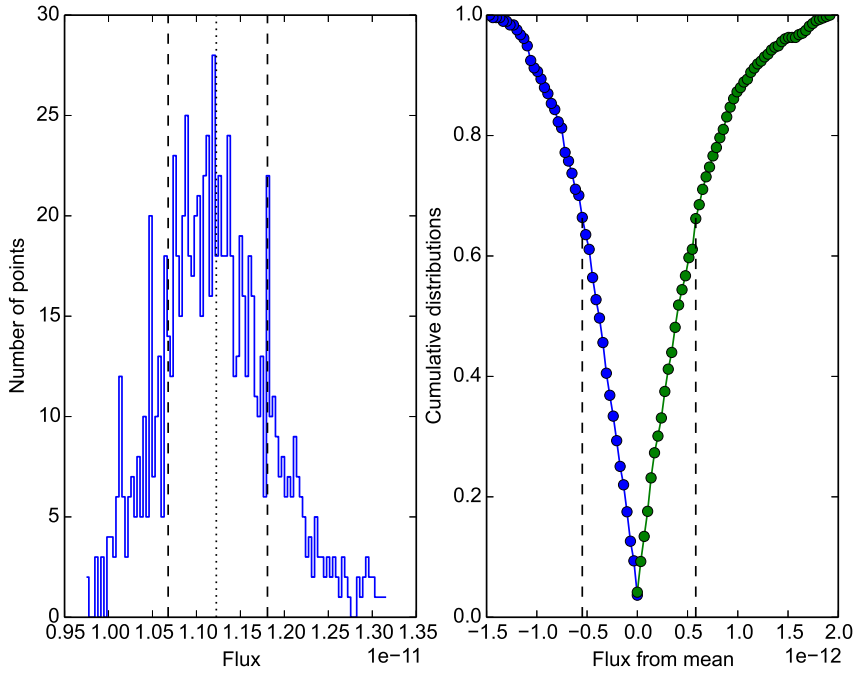
Number of points
Flux
1e−11
Cumulative distributions
Flux from mean
1e−12

Sw40

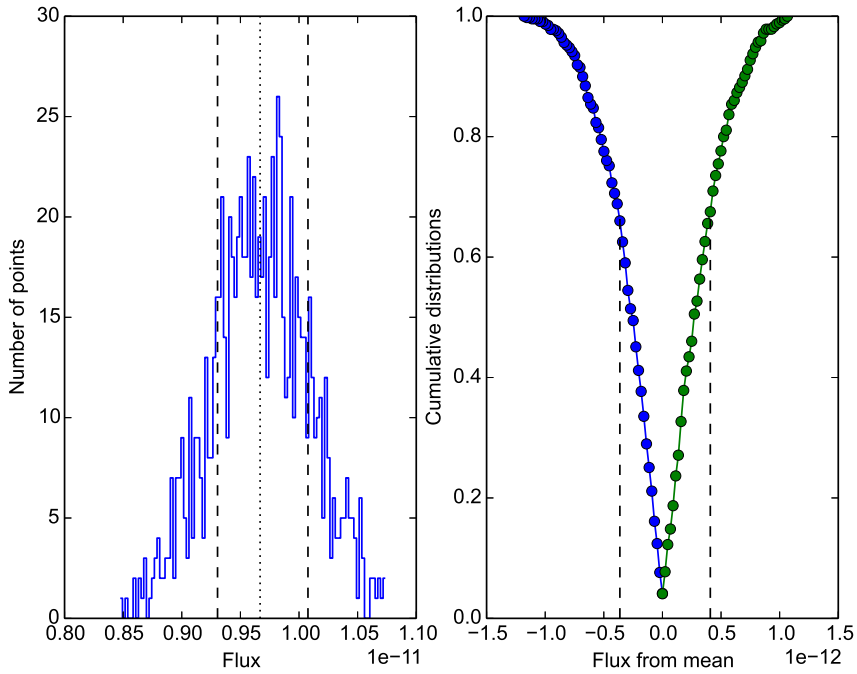
Number of points
Flux
1e−11
Cumulative distributions
Flux from mean
1e−12

Sw41

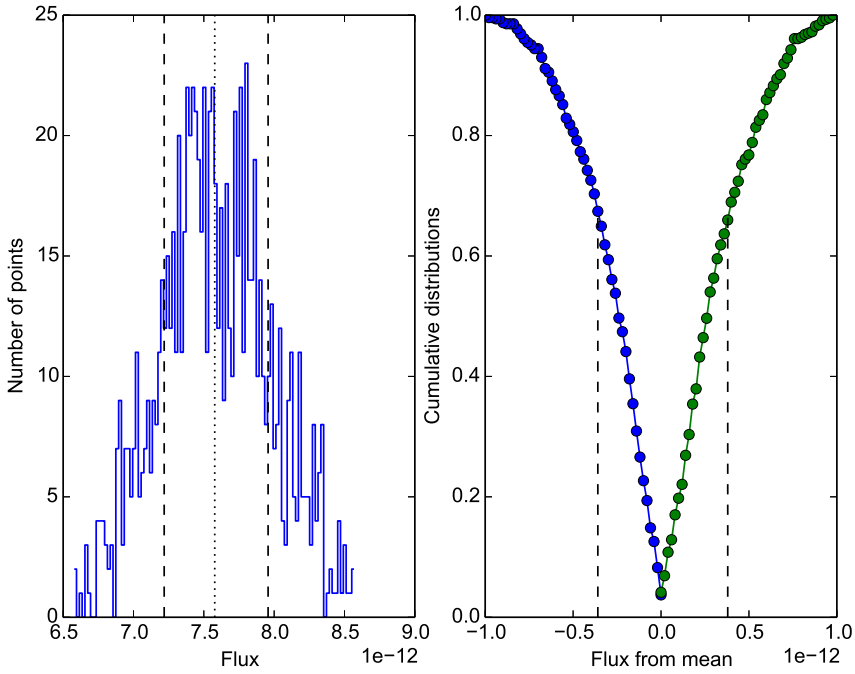
Number of points
Flux
1e−12
Cumulative distributions
Flux from mean
1e−12

Sz1

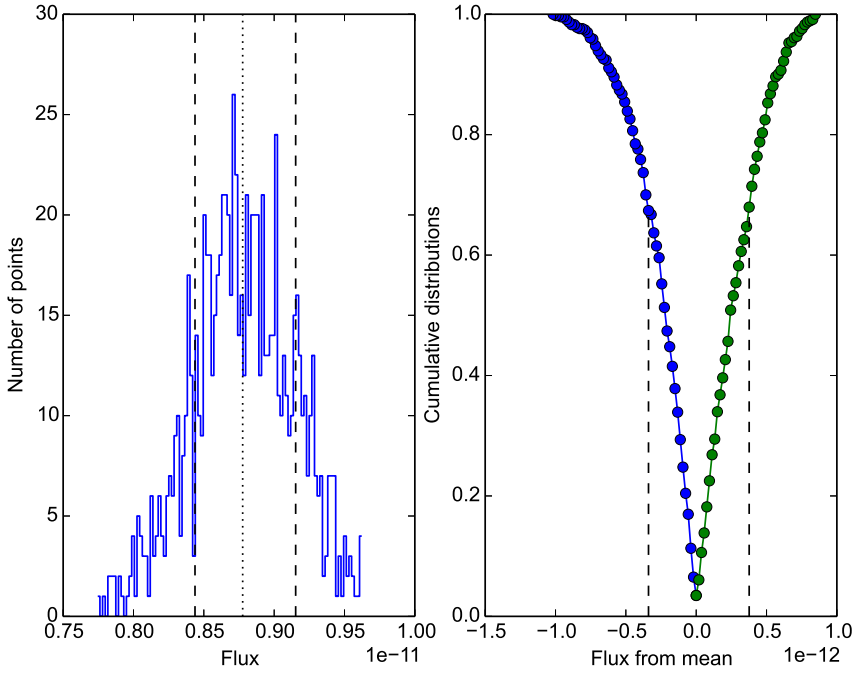
Number of points
Flux
1e−11
Cumulative distributions
Flux from mean
1e−12

Sz2

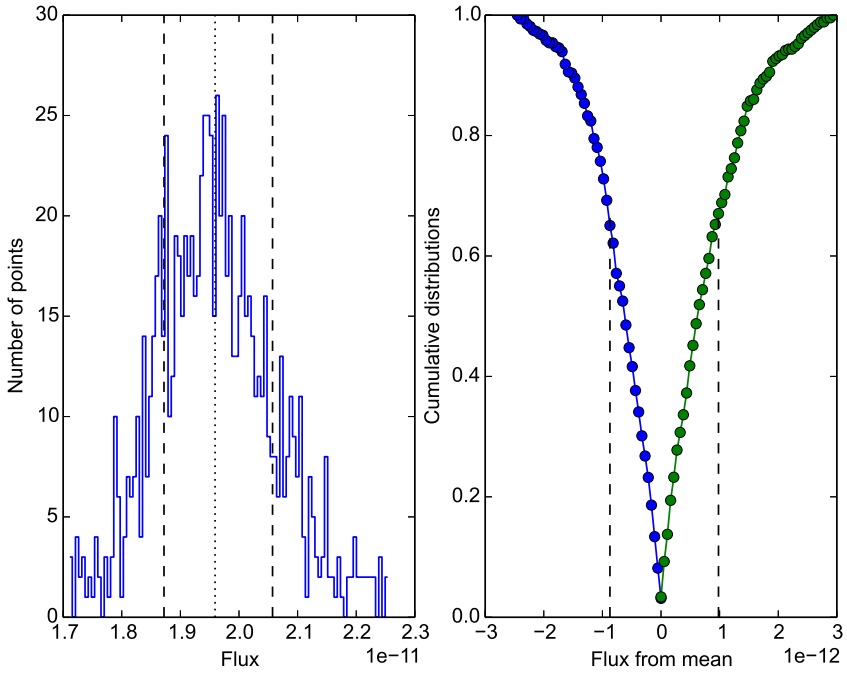
Number of points
Flux
1e−11
Cumulative distributions
Flux from mean
1e−12

Sz3

Appendix B

Monte Carlo simulations of *XMM*-Newton lightcurves for LS I +61° 303.

Here, it is shown the Monte Carlo simulated lightcurves and observed *XMM*-Newton lightcurves of LS I +61° 303.

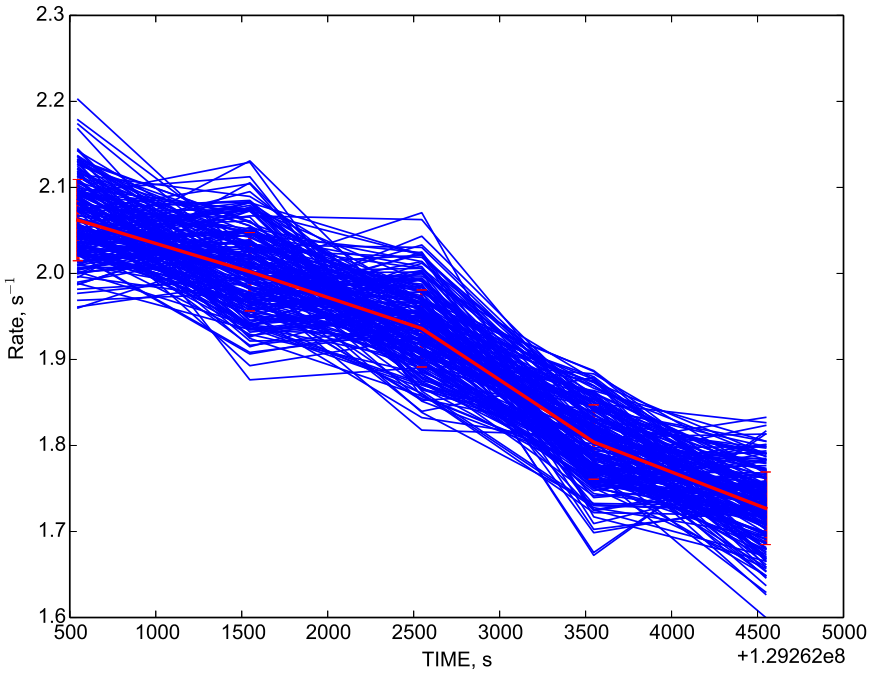

X1

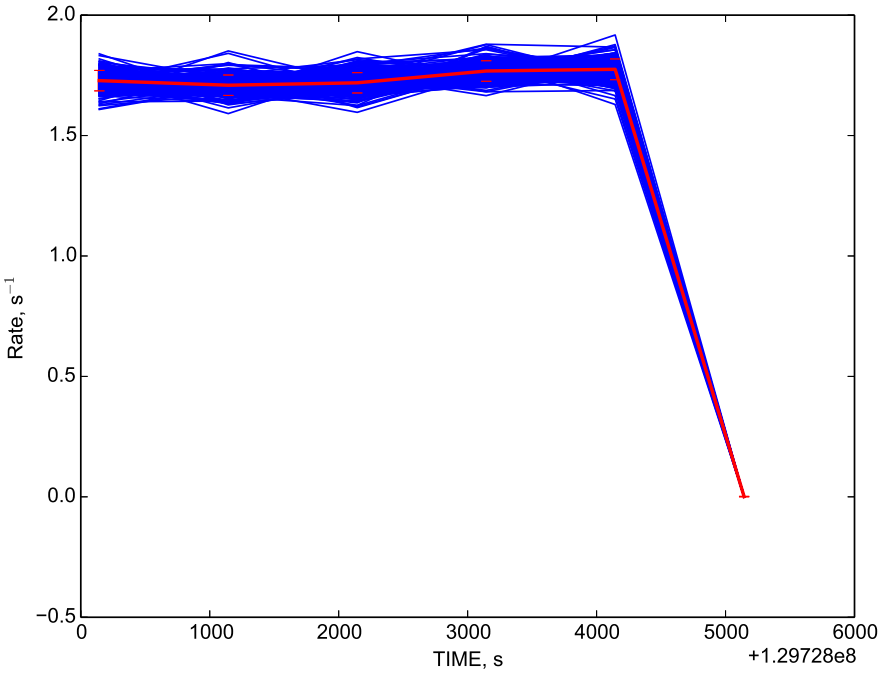
2.0
1.5
1.0
0.5
0.0
−0.5
Rate, s^{-1}
0
1000
2000
3000
4000
5000
6000
TIME, s
+1.29728e8

X2

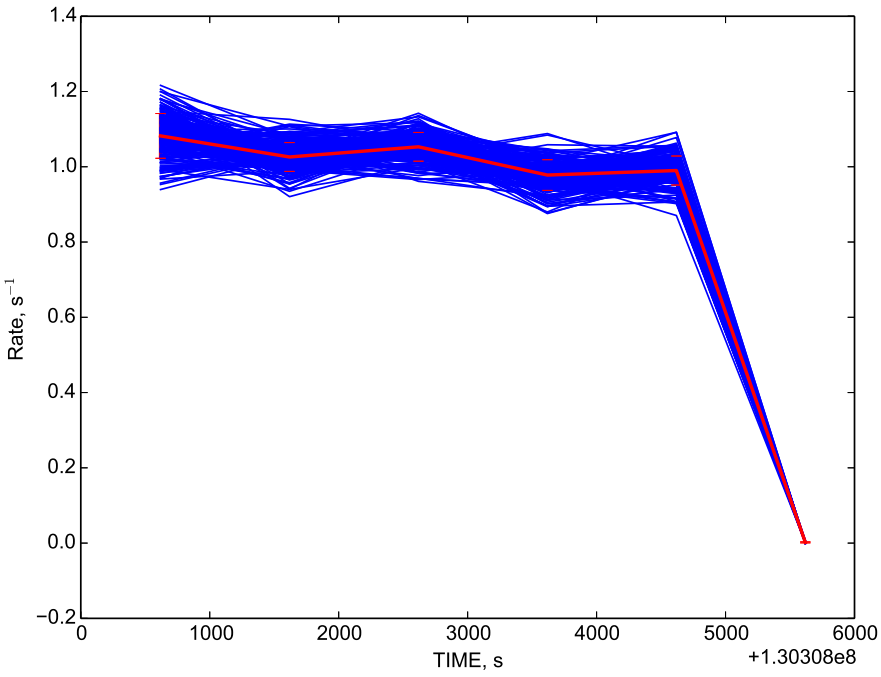
1.4
1.2
1.0
0.8
0.6
0.4
0.2
0.0
−0.2
Rate, s^{-1}
0
1000
2000
3000
4000
5000
6000
TIME, s
+1.30308e8

X3

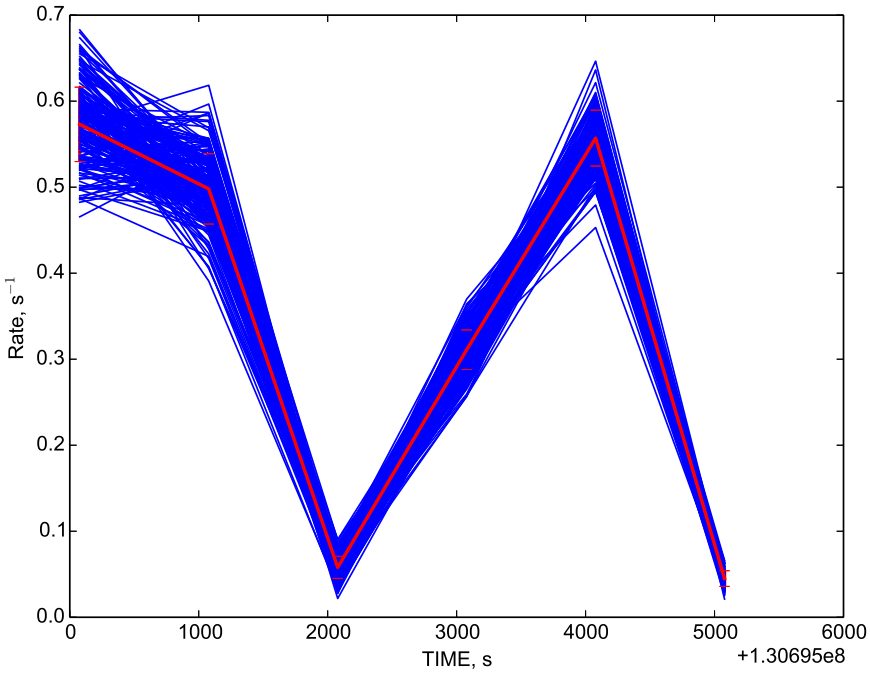
0.7
0.6
0.5
0.4
0.3
0.2
0.1
0.0
Rate, s^{-1}
0
1000
2000
3000
4000
5000
6000
TIME, s
+1.30695e8

X4

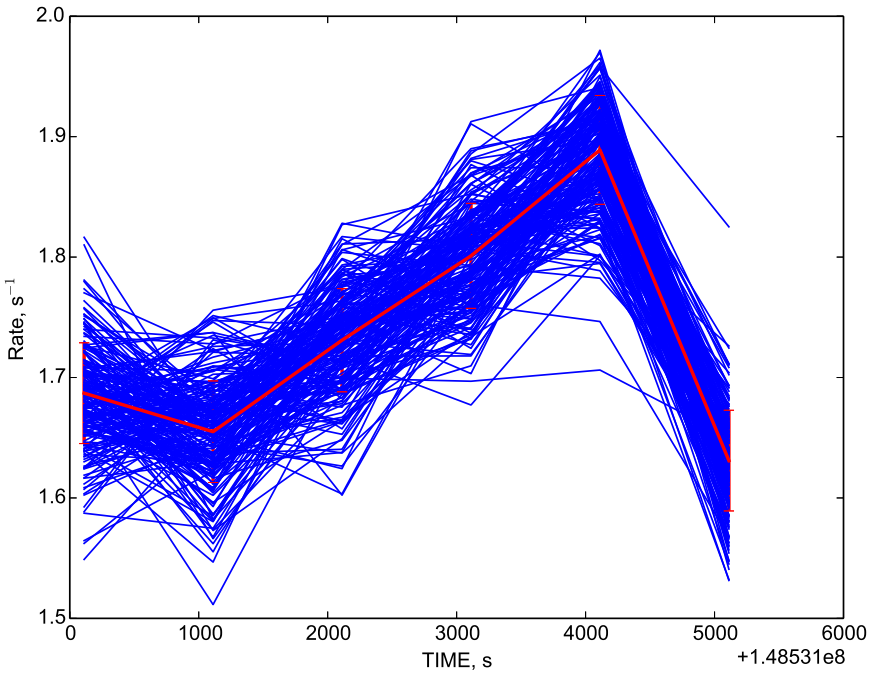
2.0
1.9
1.8
1.7
1.6
1.5
Rate, s^{-1}
0
1000
2000
3000
4000
5000
6000
TIME, s
+1.48531e8

X5

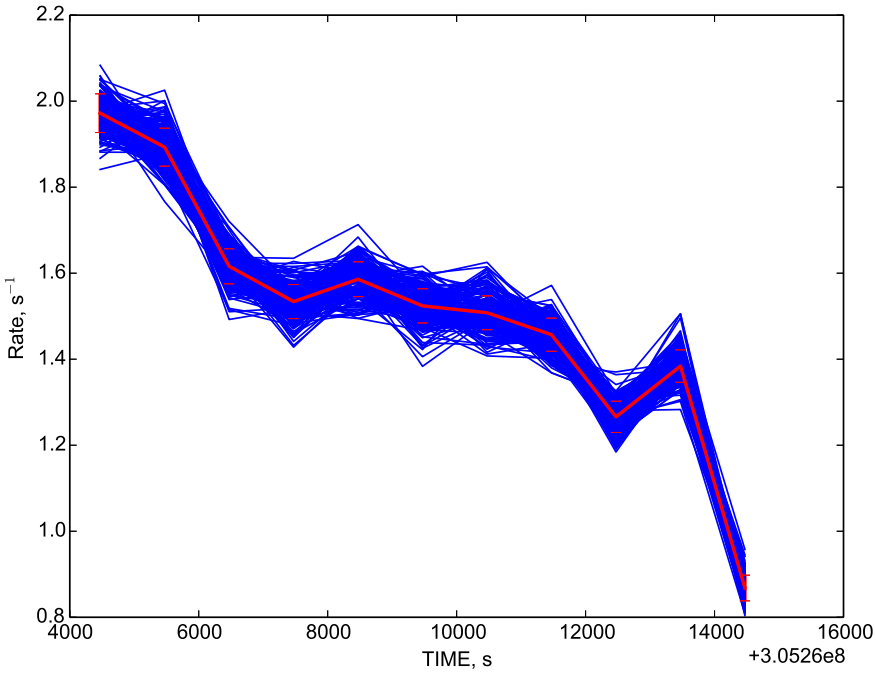
2.2
2.0
1.8
1.6
1.4
1.2
1.0
0.8
Rate, s^{-1}
4000
6000
8000
10000
12000
14000
16000
TIME, s
+3.0526e8

X7

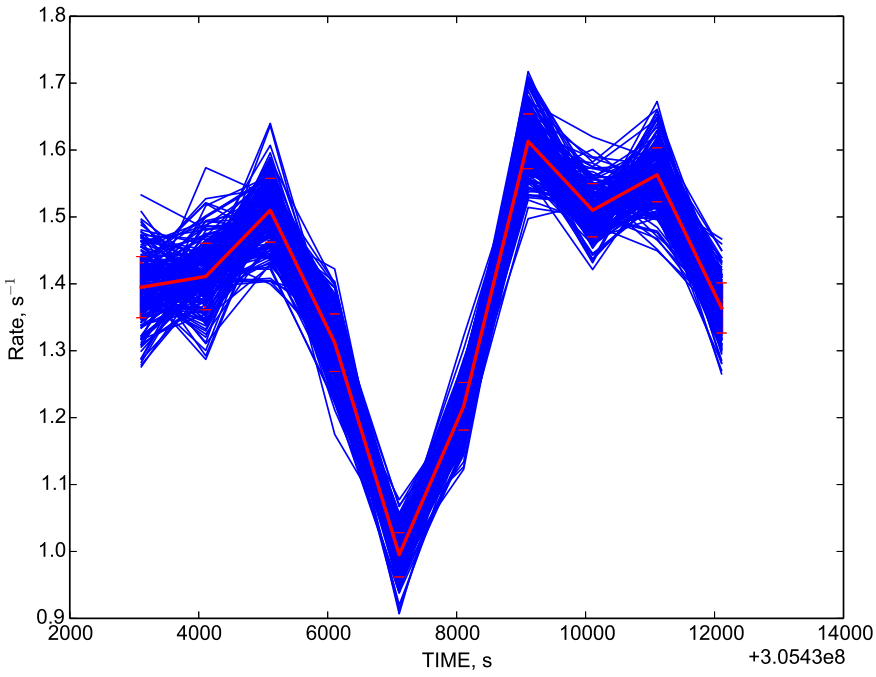
1.8
1.7
1.6
1.5
1.4
1.3
1.2
1.1
1.0
0.9
Rate, s^{-1}
2000
4000
6000
8000
10000
12000
14000
TIME, s
+3.0543e8

X8

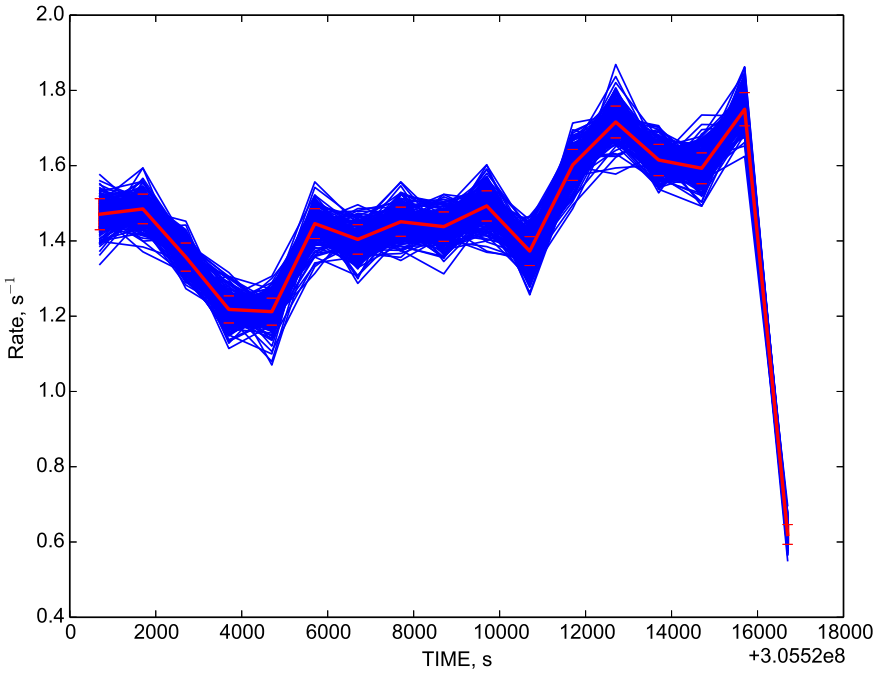
2.0
1.8
1.6
1.4
1.2
1.0
0.8
0.6
0.4
Rate, s^{-1}
0
2000
4000
6000
8000
10000
12000
14000
16000
18000
TIME, s
+3.0552e8

X9

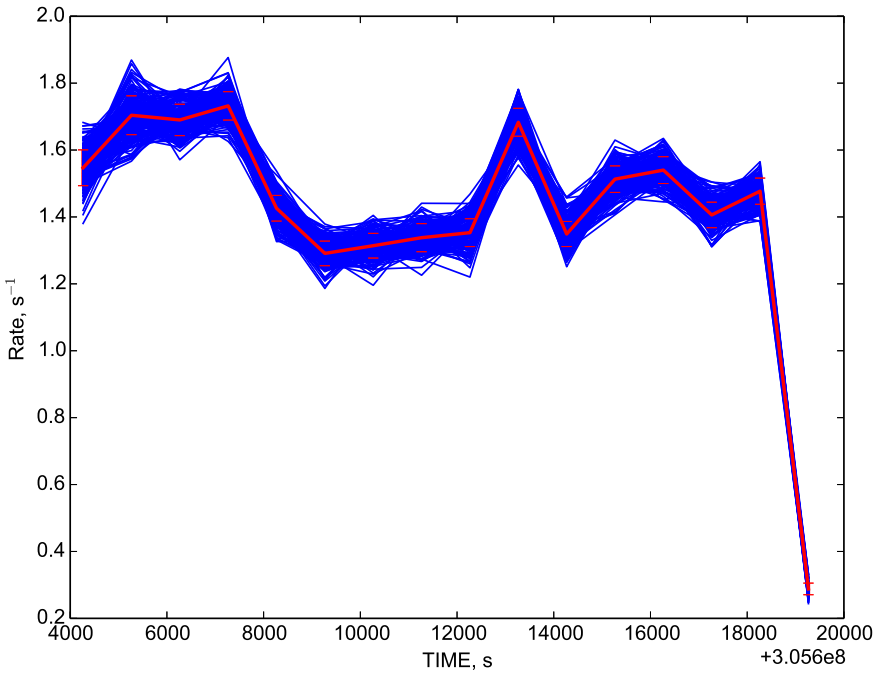
2.0
1.8
1.6
1.4
1.2
1.0
0.8
0.6
0.4
0.2
Rate, s^{-1}
4000
6000
8000
10000
12000
14000
16000
18000
20000
TIME, s
+3.056e8

X10

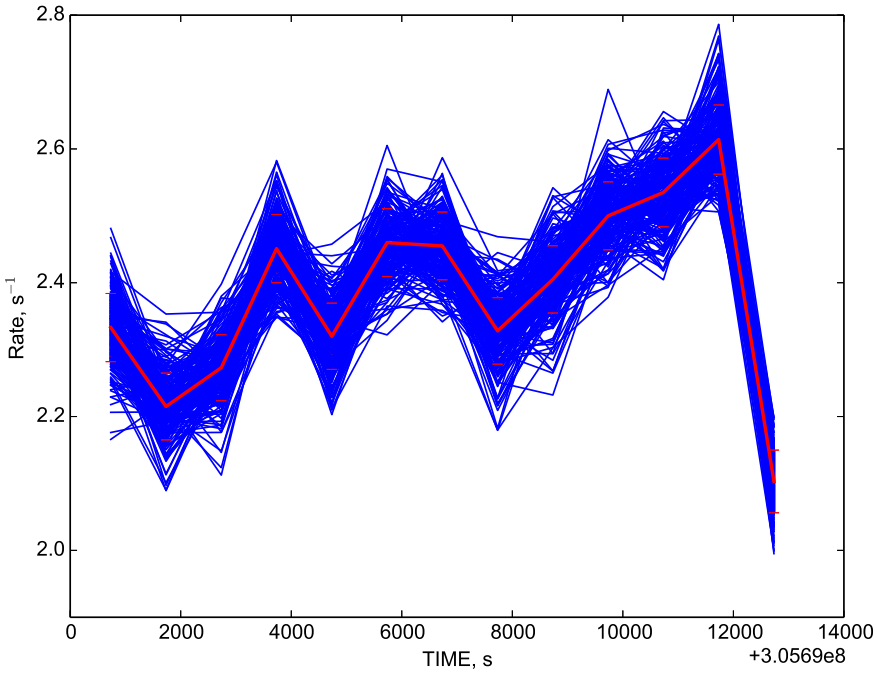
2.8
2.6
2.4
2.2
2.0
Rate, s^{-1}
0
2000
4000
6000
8000
10000
12000
14000
TIME, s
+3.0569e8

X11

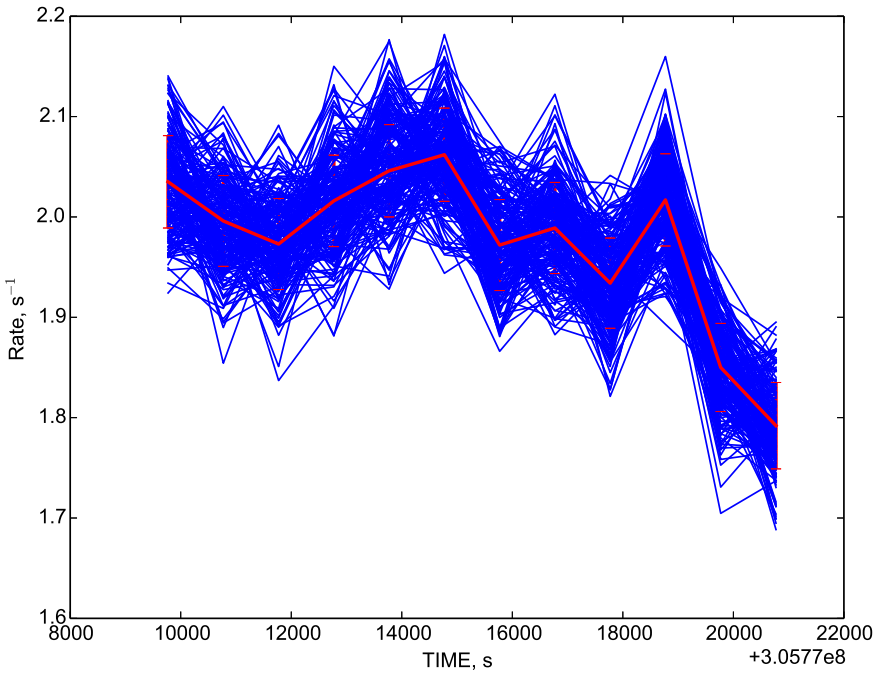
2.2
2.1
2.0
1.9
1.8
1.7
1.6
Rate, s^{-1}
8000
10000
12000
14000
16000
18000
20000
22000
TIME, s
+3.0577e8

X12

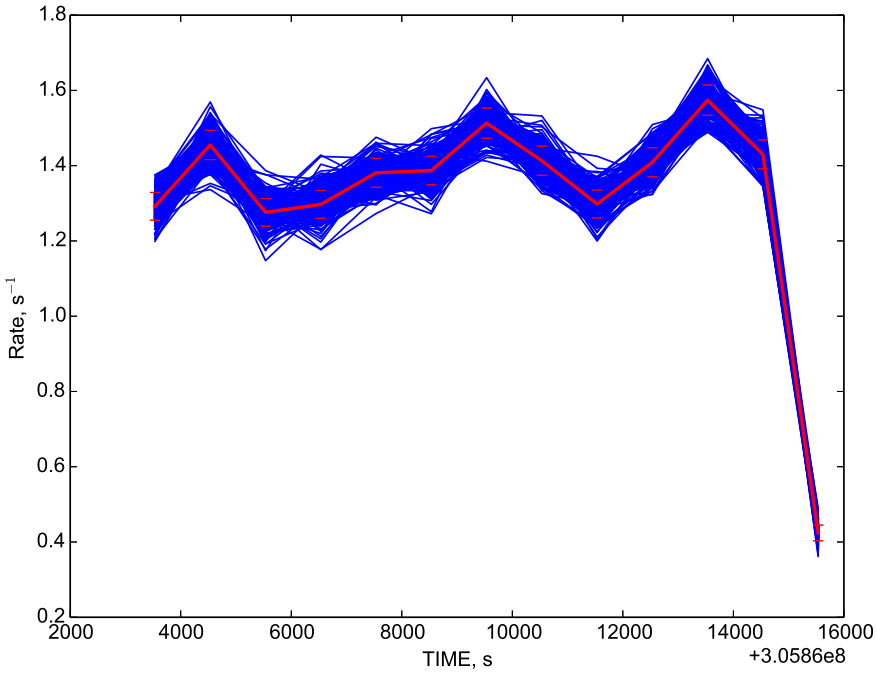
1.8
1.6
1.4
1.2
1.0
0.8
0.6
0.4
0.2
Rate, s^{-1}
2000
4000
6000
8000
10000
12000
14000
16000
TIME, s
+3.0586e8

X13

Bibliography

[1] Y. B. Zel'dovich. The Fate of a Star and the Evolution of Gravitational Energy Upon Accretion. *Soviet Physics Doklady*, 9:195, September 1964.

[2] C. R. Robinson, B. A. Harmon, M. L. McCollough, W. S. Paciesas, M. Sahi, D. M. Scott, C. A. Wilson, S. N. Zhang, and K. J. Deal. Long-Term Variability in Bright Hard X-Ray Sources: 5 + Years of BATSE Data. In C. Winkler, T. J.-L. Courvoisier, and P. Durouchoux, editors, *The Transparent Universe*, volume 382 of *ESA Special Publication*, page 249, 1997.

[3] B. C. Rubin, F. Lei, G. J. Fishman, M. H. Finger, B. A. Harmon, C. Kouveliotou, W. S. Paciesas, G. N. Pendleton, R. B. Wilson, and S. N. Zhang. A model of the gamma-ray background on the BATSE experiment. *A&AS*, 120:687–690, December 1996.

[4] J. S. Clark, S. P. Goodwin, P. A. Crowther, L. Kaper, M. Fairbairn, N. Langer, and C. Brocksopp. Physical parameters of the high-mass X-ray binary 4U1700-37. *A&A*, 392:909–920, September 2002.

[5] D. M. Marcu, K. Pottschmidt, A. M. Gottlieb, M. T. Wolff, P. A. Becker, J. Wilms, C. Ferrigno, and K. S. Wood. Looking into the Theory of Pulsar Accretion: Cen X-3 and XTE J1946+274. *ArXiv e-prints*, February 2015.

[6] A. Meilland, O. Delaa, P. Stee, S. Kanaan, F. Millour, D. Mourard, D. Bonneau, R. Petrov, N. Nardetto, A. Marcotto, A. Roussel, J. M. Clausse, K. Perraut, H. McAlister, T. ten Brummelaar, J. Sturmann, L. Sturmann, N. Turner, S. T. Ridgway, C. Farrington, and P. J. Goldfinger. The binary Be star δ Scorpii at high spectral and spatial resolution. I. Disk geometry and kinematics before the 2011 periastron. *A&A*, 532:A80, August 2011.

[7] J. M. Fierro, Z. Arzoumanian, M. Bailes, J. F. Bell, D. L. Bertsch, and et al. EGRET High-Energy gamma -Ray Pulsar Studies. II. Individual Millisecond Pulsars. *ApJ*, 447:807, July 1995.

[8] L. Kuiper, W. Hermsen, F. Verbunt, D. J. Thompson, I. H. Stairs, and et al. The likely detection of pulsed high-energy gamma -ray emission from millisecond pulsar PSR J0218+4232. *A&A*, 359:615–626, July 2000.

[9] B. M. Gaensler, D. H. Jones, and B. W. Stappers. An Optical Bow Shock around the Nearby Millisecond Pulsar J2124-3358. *ApJL*, 580:L137–L141, December 2002.

[10] T. M. Tauris and E. P. J. van den Heuvel. *Formation and evolution of compact stellar X-ray sources*, pages 623–665. April 2006.

[11] A. W. Hotan, M. Bailes, and S. M. Ord. High-precision baseband timing of 15 millisecond pulsars. *MNRAS*, 369:1502–1520, July 2006.

[12] S. A. Story, P. L. Gonthier, and A. K. Harding. Population Synthesis of Radio and Gamma-Ray Millisecond Pulsars from the Galactic Disk. *ApJ*, 671:713–726, December 2007.

[13] A. A. Abdo, M. Ackermann, W. B. Atwood, L. Baldini, J. Ballet, G. Barbiellini, M. G. Baring, D. Bastieri, and others. A Population of Gamma-Ray Millisecond Pulsars Seen with the Fermi Large Area Telescope. *Science*, 325:848, August 2009.

[14] A. A. Abdo, M. Ackermann, W. B. Atwood, L. Baldini, J. Ballet, G. Barbiellini, M. G. Baring, D. Bastieri, and others. Pulsed Gamma Rays from the Millisecond Pulsar J0030+0451 with the Fermi Large Area Telescope. *ApJ*, 699:1171–1177, July 2009.

[15] F. Camilo, D. R. Lorimer, N. D. R. Bhat, E. V. Gotthelf, J. P. Halpern, Q. D. Wang, F. J. Lu, and N. Mirabal. Discovery of a 136 millisecond radio and x-ray pulsar in supernova remnant g54.1+0.3. *ApJ*, 574:L71–L74, 2002.

[16] P. Podsiadlowski, N. Langer, A. J. T. Poelarends, S. Rappaport, A. Heger, and E. Pfahl. The Effects of Binary Evolution on the Dynamics of Core Collapse and Neutron Star Kicks. *ApJ*, 612:1044–1051, September 2004.

[17] L. Zhang, K. S. Cheng, Z. J. Jiang, and P. Leung. Gamma-Ray Luminosity and Death Lines of Pulsars with Outer Gaps. *ApJ*, 604:317–327, March 2004.

[18] L. Zhang, J. Fang, and S. B. Chen. High-Energy Properties of Pulsed Emission from Millisecond Pulsars. *ApJ*, 666:1165–1173, September 2007.

[19] N. E. White, J. H. Swank, and S. S. Holt. Accretion powered X-ray pulsars. *ApJ*, 270:711–734, July 1983.

[20] E. Flowers and M. A. Ruderman. Evolution of pulsar magnetic fields. *ApJ*, 215: 302–310, July 1977.

[21] M. Ruderman. Pulsars: Structure and Dynamics. *ARA&A*, 10:427, 1972.

[22] W. H. G. Lewin and P. C. Joss. X-ray bursters and the X-ray sources of the galactic bulge. *SSR*, 28:3–87, 1981.

[23] A. W. Strong, W. Collmar, K. Bennett, H. Bloemen, R. Diehl, W. Hermsen, A. Iyudin, H. Mayer-Hasselwander, J. Ryan, and V. Schönfelder. COMPTEL observations of a source in the direction of the galactic center. In S. Ritz, N. Gehrels, and C. R. Shrader, editors, *Gamma 2001: Gamma-Ray Astrophysics*, volume 587 of *American Institute of Physics Conference Series*, pages 21–25, October 2001.

[24] J. I. Katz. Sco X-1 and Cyg X-2 as binary systems. *A&A*, 39:241–244, March 1975.

[25] L. Cominsky, J. G. Jernigan, W. Ossmann, J. Doty, W. H. G. Lewin, and J. van Paradijs. A search for pulsations and eclipses from X-ray burst sources. *ApJ*, 242: 1102–1106, December 1980.

[26] D. R. Parsignault and J. E. Grindlay. Intensity and spectral variability of strong galactic X-ray sources observed by ANS. *ApJ*, 225:970–987, November 1978.

[27] S. E. Woosley and R. E. Taam. Gamma-ray bursts from thermonuclear explosions on neutron stars. *Nature*, 263:101–103, September 1976.

[28] J. H. Swank, R. H. Becker, E. A. Boldt, S. S. Holt, S. H. Pravdo, and P. J. Serlemitsos. Spectral evolution of a long X-ray burst. *ApJL*, 212:L73–L76, March 1977.

[29] R. Dodson, D. Legge, J. E. Reynolds, and P. M. McCulloch. The Vela Pulsar's Proper Motion and Parallax Derived from VLBI Observations. *ApJ*, 596:1137–1141, October 2003.

[30] E. D. Grundstrom, S. M. Caballero-Nieves, D. R. Gies, W. Huang, M. V. McSwain, S. E. Rafter, R. L. Riddle, S. J. Williams, and D. W. Wingert. Joint Hα and X-Ray Observations of Massive X-Ray Binaries. II. The Be X-Ray Binary and Microquasar LS I +61 303. *ApJ*, 656:437–443, February 2007.

[31] E. Chaisson and S. McMillan. *Astronomy Today, 5th Edition, by E. Chaisson and S. McMillan. Prentice Hall, 2005. ISBN 0-13-144596-0.* 2005.

[32] J. Arons. Magnetic field topology in pulsars. *ApJ*, 408:160–166, May 1993.

[33] W. Becker. Neutron Stars and Pulsars. In W. Becker, editor, *Astrophysics and Space Science Library*, volume 357 of *Astrophysics and Space Science Library*, 2009.

[34] C. Motch, F. Haberl, K. Dennerl, M. Pakull, and E. Janot-Pacheco. New massive X-ray binary candidates from the ROSAT Galactic Plane Survey. I. Results from a cross-correlation with OB star catalogues. *A&A*, 323:853–875, July 1997.

[35] T. Gold. Rotating Neutron Stars as the Origin of the Pulsating Radio Sources. *Nature*, 218:731–732, May 1968.

[36] V. F. Shvartsman. On the gamma and radio radiation from neutron stars in the state of accretion. *Astrofizika*, 6:123–134, 1970.

[37] V. F. Shvartsman. On the generation of relativistic particles by neutron stars in the state of accretion. *Astrofizika*, 6:309–317, 1970.

[38] V. F. Shvartsman. Gamma and radio emission of neutrons stars in the state of accretion. *Astrophysics*, 6:56–62, January 1970.

[39] V. M. Lipunov and N. I. Shakura. On the nature of binary-system X-ray pulsars. *Soviet Astronomy Letters*, 2:133–135, August 1976.

[40] F. Pacini. Rotating Neutron Stars, Pulsars and Supernova Remnants. *Nature*, 219:145–146, July 1968.

[41] K. Makishima, T. Mihara, F. Nagase, and Y. Tanaka. Cyclotron Resonance Effects in Two Binary X-Ray Pulsars and the Evolution of Neutron Star Magnetic Fields. *ApJ*, 525:978–994, November 1999.

[42] E. Pfahl, S. Rappaport, P. Podsiadlowski, and H. Spruit. A New Class of High-Mass X-Ray Binaries: Implications for Core Collapse and Neutron Star Recoil. *ApJ*, 574:364–376, July 2002.

[43] A. Possenti, R. Cerutti, M. Colpi, and S. Mereghetti. Re-examining the X-ray versus spin-down luminosity correlation of rotation powered pulsars. *A&A*, 387: 993–1002, June 2002.

[44] C. H. Nelson, J. W. MacKenty, S. M. Simkin, and R. E. Griffiths. Seyfert Galaxies. IV. Nuclear Profiles of Markarian Seyfert Galaxies from Hubble Space Telescope Images. *ApJ*, 466:713, August 1996.

[45] R. Giacconi, H. Gursky, E. Kellogg, E. Schreier, and H. Tananbaum. Discovery of Periodic X-Ray Pulsations in Centaurus X-3 from UHURU. *ApJL*, 167:L67, July 1971.

[46] J. E. Pringle and M. J. Rees. Accretion Disc Models for Compact X-Ray Sources. *A&A*, 21:1, October 1972.

[47] K. Davidson and J. P. Ostriker. Neutron-Star Accretion in a Stellar Wind: Model for a Pulsed X-Ray Source. *ApJ*, 179:585–598, January 1973.

[48] F. K. Lamb, C. J. Pethick, and D. Pines. A Model for Compact X-Ray Sources: Accretion by Rotating Magnetic Stars. *ApJ*, 184:271–290, August 1973.

[49] L. Bildsten, D. Chakrabarty, J. Chiu, M. H. Finger, D. T. Koh, R. W. Nelson, T. A. Prince, B. C. Rubin, D. M. Scott, M. Stollberg, B. A. Vaughan, C. A. Wilson, and R. B. Wilson. Observations of Accreting Pulsars. *ApJS*, 113:367–408, December 1997.

[50] M. H. Finger, D. T. Koh, R. W. Nelson, T. A. Prince, B. A. Vaughan, and R. B. Wilson. Discovery of hard X-ray pulsations from the transient source GRO J1744 - 28. *Nature*, 381:291–293, May 1996.

[51] G. L. Israel, A. Treves, L. Stella, G. Tagliaferri, and T. Belloni. X-Ray Sources in M31. *IAU Circ., 6156*, 6156, April 1995.

[52] P. Esposito, G. L. Israel, A. Belfiore, G. Novara, L. Sidoli, G. A. Rodríguez Castillo, A. De Luca, A. Tiengo, F. Haberl, R. Salvaterra, A. M. Read, D. Salvetti, S. Sandrelli, M. Marelli, J. Wilms, and D. D'Agostino. EXTraS discovery of an 1.2-s X-ray pulsar in M 31. *MNRAS*, 457:L5–L9, March 2016.

[53] G. Dubus, P. A. Charles, K. S. Long, P. J. Hakala, and E. Kuulkers. The eclipsing X-ray pulsar X-7 in M33. *MNRAS*, 302:731–734, February 1999.

[54] S. N. Shore, G. Sonneborn, S. Starrfield, R. Gonzalez-Riestra, and R. S. Polidan. The early bolometric evolution of Nova Cygni 1992. *ApJ*, 421:344–349, January 1994.

[55] J. M. Blondin, I. R. Stevens, and T. R. Kallman. Enhanced winds and tidal streams in massive X-ray binaries. *ApJ*, 371:684–695, April 1991.

[56] B. Warner and E. L. Robinson. Non-Radial Pulsations in White Dwarf Stars. *Nature Physical Science*, 239:2–7, September 1972.

[57] R. H. D. Corbet. The three types of high-mass X-ray pulsator. *MNRAS*, 220: 1047–1056, June 1986.

[58] L. Sidoli. Supergiant Fast X-ray Transients as transient sources in High Mass X-ray Binaries. *ArXiv e-prints*, November 2011.

[59] J. van Paradijs, R. E. Taam, and E. P. J. van den Heuvel. On the nature of the 'anomalous' 6-s X-ray pulsars. *A&A*, 299:L41, July 1995.

[60] D. T. Koh, L. Bildsten, D. Chakrabarty, R. W. Nelson, T. A. Prince, B. A. Vaughan, M. H. Finger, R. B. Wilson, and B. C. Rubin. Rapid Spin-Up Episodes in the Wind-fed Accreting Pulsar GX 301-2. *ApJ*, 479:933–947, April 1997.

[61] S. Mereghetti, D. Cremonesi, M. Feroci, and M. Tavani.

[62] A. T. Okazaki and I. Negueruela. A natural explanation for periodic X-ray outbursts in Be/X-ray binaries. *A&A*, 377:161–174, October 2001.

[63] T. Enoto, M. Sasano, S. Yamada, T. Tamagawa, K. Makishima, K. Pottschmidt, D. Marcu, R. H. D. Corbet, F. Fuerst, and J. Wilms. Spectral and Timing Nature of the Symbiotic X-Ray Binary 4U 1954+319: The Slowest Rotating Neutron Star in an X-Ray Binary System. *ApJ*, 786:127, May 2014.

[64] J. Arons. Pulsars as gamma ray sources. *A&AS*, 120:C49+, November 1996.

[65] K. S. Cheng and L. Zhang. The Statistics of Gamma-Ray Pulsars. *ApJ*, 498:327, May 1998.

[66] F. R. Harnden, Jr., B. Buehler, R. Giacconi, J. Grindlay, P. Hertz, E. Schreier, F. Seward, H. Tananbaum, and L. van Speybroeck. X-Ray Observations of the Crab Nebula with the Einstein Observatory. In *Bulletin of the American Astronomical Society*, volume 11 of *Bulletin of the American Astronomical Society*, page 789, September 1979.

[67] D. J. Thompson. Gamma ray pulsars: Observations. In F. A. Aharonian and H. J. Völk, editors, *American Institute of Physics Conference Series*, volume 558 of *American Institute of Physics Conference Series*, pages 103–114, April 2001.

[68] M. Ruderman, K. Chen, K. S. Cheng, and J. P. Halpern. Gamma-ray pulsars and Geminga. In M. Friedlander, N. Gehrels, and D. J. Macomb, editors, *American Institute of Physics Conference Series*, volume 280 of *American Institute of Physics Conference Series*, pages 259–271, 1993.

[69] I.-A. Yadigaroglu and R. W. Romani. Gamma-Ray Pulsars and Massive Stars in the Solar Neighborhood. *ApJ*, 476:347–+, February 1997.

[70] D. J. Thompson, Z. Arzoumanian, D. L. Bertsch, K. T. S. Brazier, and et al. EGRET high-energy gamma-ray pulsar studies. 1: Young spin-powered pulsars. *ApJ*, 436:229–238, November 1994.

[71] M. A. McLaughlin and J. M. Cordes. The Gamma-Ray Pulsar Population. *ApJ*, 538:818–830, August 2000.

[72] M. Ziegler, B. M. Baughman, R. P. Johnson, and W. B. Atwood. A Search for Radio-Quiet Gamma-Ray Pulsars in EGRET Data Using a Time-Differencing Technique. *ApJ*, 680:620–626, June 2008.

[73] A. Pellizzoni, M. Pilia, A. Possenti, A. Chen, A. Giuliani, and et al. Discovery of New Gamma-Ray Pulsars with AGILE. *ApJL*, 695:L115–L119, April 2009.

[74] A. Harding. Theory and Observations of the High B/Slow Radio Pulsars. In *KITP Conference: Spin, Magnetism and Cooling of Young Neutron Stars*, October 2000.

[75] P. Goldreich and W. H. Julian. Pulsar Electrodynamics. *ApJ*, 157:869, August 1969.

[76] J. K. Daugherty and A. K. Harding. Electromagnetic cascades in pulsars. *ApJ*, 252:337–347, January 1982.

[77] V. V. Usov and D. B. Melrose. Pulsars with Strong Magnetic Fields - Polar Gaps Bound Pair Creation and Nonthermal Luminosities. *Australian Journal of Physics*, 48:571, 1995.

[78] K. S. Cheng, C. Ho, and M. Ruderman. Energetic radiation from rapidly spinning pulsars. I - Outer magnetosphere gaps. II - VELA and Crab. *ApJ*, 300:500–539, January 1986.

[79] R. W. Romani. Gamma-Ray Pulsars: Radiation Processes in the Outer Magnetosphere. *ApJ*, 470:469, October 1996.

[80] K. Hirotani and S. Shibata. One-dimensional electric field structure of an outer gap accelerator - I. gamma-ray production resulting from curvature radiation. *MNRAS*, 308:54–66, September 1999.

[81] P. L. Gonthier, M. S. Ouellette, J. Berrier, S. O'Brien, and A. K. Harding. Galactic Populations of Radio and Gamma-Ray Pulsars in the Polar Cap Model. *ApJ*, 565: 482–499, January 2002.

[82] A. K. Harding and A. G. Muslimov. Pulsar Polar Cap Heating and Surface Thermal X-Ray Emission. II. Inverse Compton Radiation Pair Fronts. *ApJ*, 568:862–877, April 2002.

[83] M. G. Baring. High-energy emission from pulsars: the polar cap scenario. *Advances in Space Research*, 33:552–560, 2004.

[84] H. I. Nel, O. C. de Jager, B. C. Raubenheimer, C. Brink, P. J. Meintjes, and A. R. North. TeV Gamma-Ray Observations of Compton Gamma-Ray Observatory Pulsars: Evidence against Inverse-Compton Controlled Outer Gaps. *ApJ*, 418:836, December 1993.

[85] J. Dyks and B. Rudak. Approximate expressions for polar gap electric field of pulsars. *A&A*, 362:1004–1007, October 2000.

[86] R. W. Romani and I.-A. Yadigaroglu. Gamma-ray pulsars: Emission zones and viewing geometries. *ApJ*, 438:314–321, January 1995.

[87] L. Zhang and K. S. Cheng. High-Energy Radiation from Rapidly Spinning Pulsars with Thick Outer Gaps. *ApJ*, 487:370–379, September 1997.

[88] J. M. Rankin. Toward an empirical theory of pulsar emission. VI - The geometry of the conal emission region. *ApJ*, 405:285–297, March 1993.

[89] J. A. Gil and J. L. Han. Geometry of Pulsar Emission and Pulse Width Distribution. *ApJ*, 458:265, February 1996.

[90] G. Dubus and B. Cerutti. What caused the GeV flare of PSR B1259-63? *A&A*, 557:A127, September 2013.

[91] D. V. Khangulyan, F. A. Aharonian, S. V. Bogovalov, A. V. Koldoba, and G. V. Ustyugova. Hydrodynamics of Interaction of Pulsar and Stellar Winds and its Impact on the High Energy Radiation of Binary Pulsar Systems. *International Journal of Modern Physics D*, 17:1909–1915, 2008.

[92] P. C. Gregory. Bayesian Analysis of Radio Observations of the Be X-Ray Binary LS I +61° 303. *ApJ*, 575:427–434, August 2002.

[93] J. Casares, I. Ribas, J. M. Paredes, J. Martí, and C. Allende Prieto. Orbital parameters of the microquasar LS I +61 303. *MNRAS*, 360:1105–1109, July 2005.

[94] C. Aragona, M. V. McSwain, E. D. Grundstrom, A. N. Marsh, R. M. Roettenbacher, K. M. Hessler, T. S. Boyajian, and P. S. Ray. The Orbits of the γ-Ray Binaries LS I +61 303 and LS 5039. *ApJ*, 698:514–518, June 2009.

[95] A. A. Zdziarski, A. Neronov, and M. Chernyakova. A compact pulsar wind nebula model of the γ-ray-loud binary LS I +61° 303. *MNRAS*, 403:1873–1886, April 2010.

[96] V. Dhawan, A. Mioduszewski, and M. Rupen. LS I +61 303 is a Be-Pulsar binary, not a Microquasar. In *VI Microquasar Workshop: Microquasars and Beyond*, 2006.

[97] M. Chernyakova, A. Neronov, S. Molkov, D. Malyshev, A. Lutovinov, and G. Pooley. Superorbital Modulation of X-Ray Emission from Gamma-Ray Binary LSI +61 303. *ApJL*, 747:L29, March 2012.

[98] F. A. Harrison, P. S. Ray, D. A. Leahy, E. B. Waltman, and G. G. Pooley. Simultaneous X-Ray and Radio Monitoring of the Unusual Binary LS I +61 303: Measurements of the Light Curve and High-Energy Spectrum. *ApJ*, 528:454–461, January 2000.

[99] M. Chernyakova, A. Neronov, A. Lutovinov, J. Rodriguez, and S. Johnston. XMM-Newton observations of PSR B1259-63 near the 2004 periastron passage. *MNRAS*, 367:1201–1208, April 2006.

[100] W. B. Atwood, A. A. Abdo, M. Ackermann, W. Althouse, and et al. The Large Area Telescope on the Fermi Gamma-Ray Space Telescope Mission. *ApJ*, 697: 1071–1102, June 2009.

[101] A. Smith, P. Kaaret, J. Holder, A. Falcone, G. Maier, D. Pandel, and M. Stroh. Long-Term X-Ray Monitoring of the TeV Binary LS I +61 303 With the Rossi X-Ray Timing Explorer. *ApJ*, 693:1621–1627, March 2009.

[102] D. F. Torres, S. Zhang, J. Li, N. Rea, G. A. Caliandro, D. Hadasch, Y. Chen, J. Wang, and P. S. Ray. Variability in the Orbital Profiles of the X-ray Emission of the γ-ray Binary LS I +61 303. *ApJL*, 719:L104–L108, August 2010.

[103] J. Li, D. F. Torres, S. Zhang, Y. Chen, D. Hadasch, P. S. Ray, P. Kretschmar, N. Rea, and J. Wang. Long-term X-Ray Monitoring of LS I +61 303: Analysis of Spectral Variability and Flares. *ApJ*, 733:89, June 2011.

[104] R. K. Zamanov, J. Martí, J. M. Paredes, J. Fabregat, M. Ribó, and A. E. Tarasov. Evidence of Hα periodicities in LS I+61 303. *A&A*, 351:543–550, November 1999.

[105] J. Aleksić, E. A. Alvarez, L. A. Antonelli, P. Antoranz, and et al. Detection of the γ-Ray Binary LS I +61° 303 in a Low-flux State at Very High Energy γ-Rays with the MAGIC Telescopes in 2009. *ApJ*, 746:80, February 2012.

[106] V. A. Acciari, E. Aliu, T. Arlen, M. Bautista, M. Beilicke, and et al. Multiwavelength Observations of LS I +61° 303 with Veritas, Swift, and RXTE. *ApJ*, 700: 1034–1041, August 2009.

[107] V. A. Acciari, E. Aliu, T. Arlen, T. Aune, M. Beilicke, and et al. VERITAS Observations of the TeV Binary LS I +61° 303 During 2008-2010. *ApJ*, 738:3, September 2011.

[108] J. Marti, J. M. Paredes, and M. Ribo. The system LS 5039: a new massive radio emitting X-ray binary. *ApJ*, 338:L71–L74, October 1998.

[109] J. M. Paredes, J. Martí, M. Ribó, and M. Massi. Discovery of a High-Energy Gamma-Ray-Emitting Persistent Microquasar. *Science*, 288:2340–2342, June 2000.

[110] J. M. Paredes, M. Ribó, E. Ros, J. Martí, and M. Massi. Confirmation of persistent radio jets in the microquasar LS 5039. *A&A*, 393:L99–L102, October 2002.

[111] J. M. Paredes. Microquasars as High-energy Gamma-ray Sources. *Chinese Journal of Astronomy and Astrophysics Supplement*, 5:121–132, June 2005.

[112] M. Ribó, J. A. Combi, and I. F. Mirabel. Towards a Population of HMXB/NS Microquasars as Counterparts of Low-Latitude Unidentified EGRET Sources. *ApSS*, 297:143–154, June 2005.

[113] F. Aharonian, A. G. Akhperjanian, K.-M. Aye, A. R. Bazer-Bachi, and et al. Discovery of Very High Energy Gamma Rays Associated with an X-ray Binary. *Science*, 309:746–749, July 2005.

[114] J. S. Clark, P. Reig, S. P. Goodwin, V. M. Larionov, P. Blay, M. J. Coe, J. Fabregat, I. Negueruela, I. Papadakis, and I. A. Steele. On the radio emitting high mass X-ray binary LS 5039. *ApJ*, 376:476–483, September 2001.

[115] M. V. McSwain, D. R. Gies, W. Huang, P. J. Wiita, D. W. Wingert, and L. Kaper. The N Enrichment and Supernova Ejection of the Runaway Microquasar LS 5039. *ApJ*, 600:927–938, January 2004.

[116] J. A. Combi, P. Benaglia, G. E. Romero, and M. Sugizaki. G337.2+0.1: A new X-ray supernova remnant?. *ApJ*, 431:L9–L12, February 2005.

[117] V. Bosch-Ramon, D. Khangulyan, and F. A. Aharonian. The magnetic field and the location of the TeV emitter in Cygnus X-1 and LS 5039. *A&A*, 489:L21–L24, October 2008.

[118] J. Moldón, M. Ribó, and J. M. Paredes. Periodic morphological changes in the radio structure of the gamma-ray binary LS 5039. *A&A*, 548:A103, December 2012.

[119] T. Kishishita, T. Tanaka, Y. Uchiyama, and T. Takahashi. Long-Term Stability of Nonthermal X-Ray Modulation in the Gamma-Ray Binary LS 5039. *ApJL*, 697: L1–L5, May 2009.

[120] F. Aharonian. Relativistic Jets as Powerful Particle Accelerators and Gamma-ray Emitters. In *AAS/High Energy Astrophysics Division #9*, volume 38 of *Bulletin of the American Astronomical Society*, page 362, September 2006.

[121] A. Szostek and G. Dubus. X-ray absorption and occultation in LS 5039. *MNRAS*, 411:193–199, February 2011.

[122] F. A. Aharonian, A. G. Akhperjanian, A. R. Bazer-Bachi, B. Behera, and et al. Discovery of a point-like very-high-energy γ-ray source in Monoceros. *A&A*, 469: L1–L4, July 2007.

[123] J. Casares, M. Ribó, I. Ribas, J. M. Paredes, F. Vilardell, and I. Negueruela. On the binary nature of the γ-ray sources AGL J2241+4454 (= MWC 656) and HESS J0632+057 (= MWC 148). *MNRAS*, 421:1103–1112, April 2012.

[124] C. Aragona, M. V. McSwain, and M. De Becker. HD 259440: The Proposed Optical Counterpart of the γ-ray Binary HESS J0632+057. *ApJ*, 724:306–312, November 2010.

[125] S. D. Bongiorno, A. D. Falcone, M. Stroh, J. Holder, J. L. Skilton, J. A. Hinton, N. Gehrels, and J. Grube. A New TeV Binary: The Discovery of an Orbital Period in HESS J0632+057. *ApJL*, 737:L11, August 2011.

[126] J. Aleksić, E. A. Alvarez, L. A. Antonelli, and P. et al. Antoranz. Detection of VHE γ-Rays from HESS J0632+057 during the 2011 February X-Ray Outburst with the MAGIC Telescopes. *ApJL*, 754:L10, July 2012.

[127] G. A. Caliandro, A. B. Hill, D. F. Torres, D. Hadasch, P. Ray, A. Abdo, J. W. T. Hessels, A. Ridolfi, A. Possenti, M. Burgay, N. Rea, P. H. T. Tam, R. Dubois, G. Dubus, T. Glanzman, and T. Jogler. The missing GeV γ-ray binary: searching for HESS J0632+057 with Fermi-LAT. *MNRAS*, 436:740–749, November 2013.

[128] J. L. Skilton, M. Pandey-Pommier, J. A. Hinton, C. C. Cheung, F. A. Aharonian, J. Brucker, G. Dubus, A. Fiasson, S. Funk, Y. Gallant, A. Marcowith, and O. Reimer. The radio counterpart of the likely TeV binary HESSJ0632+057. *MNRAS*, 399:317–322, October 2009.

[129] J. Moldón, S. Johnston, M. Ribó, J. M. Paredes, and A. T. Deller. Discovery of Extended and Variable Radio Structure from the Gamma-ray Binary System PSR B1259-63/LS 2883. *ApJL*, 732:L10, May 2011.

[130] Fermi LAT Collaboration, M. Ackermann, M. Ajello, J. Ballet, G. Barbiellini, D. Bastieri, A. Belfiore, R. Bellazzini, and et al. Periodic Emission from the Gamma-Ray Binary 1FGL J1018.6-5856. *Science*, 335:189, January 2012.

[131] R. H. D. Corbet, C. C. Cheung, M. Kerr, R. Dubois, D. Donato, G. A. Caliandro, M. J. Coe, P. G. Edwards, M. D. Filipovic, J. L. Payne, and J. Stevens. 1FGL

J1018.6-5856: a New Gamma-ray Binary. *The Astronomer's Telegram*, 3221:1, March 2011.

[132] J. Li, D. F. Torres, Y. Chen, D. Götz, N. Rea, S. Zhang, G. A. Caliandro, and J. Wang. INTEGRAL Observations of the γ-Ray Binary 1FGL J1018.6-5856. *ApJL*, 738:L31, September 2011.

[133] N. Bartel. Determinations of distances to radio sources with VLBI. In M. J. Reid and J. M. Moran, editors, *The Impact of VLBI on Astrophysics and Geophysics*, volume 129 of *IAU Symposium*, pages 175–184, 1988.

[134] E. Middelberg and U. Bach. High resolution radio astronomy using very long baseline interferometry. *Reports on Progress in Physics*, 71(6):066901, June 2008.

[135] M. Lindqvist and A. Szomoru. The present status and the future of the European VLBI Network. *IAU General Assembly*, 22:2241681, August 2015.

[136] R. Petre and P. J. Serlemitsos. Properties and Performance of the Broad-Band X-ray Telescope. In *Bulletin of the American Astronomical Society*, volume 21 of *Bulletin of the American Astronomical Society*, page 1076, September 1989.

[137] R. Giacconi, H. Gursky, F. R. Paolini, and B. B. Rossi. Evidence for x Rays From Sources Outside the Solar System. *Physical Review Letters*, 9:439–443, December 1962.

[138] R. Giacconi and B. Rossi. A 'Telescope' for Soft X-Ray Astronomy. *Journal of Geophysical Research*, 65:773, February 1960.

[139] R. Giacconi, W. P. Reidy, T. Zehnpfennig, J. C. Lindsay, and W. S. Muney. Solar X-Ray Image Obtained Using Grazing-Incidence Optics. *ApJ*, 142:1274–1278, October 1965.

[140] J. DePasquale, K. Arcand, and P. Edmonds. High Energy Vision: Processing X-rays. *ArXiv e-prints*, September 2015.

[141] B. Aschenbach. Realization of X-ray telescopes-from design to performance. *Experimental Astronomy*, 26:95–109, August 2009.

[142] R. Giacconi, G. Branduardi, U. Briel, A. Epstein, D. Fabricant, E. Feigelson, W. Forman, P. Gorenstein, J. Grindlay, H. Gursky, F. R. Harnden, J. P. Henry, C. Jones, E. Kellogg, D. Koch, S. Murray, E. Schreier, F. Seward, H. Tananbaum, K. Topka, L. Van Speybroeck, S. S. Holt, R. H. Becker, E. A. Boldt, P. J. Serlemitsos, G. Clark, C. Canizares, T. Markert, R. Novick, D. Helfand, and K. Long. The Einstein /HEAO 2/ X-ray Observatory. *ApJ*, 230:540–550, June 1979.

[143] S. S. Murray, G. Fabbiano, A. Epstein, R. Giacconi, and A. C. Fabian. High-resolution X-ray observations of the Cassiopeia A supernova remnant with the Einstein Observatory. *ApJL*, 234:L69–L72, November 1979.

[144] Y. Tanaka, H. Inoue, and S. S. Holt. The X-ray astronomy satellite ASCA. *PASJ*, 46:L37–L41, June 1994.

[145] F. Jansen, D. Lumb, B. Altieri, J. Clavel, M. Ehle, and et al. XMM-Newton observatory. I. The spacecraft and operations. *A&A*, 365:L1–L6, January 2001.

[146] D. H Lumb, N. Schartel, and F. A Jansen. XMM-Newton (X-Ray Mulit-Mirror Mission) Observatory. *ArXiv e-prints*, February 2012.

[147] B. Aschenbach, U. G. Briel, F. Haberl, H. W. Braeuninger, W. Burkert, A. Oppitz, P. Gondoin, and D. H. Lumb. Imaging performance of the XMM-Newton x-ray telescopes. In J. E. Truemper and B. Aschenbach, editors, *X-Ray Optics, Instruments, and Missions III*, volume 4012, pages 731–739, July 2000.

[148] XMM-Newton SOC. *XMM-Newton Users Handbook*. 2016.

[149] M. J. L. Turner, A. Abbey, M. Arnaud, M. Balasini, M. Barbera, and et al. The European Photon Imaging Camera on XMM-Newton: The MOS cameras : The MOS cameras. *A&A*, 365:L27–L35, January 2001.

[150] A. M. Read, M. Guainazzi, and S. Sembay. Cross-calibration of the XMM-Newton EPIC pn and MOS on-axis effective areas using 2XMM sources. *A&A*, 564:A75, April 2014.

[151] A. Brinkman, H. Aarts, A. den Boggende, T. Bootsma, L. Dubbeldam, J. den Herder, J. Kaastra, P. de Korte, B. van Leeuwen, R. Mewe, F. Paerels, C. de Vries, J. Cottam, T. Decker, S. Kahn, A. Rasmussen, J. Spodek, G. Branduardi-Raymont, P. Guttridge, K. Thomsen, A. Zehnder, and M. Guedel. The Reflection Grating Spectrometer onboard XMM. In *Science with XMM*, 1998.

[152] J. W. den Herder, A. C. Brinkman, S. M. Kahn, G. Branduardi-Raymont, K. Thomsen, H. Aarts, M. Audard, J. V. Bixler, A. J. den Boggende, J. Cottam, T. Decker, L. Dubbeldam, C. Erd, H. Goulooze, M. Güdel, P. Guttridge, C. J. Hailey, K. A. Janabi, J. S. Kaastra, P. A. J. de Korte, B. J. van Leeuwen, C. Mauche, A. J. McCalden, R. Mewe, A. Naber, F. B. Paerels, J. R. Peterson, A. P. Rasmussen, K. Rees, I. Sakelliou, M. Sako, J. Spodek, M. Stern, T. Tamura, J. Tandy, C. P. de Vries, S. Welch, and A. Zehnder. The Reflection Grating Spectrometer on board XMM-Newton. *A&A*, 365:L7–L17, January 2001.

[153] K. O. Mason, A. Breeveld, R. Much, M. Carter, F. A. Cordova, M. S. Cropper, J. Fordham, H. Huckle, C. Ho, H. Kawakami, J. Kennea, T. Kennedy, J. Mittaz, D. Pandel, W. C. Priedhorsky, T. Sasseen, R. Shirey, P. Smith, and J.-M. Vreux. The XMM-Newton optical/UV monitor telescope. *A&A*, 365:L36–L44, January 2001.

[154] M. C. Weisskopf, B. Brinkman, C. Canizares, G. Garmire, S. Murray, and L. P. Van Speybroeck. An Overview of the Performance and Scientific Results from the Chandra X-Ray Observatory. *PASP*, 114:1–24, January 2002.

[155] J. E. Davis. A Pile-up Model For The Chandra HETGS. In *AAS/High Energy Astrophysics Division #10*, volume 10 of *AAS/High Energy Astrophysics Division*, page 4.03, March 2008.

[156] Chandra X-ray Center. *The Chandra Proposers' Observatory Guide*. 2015.

[157] A. Fruscione, J. C. McDowell, G. E. Allen, N. S. Brickhouse, D. J. Burke, J. E. Davis, N. Durham, M. Elvis, E. C. Galle, D. E. Harris, D. P. Huenemoerder, J. C. Houck, B. Ishibashi, M. Karovska, F. Nicastro, M. S. Noble, M. A. Nowak, F. A. Primini, A. Siemiginowska, R. K. Smith, and M. Wise. CIAO: Chandra's data analysis system. In *Society of Photo-Optical Instrumentation Engineers (SPIE) Conference Series*, volume 6270 of *Procspie*, page 62701V, June 2006. doi: 10.1117/12.671760.

[158] P. Freeman, S. Doe, and A. Siemiginowska. Sherpa: a mission-independent data analysis application. In J.-L. Starck and F. D. Murtagh, editors, *Astronomical Data Analysis*, volume 4477 of *Procspie*, pages 76–87, November 2001.

[159] P. J. Serlemitsos, Y. Soong, K.-W. Chan, T. Okajima, J. P. Lehan, and et al. The X-Ray Telescope onboard Suzaku. *PASJ*, 59:9–21, January 2007.

[160] R. L. Kelley, K. Mitsuda, C. A. Allen, P. Arsenovic, M. D. Audley, and et al. The Suzaku High Resolution X-Ray Spectrometer. *PASJ*, 59:77–112, January 2007.

[161] K. Koyama, H. Tsunemi, T. Dotani, M. W. Bautz, K. Hayashida, and et al. X-Ray Imaging Spectrometer (XIS) on Board Suzaku. *PASJ*, 59:23–33, January 2007.

[162] M. Kokubun, K. Makishima, T. Takahashi, T. Murakami, M. Tashiro, and et al. In-Orbit Performance of the Hard X-Ray Detector on Board Suzaku. *PASJ*, 59: 53–76, January 2007.

[163] T. Takahashi, K. Abe, M. Endo, Y. Endo, Y. Ezoe, Y. Fukazawa, M. Hamaya, S. Hirakuri, S. Hong, and et al. Hard X-Ray Detector (HXD) on Board Suzaku. *PASJ*, 59:35–51, January 2007.

[164] The Suzaku Team. *The Suzaku Data Reduction Guide*. 2013.

[165] Y. Uchiyama, T. Tanaka, T. Takahashi, K. Mori, and K. Nakazawa. Suzaku Observations of PSR B1259-63: A New Manifestation of Relativistic Pulsar Wind. *ApJ*, 698:911–921, June 2009.

[166] N. Gehrels, G. Chincarini, P. Giommi, K. O. Mason, J. A. Nousek, and et al. The Swift Gamma-Ray Burst Mission. *ApJ*, 611:1005–1020, August 2004.

[167] S. D. Barthelmy, L. M. Barbier, J. R. Cummings, E. E. Fenimore, N. Gehrels, D. Hullinger, H. A. Krimm, C. B. Markwardt, D. M. Palmer, A. Parsons, G. Sato, M. Suzuki, T. Takahashi, M. Tashiro, and J. Tueller. The Burst Alert Telescope (BAT) on the SWIFT Midex Mission. *Space Science Reviews*, 120:143–164, October 2005.

[168] D. N. Burrows, J. E. Hill, J. A. Nousek, A. A. Wells, A. D. Short, R. Willingale, O. Citterio, G. Chincarini, and G. Tagliaferri. Swift X-Ray Telescope. In K. A. Flanagan and O. H. Siegmund, editors, *X-Ray and Gamma-Ray Instrumentation for Astronomy XI*, volume 4140 of *Proc. SPIE*, pages 64–75, December 2000.

[169] ASI Science Data Center. *The Swift XRT Data Reduction Guide*. 2005.

[170] W. B. Atwood, A. A. Abdo, M. Ackermann, W. Althouse, B. Anderson, M. Axelsson, L. Baldini, J. Ballet, D. L. Band, G. Barbiellini, and et al. The Large Area Telescope on the Fermi Gamma-Ray Space Telescope Mission. *ApJ*, 697: 1071–1102, June 2009.

[171] W. N. Johnson, J. E. Grove, B. F. Phlips, H. Arrighi, J. Krizmanic, J. Norris, S. Ritz, S. Singh, and D. Suson. CsI Hodoscopic Calorimeter for the GLAST Mission. In *AAS/High Energy Astrophysics Division #4*, volume 31 of *Bulletin of the American Astronomical Society*, page 735, April 1999.

[172] V. Vasileiou. BKGE: Fermi-LAT Background Estimator. Astrophysics Source Code Library, November 2014.

[173] A. A. Abdo, M. Ackermann, W. B. Atwood, L. Baldini, J. Ballet, G. Barbiellini, M. G. Baring, D. Bastieri, and others. The On-orbit Calibrations for the Fermi Large Area Telescope. *Astropart. Phys.*, April 2009.

[174] R. Buehler, F. D'Ammando, and E. Hays. Fermi LAT confirmation of enhanced gamma-ray emission from the Crab Nebula region. *The Astronomer's Telegram*, 2861, September 2010.

[175] A. A. Abdo, M. Ackermann, M. Ajello, A. Allafort, L. Baldini, J. Ballet, G. Barbiellini, D. Bastieri, K. Bechtol, R. Bellazzini, B. Berenji, R. D. Blandford, E. D. Bloom, and et al. Gamma-Ray Flares from the Crab Nebula. *Science*, 331:739, February 2011.

[176] R. Buehler, J. D. Scargle, R. D. Blandford, L. Baldini, and et al. Gamma-Ray Activity in the Crab Nebula: The Exceptional Flare of 2011 April. *ApJ*, 749:26, April 2012.

[177] A. A. Abdo, M. Ackermann, M. Ajello, W. B. Atwood, M. Axelsson, L. Baldini, J. Ballet, G. Barbiellini, M. G. Baring, D. Bastieri, and et al. The First Fermi Large Area Telescope Catalog of Gamma-ray Pulsars. *ApJS*, 187:460–494, April 2010.

[178] P. L. Nolan, A. A. Abdo, M. Ackermann, M. Ajello, A. Allafort, E. Antolini, W. B. Atwood, M. Axelsson, L. Baldini, J. Ballet, and et al. Fermi LAT second source catalog (2FGL) (Nolan+, 2012). *VizieR Online Data Catalog*, 219:90031, June 2012.

[179] K. A. Arnaud. XSPEC: The First Ten Years. In G. H. Jacoby and J. Barnes, editors, *Astronomical Data Analysis Software and Systems V*, volume 101 of *Astronomical Society of the Pacific Conference Series*, page 17, 1996.

[180] R. Morrison and D. McCammon. Interstellar photoelectric absorption cross sections, 0.03-10 keV. *ApJ*, 270:119–122, July 1983.

[181] E. Anders and M. Ebihara. Solar-system abundances of the elements. *Geochimica et Cosmochimica Acta*, 46:2363–2380, November 1982.

[182] D. Barret and S. Vaughan. Maximum Likelihood Fitting of X-Ray Power Density Spectra: Application to High-frequency Quasi-periodic Oscillations from the Neutron Star X-Ray Binary 4U1608-522. *ApJ*, 746:131, February 2012.

[183] W. Cash. Parameter estimation in astronomy through application of the likelihood ratio. *ApJ*, 228:939–947, March 1979.

[184] A. Siemiginowska. *Handbook of X-ray Astronomy, eds. Arnaud, K.A., Smith, R.K. and Siemiginowska, A., Cambridge University Press, Cambridge.* 2011.

[185] S. Vaughan. A Bayesian test for periodic signals in red noise. *MNRAS*, 402: 307–320, February 2010.

[186] K. Binder. *Monte Carlo methods in statistical physics , by Binder, K. Berlin ; New York : Springer-Verlag, c1986. Topics in current physics ; 7.* 1986.

[187] D. W. K. Binder, Heermann. *Monte Carlo simulation in statistical physics: an introduction/ K. Binder, D.W. Heermann. 4th enl. ed. Berlin; New York: Springer, c2002. Springer series in solid-state sciences, ISSN 0171-1873; 80.* 2002.

[188] G. R. Blumenthal and R. J. Gould. Bremsstrahlung, Synchrotron Radiation, and Compton Scattering of High-Energy Electrons Traversing Dilute Gases. *Reviews of Modern Physics*, 42:237–271, 1970.

[189] R.A. Sunyaev. *Fizika kosmosa (The physics of space), by Sunyaev, R.A.; Moscow, 1986. Sovetskaya entsiklopediya.* 1986.

[190] A. Mastichiadis. Relativistic electrons in photon fields - Effects of triplet pair production on inverse Compton gamma-ray spectra. *MNRAS*, 253:235–244, November 1991.

[191] C. I. Moore, J. P. Knauer, and D. D. Meyerhofer. Observation of the Transition from Thomson to Compton Scattering in Multiphoton Interactions with Low-Energy Electrons. *Physical Review Letters*, 74:2439–2442, March 1995.

[192] M. Cooper, P. Mijnarends, N. Shiotani, N. Sakai, and A. Bansil. *X-ray Compton Scattering, by Cooper, M. et al.; OUP Oxford, 2004. 394pp.* 2004.

[193] M. Hoshino, J. Arons, Y. A. Gallant, and A. B. Langdon. Relativistic magnetosonic shock waves in synchrotron sources - Shock structure and nonthermal acceleration of positrons. *ApJ*, 390:454–479, May 1992.

[194] J. G. Lominadze, G. Z. Machabeli, and V. V. Usov. Theory of NP 0532 pulsar radiation and the nature of the activity of the Crab Nebula. *Ap&SS*, 90:19–43, February 1983.

[195] G. Z. Machabeli and V. V. Usov. Cyclotron instability in the magnetosphere of the Crab nebula pulsar, and the origin of its radiation. *Soviet Astronomy Letters*, 5:238–241, October 1979.

[196] N. Chkheidze and I. Babyk. Nonthermal emission model of isolated X-ray pulsar RX J0420.0-5022. *Advances in Astronomy and Space Physics*, 3:32–37, August 2013.

[197] N. Chkheidze and I. Babyk. Synchrotron emission model of gamma-ray pulsar PSR J2021+3651. *New Astronomy*, 35:27–31, February 2015.

[198] N. Chkheidze. Synchrotron emission model of RX J1856.5-3754. *New Astronomy*, 17:227–231, February 2012.

[199] F. Haberl. The magnificent seven: magnetic fields and surface temperature distributions. *Ap&SS*, 308:181–190, April 2007.

[200] F. A. Aharonian, S. R. Kelner, and A. Y. Prosekin. Angular, spectral, and time distributions of highest energy protons and associated secondary gamma rays and neutrinos propagating through extragalactic magnetic and radiation fields. *Physical Review D*, 82(4):043002, August 2010.

[201] F. Aharonian. *Very high energy cosmic gamma radiation, Heidelberg, Germany.* 2004.

[202] M. Padovani, D. Galli, and A. E. Glassgold. Cosmic-ray ionization of molecular clouds. *A&A*, 501:619–631, July 2009.

[203] M. Tavani and J. Arons. Theory of High-Energy Emission from the Pulsar/Be Star System PSR 1259-63. I. Radiation Mechanisms and Interaction Geometry. *ApJ*, 477:439–+, March 1997.

[204] M. Chernyakova, A. Neronov, F. Aharonian, Y. Uchiyama, and T. Takahashi. X-ray observations of PSR B1259-63 near the 2007 periastron passage. *MNRAS*, 397: 2123–2132, August 2009.

[205] M. Chernyakova, A. A. Abdo, A. Neronov, M. V. McSwain, J. Moldón, M. Ribó, J. M. Paredes, I. Sushch, M. de Naurois, U. Schwanke, Y. Uchiyama, K. Wood, S. Johnston, S. Chaty, A. Coleiro, D. Malyshev, and I. Babyk. Multiwavelength observations of the binary system PSR B1259-63/LS 2883 around the 2010-2011 periastron passage. *MNRAS*, 439:432–445, March 2014.

[206] M. Chernyakova, A. Neronov, B. van Soelen, P. Callanan, L. O'Shaughnessy, I. Babyk, S. Tsygankov, I. Vovk, R. Krivonos, J. A. Tomsick, D. Malyshev, J. Li, K. Wood, D. Torres, S. Zhang, P. Kretschmar, M. V. McSwain, D. Buckley, and C. Koen. Multi-wavelength Observations of the Binary System PSR B1259-63/LS 2883 around the 2014 Periastron Passage. *MNRAS*, 454:1358, August 2015.

[207] J. W. den Herder, A. C. Brinkman, S. M. Kahn, G. Branduardi-Raymont, and et al. The Reflection Grating Spectrometer on board XMM-Newton. *A&A*, 365: L7–L17, January 2001.

[208] L. Strüder, U. Briel, K. Dennerl, R. Hartmann, E. Kendziorra, N. Meidinger, E. Pfeffermann, C. Reppin, and et al. The European Photon Imaging Camera on XMM-Newton: The pn-CCD camera. *A&A*, 365:L18–L26, January 2001.

[209] G. G. Pavlov, C. Chang, and O. Kargaltsev. Extended Emission from the PSR B1259-63/SS 2883 Binary Detected with Chandra. *ApJ*, 730:2, March 2011.

[210] G. G. Pavlov, J. Hare, O. Kargaltsev, B. Rangelov, and M. Durant. An Extended X-Ray Object Ejected from the PSRB1259-63/LS2883 Binary. *ApJ*, 806:192, June 2015.

[211] M. Chernyakova, A. Lutovinov, J. Rodríguez, and M. Revnivtsev. Discovery and study of the accreting pulsar 2RXP J130159.6-635806. *MNRAS*, 364:455–461, December 2005.

[212] P. Ghosh. *Rotation and Accretion Powered Pulsars, by Ghost, P.; Hackensack, NJ 2007. World Scientific; 792pp.* 2007.

[213] R. A. Krivonos, S. S. Tsygankov, A. A. Lutovinov, J. A. Tomsick, D. Chakrabarty, M. Bachetti, S. E. Boggs, M. Chernyakova, F. E. Christensen, W. W. Craig, F. Fuerst, C. J. Hailey, F. A. Harrison, G. B. Lansbury, F. Rahoui, D. Stern, and W. W. Zhang. NuSTAR discovery of an unusually steady long-term spin-up of the Be binary 2RXP J130159.6-635806. *ApJ*, 809:140, August 2015.

[214] P. A. Evans, A. P. Beardmore, K. L. Page, J. P. Osborne, and et al. Methods and results of an automatic analysis of a complete sample of Swift-XRT observations of GRBs. *MNRAS*, 397:1177–1201, August 2009.

[215] A. A. Abdo, M. Ackermann, M. Ajello, A. Allafort, J. Ballet, G. Barbiellini, D. Bastieri, K. Bechtol, R. Bellazzini, B. Berenji, and et al. Discovery of High-energy Gamma-ray Emission from the Binary System PSR B1259-63/LS 2883 around Periastron with Fermi. *ApJL*, 736:L11, July 2011.

[216] F. Aharonian, A. G. Akhperjanian, K.-M. Aye, Bazer-Bachi, and et al. Discovery of the binary pulsar PSR B1259-63 in very-high-energy gamma rays around periastron with HESS. *A&A*, 442:1–10, October 2005.

[217] F. Aharonian, A. G. Akhperjanian, G. Anton, U. Barres de Almeida, and et al. Very high energy γ-ray observations of the binary PSR B1259-63/SS2883 around the 2007 Periastron. *A&A*, 507:389–396, November 2009.

[218] H.E.S.S. Collaboration, A. Abramowski, F. Acero, F. Aharonian, and et al. H.E.S.S. observations of the binary system PSR B1259-63/LS 2883 around the 2010/2011 periastron passage. *A&A*, 551:A94, March 2013.

[219] S. Johnston, R. N. Manchester, D. McConnell, and D. Campbell-Wilson. Transient radio emission from the PSR B1259-63 system near periastron. *MNRAS*, 302:277–287, January 1999.

[220] T. W. Connors, S. Johnston, R. N. Manchester, and D. McConnell. The 2000 periastron passage of PSR B1259-63. *MNRAS*, 336:1201–1208, November 2002.

[221] S. Johnston, L. Ball, N. Wang, and R. N. Manchester. Radio observations of PSR B1259-63 through the 2004 periastron passage. *MNRAS*, 358:1069–1075, April 2005.

[222] M. V. McSwain, W. Huang, D. R. Gies, E. D. Grundstrom, and R. H. D. Townsend. The B and Be Star Population of NGC 3766. *ApJ*, 672:590–603, January 2008.

[223] P. H. T. Tam, K. L. Li, J. Takata, A. T. Okazaki, C. Y. Hui, and A. K. H. Kong. High-energy Observations of PSR B1259-63/LS 2883 through the 2014 Periastron Passage: Connecting X-Rays to the GeV Flare. *ApJL*, 798:L26, January 2015.

[224] J. H. Simonetti, J. M. Cordes, and D. S. Heeschen. Flicker of extragalactic radio sources at two frequencies. *ApJ*, 296:46–59, September 1985.

[225] P. Favre, T. J.-L. Courvoisier, and S. Paltani. AGN variability time scales and the discrete-event model. *A&A*, 443:451–463, November 2005.

[226] V. Savchenko, A. Neronov, and T. J.-L. Courvoisier. Timing properties of gamma-ray bursts detected by SPI-ACS detector onboard INTEGRAL. *A&A*, 541:A122, May 2012.

[227] L. Cominsky, M. Roberts, and S. Johnston. Detection of X-ray emission from the PSR 1259-63/SS 2883 binary system. *ApJ*, 427:978–983, June 1994.

[228] E. D. Grundstrom and D. R. Gies. Estimating Be Star Disk Radii using Hα Emission Equivalent Widths. *ApJL*, 651:L53–L56, November 2006.

[229] D. R. Gies, W. G. Bagnuolo, Jr., E. K. Baines, T. A. ten Brummelaar, and et al. CHARA Array K'-Band Measurements of the Angular Dimensions of Be Star Disks. *ApJ*, 654:527–543, January 2007.

[230] A. T. Okazaki, S. Nagataki, T. Naito, A. Kawachi, K. Hayasaki, S. P. Owocki, and J. Takata. Hydrodynamic Interaction between the Be Star and the Pulsar in the TeV Binary PSR B1259-63/LS 2883. *PASJ*, 63:893, August 2011.

[231] J. Takata, A. T. Okazaki, S. Nagataki, T. Naito, A. Kawachi, S.-H. Lee, M. Mori, K. Hayasaki, M. S. Yamaguchi, and S. P. Owocki. Modeling High-energy Light curves of the PSR B1259-63/LS 2883 Binary Based on 3D SPH Simulations. *ApJ*, 750:70, May 2012.

[232] N. Wang, S. Johnston, and R. N. Manchester. 13 years of timing of PSR B1259-63. *MNRAS*, 351:599–606, June 2004.

[233] I. Negueruela, M. Ribó, A. Herrero, J. Lorenzo, D. Khangulyan, and F. A. Aharonian. Astrophysical Parameters of LS 2883 and Implications for the PSR B1259-63 Gamma-ray Binary. *ApJL*, 732:L11, May 2011.

[234] J. E. Bjorkman and A. C. Carciofi. Modeling the Structure of Hot Star Disks. In R. Ignace and K. G. Gayley, editors, *The Nature and Evolution of Disks Around Hot Stars*, volume 337 of *Astronomical Society of the Pacific Conference Series*, page 75, November 2005.

[235] A. C. Carciofi and J. E. Bjorkman. Non-LTE Monte Carlo Radiative Transfer. I. The Thermal Properties of Keplerian Disks around Classical Be Stars. *ApJ*, 639: 1081–1094, March 2006.

[236] E. Moreno, G. Koenigsberger, and D. M. Harrington. Eccentric binaries. Tidal flows and periastron events. *A&A*, 528:A48, April 2011.

[237] A. S. Miroshnichenko, J. Fabregat, K. S. Bjorkman, D. C. Knauth, N. D. Morrison, A. E. Tarasov, P. Reig, I. Negueruela, and P. Blay. Spectroscopic observations of the δ Scorpii binary during its recent periastron passage. *A&A*, 377:485–495, October 2001.

[238] A. S. Miroshnichenko, K. S. Bjorkman, N. D. Morrison, J. P. Wisniewski, N. Manset, H. Levato, M. Grosso, E. Pollmann, C. Buil, and D. C. Knauth. Spectroscopy of the growing circumstellar disk in the delta Scorpii Be binary. *A&A*, 408:305–311, September 2003.

[239] O. Kargaltsev, G. G. Pavlov, M. Durant, I. Volkov, and J. Hare. The Dynamic X-Ray Nebula Powered by the Pulsar B1259-63. *ApJ*, 784:124, April 2014.

[240] M. Massi and M. Kaufman Bernadó. Radio Spectral Index Analysis and Classes of Ejection in LS I $+61^{\rm deg}$ 303. *ApJ*, 702:1179–1189, September 2009.

[241] M. van der Klis. Fourier techniques in X-ray timing. In H. Ogelman and E. P. J. van den Heuvel, editors, *NATO Advanced Science Institutes (ASI) Series C*, volume 262 of *NATO Advanced Science Institutes (ASI) Series C*, page 27, 1989.

[242] R. Wijnands and M. van der Klis. The Broadband Power Spectra of X-Ray Binaries. *ApJ*, 514:939–944, April 1999.

[243] L. Sidoli, A. Pellizzoni, S. Vercellone, M. Moroni, S. Mereghetti, and M. Tavani. XMM-Newton observation of a spectral state transition in the peculiar radio/X-ray/γ-ray source LS I +61 303. *A&A*, 459:901–907, December 2006.

[244] J. Albert, E. Aliu, H. Anderhub, P. Antoranz, M. Backes, C. Baixeras, J. A. Barrio, H. Bartko, D. Bastieri, J. K. Becker, W. Bednarek, K. Berger, C. Bigongiari, A. Biland, R. K. Bock, G. Bonnoli, P. Bordas, V. Bosch-Ramon, T. Bretz, and I. Britvitch. Multiwavelength (Radio, X-Ray, and γ-Ray) Observations of the γ-Ray Binary LS I +61 303. *ApJ*, 684:1351–1358, September 2008.

[245] H. Anderhub, L. A. Antonelli, P. Antoranz, M. Backes, C. Baixeras, S. Balestra, J. A. Barrio, D. Bastieri, J. Becerra González, J. K. Becker, W. Bednarek, K. Berger, E. Bernardini, A. Biland, O. Blanch Bigas, R. K. Bock, G. Bonnoli, and P. Bordas. Correlated X-Ray and Very High Energy Emission in the Gamma-Ray Binary LS I +61 303. *ApJL*, 706:L27–L32, November 2009.

[246] J. M. Paredes, M. Ribó, V. Bosch-Ramon, J. R. West, Y. M. Butt, D. F. Torres, and J. Martí. Chandra Observations of the Gamma-Ray Binary LS I +61 303: Extended X-Ray Structure? *ApJL*, 664:L39–L42, July 2007.

[247] J. Li, D. F. Torres, S. Zhang, D. Hadasch, N. Rea, G. A. Caliandro, Y. Chen, and J. Wang. Unveiling the Super-orbital Modulation of LS I +61 303 in X-Rays. *ApJL*, 744:L13, January 2012.

[248] A. Melatos, S. Johnston, and D. B. Melrose. Stellar wind and stellar disc models of dispersion and rotation measure variations in the PSR B1259 - 63/SS2883 binary system. *MNRAS*, 275:381–397, July 1995.